Hydro-mechanical behaviour of pellet/powder mixture of bentonite and impact of gas migration

Arisleidy Mesa Alcantara

ADVERTIMENT La consulta d'aquesta tesi queda condicionada a l'acceptació de les següents condicions d'ús: La difusió d'aquesta tesi per mitjà del repositori institucional UPCommons (http://upcommons.upc.edu/tesis) i el repositori cooperatiu TDX (http://www.tdx.cat/) ha estat autoritzada pels titulars dels drets de propietat intel·lectual **únicament per a usos privats** emmarcats en activitats d'investigació i docència. No s'autoritza la seva reproducció amb finalitats de lucre ni la seva difusió i posada a disposició des d'un lloc aliè al servei UPCommons o TDX. No s'autoritza la presentació del seu contingut en una finestra o marc aliè a UPCommons (*framing*). Aquesta reserva de drets afecta tant al resum de presentació de la tesi com als seus continguts. En la utilització o cita de parts de la tesi és obligat indicar el nom de la persona autora.

ADVERTENCIA La consulta de esta tesis queda condicionada a la aceptación de las siguientes condiciones de uso: La difusión de esta tesis por medio del repositorio institucional UPCommons (http://upcommons.upc.edu/tesis) y el repositorio cooperativo TDR (http://www.tdx.cat/?locale-attribute=es) ha sido autorizada por los titulares de los derechos de propiedad intelectual **únicamente para usos privados enmarcados** en actividades de investigación y docencia. No se autoriza su reproducción con finalidades de lucro ni su difusión y puesta a disposición desde un sitio ajeno al servicio UPCommons No se autoriza la presentación de su contenido en una ventana o marco ajeno a UPCommons (*framing*). Esta reserva de derechos afecta tanto al resumen de presentación de la tesis como a sus contenidos. En la utilización o cita de partes de la tesis es obligado indicar el nombre de la persona autora.

WARNING On having consulted this thesis you're accepting the following use conditions: Spreading this thesis by the institutional repository UPCommons (http://upcommons.upc.edu/tesis) and the cooperative repository TDX (http://www.tdx.cat/?locale- attribute=en) has been authorized by the titular of the intellectual property rights **only for private uses** placed in investigation and teaching activities. Reproduction with lucrative aims is not authorized neither its spreading nor availability from a site foreign to the UPCommons service. Introducing its content in a window or frame foreign to the UPCommons service is not authorized (framing). These rights affect to the presentation summary of the thesis as well as to its contents. In the using or citation of parts of the thesis it's obliged to indicate the name of the author.

UNIVERSITAT POLITÈCNICA DE CATALUNYA
BARCELONATECH

Department of Civil and Environmental Engineering
Geotechnical Engineering and Geosciences

A thesis submitted to the Doctoral Programme in

Geotechnical Engineering

Hydro-mechanical behaviour of pellet/powder mixture of bentonite and impact of gas migration

Presented by

Arisleidy Mesa Alcantara

Supervisor: Prof. Enrique Romero Morales
Co-supervisor IRSN: Dr. Nadia Mokni

Barcelona, May 2021

Universitat Politècnica de Catalunya
BARCELONATECH

This research was funded by

Institut de Radioprotection et de Sûreté Nucléaire-IRSN (France) through a PhD collaboration agreement with International Centre for Numerical Methods in Engineering-CIMNE (Spain)

IRSN
INSTITUT
DE RADIOPROTECTION
ET DE SÛRETÉ NUCLÉAIRE

En memoria:
Mi querida Abuela Maria de las Nieve (Nene), mi queridad Mai. Te amare por siempre. (1952-2019)

ABSTRACT

The hydro-mechanical behaviour of MX80 bentonite pellet-based mixture (80% high-density pellets in dry mass and crushed granular powder) has been explored in this thesis within the context of the French 'Vertical Sealing Systems' (VSS, Cigeo) to appropriately seal these critical vertical pathways between the long-lived radioactive waste and the biosphere. The VSSs will undergo complex hydration scenarios: fast hydration from the upper surface by water from the Calcareous Oxfordian formation and slower hydration in the lateral direction arriving from the more impermeable Callovo-Oxfordian rock. These distinct hydrations will induce gas entrapment with time at the bottom of the seal, which will also be affected by gas generated by long-term metallic corrosion processes. Hence, a complete understanding of the VSSs under hydraulic and gas solicitations will be required, in which the French IRSN has played a significant role by supporting the current research and launching the VSEAL in situ tests currently being performed in Tournemire URL (France) at a scale of 1/10 of the VSS.

The thesis initially addressed a thorough characterisation of the as-poured mixture's initial and saturated states (both at the microstructural and macroscopic scales) and the mixture's hydro-mechanical behaviour and its components. The pellets constitute the shielding skeleton, whereas the crushed powder filled the inter-pellet space to reach an overall dry density of 1.49 Mg/m^3 that ensured a swelling pressure around 4 MPa. The hydro-mechanical characterisation involved water permeability tests under constant volume, water retention curves under different mechanical boundary conditions, swelling pressure tests and loading/unloading oedometer tests at different hydraulic states.

A mock-up at a scale of 1/100 of the VSS and independent control of fast hydration at the top and slow lateral hydration was developed, calibrated, and set up. The bentonite mixture (100 mm in diameter and 350 mm high) was asymmetrically wetted under constant volume conditions. The hydration cell was fully instrumented with pore pressure, total stress and relative humidity sensors, and four independent water pressure/volume controllers to monitor all processes comprehensively. A long-term hydration stage (around 300 days) was initially performed. At the end of this stage, gas was injected at a controlled volume/pressure rate at different boundaries (top and bottom) to determine the maximum gas

overpressure that the bentonite-based barrier could withstand. The gas experiments were also devoted to detecting gas flows at the interface in zones with low effective stresses.

The experimental program’s data allowed using different double porosity models and their coupled interactions via Code_Bright. The model parameters were determined based on the back-analysis of laboratory test results on the pellets, the powder and the mixture. Two modelling approaches were adopted to simulate the hydration phase at constant volume. A fully coupled elastic-plastic model (Barcelona Expansive Model in 2D axisymmetric representation) that considers the micro and macro-porosity, was initially used to simulate infiltration results and better understand the different coupled and double porosity processes involved. A numerical dual-porosity model (plane strain) was also considered to account for the mixture’s heterogeneous dry density distribution and represent the mixture’s double structure with pellets and powder as two distinct materials. The simulation results showed that the mixture on hydration tended to a more homogeneous distribution of porosity, despite starting from contrasting porosities of the components, as the pellets expanded and compressed the highly deformable clay powder. The models predicted a faster suction decrease rate (faster saturation rate), demonstrating the significant role of the intrinsic permeability on the mixture’s hydro-mechanical behaviour.

RESUMEN

Esta tesis estudia el comportamiento hidromecánico de una mezcla a base de pellets de bentonita MX80 (80% en masa de pellets de alta densidad añadiendo polvo) en el contexto de los "Vertical Sealing Systems" franceses (VSS, Cigeo) para sellar adecuadamente estas vías verticales críticas entre los residuos radiactivos almacenados y la biosfera. Estos VSS están sometidos a una hidratación compleja: una hidratación rápida desde la parte superior de la formación calcárea oxfordiana y una hidratación lateral más lenta desde la argilita callovo-oxfordiana. Estas distintas hidrataciones favorecen el atrapamiento de gas en el fondo del sello, que también se verá afectado por el gas generado por los procesos de corrosión metálica a largo plazo. Por ende, se requiere una visión completa de los VSS bajo solicitaciones hidráulicas y de gas, en la que el IRSN francés ha desempeñado un papel importante al apoyar la investigación actual y poner en marcha la prueba in situ VSEAL, que se está realizando actualmente en el URL de Tournemire (Francia) a una escala de 1/10 del VSS.

Primero la tesis realiza una caracterización exhaustiva de los estados inicial y de saturación de la mezcla vertida (a escala micro-estructural y macroscópica), así como del comportamiento hidromecánico de la mezcla y de sus componentes. Los pellets constituyen el esqueleto, mientras que el polvo rellena el espacio inter-pellet para alcanzar una densidad seca global de 1.49 Mg/m^3 con una presión de hinchamiento alrededor de 4 MPa. La caracterización incluyó ensayos de permeabilidad al agua a volumen constante, curvas de retención a diferentes condiciones de contorno mecánicas, ensayos de presión de hinchamiento y edométricos de carga/descarga a distintos estados hidráulicos.

Se desarrolló, calibró y puso a punto una columna a escala 1/100 del VSS y con control independiente de la hidratación superior rápida y lateral lenta. La muestra de bentonita (100 mm de diámetro y 350 mm de altura) se humedeció en condiciones de volumen constante. La columna de hidratación estaba instrumentada con transductores de presión de poros y tensión total, sensores de humedad relativa y cuatro controladores independientes de presión/volumen de agua. Inicialmente se realizó una etapa de hidratación de unos 300 días de duración. Al final de esta etapa, se inyectó gas a una velocidad controlada de volumen/presión en dos diferentes contornos (superior e inferior) para determinar la máxima

sobrepresión de gas que podía soportar la barrera. Los experimentos también se centraron en la detección de flujos de gas en la interfase en zonas con bajas tensiones efectivas.

Los datos del programa experimental han permitido utilizar diferentes modelos de doble porosidad utilizando Code_Bright. Los parámetros del modelo se determinaron a partir de los resultados de laboratorio de los pellets, el polvo y la mezcla. Se adoptaron dos enfoques de modelación diferentes para simular la fase de hidratación a volumen constante. Inicialmente se utilizó un modelo elasto-plástico (Modelo Expansivo de Barcelona en una representación axisimétrica 2D), que considera la micro y la macro-porosidad para comprender mejor los diferentes procesos acoplados y de doble porosidad. También se consideró un modelo numérico de doble porosidad (deformación plana) para considerar la distribución heterogénea de la mezcla y representar la doble estructura con pellets y polvo como dos materiales distintos. Los resultados de la simulación evidenciaron que la mezcla al hidratarse tendía a una distribución más homogénea de la porosidad, a pesar de partir de porosidades contrastantes de las componentes, a medida que los pellets expandían y comprimían el polvo altamente deformable. Los modelos predijeron una tasa de disminución de la succión más rápida (tasa de saturación más rápida), lo que evidencia el papel significativo de la permeabilidad intrínseca en el comportamiento hidromecánico de la mezcla.

AGRADECIMIENTOS

En primer lugar, agradecer al ser que nos da fuerza para seguir cuando no tenemos fuerza, cuando pensamos que no hay solución a los problemas; Él nos ayuda a encontrar lo que nos conviene, que cuando nos quita algo que queremos es porque nos tiene cosas mejores y necesitamos las manos libres para tomarlas. A ti Dios por esta oportunidad y por todo lo que me permites aprender y conocer.

A mis padres Efraín Mesa y Mariana Alcántara, porque siempre me apoyan en mis decisiones y me ayudan a seguir cumpliendo mis metas. A mis hermanos que amo y adoro con toda mi alma, Ericka y Edwin. A mis familiares por su apoyo y su amor, que a pesar de la distancia siempre tratan de hacerme sentir querida. A mi persona favorita, *mi hija Ana Marí*, que sin saberlo hacía que mis días más difíciles se convirtieran en felices tan solo con verla y abrazarla. A Wilson Ramírez por estar ahí dandome apoyo en este camino. A mis sobrinos hermosos Erienny, Edison Romariel y Alexail por llenar mis dias de alegria con una video llamada.

A mi tutor Enrique Romero, por dedicarme tiempo de su colapsada agenda y confiar en mí para llevar a cabo este proyecto. También agradecer la financiación de IRSN que ha hecho posible el desarrollo de esta tesis doctoral, pero sobre todo a las personas implicadas en este proyecto como es el caso de mi co-tutora Nadia Mokni.

A Mercedes Sondon (técnica de laboratorio) por ayudarme a resolver todos los inconvenientes que se presentaron durante la elaboración del equipo. A Tomás Pérez (técnico del laboratorio) que a pesar de estar jubilado siempre estaba disponible para ayudarme con cualquier inquietud e inconveniente que se me presentara. También a Rodrigo Gómez, Núria Sau and Laura González por la ayuda y los consejos durante esta etapa.

En el transcurso de cada etapa de nuestra vida nos encontramos con personas que nos enseñan que la vida no es más que la acumulación de momentos buenos y malos que nos ayudan a construir nuestro edificio. Gracias a Claudia Matos por estar ahí con su frase ¨tu puede mana¨ que me ayuda a reiniciar mi mente y volver a la carga. A Janil por nuestro ratito de tomar el café y desahogarnos con nuestras penas. Ramona (Ma) por siempre estar para mí. A mi amigos y compañeros de doctorado que fueron un apoyo en el transcurso de este camino que de una u otra forma hicieron que este recorrido sea fácil y divertido: Sheila Cordone, Gaia Di Carluccio,

Jatnna Sánchez, Ricardo Rorato, Ferran Parera, Gerald, Ramon Barboza, Miquel de Francisco y Alessandro.Fraccica, Celia Riera, Gerald Matas, Ningning Zhang, Clara Alvarado.

Si fuera fácil cualquiera lo haría,
así que, lucha por tus metas,
porque nadie lo hará por ti.
Anónimo.

TABLE OF CONTENTS

LIST OF FIGURES

LIST OF TABLES

ABBREVIATIONS / ACRONYMS

AITEMIN	Asociación para la Investigación y Desarrollo Industrial de los Recursos Naturales (Association for the Research and Industrial Development of Natural Resources) (Madrid)
ANDRA	Agence Nationale pour la gestión des Déchets RAdioactives (France)
ASTM	American Society of Testing Materials BMT
BBM	Barcelona Basic model
BexM	Barcelona Expansive Model
CEC	Cation exchange capacity
EB	Engineered barrier experiment
EBS	Engineered Barrier System
FE	Full-scale experiment
FEBEX	Full Scale Engineered Barrier Experiment
FESEM	Field Emission Scanning Electron Microscopy
FoCa	French Fourges-Cahaignes smectite, used as the reference material in the ANDRA disposal concept.
HE-E	Heating experiments
HLW	High Level radioactive Wastes
HPVC	High pressure-volume controller
ILW	Intermediate-level
IRSN	Institute for Radiological Protection and Nuclear Safety (France)
MC	Microstructural comression
MIP	Mercury Intrusion Porosimetry
MS	Microstructural swelling
NL	Neutral Loadig
PSD	Pore Size Distribution
PVC	Pressure-volume controller
RESEAL	Repository Sealing in an Argillaceous Host Rock
SEALEX	SEALing performance Experiments
SEM	Scanning Electron Microscopy
SSA	Specific surface area of clay particles
URL	Underground Research Laboratory
Vseal	Vertical sealing project.
VSS	Vertical Sealings Systems

SYMBOLS USED

a_1, a_2	Parameter material (pellet and powder) dependence of κ_i and κ_s
b	Parameter of the exponential law
$d\varepsilon_v^e$	Increment of the total elastic volumetric strain
$d\varepsilon_v^{emicro}$	Increment of the volumetric elastic strain in changes in the micro-porosity
$d\varepsilon_v^{eMacro}$	Increment of the volumetric elastic strain in changes in the macro-porosity
$d\varepsilon_v^{p\,Macro}$	Total plastic macrostructural strain

$d\varepsilon_{vLC}^{p}$	Plastic deformations induced when yielding macrostructure
du	Differences of gas pressures
dx	Differences of heigh
D_{pow}	Maximum particle size of powder
e	Void ratio
e_{int}	Intruded void ratio
e^{micro}	Microstructural void ratio
e^{Macro}	Microstructural void ratio
$e^{micro\ pow}$	Microstructural void ratios of powder
$e^{micro\ pe}$	Microstructural void ratios of pellet
e_{w}	Void ratio of water
E_{pex}	Elastic modulus of perspex
f	*P*artially filling of powder in the inter-pellet pores
f_{c0}	BExM parameter for micro–macro coupling functions when SI is activated
f_{c1}	BExM parameter for micro–macro coupling functions when SI is activated
f_{S0}	BExM parameter for micro–macro coupling functions when SD is activated
f_{S1}	BExM parameter for micro–macro coupling functions when SD is activated
$f(x)$	*P*ore size density function
f_{α}	Interaction functions
G	Shear modulus.
k_{rl}	Liquid relative permeability
F	*V*olumetric degree of powder filling
k_{o}	Reference Intrinsic permeability
K	Intrinsic permeability
K_{exp}	Intrinsic permeability using exponential law
K_{Ko}	Intrinsic permeability using Kozeny`s model.
K_{g}	Intrinsic permeability to gas
K_{pe}	Intrinsic permeability of pellet
L_{pex}	Length of perspex
L_{steel}	Length of steel
n	Power (typically 3)
n_{S}	BExM parameter for micro–macro coupling functions when SD is activated
n_{c}	BExM parameter for micro–macro coupling functions when SI is activated
M	BBM and BExM slope of the critical state line
M_{w}	Molecular mass of water
p	Net stress
$\mathrm{p}_{\mathrm{atm}}$	Atmospheric pressure
p_{c}	BBM and BExM reference pressure for the p_0 function [MPa]
p_{m}	Absolute non-wetting mercury pressure
p_{0}^{*}	BBM and BExM pre-consolidation mean stress for saturated soil [MPa]
p'	Mean effective stress
P_{0}	Measured P at certain temperature
P_{to}	BExM cohesion for suction equal to zero [MPa]
$P_{w\mathrm{f}}$	Final liquid pressure
P_{wi}	Initial liquid pressure
q	Liquid flow of gas follow Darcy's law
$\mathrm{q_h}$	Horizontal liquid flow follow Darcy's law

q_s	Deviatoric stress
q_v	Vertical liquid flow follow Darcy’s law
Q_h	Horizontal flow
Q_v	Vertical flow
r	BBM and BExM parameter for the slope void ratio – mean net stress at
R	Gas constant
RH	Relative humidity
S_e	Effective degree of saturation
s	Total suction
s_f	Final measured suction)
s_{pow}	Suction of powder
s_{pe}	Suction of pellet
S_r	Degree of saturation
S_{ls}	Maximum saturation
S_{rl}	Residual saturation
t_0	Initial time
T	Absolute temperature
T_{fs}	Total effective stress
T_s	Total stress
v^m	BExM Poisson’s ratio
V_p^{micro}	Volume of micropores
V_P^{Macro}	Volume of macropores
V_t	Total volume
V_s	Volume of solid
w	Water content
x	Entrance pore size
x_{max}	Maximum pore sizes detected by MIP
x_{min}	Minimum pore sizes detected by MIP

Greek symbols

α	Parameter of shape factor, tortuosity and connectivity
β	BBM and BExM parameter for the slope void ratio – mean net stress at variable suction [MPa-1]
β_m	Parameter describes the change in e^{micro}
Δe	Delta void ratio
$\Delta\sigma$	Delta vertical stress
$\Delta\sigma'$	Delta effective vertical stress
ΔP_w	Delta liquid pressure
Δ_t	Delta time
ε_a	Axial deformation
ε_r	Radial deformation of perspex
$\overline{\varepsilon_r}$	Weighted radial deformation
$\varepsilon_{r\ steel}$	Radial deformation of steel
ε_t	Tensile deformation
ε_v	Volumetric deformation
ε_q^e	Shear strain

θ_{Hg}	Angle between mercury and the particle surface
κ	Compressibility parameter on unloading (post-yield)
κ_i	Slope of the unload/reload curve in the (e - lnp') diagram for pellet and powder.
κ^{Macro}	BExM elastic compressibility parameter at macro level for changes in mean net stress
κ^{micro}	BExM elastic compressibility parameter at micro level for changes in mean effective stress
κ_s	Slope of the unload/reload curve in the (e - ln((s+0.1)/0.1)) diagram
κ_s^{Macro}	BExM elastic macro compressibility parameter for changes in (total) suction
λ	Shape function for retention curve
$\lambda(s)$	Compressibility parameter on loading (post-yield)
$\lambda(0)$	BBM and BExM slope of void ratio mean net stress curve at null suction
μ_a	Air dynamic viscosity
μ_w	Water dynamic viscosity
ρ_d	Dry density
$\rho_{d\ mix}$	Dry density of the mixture
$\rho_{d\ pack}$	Dry density of packing of pellets
$\rho_{d\ pe}$	Dry density of pellet
$\rho_{d\ pow}$	Dry density of powder
$\rho_{d\ pow}^{min}$	Minimum dry density of the powder
ρ_s	Density of solids
ρ_w	Density of pure water.
σ_{ap}	Applied stress in the column during the calibration of the sensors
σ_{Hg}	Tension of non-wetting phase
σ_t	Tensile strength of perspex
σ_{tmax}	Maximum tensile strength
σ_{sp}	Swelling pressure
σ_v	Vertical stress
σ_i	Initial vertical stress
σ_i'	Initial effective vertical stress
σ_f	Final vertical stress
ϕ_0	Reference total porosity
ϕ	Total porosity
$\phi_{\mathrm{int}\ pe}$	Intruded porosity of pellet
$\phi_{\mathrm{int}\ pow}$	Intruded porosity of powder
ϕ_{Pack}	Porosity of packing of pellet
ϕ^{micro}	Microstructural porosity
$\bar{\phi}_{micro}$	Microporosity over the volume of aggregates
ϕ^{Macro}	Macrostructural porosity
ϕ_0^{Macro}	Reference macrostructural porosity
ϕ_{pow}	Total porosity of powder

1. INTRODUCTION

1.1. Background of the thesis

Nuclear radioactive wastes are inevitably generated from many industrial activities, such as electricity production in nuclear power plants, scientific research, and nuclear medicine. These wastes are treated differently depending on their activity and their half-life period of radioactive decay. The most dangerous wastes are high-level (HLW) and intermediate-level (ILW) radioactive wastes, containing long-lasting and heat-emitting radionuclides. Consequently, the countries that produce or use nuclear energy have a great concern about how to manage the safety of these radioactive wastes.

The internationally accepted solutions for the safe storage of HLWs and ILWs consist in the disposal of the wastes in deep and stable geological formations (typically plastic clay, claystone or granite) with an adequate capacity of isolation (low permeability). The host formation is complemented by placing an Engineered Barrier System (EBS), introduced through technological activities, around the radioactive wastes.

Different configurations of deep geological disposal have been considered (Sellin & Leupin, 2013), which rely on a multi-barrier concept. The metallic canister is the first barrier. Pure bentonite and bentonite-based mixtures are often used as a buffer that surrounds the waste packages (canisters) and as a backfill that seals the disposal galleries and vertical shafts. These bentonite-based buffers/backfills display low permeability under saturated states, high radionuclide migration retardation properties, and elevated swelling pressures on saturation (Pusch, 1979; Yong *et al.*, 1986; Villar & Lloret, 2008). This high swelling pressure ensures the closure of technological gaps and the fissures in the excavation-damaged zone around the emplacement tunnels.

Different types of bentonite-based EBSs have been proposed. Pure bentonite has been used either in high-density blocks, pellets and granular bentonite. A combination of blocks and pellets (dry density 1.97Mg/m^3) was used in the 'Engineered Barrier' *in situ* tests at an overall dry density between 1.3–1.5 Mg/m^3 (Mayor *et al.,* 2005; Hoffmann, 2005; Hoffmann *et al.*, 2007). Sand and granular bentonite mixtures have also been considered at different proportions (Karnland *et al.*, 2008; Tang *et al.*, 2008; Wang *et al.*, 2012; Saba, 2014; Saba *et al.*, 2014). A binary mixture of crushed Callovo-Oxfordian claystone (COXc) and granular bentonite has also been proposed to re-use the excavated material of the host rock (Wang *et al.*, 2012; Cuisinier *et al.*, 2014; Zeng *et al.*, 2019; Middelhoff, 2020). Imbert & Villar (2006) studied the hydro-mechanical behaviour of a binary mixture of 50% pellets and 50% powder of FoCa clay. Moreover, an MX80 bentonite mixture of high-density pellets and granular bentonite from crushed pellets at a mass proportion of 80/20 has been recently investigated by Molinero-Guerra, (2018); Mokni *et al.* (2019); Molinero-Guerra *et al.* (2020). Specifically, the current thesis will study this latter mixture within the context that will be explained below.

A long-term issue that affects the integrity of the EBSs is the gas production and accumulation due mainly to anaerobic corrosion of the metallic canisters, the degradation of organic substances and radiolysis of water. The rate of gas production will depend on the waste composition, availability of water and disposal concept. Nevertheless, in scenarios where the rate of gas production exceeds the rate of gas diffusion, gas will build up and cause local overpressure on the EBSs (Horseman *et al.,* 1997; Harrington *et al.*, 2017). A crucial aspect of the gas generated is how the gas will migrate away from the repository. Marshall *et al.* (2005) presented a phenomenological description of the different gas transport mechanisms typically involved in EBSs and host rocks, some of which occur simultaneously. The transport mechanisms in EBSs are diffusive transport of gas dissolved in the pore-water, visco-capillary two-phase flow with invading gaseous phase, and dilatancy-controlled gas flow through pathways and interfaces. Several experiments have been carried out in the laboratory to study the gas migration in compacted bentonite and binary mixtures (Romero *et al.*, 2003; Horseman *et al.*, 2004; Arnedo *et al.*, 2008; Graham *et al.*, 2012; Liu *et al.*, 2014; Harrington *et al.*, 2017; Villar *et al.*, 2020; Gutiérrez-Rodrigo *et al.*, 2021; Gonzalez-Blanco *et al.*, 2020). However, no studies have been conducted to investigate the impact of gas migration on a mixture composed of pellets and granular bentonite to the author's knowledge.

1.2. Context of the investigation within Vertical Sealing Systems

The French agency of radioactive waste management (ANDRA) bases its reference concept for disposing of long-lived radioactive waste in a deep clay-rich Callovo-Oxfordian sedimentary rock formation (Cigéo Project, ANDRA Dossier, 2005). The disposal system relies on this natural barrier, and particularly on the vertical closure structures that ensure safety over the long term. These Vertical Sealing Systems (VSS) are crucial to properly close the main potential pathways between nuclear waste and the biosphere. Figure 1-1 presents a schematic of the different vertical and horizontal sealing systems. As observed, the VSS will experience fast hydration from the upper surface by water coming from the Calcareous Oxfordian, leading to a rapid increase of water pressure in this zone, which should rapidly reach 3 to 4 MPa. Simultaneously, slower hydration occurs in the lateral (radial) direction arriving from the more impermeable Callovo-Oxfordian formation (Figure 1-1). Another schematic of the vertical bentonite core confined between two concrete blocks is presented in Figure 1-2, together with a simplified schematic of the saturation process of the VSS. Over time gas will be entrapped by this dominant upper hydration, and depending on the rate of gas production of the metallic corrosion and other phenomena, gas may reach the VSS while the bentonite core is only partially saturated. Therefore, understanding the gas migration process of the VSSs, either through the bentonite core or throughout the bentonite/rock interface, is of great importance.

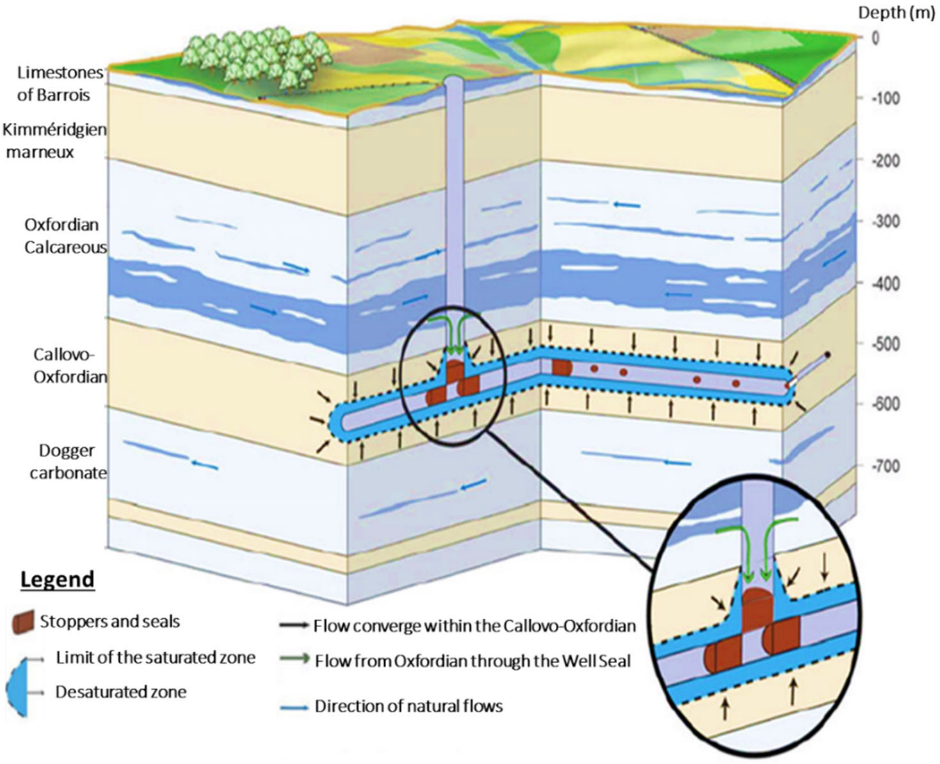

Figure 1-1. Schematic of the saturation of sealing systems (modified after ANDRA Dossier 2005).

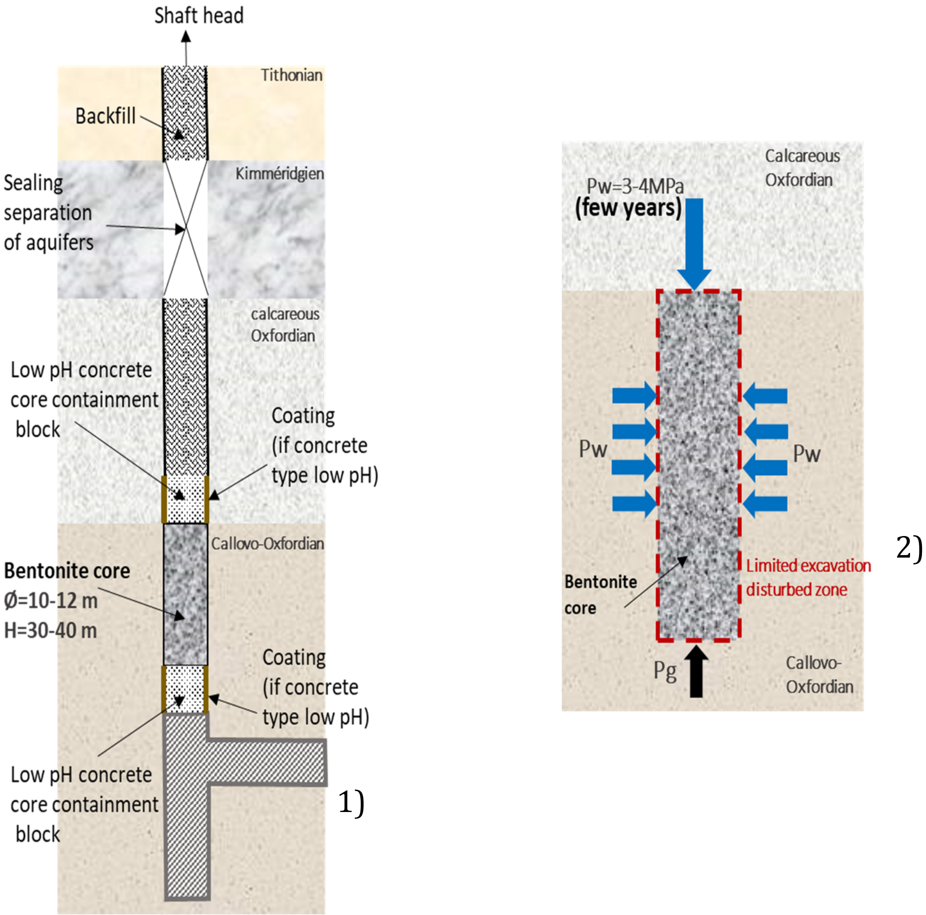

Figure 1-2. 1) Schematic of the shaft with bentonite core between concrete blocks. 2) Saturation schematic of VSSs. Modified after Mokni (2016).

1.3. In situ VSEAL Project

Within the context of the VSSs, the French Institute for Radiological Protection and Nuclear Safety (IRSN) has launched the 'VSEAL Project' to study the impact of gas migration on the long-term performance of these sealing systems. The 'VSEAL Project' relies on a series of *in situ* experiments performed in IRSN's Underground Research Laboratory (URL) (Tournemire, France) at a scale of 1/10 of the VSS. These experiments aim at studying the vertical barrier's asymmetric hydration process and its consequences on gas migration at different hydraulic states.

Two VSEAL *in situ* tests will be emplaced at the URL in the Toarcian argillite formation. Two vertical boreholes will be drilled in the north_08 Gallery or in Niche_08 (Figure 1-3). Installation and drilling will be based on the previous experience obtained from the SEALEX experiments (Barnichon & Deleruyelle, 2009; Barnichon *et al.*, 2012; Mokni & Barnichon, 2016a; Mokni & Barnichon, 2016b). The bentonite buffer constituted by high-density MX80 bentonite pellets (80% mass ratio) and crushed bentonite powder (produced by crushing pellets) prepared at a dry density mixture around 1.49 Mg/m^3 will be artificially re-saturated by water injection from the top. *In situ* injection rate should correspond to natural disposal conditions. Radial hydration of the bentonite core will be ensured by water coming from the host rock.

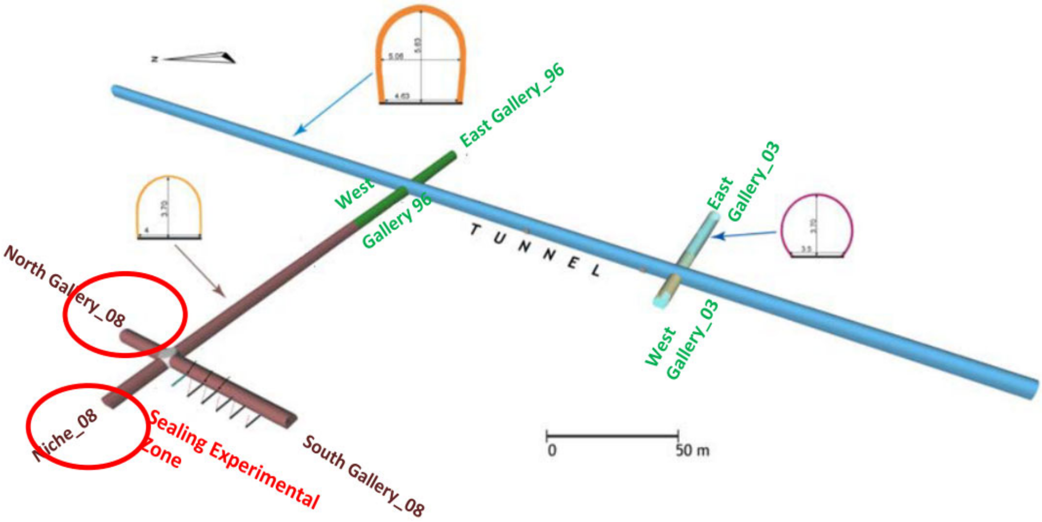

Figure 1-3. Tournemire URL. The red circles represent locations for VSEAL in situ tests (Mokni, 2016).

The first *in situ* test VSEAL_1 will be a reference test used to observe bentonite re-saturation without gas injection. For the second *in situ* test Bexm_2 gas will be injected from the bottom surface during the re-saturation phase at time $t_0+\Delta_t$ to observe the perturbation induced by gas. In each borehole, multiple pore pressure, total stress, and RH sensors will be installed to follow the swelling pressure evolution and water saturation. Various injection gas phases could be performed once the bentonite reaches full saturation.

The generic layout of VSEAL *in situ* experiments is based on a swelling clay core (MX80 pellets/granular bentonite confined between two packers). All these elements are inserted in a vertical large diameter borehole excavated in Tournemire argillite (Figure 1-4). The core will be emplaced out of the gallery EDZ. Water will be injected from the top surface through injection lines connected to the top packers, which will slowly saturate the upper part of the bentonite core. For VSEAL_2, during the saturation phase, the gas will be injected from the bottom surface to observe the perturbation induced by the gas. Bottom and top hydration systems will be connected to the respective gas and water reservoirs.

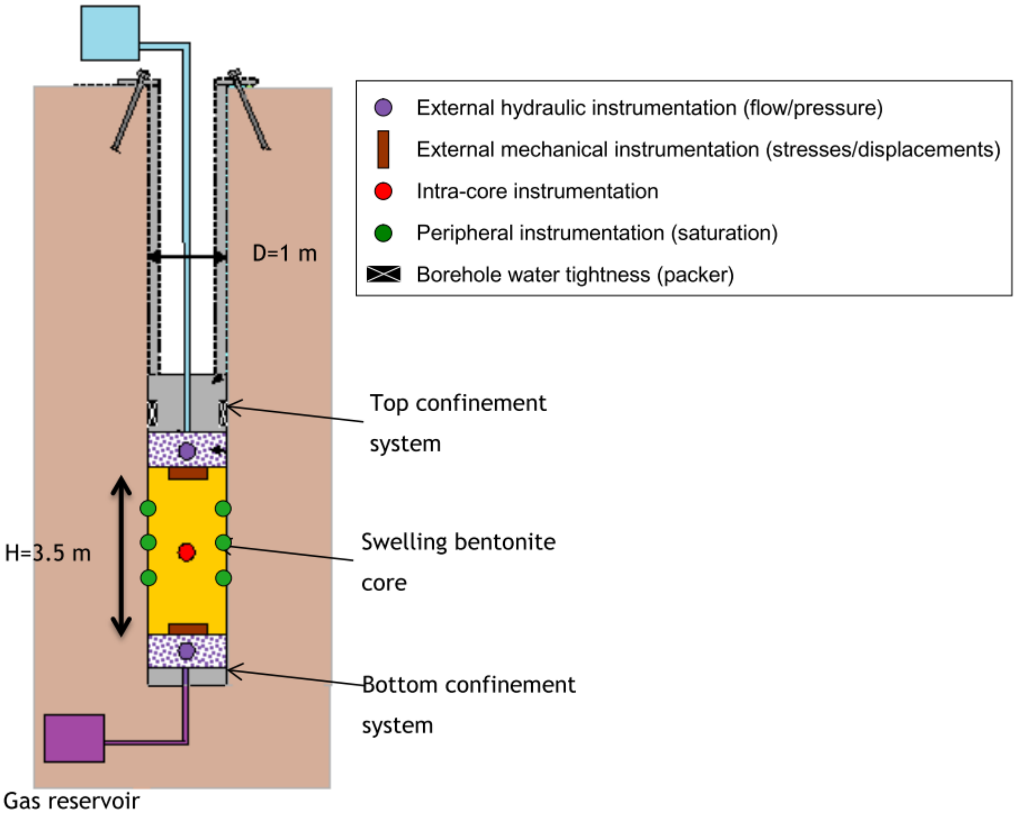

Figure 1-4. Schematic of the main components of VSEAL in situ tests (Mokni, 2016).

This thesis is framed within this specific project to provide experimental support (at laboratory mock-up scale) of the asymmetric hydration of the bentonite core, as well as to understand the impact of gas injection when the core is still under partially saturated conditions, and the lateral swelling pressure has not reached its full capacity. A new axisymmetric cell (100 mm in diameter and 350 mm high) has been developed at a reduced scale of 1/100 of the VSS (i.e., at 1/10 of the *in situ* VSEAL test) to reproduce this asymmetric hydration using independent top (fast injection) and radial (slow injection) water pressure systems. It also allows performing gas injections at different locations of the core of the bentonite mixture (top and bottom boundaries) and under various hydraulic states.

The pellet-powder mixture used as bentonite core has been extensively characterised by Molinero-Guerra (2018) and Molinero-Guerra *et al.* (2020), not only at the phenomenological scale (hydro-mechanical behaviour) but also at the microstructural scale using X-ray computed microtomography (Molinero-Guerra *et al.*, 2017). However, this thesis complements the study by focusing on the hydro-mechanical characterisation of each of the components (pellets and powder), besides the mixture. Loading/unloading oedometer tests at different hydraulic states, as well as wetting under load and swelling pressure tests, have been carried on the mixture and each of the components. This characterisation approach has allowed a better understanding of the laboratory mock-up test and the progressive homogenisation of the medium by the simulation of the hydration process considering the representation of the pellets and powder. In this case, pellets of bentonite and powder are simulated as two distinct materials that progressively tend to approximately the same porosity on hydration.

1.4. Objectives and methodology followed

The thesis follows an experimental methodology to provide quantitative data to understand better the hydro-mechanical and gas migration behaviour of an MX80 bentonite mixture constituted by 80%/20% (mass basis) of high-density pellets and powder. More specifically, the objectives of the research addressed the following topics:

- To perform a microstructural characterisation –focusing on pore size distribution– of the binary mixture under as-prepared conditions and its evolution during hydration at constant volume conditions using different techniques (mercury intrusion porosimetry and field-emission scanning electron microscopy).

- To develop a preparation protocol of the mixture that ensures low segregation of the powder together with adequate control of the initial heterogeneity. The heterogeneity of the mixture is verified by computerised axial tomography.

- To study the hydro-mechanical properties of the mixture and its components, focusing on compressibility on loading, collapse/swelling properties on wetting at different stresses, swelling pressure evolution during wetting, water permeability and water retention properties. The gas migration properties of the saturated mixture have also been studied under oedometer conditions using controlled pressure gas injection tests.

- To design and develop a small scale and constant volume mock-up (100 mm in diameter and 350 mm high) to mimic the saturation process of the VSEAL test with independent top and lateral hydration systems, as well as with gas injection at different boundaries (top and bottom). The prototype is fully automated with pressure/volume controllers for liquid and gas, and instrumented with water pressure transducers and total pressure cells at different heights and on top/bottom caps. It also includes miniature and removable relative humidity sensors with loggers to monitor the hydration process.

- To analyse the gas migration process at different saturation states with a controlled rate of gas injection tests at the top or bottom boundary of the constant volume cell. The remaining boundaries will be kept at constant fluid pressure and monitoring outflow/inflow volumes.

- To model the components of the binary mixture explicitly using detailed information of the properties of pellets and powder with a coupled numerical analysis with Code_Bright to study the hydro-mechanical response during constant volume hydration.

- To simulate selected stages of the tests mentioned above with a THM coupled finite element code (Code_Bright, Olivella *et al.*, 1996) focusing on the constant volume hydration process and aiming at better understanding the different coupled and double porosity processes involved. The hydro-mechanical properties of the mixture associated with a double-porosity model are calibrated from the different experimental result.

1.5. Outline of the thesis

The results of this work are presented in 7 chapters covering the developments achieved during the PhD thesis. The chapters are organised in a logical sequence and adapted to already published papers and future publications. The thesis starts with the properties of the studied mixture and components, followed by a description of their hydro-mechanical behaviour. It follows by explaining the experimental equipment designed and constructed for this research with protocols and the coupled hydro-mechanical results. Finally, it addresses some simulations of the mock-up test under different conditions.

Chapter 1 introduces the background and objectives of the thesis.

Chapter 2 deals with the experimental program performed to study the characterization of the mixture and its components from a microstructural point of view with mercury intrusion porosimetry and field-emission scanning electron microscopy. Moreover, this chapter explains the verification of the segregation of the powder, the different protocols followed to prepare the mixture and the verification of the heterogeneity by computerised axial tomography scans.

Chapter 3 is devoted to the hydro-mechanical experiments (intrinsic permeability, water retention, swelling under load, swelling pressure and compressibility properties of the mixture). It also includes the modelling of the loading/unloading tests with a double-porosity framework.

Chapter 4 is devoted to present the laboratory mock-up (fully instrumented axis-symmetric infiltration/gas injection column) at constant volume conditions and the protocols used. The results of the hydration phase are also described.

Chapter 5 describes and interprets the experimental results of the gas injection tests. It presents the preliminary gas injection test under oedometer conditions, followed by the two gas tests performed on the infiltration column and hydration results after the first gas injection test.

Chapter 6 presents two numerical analyses. The first one considers the components of the binary mixture explicitly in the coupled numerical analysis with Code_Bright during constant volume hydration. The second one uses the Barcelona Expansive

Model (BExM) to describe the mechanical behaviour of the double porosity mixture (micro and macro-porosity) taking into account the correct hydraulic boundary conditions from the laboratory mock-up test.

Finally, **Chapter 7** concludes with a summary, conclusions and outlooks for future works.

1.6. Research activities performed throughout the thesis

The activities are presented chronologically.

PhD thesis proposal defence: "Hydro-mechanical behaviour of binary pelletised mixtures of bentonite and impact on gas migration" within the Doctoral Programme of Geotechnical Engineering, Barcelona. ***February 2017***.

Report: Hydro-mechanical behaviour of binary pelletised mixtures of bentonite and impact of gas migration within the context of 'VSEAL Project: Long-term performance of vertical sealing systems and impact of gas migration *PhD collaboration agreement with IRSN.* First progress report ***(June 2016-June 2017).*** A. Mesa-Alcantara, E. Romero and N. Mokni.

Progress meeting: between IRSN (N.Mokni) and CIMNE/UPC (E. Romero and A. Mesa-Alcantara) in Paris. ***June 30th, 2017***.

Progress meeting: between IRSN (N.Mokni) and CIMNE/UPC (E. Romero and A. Mesa-Alcantara) in Paris. ***February 16th, 2018.***

Oral presentation: A. Mesa-Alcantara, E. Romero and N. Mokni. Mock-up demonstration tests to support the VSEAL Project. Young Researchers Meeting 2018 in IRSN, Paris. ***February 17th, 2018***. (Speaker: A. Mesa-Alcantara).

Report: Hydro-mechanical behaviour of binary pelletised mixtures of bentonite and impact of gas migration within the context of 'VSEAL Project: Long-term performance of vertical sealing systems'. *PhD collaboration agreement with IRSN.* Second progress report ***(June 2017-April 2018).*** A. Mesa-Alcantara, E. Romero and N. Mokni.

Progress meeting: between IRSN (N. Mokni) and CIMNE/UPC (E. Romero and A. Mesa-Alcantara) in Paris. ***June 26th, 2018.***

Research seminary and oral presentation: ALERT Olek Zienkiewicz Winterschool 2018. Natural versus compacted clayey soils: from micro to macro behaviour and modelling. Bari, ***5th-9th November 2018***, Politecnico di Bari, Italy. *Lectures by Prof. E. Romero in which part of the results of the current investigation was presented*.

Seminary: Workshop, Management Meeting and Technical Lectures within the European project TERRE Horizon 2020. Universitat Politècnica de Catalunya. Barcelona. ***29th -30th January 2019.***

Oral presentation: A. Mesa-Alcantara, E. Romero and N. Mokni. *Mock-up demonstration tests to support the VSEAL Project. Long-term hydration and impact of gas migration on sealing systems* in IRSN, Paris. ***February 12th, 2019.*** (Speaker: A. Mesa-Alcantara).

Oral presentation: A. Mesa-Alcantara, E. Romero and N. Mokni. Mock-up demonstration tests to support the VSEAL Project. Long-term hydration and impact of gas migration on sealing systems. *Young Researchers Meeting 2019* in IRSN, Paris. ***February 13th, 2019***. (Speaker: A. Mesa-Alcantara).

Seminary: CODE_BRIGHT Workshop. Universitat Politècnica de Catalunya, Barcelona. ***16th -17th May 2019.***

Supervision of the master's thesis: *Modelación mezcla de pellets y polvo de bentonita en condiciones de hidratación*. Universitat Politècnica de Catalunya. Barcelona. ***October 2018 - May 2019***. Author: Camilo Ernesto Mejia Sanchez. Supervisors: S. Olivella, A. Mesa-Alcantara and E. Romero.

Report: Hydro-mechanical behaviour of binary pelletised mixtures of bentonite and impact of gas migration within the context of 'VSEAL Project: Long-term performance of vertical sealing systems'. *PhD collaboration agreement with IRSN.* Second progress report ***(April 2018-June 2019).*** A. Mesa-Alcantara, E. Romero and N. Mokni.

Seminary: ALERT Workshop and School 2019, Aussois, ***France. 30th September - 4th October 2019.***

Poster presentation: Hydro-mechanical modelling of infiltration test to study the behaviour of binary bentonite mixtures. ALERT Workshop and School 2019. Aussois, France. ***4th October 2019.***

Progress meeting: between IRSN (N. Mokni) and CIMNE/UPC (E. Romero and A. Mesa-Alcantara) in Barcelona. **November 22nd*, 2020.***

Seminary: EURAD doctoral school (GAS &HITEC WPs within EURAD-GAS project) Multiphysical coupling in Geomechanics, a focus on thermal effect and gas transfer impact on the behaviour of geomaterials. Liege University, Belgium. ***22nd-24th January 2020.***

Progress meeting: between IRSN (N. Mokni) and CIMNE/UPC (E. Romero and A. Mesa-Alcantara) in Paris. ***February 25th -28th, 2020.***

Oral presentation: A. Mesa-Alcantara, E. Romero and N. Mokni. Mock-up demonstration tests to support the VSEAL Project. Long-term hydration and impact of gas migration on sealing systems. *Young Researchers Meeting 2020* in IRSN. Paris. ***February 29th, 2020***. (Speaker: A. Mesa-Alcantara).

Seminary: ALERT Workshop and School 2020. Online ***28th September-1st October 2020.***

Oral presentation: A. Mesa-Alcantara, E. Romero, N. Mokni and S. Olivella. Hydro-mechanical behaviour of binary bentonite pellet and powder mixtures. Unsaturated Horizons 4th European Conference on Unsaturated Soils, Lisbon. (Speaker: A. Mesa-Alcantara).

Conference paper: A. Mesa-Alcantara, E. Romero, N. Mokni and S. Olivella. Microstructural and hydro-mechanical behaviour of bentonite pellet and powder mixtures. Unsaturated Horizons 4th European Conference on Unsaturated Soils. *(E-UNSAT-2020,* Lisbon*)*, *195*, 04003.
https://doi.org/10.1051/e3sconf/202019504003.

Oral presentation: A. Mesa-Alcantara, E. Romero, N. Mokni and S. Olivella. Oedometer tests modelling of pellet-powder mixture experiments to support mock-up test analysis. Unsaturated Horizons 4th European Conference on Unsaturated Soils, Lisbon. (Speaker: A. Mesa-Alcantara).

Conference paper: A. Mesa-Alcantara, E. Romero, N. Mokni and S. Olivella. Oedometer tests modelling of pellet-powder mixture experiments to support mock-up test analysis. Unsaturated Horizons 4th European Conference on Unsaturated Soils *(E-UNSAT 2020,* Lisbon*)*, *195*, 04004. https://doi.org/10.1051/e3sconf/20201950400. Lisbon.

Accepted poster: Pellet/powder mixture swelling induced by hydration. A model based on pellet representation. 8th International Conference on Clays in Natural and Engineered Barriers for Radioactive Waste Confinement, Clay Conference 2021, June 2021, Nancy.

Accepted poster: Hydration and gas tests at mock-up scale to understand the hydro-mechanical behaviour of a bentonite pellet/powder mixture. 8th International Conference on Clays in Natural and Engineered Barriers for Radioactive Waste Confinement, Clay Conference 2021***, June 2021, Nancy.***

Journal paper: A. Mesa-Alcantara, E. Romero, N. Mokni and S. Olivella. A contribution to the understanding of bentonite pellet/powder mixture under hydration'. Géotechnique Letters. In preparation.

2. MATERIAL AND EXPERIMENTAL PROGRAMME

2.1. Introduction

MX80 bentonite (Wyoming, USA) is considered a reference buffer and backfill material for high-level nuclear waste repositories in several countries such as France, Sweden, and Switzerland because of its high swelling rate, low permeability and high radionuclide migration retardation properties (Pusch, 1979; Yong *et al.*, 1986; Karnland *et al.*, 2008; Molinero-Guerra, 2018; Darde *et al.*, 2020). This clay material is composed of different mineral, mainly of smectites (main montmorillonite with 80%) and small quantities of non-clayed mineral as pyrite<1%, albite 2%, anorthite 8%, quartz 4% and muscovite 4% (Molinero-Guerra *et al.*, 2016). The montmorillonite show volume changes when it adsorbs water or organic molecules within the structural layers.

Bentonite has been formed as a result of hydrothermal alteration of volcanic ash during the Cretaceous period (Smellie & Contrerra, 2001). Compacted bentonite has different types of porosity (Figure 2-1). The first is the organisation of the laminae called unit layers or clay layer, where the water accessing this porosity is influenced by the electrical field and is firmly bound with a basal spacing d_{001} typically ranging from 1 to 2 nm (i.e., one to four discrete layers of water molecules). In the case of smectites, these unit layers are of the TOT type (2:1 layer phyllosilicate, i.e. an octahedral sheet between two tetrahedral sheets) with spacing more than 2 nm.

The second is the microporosity (intra-aggregate), which is heterogeneous and includes the pores inside each particle constituting the intra-particle porosity, and the pores between particles, or inter-particle porosity. The microporosity does not depend on the compacted sample's dry density (Romero *et al.*, 1999; Villar & Lloret, 2007). Finally, the pores between aggregates, called inter-aggregates or macro-porosity that retain the water by gravitational or capillary forces with pore sizes that can range up to the order of μm (Romero *et al.*, 2011).

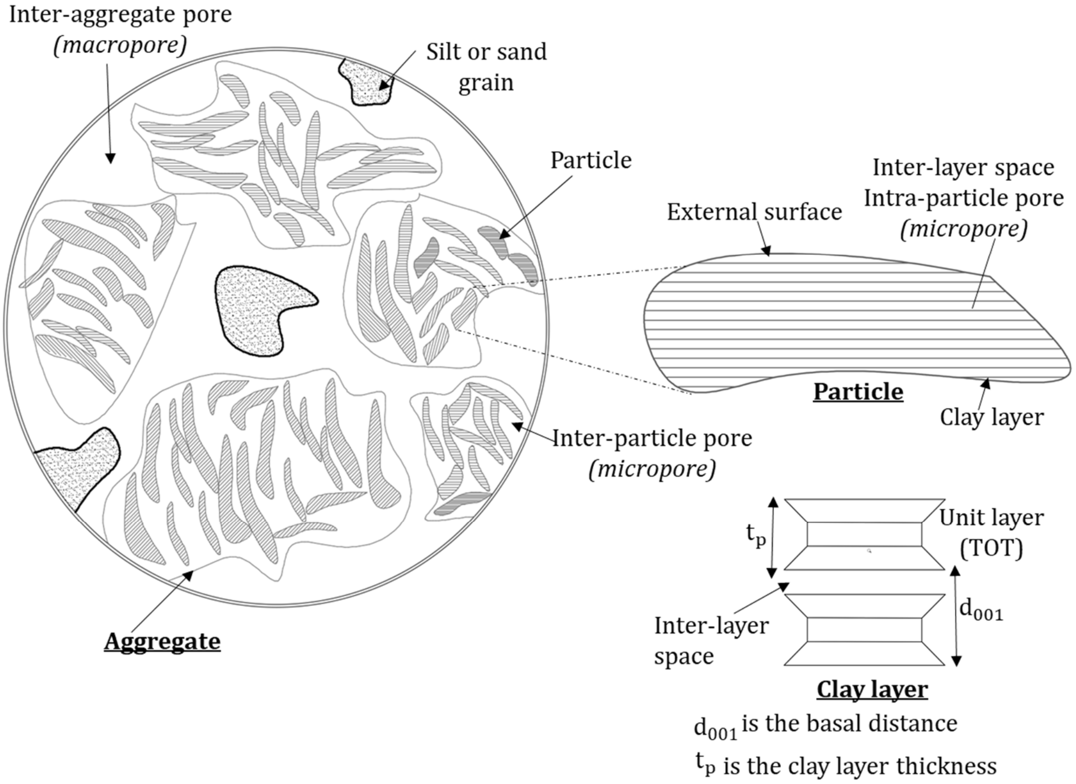

Figure 2-1. Conceptual representation of the structure of compacted bentonite (modified after Gens & Alonso, 1992; Jacinto *et al.*, 2012)*.*

Several authors (Pusch *et al.*, 1992; Lloret *et al.*, 2003; Gens *et al.*, 2011; Villar *et al.*, 2012; Saba, 2014; Molinero-Guerra, 2018) have already investigated the relationship between the dry density and swelling pressure, observing a clear dependence and also the evolutions of microstructure as a consequence of changes in dry density. Wieczorek *et al.* (2017) observed some heterogeneities in mixtures of pellet/powder, as a function of dry density and water content, after almost ten years of hydration, indicating that the complete hydration of the engineered barrier can take a long time.

Changes in microfabric during hydration under constant volume conditions of a 50/50 of FoCa pellet/powder mixture were presented by Van Geet *et al*. (2005) using µ-CT. However, the resolution of the images was not enough to study the microstructure changes in a single pellet at this scale. Nevertheless, Molinero-Guerra (2018) presented the changes in microfabric during hydration under constant volume conditions of a mixture of MX80 bentonite at a dry unit weight of 1.49 Mg/m^3 using µ-CT and significant changes of the pellet/powder mixture during hydration could be observed. Also, the microstructure of an elementary pellet was studied, showing the behaviour of the pellet during the saturation using MIP and µ-CT.

Different *in situ* experiments have been carried out along the last years using high-density pellets bentonites such as mixtures of FoCa high-density pellet (50%)/bentonite powder (50%) (Volckaert *et al.*, 2000; Gens *et al.*, 2011) (project RESEAL), Febex bentonite pellets with different sizes (AITEMIN, 2001; Hoffmann, 2005; Hoffmann *et al.*, 2007; Alonso *et al.*, 2011; Mesa-Alcantara, 2014) (project EB), mixtures prepared using pellets and blocks of MX80 bentonite and also with 65% of sand and 35% of bentonite (Gaus 2011) (project HE-E and FE), and MX80 bentonite mixture composed of 80% of pellets and bentonite powder (crushed pellets) at an emplacement dry density of 1.49 Mg/m^3 (project SEALEX) (Barnichon & Deleruyelle, 2009; Barnichon *et al.*, 2012; Mokni & Barnichon, 2016a: Mokni & Barnichon, 2016b; Molinero-Guerra *et al*., 2016). This last mixture has also been investigated in this study within project VSEAL. Table 2-1 summarises some of the *in situ* tests in which the different mixtures have been considered. The table includes information on the mixture dry density (typically between 1.40 and 1.50 Mg/m^3), as well as on the dry density of the pellets (typically between 1.95 and 2.10 Mg/m^3).

The pellet mixtures have many advantages, such as reducing gaps between the rock and the seal, easy emplacement, and decreasing the compaction effort required to achieve the target dry density (Alonso *et al.*, 2011; Gens *et al.*, 2011; Molinero-Guerra, 2018). Once installed in the repository, this sealing material will be affected by coupled hydro-mechanical (HM) processes and gas migration: hydration under constant volume due to water infiltration from the geological barrier and the corresponding increase in confining stresses (swelling pressure) and at long term, gas pressurisation and migration because of the gas production induced primarily by metallic corrosion of the canisters.

Table 2-1. Several in situ tests with mixtures of bentonite pellets.

Clay material	Test (years)	URL
FoCa clay 50% pellets / 50% powder (overall dry density 1.40 to 1.55 Mg/m^3)	RESEAL (1999-2007)	HADES URL (Belgium)
Febex bentonite Pellets (overall dry density 1.36 Mg/m^3) + blocks (1.70 Mg/m^3) Dry density of pellets 1.95 Mg/m^3	EB (2002-2014)	Mont Terri URL (Switzerland)
MX-80 bentonite Pellets (overall dry density 1.46 Mg/m^3) + blocks (1.80 Mg/m^3) Also 65% sand / 35% bentonite (overall dry density 1.48 Mg/m^3) + blocks (1.80 Mg/m^3)	HE-E (2010-2014) FE (2009-2022)	Mont Terri URL (Switzerland)
MX-80 bentonite Pellets (overall dry density 1.49 Mg/m^3) + powder Dry density of pellets 2.00 – 2.12 Mg/m^3 Dry density of powder 1.10 Mg/m^3 *(present study)*	SEALEX (2010-2016) VSEAL (2020)	Tournemire URL (France)

This chapter deals with the experimental program performed to study the characterisation of the mixture and its components from a microstructural point of view with mercury intrusion porosimetry and field-emission scanning electron microscopy. Moreover, it explains the verification of the segregation of the powder, the different protocols followed to prepare the mixture and the verification of the heterogeneity by computerised axial tomography scans.

2.2. Material

MX80 bentonite has been formed as a result of hydrothermal alteration of volcanic ash during the Cretaceous period (Smellie & Contrerra, 2001). MX80 presents a montmorillonite content around 80% and non-clayey mineral as pyrite (<1%), albite (2%), anorthite (8%), quartz (4%), muscovite (4%) (Molinero Guerra et al., 2016). The montmorillonite is a mineral that shows volume changes when it adsorbs water or organic molecules within the structural layers. The liquid limit and plastic limits of the MX80 bentonite are 560% and 53 %, respectively, according to Molinero-Guerra *et al.* (2016). The density of the bentonite grains in the study was taken as 2.77 Mg/m^3 (Saba, 2014; Saba *et al.*, 2014). The total specific surface is around 523 m^2/g, and the cation exchange capacity (CEC) is 98 meq/100g (Molinero-Guerra, 2018). Table 2-2 presents the main properties of MX80 bentonite with the comparison with the other authors (Lajudie *et al.*, 1994; Villar *et al.*, 2012; Wang *et al.*, 2013a; Saba, 2014; Seiphoori *et al.*, 2014; Molinero-Guerra, 2018). The difference in the values of the authors is because the material is from different batches. The MX80 bentonite used in this study is consistent with the material used by Saba (2014) and Molinero-Guerra (2018). **Error! Reference source not found.** shows the pellets of MX80 bentonite, together with the mixture with a mass base proportion of 80% high-density pellets and 20% powder (crushed pellets). Also, the packing of pellets is observed in the figure.

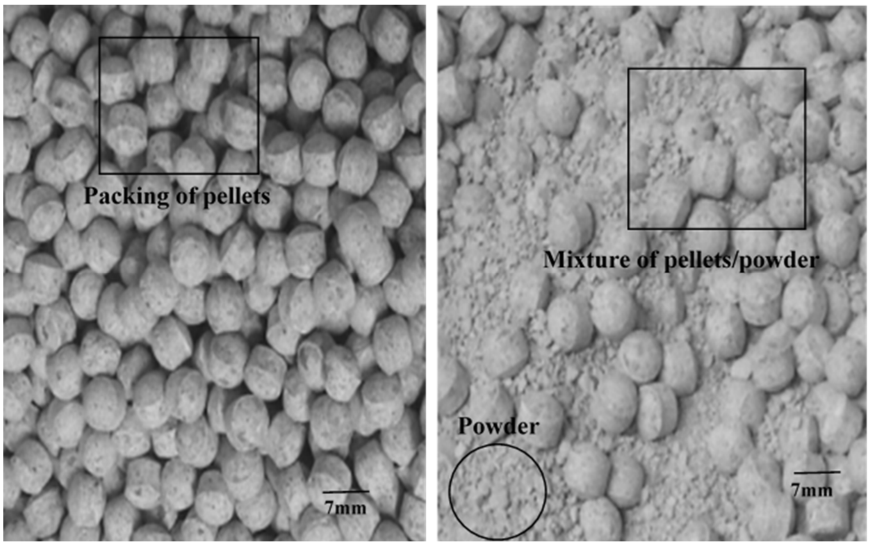

Figure 2-2. (a) Shows quasi-cylindrical pellets with spherical caps and diameter around 7 mm and height around 7 mm, (b) mixture of pellets and powder.

Table 2-2. Literature reported properties for MX80 bentonite.

Properties	**MX80 bentonite**						
	Lajudie *et al.* (1994)	Villar (2005) Villar *et al.* (2012)	Seiphoori *et al.* (2014)	Wang *et al.* (2013a)	Saba (2014)	Molinero-Guerra *et al.* (2016)	Present study
Mont-morillonite content (%)	75	65-83	[b]85	80	92	80	[c]80
Liquid limit (%)	400	350-570	420	575	520-575	560	[c]560
Plastic limit (%)	70	46-70	65	53	42-53	53-62	[c]53-62
Density of solids, Mg/m^3 (ρs)	2.70	2.82	2.74	2.77	2.77	[a]2.77	[a]2.77
Clay fraction dispersed (< 2 µm) (%)	80-90	80-90	-	84	84	-	40
Cation exchange capacity (CEC)(meq /100g)	79	65-74	-	76	76	98	[c]98

[a]Saba (2014), Saba *et al.*(2014) [b]Weber & Plötze (2007) [c]Molinero-Guerra *et al.* (2016)

Pellets have been compacted in Laviosa-MPC company (France) under the commercial name ‘Expangel SP7’ using powder of MX80 bentonite in a mould with a diameter of 7mm. The compaction process was done at water content w = 6±1% and dry density $\rho_{d\,pe}$ = 2.06±0.06 Mg/m^3, corresponding to a void ratio e = 0.30±0.07. The initial total suction measured with WP4 chilled-mirror dewpoint psychrometer (Decagon) was s = 163 MPa at slightly higher water content w = 6.13-9.36% (determined after oven-drying at 110 °C during 48 h). The 7 mm pellets were received under packed conditions (20 kg) and stored at room temperature (22°C). The average dry density of the pellets at w = 6.13-9.36% was $\rho_{d\,pe}$= 1.99 Mg/m^3

(void ratio e = 0.392, porosity ϕ = 0.282 and degree of saturation S_r between 0.433 and 0.661). The variations in dry density of pellets were also associated with some fissuring observed on the surface of the pellet and with expansion related to water absorption.

The MX80 bentonite powder was fabricated by crushing pellets by Laviosa-MPC Company under the commercial name 'Concasse d' Expangel' with a maximum particle size D_{pow} = 4.75 mm. The initial suction measured in the laboratory displayed a value of 85 MPa at w = 9.51% (w varied between 9.51% and 10.64%). The dry density of the powder has been estimated based on three tests, in which the powder has been placed in layers using a mould of known volume and different procedures. The first test one has been made with some vibration in each layer, obtaining a dry density of $\rho_{d\,pow}$ = 1.26 Mg/m^3. In the second test, the sample was installed by layers without vibration, reaching a dry density of $\rho_{d\,pow}$ = 1.10 Mg/m^3. Finally, in the last test, the sample has been installed by layers, and then the whole sample vibrated to obtain $\rho_{d\,pow}$ = 1.16 Mg/m^3. The dry density of the powder assumed when placing the mixture is the one without vibration, i.e. $\rho_{d\,pow}$ = 1.10 Mg/m^3 (e = 1.52, S_r between 0.173 and 0.194).

Figure 2-3 presents a schematic of the MX80 mixture (80%pellet and 20% powder) together with a horizontal and vertical section of x-ray computed microtomography (μ-CT) pellet (initial state) from Molinero-Guerra et al. (2016) to visualise the microstructure. The mixture has inter-pellet voids that are filled by the powder. The compacted pellets do not show important macro-porosity between aggregates. They mainly display inter-particle pores and intra-particle pores that conform to the microporosity.

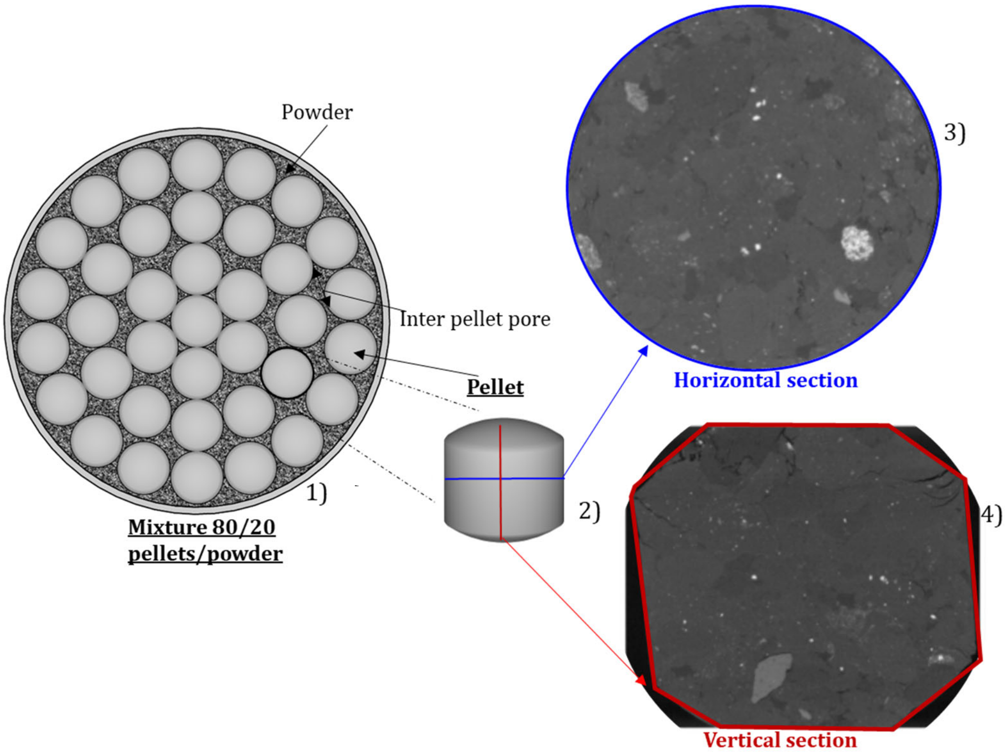

Figure 2-3. 1) Schematic view of MX80 bentonite mixture (80% pellets and 20% powder), 2) schematic view of pellet, 3) and 4) horizontal and vertical section of x-ray computed microtomography (μ-CT) pellet (initial state) from Molinero-Guerra et al. (2016)

2.3. Verification of configuration of packing of pellets

An important step to install the MX80 bentonite mixture is to guarantee an excellent coordination number between the pellets getting good packing of pellets (skeleton of pellets without powder). Several laboratory tests have been performed by placing pellets on a known volume (diameter of 100 mm and height of 35 mm).

The first test has been made by placing the pellets disorganised, obtaining a low dry density of $\rho_{d\,pack}$ = 1.01 Mg/m^3. In the next test, the sample was installed in an organised manner layer by layer and placing pellet by pellet, reaching a dry density of $\rho_{d\,pack}$ = 1.19nMg/m^3 with a coordination number of 8 (cubical–tetrahedral). Finally, in the last test, the sample has been made with some vibrations every three layers obtaining a dry density of $\rho_{d\,pack}$ = 1.11 Mg/m^3. Figure 2-4a shows the packing of pellets (second test) with coordination number close to 8, and Figure 2-4b show the first layer the mixture prepared mock-up test with a dry density of packing of pellets 1.19 Mg/m^3 (coordination number close to 8) where the pellets were placed one by one and powder with a dry mass fraction f = 0.20 is then poured (partially filling the inter-pellet pores).

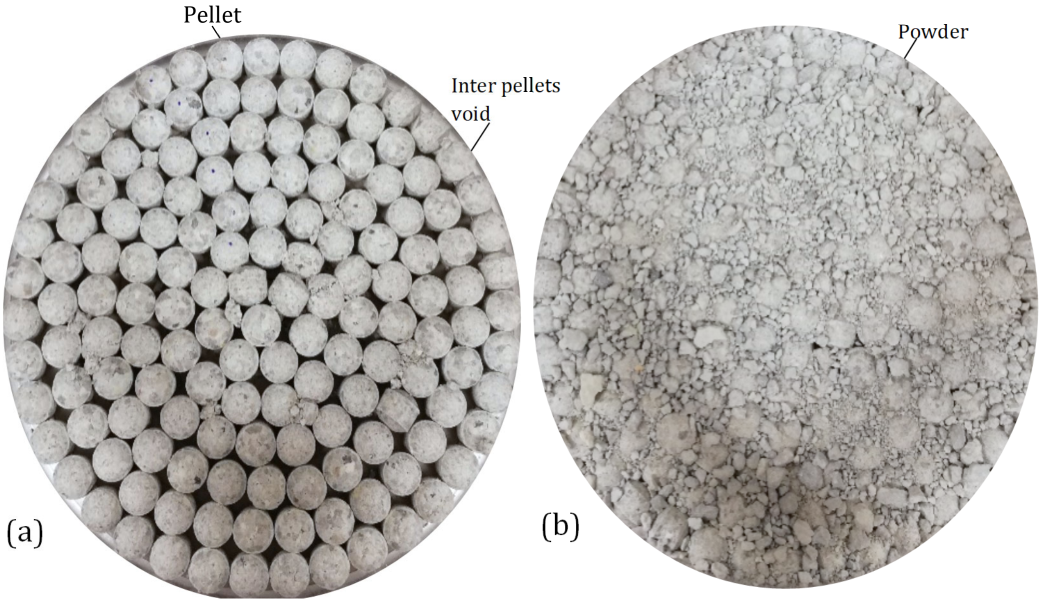

Figure 2-4. a) Packing of pellets close to coordination number of 8; b) MX80 bentonite mixture with dry density 1.47 Mg/m³ (80% pellets and 20% powder).

Table 2-2 indicates the dry density of the packing of pellets (porosity and void ratio) of different configurations. The table includes theoretical arrangements of spheres (simple cubic and cubical-tetrahedral), as well as the ones arranged in the laboratory by placing quasi-spheroidal pellets. The dry density of the packing of pellets in the laboratory varied from 1.11 to 1.19 Mg/m^3, corresponding to configurations between simple cubic (coordination number 6) and cubical-tetrahedral (coordination number 8). The latter is the configuration that is intended to be reached when placing the mixture on the mock-up with known volume (see Figure 2-4 the first layer of the mock-up test) and that cannot be efficiently achieved by merely pouring the pellets.

Mixtures of these pellets (80% by dry mass) and powder were prepared for this study. If the packing of pellets is first placed to ensure a coordination number close to 8 ($\rho_{d\,pack}$ = 1.19 Mg/m^3), and powder with a dry mass fraction f = 0.20 is then poured (partially filling the inter-pellet pores), the dry density of the mixture is obtained as

$$\rho_{d\,mix} = \frac{1}{1-f}\rho_{d\,pack} \tag{2-1}$$

The minimum dry density of the powder ($\rho_{d\,pow}^{min}$) with mass fraction f = 0.20 to fill all the inter-pellet porosity is presented in Equation 2-2. Where the inter-pellet porosity or packing of pellet porosity (ϕ_{Pack}) is determinate with $\rho_{d\,Pack}$ through a dry density of the pellet of 1.99 Mg/m^3.This minimum dry density allowed determining the volumetric degree of powder filling F, assuming a poured powder dry density $\rho_{d\,pow}$ = 1.10 Mg/m^3, this is given by equation (2-3). The dry density of the mixture obtained in the laboratory was 1.47 Mg/m^3 with a void ratio of 0.88 and porosity equal to 0.47 with an initial water content of 8.47% as measured by oven drying during more than 24 hours.

$$\rho_{d\,pow}^{min} = \frac{f}{\phi_{Pack}} \rho_{d\,mix} \tag{2-2}$$

$$F = \frac{\rho_{d\,pow}^{min}}{\rho_{d\,pow}} \tag{2-3}$$

Table 2-3. Properties of packing of pellets.

Packing (coordination number)	Dry density of packing of pellets $\rho_{d\,Pack}$ (Mg/m^3)	Inter-pellet porosity (ϕ_{Pack})	$\rho_{d\,mix}$	$\rho_{d\,pow}^{min}$ (Mg/m^3)	Degree of powder filling, F
Simple cubic pellet packing (6)	1.04	0.47	1.30	0.55	0.50
Cubical-tetrahedral pellet packing (8)	1.20	0.39	1.50	0.76	0.69
Arrangement in laboratory	1.11 to 1.19	0.44 to 0.40	1.39 to 1.49	0.63 to 0.74	0.57 to 0.67

As observed, the table reports values of $F < 1$, which indicates a medium amount of powder filling the voids between coarse pellets (underfilled packing with coarse pellet supported structure at initial conditions).

2.4. Particle size distribution of the components and mixture

It is important to check the possibility of segregation on pouring the binary mixture or powder migration into the coarser pellets. Such a condition can be preliminarily studied by filter design criteria: the size of the inter-pellet voids should be small enough to hold the larger powder particles in place. The larger powder grains passing 85% are around $d85_{pow}$ = 1.70 mm ($d85_{pow}$ = 1.45 mm from Molinero-

Guerra *et al.*, 2016). The estimated pore size of d = 7 mm pellets is around $0.2d15_{pe}$ (0.2 of the pellet size passing 15%)(Kamiya & Uno, 2000). Since $0.2d15_{pe}$ (1.40 mm) is slightly below $d85_{pow}$ it appears that larger powder particles are held in place, and no important movements of powder within the pellet skeleton are expected, and no significant segregation effects will develop on powder pouring.

Figure 2-5 presents the particle size distribution curves of the pellets, powder and mixture and results reported on powder grain size distribution by Molinero-Guerra (2018) have also been included. The figure also presents the distribution curves obtained for the finer fraction passing ASTM #200 (76 μm) using sedimentation and laser techniques. The laser technique on dispersed fine powder reports 40% of particles < 2 μm.

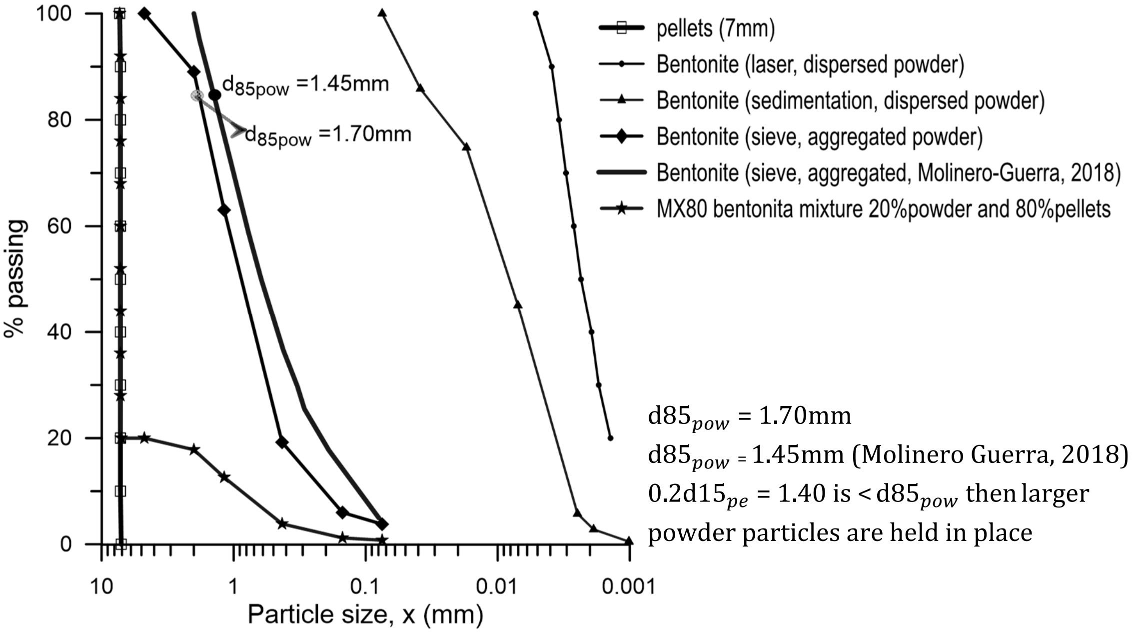

$d85_{pow}$ = 1.70mm
$d85_{pow}$ = 1.45mm (Molinero Guerra, 2018)
$0.2d15_{pe}$ = 1.40 is < $d85_{pow}$ then larger powder particles are held in place

Figure 2-5. Particle size distribution of powder (sieve, sedimentations and dispersed powder), pellets and mixture and comparison with sieve aggregate powder by Molinero-Guerra (2018).

2.5. Preparation of the mixture with different protocols

It is crucial to prepare powder/pellet mixture as homogeneous as possible at the required target dry density (1.49 Mg/m^3) because it governs both the saturated permeability and the swelling pressure of the mixture (Saba, 2014; Saba *et al.*, 2014). Three different protocols have been followed to verify the mixture's dry density and identify the one that displays the lowest heterogeneity to be used for the mock-up test.

The first protocol (protocol 1) (Figure 2-6a) consisting of filling the cell (102.9 mm diameter and 300 height) with two or three layers of pellets and then adding the corresponding amount of powder (20% powder in dry mass) resulted in a dry density value of 1.38Mg/m^3. The second protocol (protocol 2)(Figure 2-6b) consists of placing only one layer of pellets in the cylinder (94 mm in diameter) and placing the pellets one by one with the help of tweezers and ensuring almost the coordination number of eight and then adding the corresponding amount of powder. In this protocol, the dry density was 1.47 Mg/m^3. The lowest dry density (1.30Mg/m^3) was obtained using the last protocol (protocol 3) (Figure 2-6c), which consisted of mixing the sample before pouring it into the cell.

In the following, the mixture will be prepared following the second protocol, which ensures a dry density of 1.47 Mg/m^3 (close to the target dry density of 1.49 Mg/m^3).

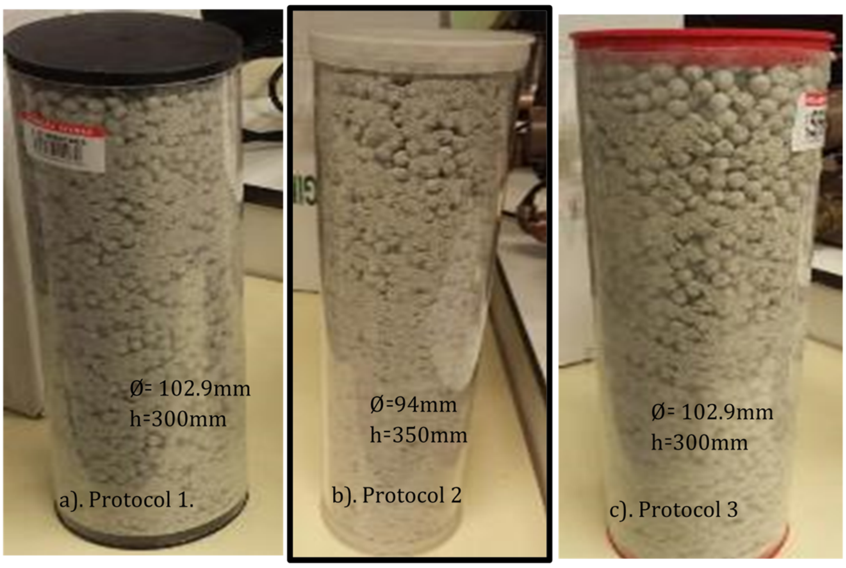

Figure 2-6. Different preparation protocols. a) Protocol 1. b) Protocol 2. c) Protocol 3.

2.6. Homogeneity verification by computerised axial tomography

Computerised Axial Tomography (CAT) has been used to obtain radiographic images of the samples and examine the homogeneity of the three different protocols. Figure 2-7 shows the medical CT used (Third Generation Multislice CT scan, Siemens Somatom Spirit® scanner) and the three different cells with varying protocols. The CT scan has a resolution of 60 µm x 60 µm x 1 mm.

Some artefacts can affect the CT images (Sau, 2013). The image quality depends primarily on two types of scan parameters: dose-related parameters and those related to processing and viewing of the image. Both are hardware related. Dose-related parameters are the slice thickness, inter-slice distance, pitch factor, volume of investigation, exposure factors and gantry tilt. Processing parameters are field of view, number of measurements, reconstruction matrix size, reconstruction algorithm and window settings (width and centre). The quality of a CT image may be expressed in terms of physical parameters such as uniformity, linearity, spatial resolution, low contrast resolution and absence of artefacts according to IEC recommendations (1994) (Sau, 2013). Quality may be assessed by quantitative measurement of the parameters listed above, using suitable test phantoms, and by the appearance of artefacts. Table 2-4 summarises the different parameters used for image acquisition.

Figure 2-7. The three samples during testing using a third-generation Multislice CT scan.

Image processing was done by ImageJ (Fiji) (Schindelin *et al.*, 2012) to analyse the DICOM standard files and obtain rendering volume, histograms, and complementary data. ImageJ is a public domain software with an open architecture that provides extensibility via Java plugins. ImageJ can read many image formats (TIFF, GIF, JPEG, BMP, DICOM, FITS 'raw) and calculate area and pixel value statistics of user-defined selections.

Table 2-4. Image acquisition parameters.

Image acquisition parameters	**Reference CT scan tests**		
	Mixture pellet 7mm / bentonite powder		
	Protocol 1	**Protocol 2**	**Protocol 3**
Scan protocol	Hip	Hip	Hip
Scan mode	Spiral	Spiral	Spiral
X-ray tube voltage (kVp)	130	130	130
Tube current (mA)	35	51	33
Rotation time (s)	1000	1000	1000
Distance source to sample	535	535	535
Rescale intercept	-1024	-1024	-1024
Rescale slope	1	1	1
Reconstruction diameter	367	416	362
Pixel spacing	0.070703125/0.70703125	0.8125\0.8125	0.070703125/0.70703125
Reconstruction matrix	512x512	512x512	512x512
Window center	40	40	40
Window width	350	350	350
Kernel	U90s	U90s	U90s

Vertical cross-sections of the different protocols are indicated in Figure 2-8. Protocol 2 (1 layer), which displays the highest dry density (1.47 Mg/m^3) and almost coordinations number of 8 (cubical-tetrahedral), also presents a pretty homogeneous distribution of pellets and powders where the powder grains within the pores located between the granules presented a regular dispersion compared with protocol 3. Protocol 1 (2 layers) presented much more unfilled inter-pellet voids, and low dry density (1.38 Mg/m^3) in comparison with protocol 1.Protocol 3 presented the lowest dry density displays inevitable heterogeneity with local concentrations of powder overfilling inter-pellet voids (enclosed by yellow dashed lines) and regions with empty inter-pellet voids, also with the lowest dry density (1.38 Mg/m^3). At the top of the sample, several voids between the pellets are observed in the three protocols.

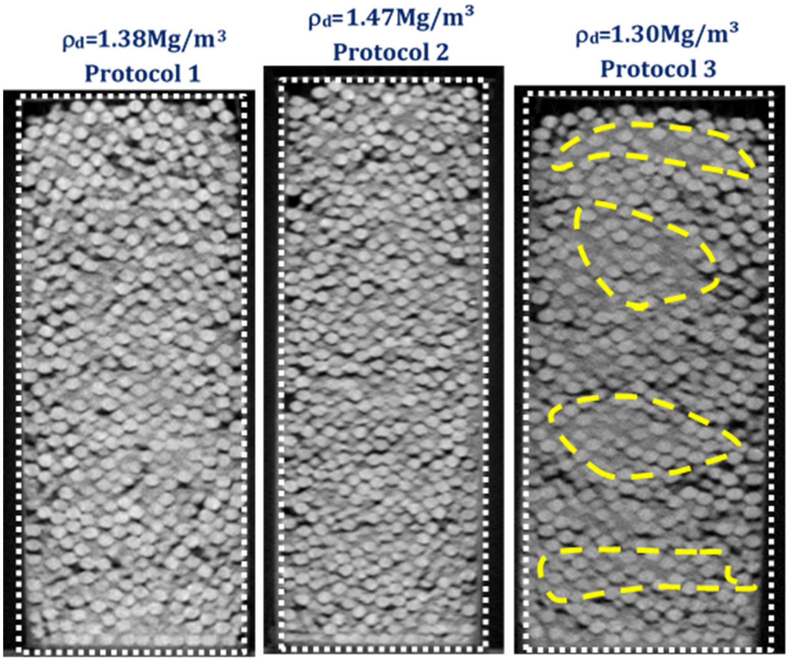

Figure 2-8. Cross-section of CAT images of the three protocols followed.

The images were processed in a 3D form with a plugin ImageJ called 3D viewer (Figure 2-9a) in 16 bits format and resolution around 800 μm. After that, the region of interest (ROI) within the specimen was selected to avoid sample irregularity (Figure 2-9b). The ROI used was the same for each protocol (1184.27 cm^3). For the quantitative treatment, stacks were scaled to an 8 bits format to calculate the macro-porosity. To convert the image to 8 bits format, different thresholds were considered taking into account the different dry densities of the protocols and following the method presented by Ando (2013)and used by Fraccica (2019), where the threshold is calculated with the dry density of the sample and the density of the solids. Figure 2-9c shows the binarised selected ROI of protocol 2. Finally, the selected ROI was divided into six parts to calculate the macro-porosity in the centre of each zone and verify the homogeneity of the different protocols (Figure 2-9d).

Figure 2-12 presents the evolution of the obtained macroporosity throughout the height of the sample for the three protocols. Protocol 1 presented minimum and maximum porosities of 0.26 and 0.33, respectively. In protocol 2, the minimum and maximum porosities are 0.28 and 0.31, respectively, corresponding to one layer of pellets. These values followed the results of Molinero-Guerra (2018). Finally, for protocol 3, porosity ranges from 0.25 to 0.32 and corresponds to mixing the sample before pouring it into the cell. Considering the target dry density (1.49 Mg/m^3), the homogeneity observed in Figure 2-8 (less heterogeneous protocol 2) and image analysis data, the second protocol should be selected to prepare the mixture.

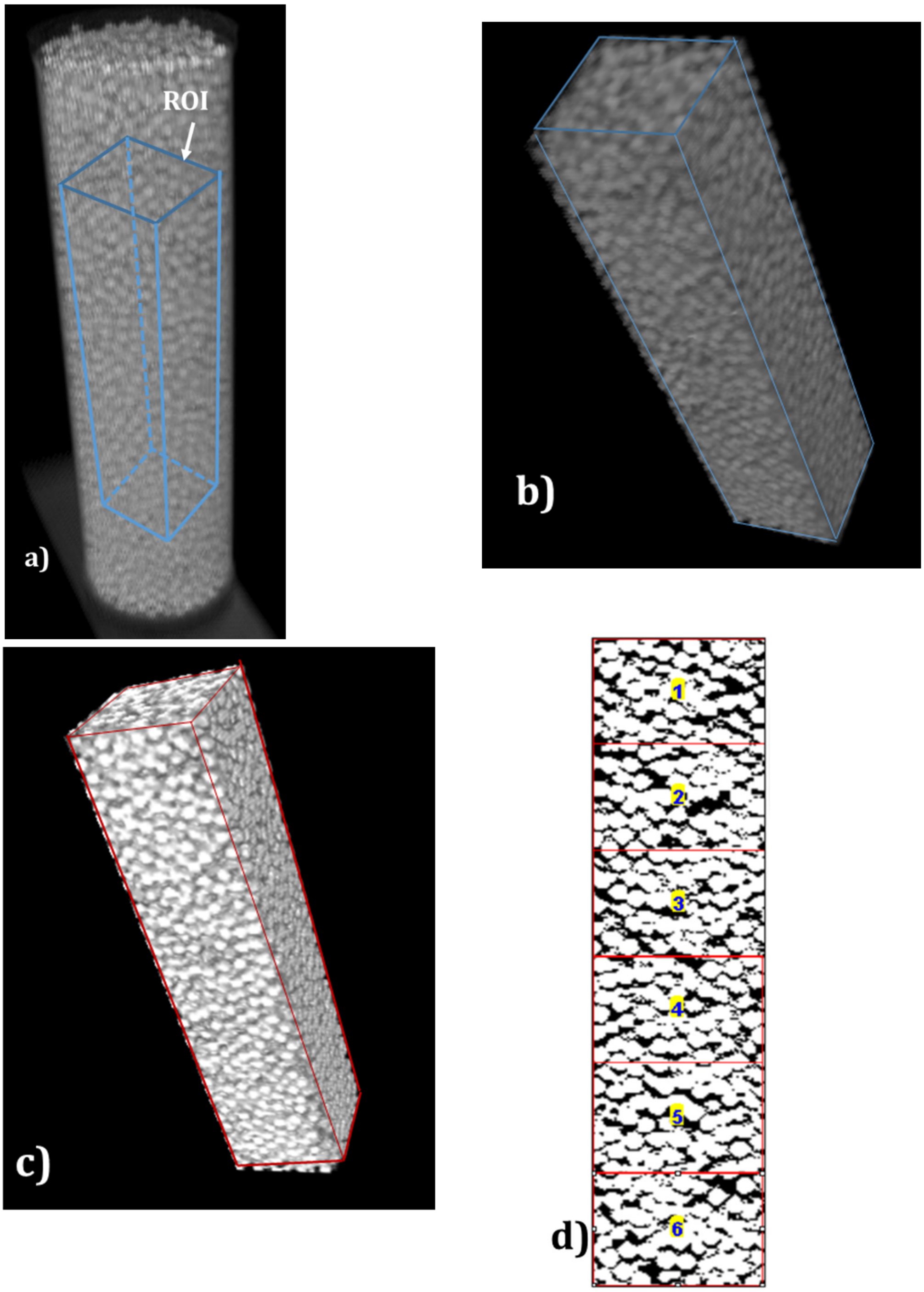

Figure 2-9. Procedure followed to perform the quantitative analyses. a) 3D view of the protocol 2, b) selected ROI is the same for the three protocols, c) binarised ROI, and d) binarised slide.

As previously indicated, the porosity calculated corresponds to macro-porosity due to the CAT's resolution of around 800 µm. The macro-porosity or inter-pellet porosity (explained in section 2.7.1 and mainly associated with the large pores between pellets) that corresponds to a dry density of 1.47 Mg/m^3 is 0.29 and matches the average porosity of protocol 2.

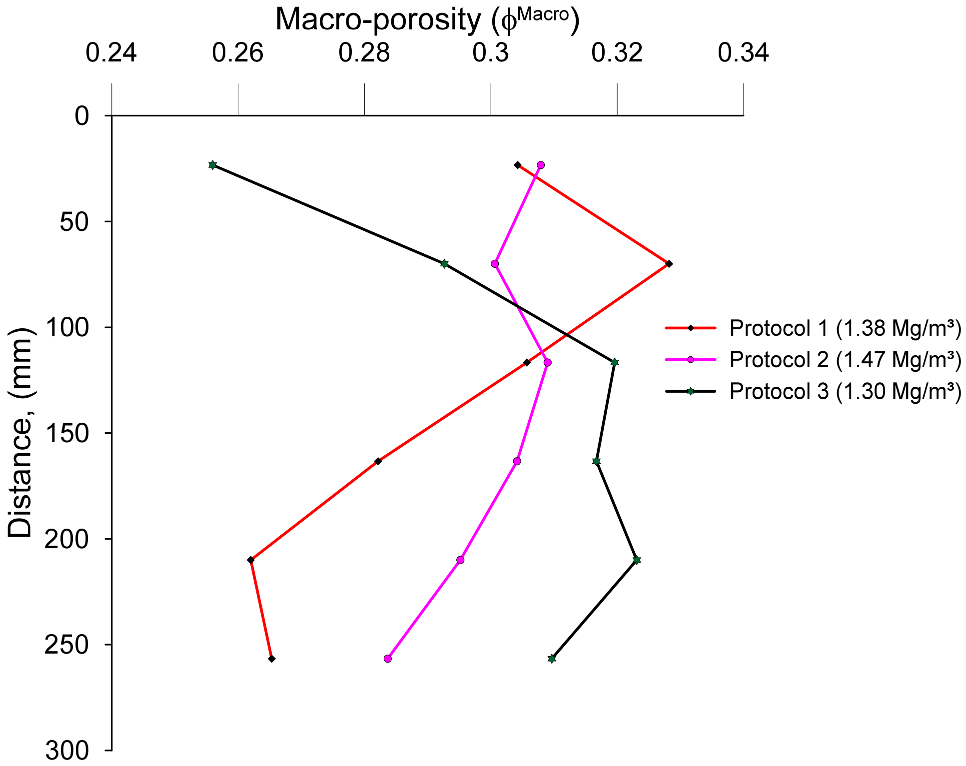

Figure 2-10. Evolution of the macro-porosity throughout the height of a pellet/powder MX80 bentonite mixture (80/20) fabricated by three protocols.

2.7. Microstructural characterisation of pellets, powder and binary mixture

Several investigations have been carried out on the microstructure of bentonite-based materials by using several methods, including mercury intrusion porosimetry (MIP), scanning electron microscopy (SEM), and field emission scanning electron microscopy (FESEM)(Romero *et al.*, 2011; Wang *et al.,* 2013b; Saba, 2014; Molinero-Guerra *et al.*, 2016). Also, nitrogen gas adsorption to determine pore sizes below 10 nm (Gonzalez-Blanco, 2017). The MIP, SEM and FESEM are techniques that require preliminary dehydration of the samples, often carried out by freeze-drying. Due to the size of the sample investigated, these techniques provide local observations of a part of millimetric samples. In this study, two techniques (MIP and FESEM) were taken into account to understand the material's microstructural behaviour better.

2.7.1. Pore size distributions of the material studied

In this thesis, the microstructural characterisation of the pellets and powder have been performed at two hydraulic states (dry and saturated) using the mercury intrusion porosimetry (MIP) and the nitrogen gas adsorption techniques. Firstly, the pore size distribution has been determined by MIP using the Micrometrics Auto Pore IV 9500 equipment (Figure 2-11a) and covering pore ranging from 7 nm to almost 500 µm (for more detail, see Delage *et al.*, 2006; Romero & Simms, 2008; Romero, 2013; Desbois *et al.*, 2014). The samples have been freeze-dried to minimize shrinkage effects. The freeze-drying process consists of plunging the sample into liquid nitrogen (-196°C) and applying a vacuum to remove the pore water. According to Delage *et al*. (2006) and Desbois *et al*. (2014), this process causes minor changes in the pore size and morphologies, obtaining good microstructure preservation. The principle of the MIP is based on Washburn equation (Equation 2-4), used to provide a relationship between the applied (absolute) non-wetting mercury pressure (p_m), and a characteristic entrance size of the intruded pores (x), so that:

$$p_m = -\frac{4\sigma_{Hg}\ \cos\theta_{Hg}}{\mathrm{x}} \tag{2-4}$$

Where σ_{Hg} = 0.484 N/m at 25°C is the surface tension of non-wetting phase (mercury) and θ_{Hg} = 140° the contact angle between mercury and the particle surface. This equation is used for fissure-like microstructure and cylindrical pores (Webb, 2001). Data on the retention behaviour can be obtained through the mercury intrusion procedure. According to Romero (1999), the mercury intrusion can become assimilated to the desorption path of the water retention curve by applying to an initially saturated sample an increasing external air pressure (non-wetting fluid) to dry the soil gradually.

Romero & Simms (2008) presented several limitations of the MIP, such as (1) the apparatus may not have the capacity to enter the smallest pores of the sample (non-intruded porosity), (2) isolated pores enclosed by surrounding solids are not measured— this enclosed porosity is not significant in soils; (3) pores that are accessible only through smaller ones (constricted porosity) are not detected until the smaller pores are penetrated; and (4) the minimum practical pressure of the apparatus limits the maximum pore size to be detected (non-detected porosity). In this way, when the clay sample is intruded by mercury, the intruded void ratio estimated under the maximum applied pressure does not coincide with the estimated void ratio of the sample. Differences mainly arise due to the non-intruded porosity with entrance pore sizes lower than 10 nm and the non-detectable porosity for pore sizes larger than 400 μm.

The nitrogen gas adsorption technique was used to complement the pore network description. It has been determined with Micrometrics Instrument Corporation equipment ASAP 2020 (Figure 2-11b) using the desorption information (Webb & Orr, 1997) with Barrett, Joyner and Halenda method. This technique allows complementing the information of the pore size distribution.

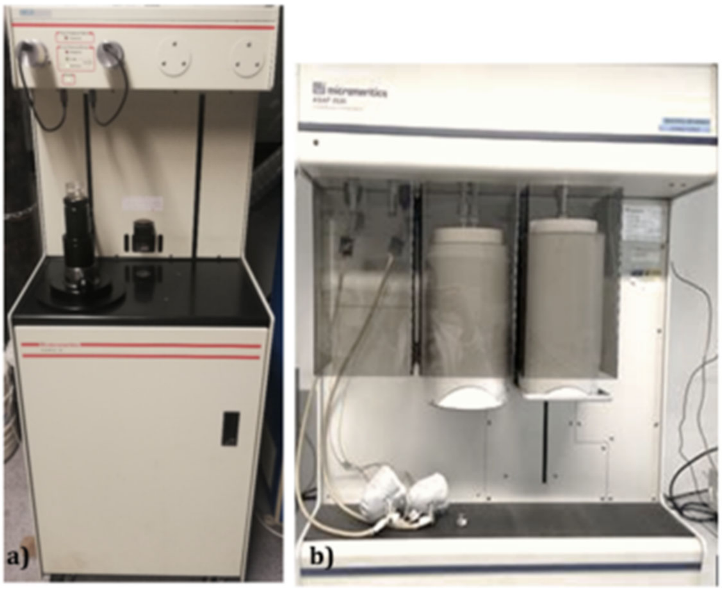

Figure 2-11. a) Equipment used for MIP (Micrometrics Auto Pore IV 9500).b) Equipment used for nitrogen adsorption tests (Micrometrics Instrument Corporation equipment ASAP 2020).

The micro-macrostructure of the pellet was studied at the initial state (w = 6.51% and (total) suction s = 162 MPa) and was compared with the results of Molinero-Guerra *et al*. (2016), obtaining a good agreement.

The saturated state of packing of pellets was achieved by placing pellets in an isochoric cell (50 mm in diameter, 20 mm in height) at a dry density of 1.19 Mg/m^3 (e = 1.33) with an initial water content of 6.51% and suction of 160 MPa and allowing the pellets to saturate for around six months reaching a final water content = 41.16% and s = 3.5 MPa (measured after unloading). The saturation was carried out with a water pressure of 2 MPa applied from the bottom part of the isochoric cell using distilled water. The sample to carry out the MIP was taken from the area where a pellet was located, exactly at the centre of the sample, to ensure that the tested sample was part of a pellet. Figure 2-12 shows the cumulative intruded void ratio (e_{int}) as a function of the entrance pore size for the pellets at initial state and saturated state of packing of pellets (this sample was considered with similar behaviour of the pellet).

The volume intruded at sizes larger than 40 µm has been assumed negligible, although some fissures have been detected. There is some deviation from the void ratio of the pellets, due to the limited capacity of the porosimeter to enter the smallest pores (non-intruded void ratio with entrance pore sizes below 7 nm). The intruded void ratios (e_{int}) is 0.36 for initial state of the pellet and 1.08 for saturated states (packing of pellets). The intruded void ratio is 0.36 represents 91.8% of the total void ratio of pellet at the initial state. The saturated packing of pellets displayed a total intruded void ratio of $e_{\text{i}nt}$ =1.08. The non-intruded void ratio is around $e - e_{\text{int}}$ = 0.25. The nitrogen adsorption test data are presented in Figure 2-12, where the behaviour from 10nm to 1.6nm can be observed. The nitrogen adsorption test helps reach the total void ratio of the pellet (e = 0.392) at the initial state, getting a void ratio of 0.384.

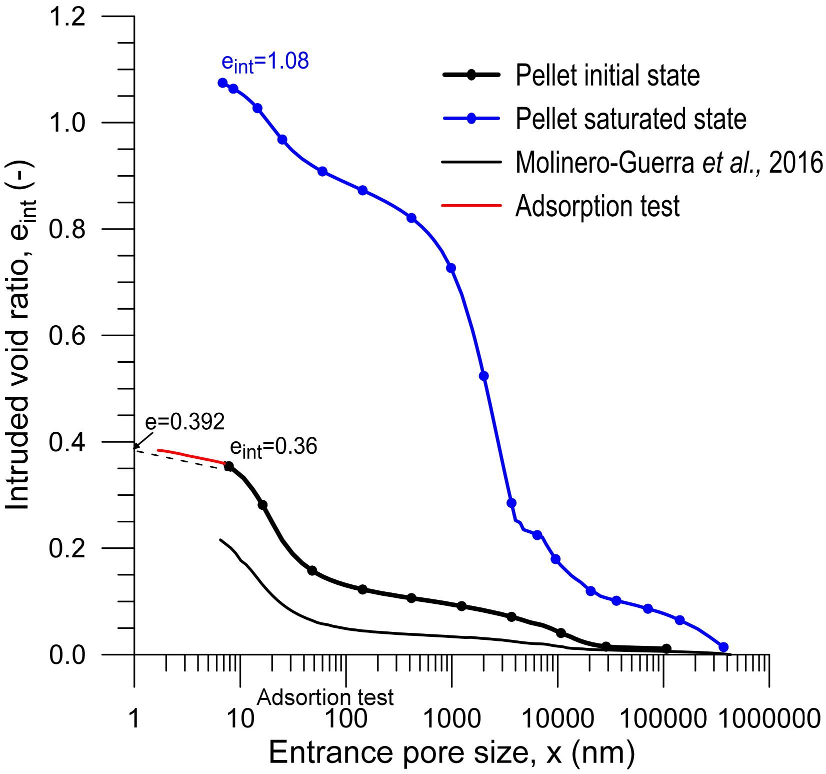

Figure 2-12. Cumulative void ratio curves for pellet (initial state and packing of pellets saturated) from MIP, together with data from nitrogen adsorption test (pellet initial state) and comparison with Molinero Guerra et al. (2016).

Figure 2-13 presents the cumulative intruded void ratio against the entrance pore size for the freeze-dried powder (w = 9.51% and s = 82 MPa). A good agreement is obtained compared to results reported by Molinero-Guerra *et al.* (2016) on bentonite powder, which has been also included in Figure 2-13. The intruded void ratio is 0.879, and this represents 58.5% of the total void ratio. The nitrogen adsorption test was also applied in the powder (initial state), observing the behaviour from 1.6 nm to 6 nm, reaching a void ratio of 0.914. The deviation with the expected void ratio (around e = 1.52 for a dry density of 1.10 Mg/m^3) corresponds mainly to the non-detected void ratio with pore sizes larger than 400 µm. The saturated state of the powder (Figure 2-13) was achieved by pouring powder in an isochoric cell (50 mm in diameter, 20 mm in height) at constant volume conditions with a dry density of 1.10 Mg/m^3 (e = 1.52) with an initial water content w = 9.51% and s = 82 MPa and allowing the powder to saturate for around eight months. The water pressure of 2 MPa was applied from the bottom part of the cell and was used distilled water. The saturated water content was 54.95%, corresponding to a value of the degree of saturation S_r = 1. The saturated powder displayed a total intruded void ratio of e_{int} = 1.01 with a non-detected void ratio around 0.51.

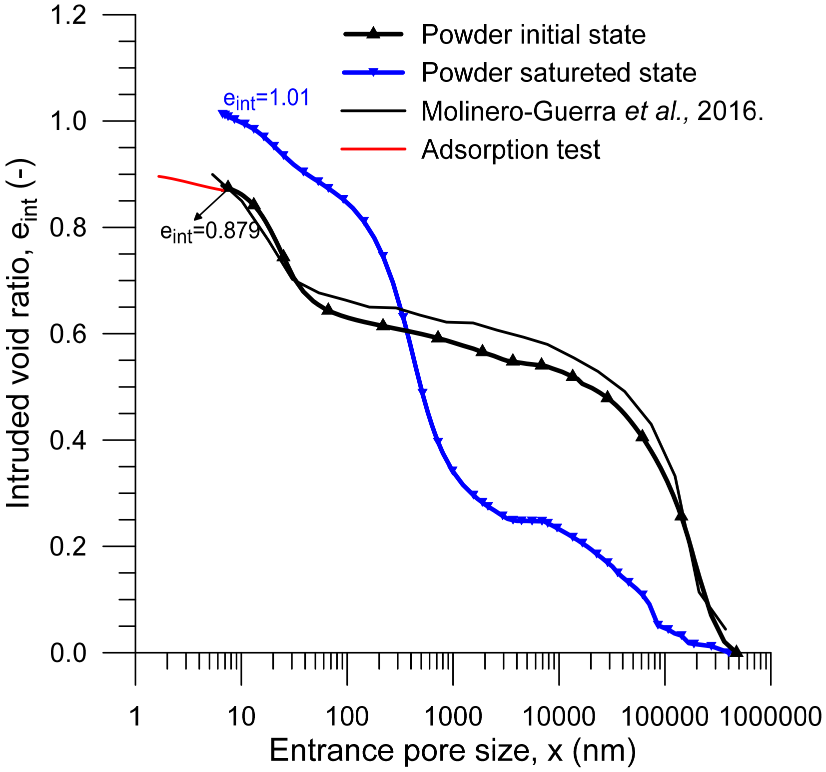

Figure 2-13. Cumulative void ratio curves for powder (initial and saturated state) from MIP, together with data from nitrogen adsorption test and comparison with Molinero Guerra et al. (2016).

The pore size distribution (PSD) function is defined as

$$PSD = f(log\mathrm{x}) = -\frac{\mathrm{d}e_{\mathrm{int}}}{\mathrm{dlogx}} \tag{2-5}$$

This equation was used to determine the PSD function of the MIP and the nitrogen adsorption test.

As observed in Figure 2-14, the PSD functions of the pellet at the initial state display two dominant pore modes at approximately 10 nm to 20 nm corresponding to the microstructure and between 10 µm and 20 µm belonging to the macrostructure (and mainly associated with fissures at the surface). A value of 1µm can be considered to separate these two pore domains inside the pellet (Romero *et al.*, 2011; Alonso *et al.*, 2011; Romero, 2013) (this value corresponds to the valley between peaks of the PSD). Moreover, figure 2-9 also shows the comparison with Molinero-Guerra *et al.* (2016). The data from a nitrogen adsorption test show a less important smaller peak around 2.7 nm, likely part of micropores.

The PSD of a saturated pellet (Figure 2-14) has been also plotted, which was retrieved from a saturated packing of pellets that were soaked under constant volume conditions ($\rho_{d\,pack}$ = 1.19 Mg/m^3, e = 1.33). As observed, the pore network underwent significant changes during saturation, in which the saturated PSD function of the pellet displayed a dominant pore around 2.5μm corresponds to macro-pores (inter-aggregate pores and fissures) The saturated packing of pellets also displays some pore volume at around 270 μm (the expanding pellets do not fill the inter-pellet porosity).

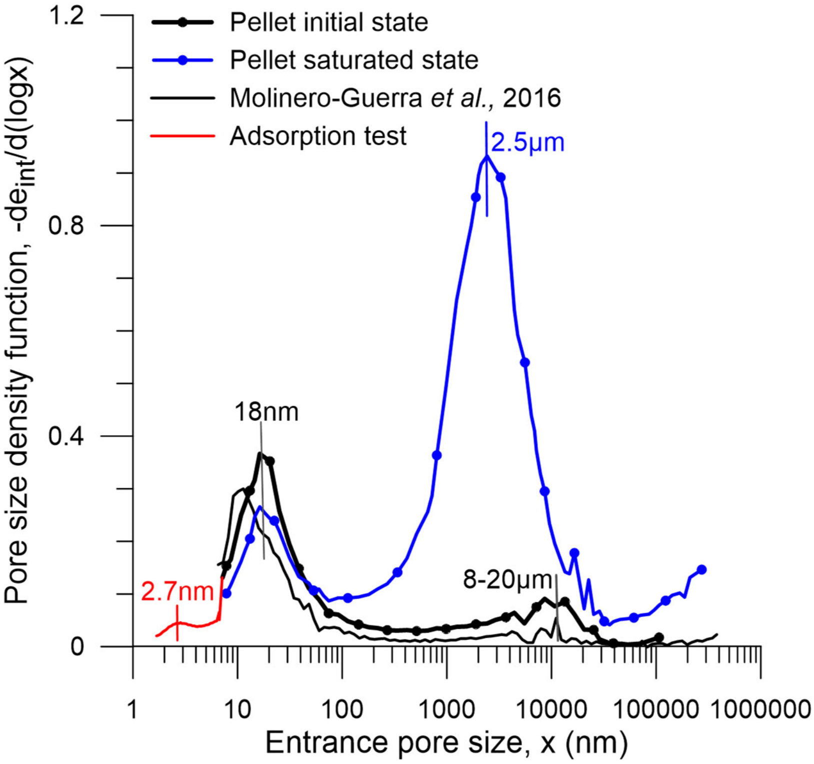

Figure 2-14. Pore size density function for pellets (initial state and packing of pellets saturated) from MIP together data from nitrogen adsorption test and comparison with data from Molinero Guerra et al. (2016).

Figure 2-15 presents the equivalent PSD functions of the bentonite powder at as-poured (e = 1.52) and the powder saturated in constant volume conditions at a dry density of 1.10 Mg/m^3 (e = 1.52). Two dominant pore modes at 22 nm (inside bentonite aggregates pores) and between 170 μm and 190 μm (inter-aggregate pores between aggregates). The same value of 1μm was considered to separate these two pore domains of the powder at the initial state (Alonso *et al.*, 2011; Romero *et al.*, 2011; Romero, 2013). The compaction of the powder to form pellets mainly induces the changes of porosity between aggregates, that is, the changes in the dry density did not affect the intra-aggregate porosity much. A less important smaller peak is observed around 2.7nm in the nitrogen adsorption test, which can be part of microporosity. This double pore network changes during saturation at constant volume conditions displaying the PSD function as a dominant pore mode at around 0.35 µm for the saturated powder. In saturated conditions, the powder presents a bimodal microporosity with pores of 22nm and 0.35 µm. Moreover, displays some peak between 30-70µm due to the swelling of aggregates that reduce the porosity of inter-aggregate (macro-porosity).

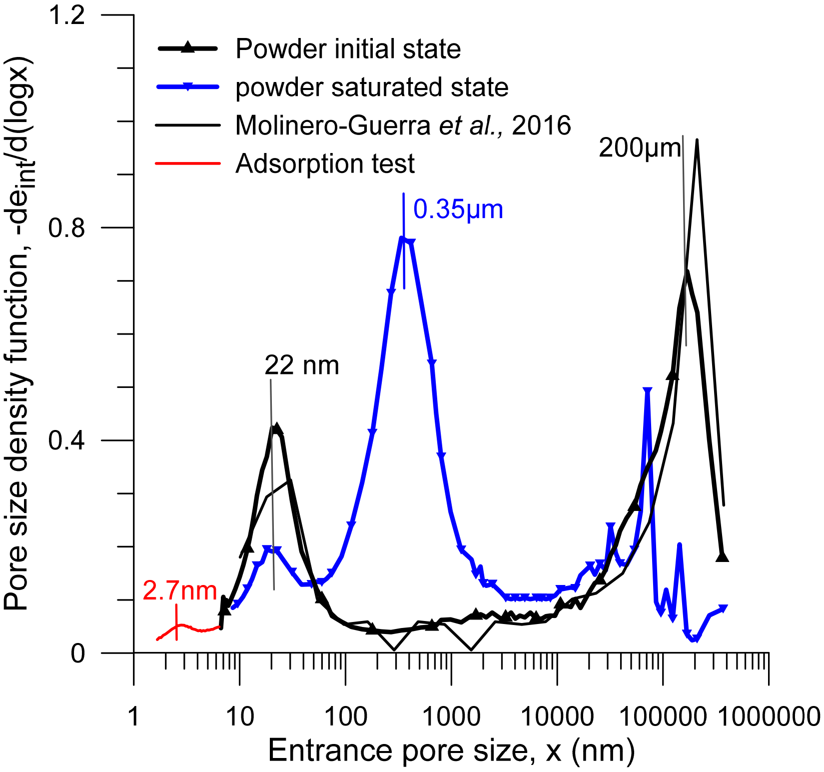

Figure 2-15. Pore size density function for powder (initial and saturated state) from MIP, together with data from nitrogen adsorption test and comparison with data from Molinero Guerra et al. (2016).

Table 2-5 summarises the microstructural characterisation at the different hydraulic states of the pellet and the powder. The second column presents the intruded void ratio e_{int} by MIP. e_{int} is usually smaller than the real void ratio e (first column) due to the non-intruded void ratio with pore sizes below 7 nm and the non-detected void ratio with pore sizes above 470 µm (Romero & Simms, 2008). This smaller e_{int} compared to e is consistent for powder at both hydraulic states and the saturated pellet.

The measured microstructural void ratio e^{micro} (with pore sizes smaller than 1µm) to the total intruded void ratio e_{int} was determined with the following expression (x_{min} = 7 nm and x_{max} = 400 µm refer to the minimum and maximum pore sizes detected by MIP):

$$\frac{e^{micro}}{e_{\text{int}}} = \frac{\int_{\mathrm{x}_{min}}^{\mathrm{x}=1\mu m} f(logx)\ dlogx}{\int_{\mathrm{x}_{min}}^{\mathrm{x}_{max}} f(logx)\ dlogx} \tag{2-6}$$

The ratios given by Equation (2-6) and shown in the third column were then multiplied by the real void ratios (e) of the different states to estimate the corresponding microstructural void ratios e^{micro}(fourth column). The macrostructural void ratios with sizes larger than 1 μm were finally calculated as $e^{Macro} = e - e^{micro}$(the fifth column).

Table 2-5. Micro and macrostructural void ratios for powder and pellets at different hydraulic states.

Component	**e_{int} (MIP)**	**e^{micro}/e_{int} (MIP)**	**e^{micro}**	**e^{Macro}**	**β_m**
Powder (as-poured) e = 1.52 w = 10.64%	0.879	0.349	0.530	0.99	0.421
Powder (isochoric saturation) e = 1.52 e = 54.95%	1.01	0.689	1.047	0.473	
Pellet (Initial state) e = 0.392 w = 6.54%	0.359	0.746	0.292	0.10	0.216
Pellet (saturated) from packing of pellets. e = 1.33 w = 41.16%	1.08	0.375	0.499	0.831	

As observed, e^{micro} significantly increased with water content. The parameter βthat describes the change in e^{micro} for a water ratio e_w change (volume of water to the volume of solids) is given by:

$$\beta_m = \frac{\Delta e^{micro}}{\Delta e_w}\ with\ e_w = \frac{\rho_s}{\rho_w} w \tag{2-7}$$

Table 2-3 also presents different β_m for the powder and the pellet undergoing saturation. The values are consistent with data reported by Romero (2013) on clays with a high content of montmorillonite (ranging between 0.40 and 0.43). The microstructural void ratios for each component ($e^{micro\ pow}$ and $e^{micro\ pe}$ for the powder and the pellet, respectively) were used to estimate the corresponding values e^{micro} for the mixture at the two hydraulic states:

where *f* = 0.20 is the dry mass fraction of the powder (equivalent to the fraction of the volume of solids of the powder to the total volume of solids V_s of the mixture), and V_p^{micro} is the volume of micropores (powder and pellets).

$$e^{micro} = \frac{V_p^{micro}}{V_s} = e_{mPo} f + e_{mPe}(1-f) \tag{2-8}$$

The following microstructural variables (microstructural porosity ϕ^{micro} and macrostructural porosity (ϕ^{Macro}) (equation 2-9) were also considered for the mixture at the two hydraulic states (as-prepared and saturated).

$$\begin{gathered}\bar{\phi}_{micro} = \frac{V_p^{micro}}{V_s + V_p^{micro}} = \frac{e^{micro}}{1+e^{micro}}; \\ \phi^{Macro} = \frac{V_P^{Macro}}{V_t}; \phi^{micro} = \frac{V_p^{micro}}{V_t} \\ \phi = \phi^{Macro} + \phi^{micro} = \phi^{Macro} + \bar{\phi}_{micro}\left(1-\phi^{Macro}\right)\end{gathered} \tag{2-9}$$

where V_p^{micro} is the volume of micropores and $V_P^{Macro} = V_t - V_p^{micro}$ the volume of macro-pores. Table 2-6 summarises these microstructural variables for the mixture (the saturation path was assumed under constant volume condition). As observed, ϕ^{micro}increased with saturation and significantly reduced the macro-porosity (ϕ^{Macro}).

Table 2-6. Microstructural variables for the mixture at two hydraulic states.

Material	**Microvoid ratio, e^{micro}**	**Macro-porosity, ϕ^{Macro}**	**Micro-porosity, $\bar{\phi}_{micro}$ and (ϕ^{micro})**
Mixture as prepared $\phi = 0.46$ $w = 8.47\%$	0.340	0.28	0.254 (0.18)
Mixture saturated $\phi = 0.46$ $w = 31.0\%$	0.61	0.14	0.378 (0.32)

Figure 2-16 shows the PSD of the mixture in a saturated condition compared with the components in a saturated state. The mixture was prepared at a dry density of

1.49 Mg/m^3 (e = 0.86) and isochoric cell (50 mm in diameter, 20 mm in height) and saturated at constant volume conditions for a long-time (200 days) to ensure a degree of saturation of 100%. The water pressure of 2 MPa was used for the hydration with distilled water. The PSD curve shows a bimodal structure with micropores with a pore mode of 18nm, which is in the range of the small pores detected within a single pellet of bentonite and also in the powder. The macro-pores with pore mode of 45µm correspond to inter-aggregate pores (macro-pore), likely the inter-grain pores (between pellets and power).

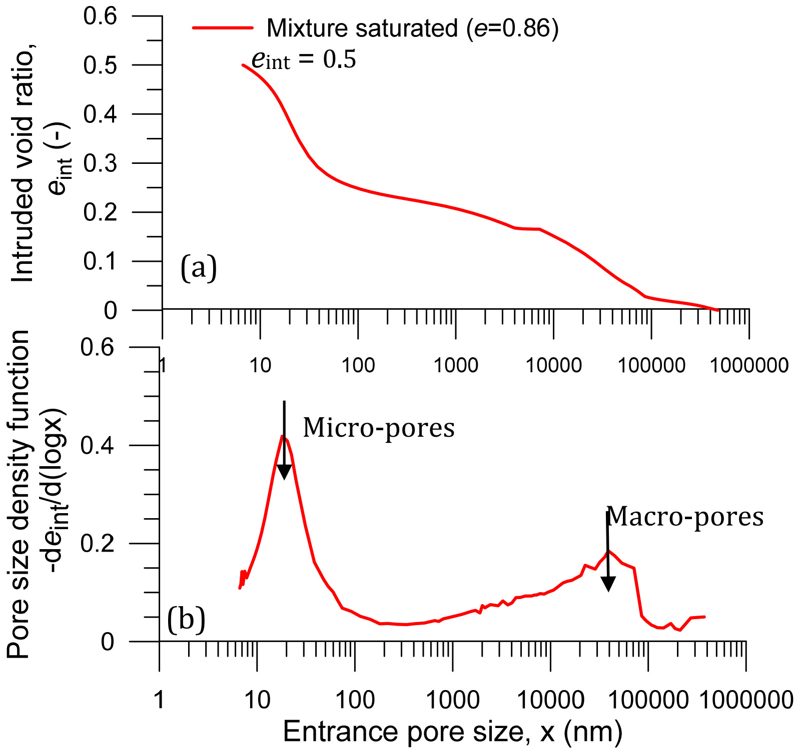

Figure 2-16. Cumulative porosity curve (a) and derivative curve (b) for the mixture saturated at constant volume condition.

2.7.2. Field Emission Scanning Electron Microscopy (FESEM) on pellet

The field emission scanning electron microscope (FESEM) is a high-resolution instrument that can show topographical information on the surface of the sample (aggregates, pore diameter, and fissures, the orientation of pores and particles) up to high magnifications (Janssen, 2015). Figure 2-17 shows the microscope used (JEOL JSM-7001F). FESEM requires dehydrated samples, and the same freeze-drying process was used. Samples were also prepared for thin conducting coating for clearer images. Many authors (Delage *et al.*, 2006; Romero & Simms, 2008; Liu *et al.*, 2011; Cotecchia *et al.*, 2016) have used scanning electron microscopy to study the surface of the material in detail.

Figure 2-17. FESEM microscope microscope (JEOL JSM-7001F).

The first stage of the FESEM study was focused on studying the surface of as-compacted pellets to observe patterns of fissures. Figure 2-18 shows the top surface of a 7-mm pellet at low magnifications, in which some fissures are clearly detected. Larger magnifications were further used to better observe these fissures, which concentrated around the perimeter of the lateral surface and the spherical cap, as well as on the top of the cap around compressed aggregates. Figure 2-19 presents these top fissures on the cap and around the perimeter.

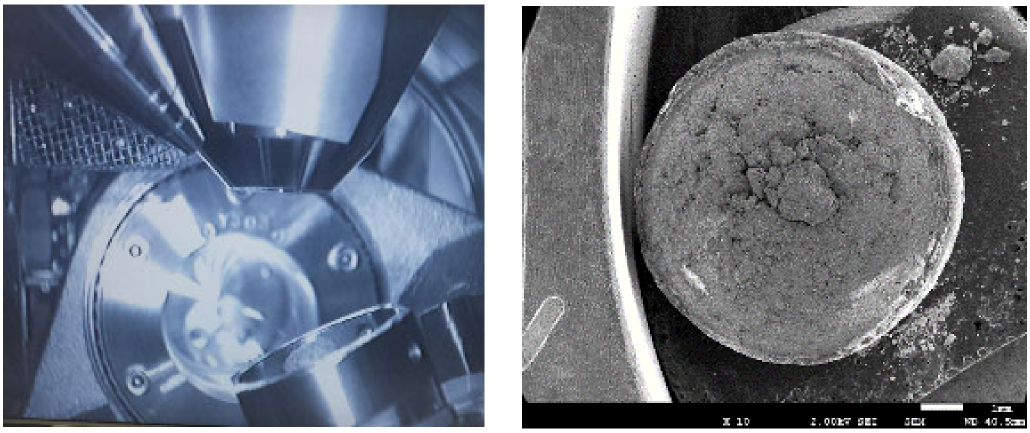

Figure 2-18. Picture of a 7-mm pellet during the FESEM test.

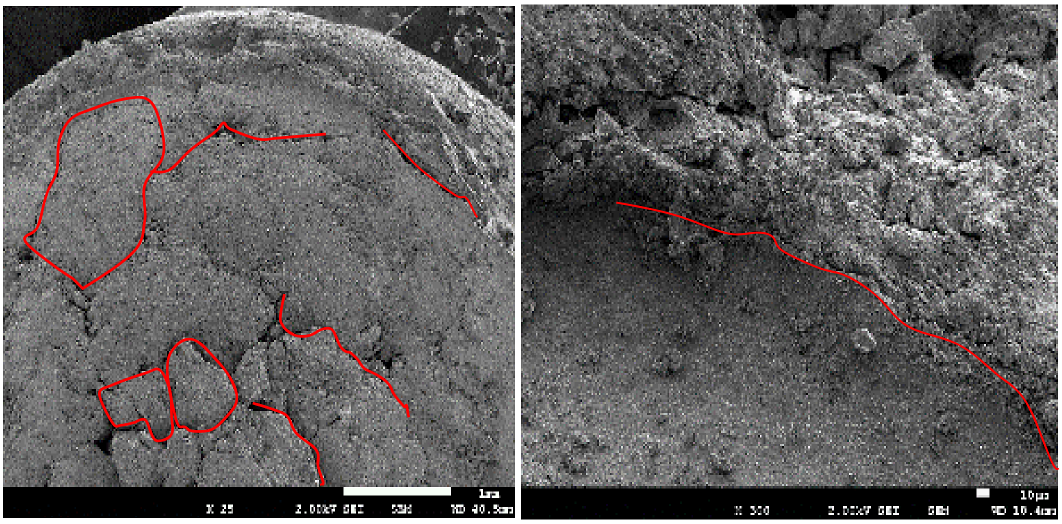

Figure 2-19. Picture of the surface of the spherical cap of the pellet. Fissures between aggregates and around the perimeter.

It is also expected that during hydration new fissures will develop since swelling will progress from the external boundary towards the centre of the pellet. During the initial swelling of the outer lateral surface, peripheral detachment may occur from the core of the pellet, possibly along the pre-existing fissures. Final swelling of the inner core may induce further fissuring, as suggested by Cardoso & Alonso (2009). These patterns of cracking, which evolve from the exterior towards the interior of the pellet, are controlled by the evolution of suction inside the pellet. Figure 2-20a on the left presents the expected pattern of cracking in fragments of marl (Cardoso & Alonso, 2009). Figure 2-20b on the right shows fissures between dry aggregates at the as-compacted state of the pellet.

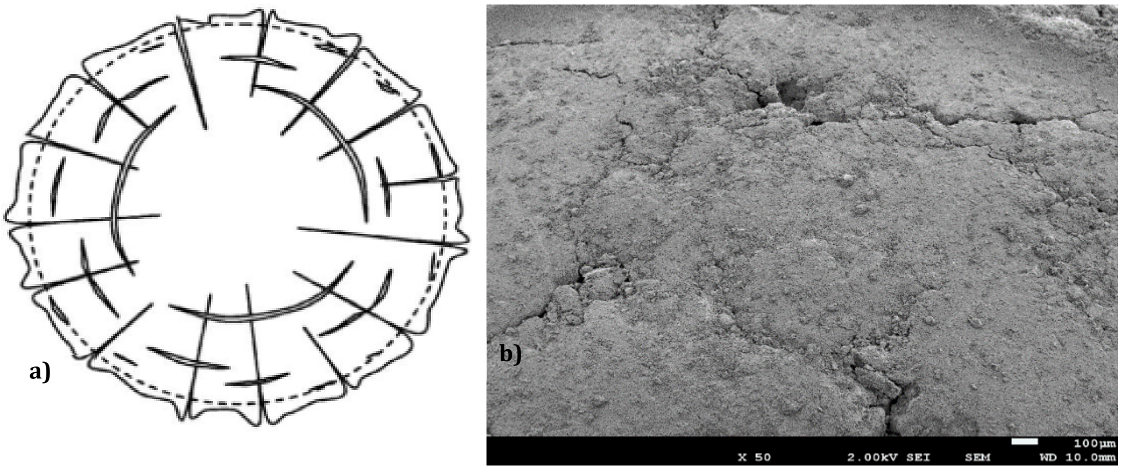

Figure 2-20. a) Cracking pattern of the fragment by Cardoso & Alonso (2009)*, b). Fissures on the pellet surface at the as-compacted state.*

2.8. Concluding remarks

This chapter presented an experimental study on a binary mixture of MX80 bentonite pellets (80% in mass) and powder and mixture components focused on characterising the initial and saturated states.

This mixture does not present significant segregation effects that mean particles are held in place, and no important movements of powder within the pellet skeleton are expected. Moreover, it is crucial to guarantee excellent arrangement close to cubical–tetrahedral between pellets reaching dry density between 1.19-1.17Mg/m^3 to obtain the target of the dry density (1.49 Mg/m^3).

The better way to install the sample is using protocol 2, which consists of placing layer by layer the pellets and pouring the powder. The procedure ensured almost the coordination number of 8 between pellets, reaching a dry density of 1.47 Mg/m^3 close to the target dry density (1.49 Mg/m^3). Also, this protocol presents more homogeneity in the image of CAT and more uniformity in the data of images analysis. According to the CAT performed, the less homogeneous is protocol three, which presented concentrations of powder overfilling inter-pellet voids and regions with empty inter-pellet voids.

The components and the mixture displayed multi-modal PSDs that significantly changed during saturation. As expected, the pellet and powder display similar micropores at the initial state because the powder was fabricated by crushing the pellet of bentonite. The double porosity in the powder changes during saturation at constant volume conditions displaying the PSD function a dominant pore mode at around 0.35 μm and presenting some peak between 30-70μm due to the swelling of aggregates that reduce the porosity of the inter-aggregate porosity. Consequently, the mixture displays a multi-modal PSD after saturation at constant volume conditions, with micropores with a pore domain similar to the powder and pellet (around 18nm) and macro-pores with a pore domain of 45μm, which can be associated with some pores between the pellets and powder.

The FESEM shows topographical information of the pellet's surface, observing many fissures at the top and bottom part. These fissures were also detected in the MIP results of the pellet, corresponding to macro-pore volume. The same behaviour was reported by Molinero-Guerra *et al*. (2016) but using µ-CT and MIP

.

3. HYDRO-MECHANICAL PROPERTIES

3.1. Introduction

Heterogeneous mixtures of high-density bentonite have been suggested as a suitable sealing material for nuclear disposals of high-level radioactive waste. This heterogeneous mixture will have consequences on the short-term HM behaviour of the material and its long-term response to gas migration. It is, therefore, essential to understanding these HM behaviour features when assessing the overall repository safety. These bentonite-based mixtures can efficiently decrease the gaps between the rock and the seal due to operational advantages in terms of emplacement (Alonso *et al.*, 2011; Gens *et al.*, 2011; Molinero-Guerra, 2018; Mokni *et al.*, 2019). Also, these mixtures display a high swelling capacity, low permeability and high radionuclide migration retardation properties (Hoffmann, 2005; Gens *et al.*, 2011; Darde *et al.*, 2018; Molinero-Guerra, 2018).

In the context of radioactive waste disposal, several investigations have been performed on the hydro-mechanical behaviour of engineered barriers composed for compacted pure bentonite or compacted bentonite/sand mixtures and bentonite pellet (Imbert & Villar, 2006; Hoffmann *et al.*, 2007; Wang *et al.*, 2013c; Saba, 2014; Sun *et al.*, 2013; Ye *et al.*, 2014; Molinero-Guerra, 2018; Mokni *et al.*, 2019; Darde *et* *al.*, 2020 among other). Several tests were performed by Hoffmann *et al.* (2007) on compacted granular Febex bentonite mixtures at different dry densities considered within the Engineered Barrier (EB) project. Imbert & Villar (2006) investigated the hydro-mechanical behaviour of a 50/50 FoCa bentonite pellet/powder mixture by a series of infiltration tests. Molinero-Guerra (2018) carried out several tests on compacted granular mixture and pellet with different vapour exchange within the SEALEX project.

The hydro-mechanical behaviour of bentonite-based materials is controlled by the water mobility (permeability), water retention capacity, swelling response and compressibility. The saturated permeability is one of the most crucial soil properties related to all those hydro-mechanical processes governing the transport, the changes in the amount of water stored in pores and the development of the stresses and deformations generated in a mass of soil due to changes in external loadings. Permeability is controlled by the soil fabric, characterized by its dry density (Hoffmann *et al.,* 2007). Consequently, permeability is lower in fine-grained soils, like clays. Moreover, it reduces with the increase in the compaction effort required to produce a denser soil skeleton.

Numerous investigations (Pintado, 1999; Villar, 2002; Hoffmann, 2005; Karland *et al.* 2008 among others) were carried out to relate some expected phenomena during the re-saturation of a constant volume of bentonite-based material to changes in the water flux conditions. These investigations providing a wide database on the hydraulic behaviour of bentonite-based materials and their dependence on the dry density, the water content, the chemical composition of pore-water and temperature and also corroborate the expected decrease of water permeability as the dry density of compacted samples increases due to the reduction in their initial porosity.

The water retention capacity of bentonites depends on the type, fabric and mineralogy of the soil (Rizzi *et al.,* 2012) and also the complex Physico-chemical interactions at particle level involving the microstructural water, the clay layers and the exchangeable cations present in the inter-lamellar space (Jacinto *et al.,* 2012). Furthermore, the confinement conditions (constant volume or free swelling) affect the shape of this curve. The hydration under free swell conditions allows the expansive clays to fully develop their swelling, which leads to a significant increment of pore volume and, consequently, to a higher water retention capacity near saturation (Lloret & Villar, 2007), whereas, a constant volume, the increase of the initial dry density leads to a reduction in their water retention capacity at lower suction values (Hoffmann et al., 2007). Actually, the increase in dry density implies a reduction in porosity and in the water content that can be retained in the macro-pores, where the main mechanism of water retention is capillarity (a mechanism that drives the saturation state of macro-pores). The changes in the soil density play a crucial role during the initial stages of dehydration when suction is still small. In fact, on the word of Dieudonné *et al.* (2017), an increase in the initial dry density of an expansive clay implies not only a decrease in the macrostructural pore volume but also a reduction in the size of these pores

According to Romero *et al*. (1999) and Jacinto *et al.* (2012), there is a zone (between 20 MPa to 500 MPa) of the water retention curve that is mainly related to the water content in micro-pores and depends on the specific surface area and the mineralogical composition of the clay particle, in this zone the volume of water stored in pores is not affected by the dry density. The water retention curves of MX80 bentonite have been used by De la Morena *et al.* (2018) to determine the water content present in the microstructure. Also, their model interprets the microstructural deformability of the bentonite. The last one is an essential issue for double porosity material modelling. Several authors have investigated the permeability of clays (Lajudie *et al.*, 1994; Villar, 2005; Karnland *et al.*, 2008; Ye *et al.*, 2014; Gonzalez-Blanco *et al.*, 2017; Mesa-Alcantara *et al.*, 2020a, among others) and the water retention curve of clays (Delage *et al.*, 2006; Villar, 2007; Seiphoori, 2014; Molinero-Guerra, 2018), detecting that the permeability and retention capacity decrease with the increase in dry density.

The main hydro-mechanical behaviour of bentonite is its expansivity on wetting and the shrinkage on drying. The swell-shrink behaviour of clay-rich soils is enabled by the mechanical, geological and environmental conditions prevailing during the genesis and the geological history of such materials (Gens & Alonso, 1992). The three groups of mechanisms that affect the expansion of soil, according to Pousada (1984) are the intrinsic properties of the particles (clay mineralogy, the specific surface area (SSA) of clay particles, the cation exchange capacity (CEC) and the pore fluid nature) and the conditions of the soil, the composition and properties of the saturation water and external factors such as soil stress history, temperature, dry density, the compaction procedures and the availability of water. Previous studies (Pusch *et al.*, 1992; Lloret *et al.*, 2003; Gens *et al.*, 2011; Villar *et al.*, 2012; Saba *et al.*, 2014; Schanz & Al-Badran, 2014; Darde *et al.*, 2018; Molinero-Guerra, 2018; Darde *et al.*, 2020) documented that there is a well-defined relationship between the dry density of bentonite and the swelling pressure, where the swelling pressure increase as increasing the dry density.

The influence of water salinity on the behaviour of swelling pressure in the bentonite has been studied by many authors (Villar, 2006; Lloret & Villar, 2007; Castellanos *et al.*, 2008; Zhu *et al.*, 2013; Chen *et al.*, 2015; Chen *et al.*, 2017; Navarro *et al*. 2017a) detecting that the increase in salinity of the pore water of the bentonite induced decreases in the swelling capacity, this difference is less for high densities and high vertical load and also when the salinity of the solution is very low. Navarro *et al.* (2017b) developed a model to estimate the swelling pressure of bentonites taking into account the coupled hydro-chemo-mechanical behaviour.

Another main property is the compressibility of the material, this property can be investigated with an oedometer test to allow determine the speed and magnitude of the consolidation of a laterally confined soil when axially loaded and drained. Different authors (Villar, 2005; Hoffmann *et al.*, 2007; Pintado *et al.*, 2009; Molinero-Guerra, 2018) have carried out several oedometer tests to know this behavioural feature in compacted bentonite and granular mixtures. According to Moliero-Guerra (2018), the pellets mixture has a lower value of yield stress than pure bentonite, except for sample hydrated at zero suction because the granular structure in the case of non-zero suction where the volume change behaviour is governed by the rearrangement and crushing of pellets, and the loss of the granular structure in the case of zero suction.

In this Chapter, hydro-mechanical experiments (intrinsic permeability, water retention, swelling under load, swelling pressure and compressibility properties of the mixture) are described and interpreted. It also includes the modelling of the loading/unloading tests with a double-porosity framework.

3.2. Water permeability tests after long-term saturation

Several laboratory tests were performed on the MX80 bentonite mixture and powder in order to know the water permeability.

3.2.1. Methodology

Variations of intrinsic permeability with porosity have been derived from controlled-gradient permeability tests performed on a cell (50 mm in diameter and 20 mm high) at constant volume conditions (isochoric cell from Hoffmann (2005)). The samples were subjected to a long-term back-pressure application (2 MPa applied to the bottom cap with a standard pressure-volume controllers-PVC). Water permeability was determined under steady-state conditions at a constant high hydraulic gradient around 10200. Distilled water was used for each test. The saturated permeability is calculated by considering Darcy's law.

The intrinsic permeability K, considering a water property factor of $\rho_w g / \mu_w$ = 9.744×10^6 $(m.s)^{-1}$ at 20°C (water density ρ_w = 998.2 kg/m^3 and water dynamic viscosity μ_w = 1.005×10^{-3} $N.s/m^2$).Figure 3-1a shows a schematic of the permeability test during the saturation of the material.

The outflow tube was placed in a container with water to keep atmospheric conditions and prevent evaporation. Once the material is saturated and the water flows in the outlet tube (red line), another PVC is installed to measure the volume of water at zero pressure applied, as shown in Figure 3-1b.

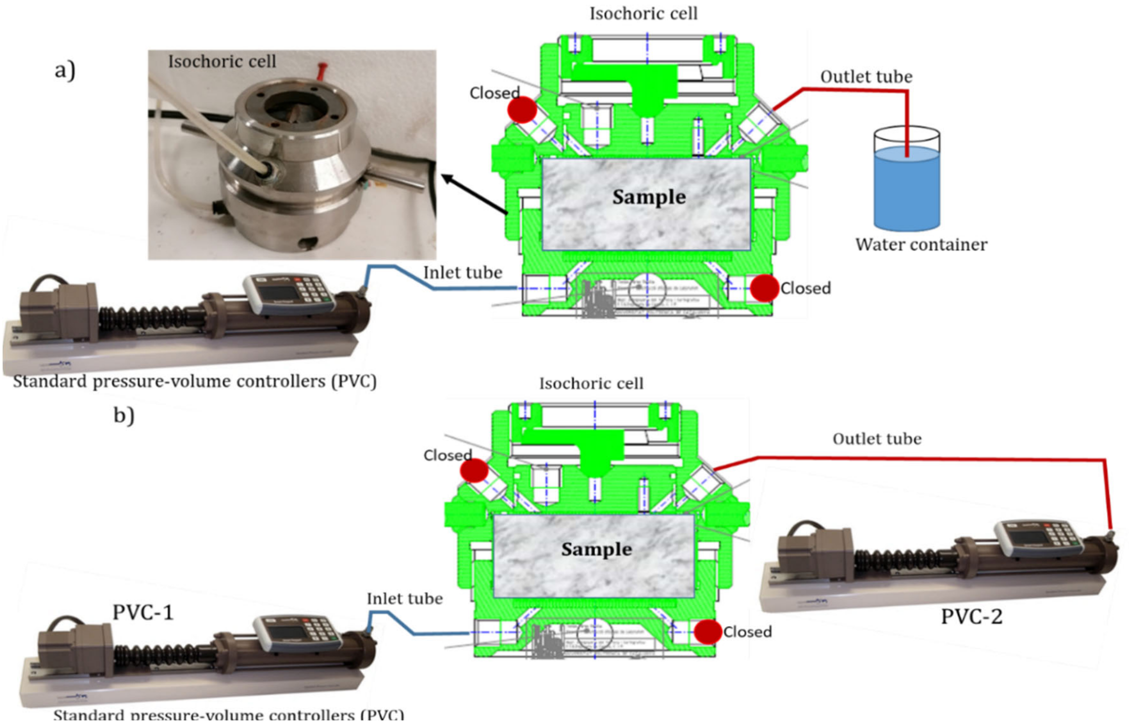

Figure 3-1. Schematic representation of permeability test. Isochoric cell from Hoffmann (2005).

3.2.2. Results

Three long-term saturation tests were carried out. Two tests were performed on specimens of pellet/powder mixture prepared at a total porosity $\phi=0.46$ ($\rho_{d\ mix}$ = 1.49 Mg/m^3). Another test was performed on powder prepared by pouring at a total porosity equal to 0.60 ($\rho_{d\ pow}$ = 1.10 Mg/m^3). The initial water contents were w = 7.66% (total suction s = 111 MPa) and w = 9.51% (s = 82 MPa) for the mixture and powder, respectively.

The first experiment of the MX80 bentonite pellet/powder mixture was carried out for 136 days and reached an intrinsic permeability of 8.16 x10^{-21} m^2. The second test was performed under steady-state condition for 200 days, reaching an average of the intrinsic permeability of 1.17 x10^{-20} m^2. After long-term saturation, the final water contents were 30.93% for the two tests of the mixture, and this value corresponded to a degree of saturation of around S_r = 0.99 for the mixture at 0.46 ($\rho_{d\ mix}$ = 1.49 Mg/m^3).

The powder experiment was carried out for 142 days, and the average value of intrinsic permeability was 5.64 x10^{-20} m^2. The saturated water content was 54.95%, corresponding to a value of the degree of saturation S_r = 1.00 for powder at 0.60 ($\rho_{d\ pow}$ =1.10 Mg/m^3).

Figure 3-2 presents the evolution of the intrinsic permeability (K) for powder and two mixture tests under steady-state conditions. The value of the permeability test of 1.17 x10^{-20} m^2 (Test 2) will be considered for the modelling since it presented a more stable value during the test.

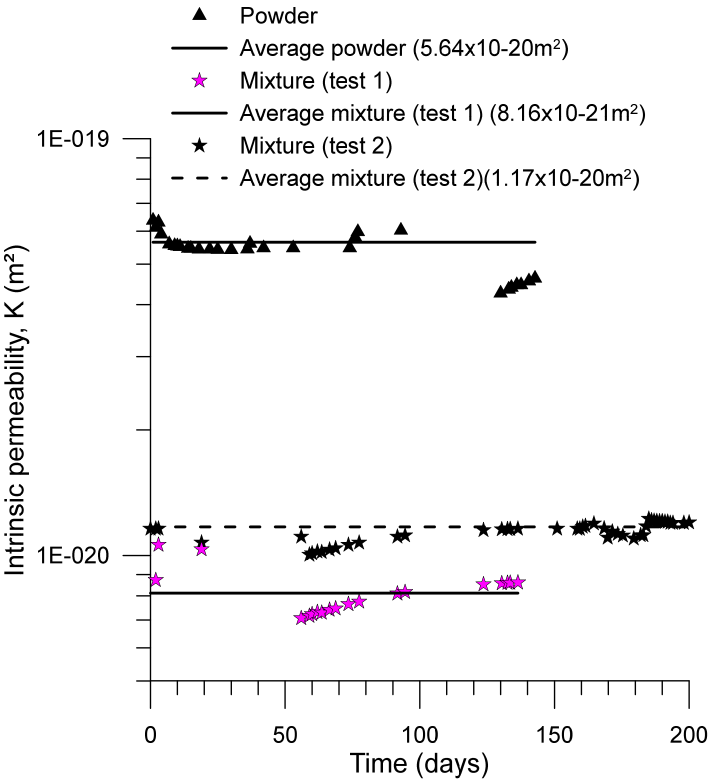

Figure 3-2. Evolution of the intrinsic permeability of the powder and mixture.

The intrinsic permeability of the pellet was estimated using MIP data considering the Hagen-Poiseuille equation for laminar flow through cylindrical tubes of diameter x (Romero *et al.*, 1999), according to the following expression

$$\mathrm{K}_{pe} = \alpha\,\phi_{\mathrm{int}\,pe}\int_{x_{max}}^{x_{min}} x^2 f(x)dx = 1.60x10^{-21}m^2 \qquad (3\text{-}1)$$

where $\phi_{\mathrm{int}\,pe}$ = 0.265 is the intruded porosity, x the pore size, and *f(x)* the pore size density function (x_{min} = 7nm and x_{max} = 400μm refer to the minimum and maximum pore sizes detected by MIP. Parameter α = 8.2x10^{-12}, which takes into account the shape factor, tortuosity and connectivity, was fitted with the measured intrinsic permeability and the pore size distribution of the powder at the same hydraulic state of the pellet ($\phi_{\mathrm{int}\,pow}$ = 0.468). Intrinsic permeability results are shown in Figure 3-3 as a function of porosity with data reported by different authors (Villar, 2005; Karnland *et al.*, 2008) on MX80. The measured results were consistent with data reported by different authors.

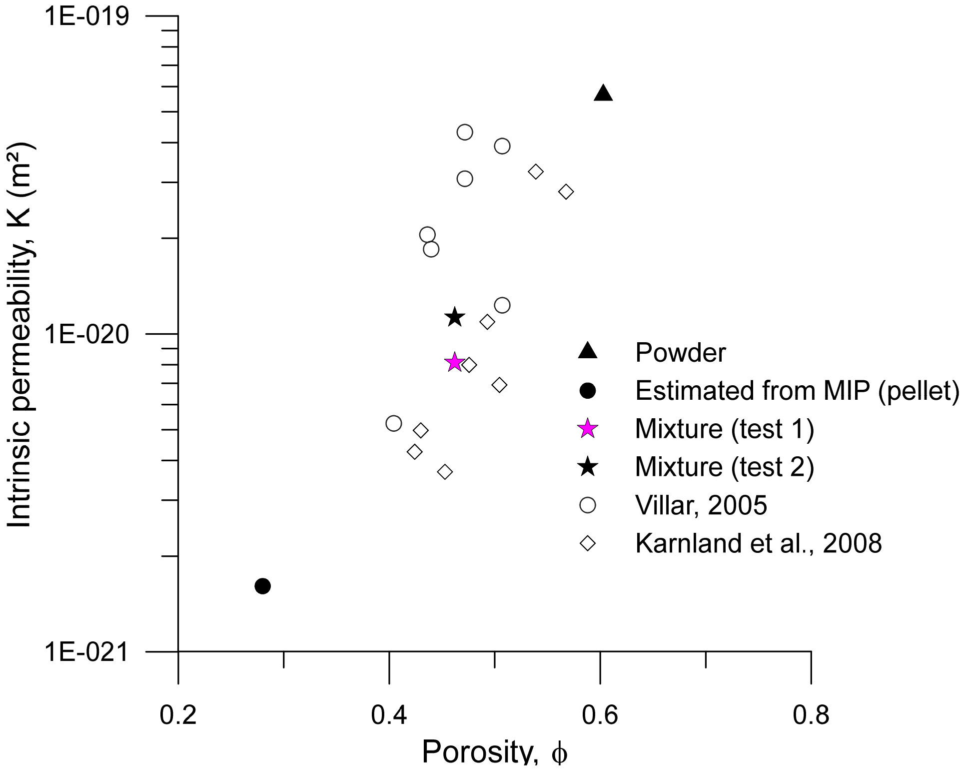

Figure 3-3. Water permeability results as a function of the porosity. Compared with several authors (Villar, 2005; Karnland *et al.*, 2008).

3.3. Water retention curves

3.3.1. Methodology

The water retention curve of powder was investigated under constant volume using several samples (15 samples) compacted with different water contents at the same dry density (1.10 Mg/m^3) (e = 1.52). Water was added and put under equilibrium for several days. Each sample was placed in a small container with 20 mm in diameter and 5 mm high. Then, total suction with Decagon WP4 dew point chilled-mirror psychrometer was measured. Finally, the water content of each sample was verified and determined by oven-drying at 110°C for more than 24 hours. Table 3-1 presents the results of the tests.

Additionally, a water retention curve on drying the powder was carried out under free shrinkage condition. The sample used was taken from the swelling pressure test **(explained in section 3.63)** at a water content of 55.02% (S_r = 1). The total suction was measured in the laboratory with Decagon WP4. The sample was dried in steps in a desiccator under controlled relative humidity. Every two days the sample was weighed before and after measuring the total suction.

The water retention curve of the pellets was derived using data from mercury intrusion porosimetry MIP data. The non-wetting mercury penetration is assumed to be equivalent to the air-intrusion path for the same diameter of pores being intruded (Romero & Simms, 2008).

Finally, the water retention curve of the mixture was performed along a drying path under unloaded conditions. The sample was taken from the oedometer under saturated conditions **(explained in section 3.4).** The sample used to measure the suction in the Decagon WP4 presented a dry density of 1.40 Mg/m^3 (to calculate the dry density of the sample, it was trimmed at known volume) with a final water content of 35.4% (S_r = 1). The drying path was performed in steps under free shrinkage conditions in a desiccator under controlled relative humidity. The total suction was measured every week and after that, the sample was kept in the desiccator to ensure the equilibrium of water potential. The sample was weighed before and after measuring the suction.

3.3.2. Results

Figure 3-4 shows experimental data with the fitting with the expression of van Genuchten (1980)(equation 3-2) for a reference void ratio e = 1.52 (1.10 Mg/m^3) with $P_0 = 2$ MPa; $\lambda = 0.32$.

$$S_r = \left(1 + \left(\frac{s}{P_0}\right)^{1/(1-\lambda)}\right)^{-\lambda} \; ; \; e_w = \frac{\rho_s}{\rho_w} w = 2.77\, w \qquad (3\text{-}2)$$

Table 3-1. Water retention results of the powder with an initial dry density of 1.10 Mg/m³.

Sample	Water content	Total suction	Degree of saturation
P1	10.26	89.54	18.698
P2	11.80	65.60	21.511
P3	12.40	61.00	22.595
P4	13.64	55.01	24.857
P5	13.86	51.30	25.258
P6	14.67	43.35	26.734
P7	15.50	35.18	28.247
P8	17.03	25.64	31.035
P9	16.33	29.91	29.759
P10	17.63	21.20	32.128
P11	18.97	16.28	34.570
P12	20.12	12.81	36.669
P13	20.81	11.75	37.933
P14	22.27	9.02	40.576
P15	23.51	7.09	42.843

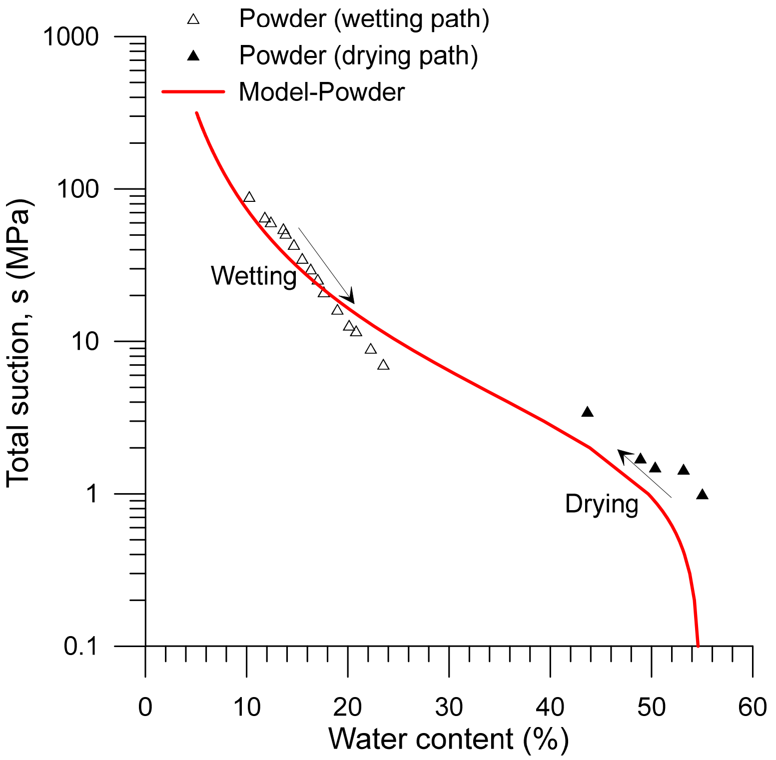

Figure 3-4. Water retention curve of powder (experimental data) and fitting (van Genuchten, 1980) curves of powder at an initial dry density of 1.10 Mg/m³ (e = 1.52).

Figure 3-5 shows the experimental data and the fitting with equation 3-2 (van Genuchten., 1980) for a reference void ratio e = 0.39 with $P_0 = 35$ MPa; $\lambda = 0.32$ together with the comparison data from Molinero-Guerra (2018) under free swelling conditions in wetting and drying path for the pellet (void ratios are indicated as labels in the figure). As observed, if the pellet is hydrated under free swelling conditions, it will change the void ratio affecting water content, confirming a significant swelling at low suction and even reaching a value of total porosity higher than the powder. The difference between Molinero-Guerra (2018) and this study is the measurement of the change in suction under free conditions. Good agreement between the results of Molinero-Guerra (2018) and the estimated values with MIP data is observed.

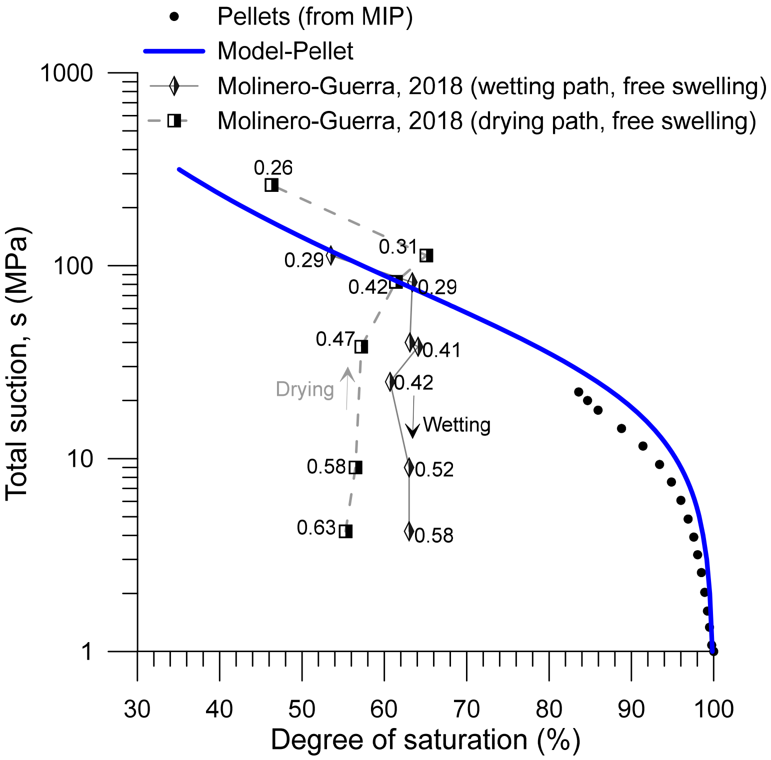

Figure 3-5. Water retention curve of the pellet (derived from MIP), fitting (van Genuchten, 1980) curves of pellet and comparison with Molinero-Guerra (2018). Labels correspond to porosity.

The experimental results are displayed in Figure 3-6, together with the data reported by different authors. Seiphoori *et al.* (2014) investigated the water retention curve at constant volume with a dry density of 1.5Mg/m^3 (compacted bentonite), and Molinero-Guerra (2018) carried out the test at a constant volume (dry density of 1.49Mg/m^3 of the mixture). Furthermore, the initial suction of the pellet and powder are also displayed together with the fitting of van Genuchten (1980)(equation 3-2) (in terms of water content w) for a reference void ratio e = 0.86 (as-compacted state of the mixture with w_{sat} = 30.68% and $P_0 = 10$ MPa; $\lambda =$

0.32). Table 3-2 presents the parameter of van Genuchten (equation 3-2) curve for the mixture and the components.

Table 3-2. summary of the parameter of van Genuchten curve for the mixture and the components.

Material	P_0	λ
Pellet (e = 0.39)	35	0.32
Powder (e = 1.52)	2	0.32
Mixture (e = 0.86)	10	0.32

As observed, no important total suction changes have been detected between the powder, the pellets and the mixture at the same water content (at water contents w < 10%). This fact indicates that at these water contents the water retention curve of MX80 is not sensitive to void ratio and pore size distribution changes and is mainly dependent on water content (Romero *et al.*, 2011).

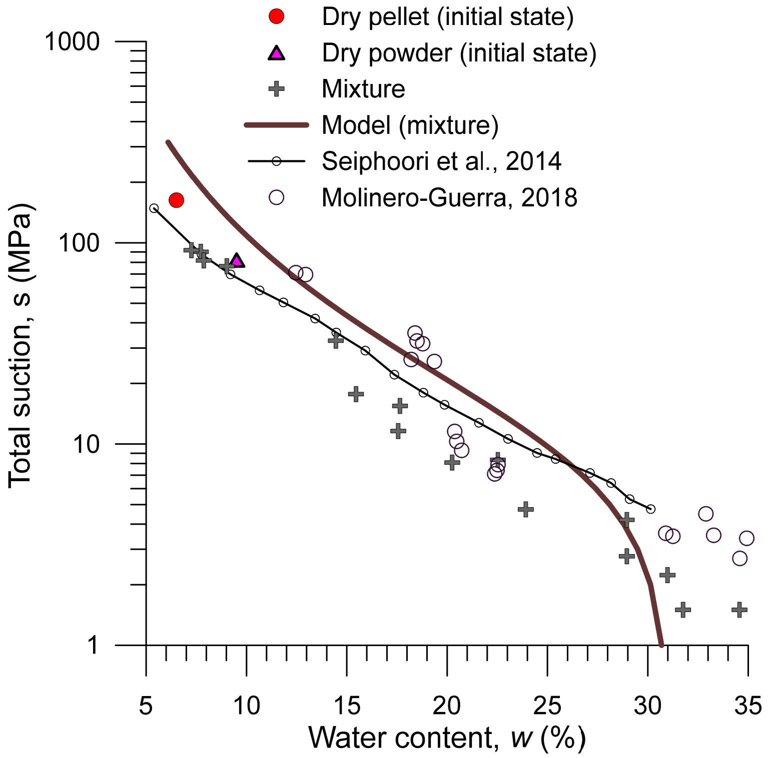

Figure 3-6. Water retention curve on drying of the mixture together with pellets and powder at the initial state and comparison with data from Seiphoori *et al.* (2014) and *Molinero-Guerra (2018) and fitting with van Genuchten (1980) model.*

Table 3-3 summarises water retention data for powder, pellets (single and packing) and mixture at different hydraulic states. Total suctions were measured with a dew point psychrometer.

Table 3-3 Water retention data for powder, pellets (single and packing) and mixture.

Material	Initial state Saturation at constant volume			
	Initial suction	**Initial water content**	**Final suction**	**Final water content**
Pellet (single and packing)	163 MPa	6.51%	0.63 MPa	53.83%
Powder	82 MPa	9.51%		
	82 MPa	10.43%	3.28 MPa	54.95%
Mixture	122 MPa	8.47%	5.27 MPa	30.93%

3.4. Compressibility on loading

To determine the compressibility parameters for the mixture (dry and saturated state), packing of pellets (dry and saturated state), powder (dry and saturated state) and pellet (compacted powder of the dry density 1.99 Mg/m^3) different tests under oedometer conditions were carried out using the setup presented in Figure 3-7. The oedometer tests were carried out in a cell with a diameter of 50 mm and high of 20 mm high. For saturated tests were used distilled water and PVC to apply the water pressure. The increase in vertical stress was realised when the previously applied vertical stress strain reached less than 0.01%/day.

Figure 3-7. Setup for oedometer tests.

3.4.1. Powder and pellet (compacted powder) compressibility

The poured powder was prepared at a dry density $\rho_{d\ pow}$ = 1.10 Mg/m^3(e = 1.52), w = 9.51% and at total suction of 82 MPa. The oedometer of the MX80 bentonite pellets (compacted powder) was prepared at $\rho_{d\,pe}$= 1.99 Mg/m^3 (e = 0.39) and constant water content of w = 9.56% at total suction of 88 MPa.

Figure 3-8 shows the compression behaviour on loading and unloading experimental of the compacted powder at the pellet's density (compacted powder at a dry density of 1.99 Mg/m^3) and compression curves on loading/unloading of powder. The maximum compressibility parameter on loading (assumed post-yield compressibility) of the pellet was $\lambda(s)$ = -$\Delta e/\Delta(\ln\sigma_v)$ =0.030, and the pre-yield compressibility value on unloading was κ = -$\Delta e/\Delta(\ln\sigma_v)$ = 0.008. The maximum compressibility parameter on virgin loading (post-yield) of powder was $\lambda(s)$ = 0.264, and the pre-yield compressibility on unloading κ = 0.016. As observed, the powder displayed larger compressibility on loading/unloading compared to the pellet.

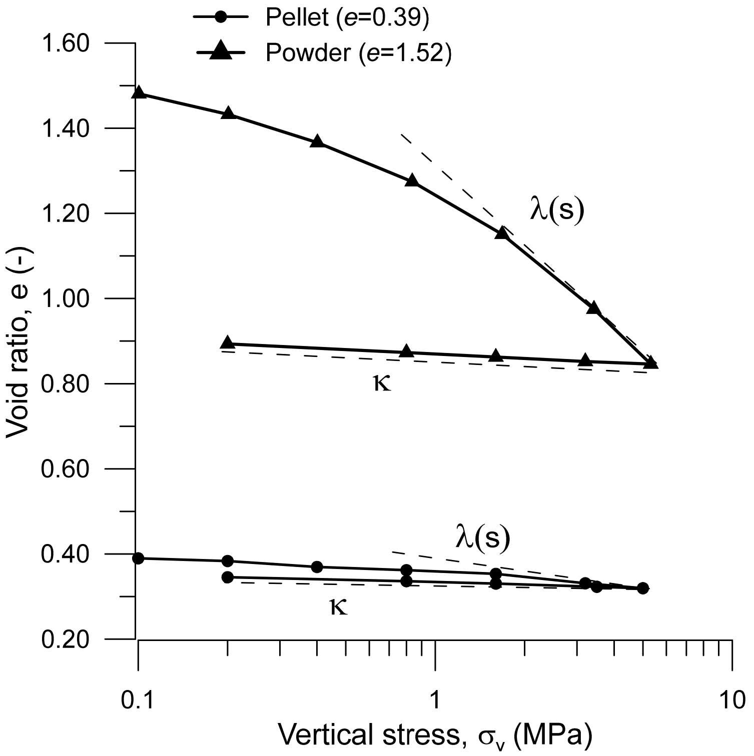

Figure 3-8. Compression behaviour on loading/unloading of pellet at constant water content for powder (e=1.52, w=9.51% and s= 82 MPa) and pellet (e=0.39, w=9.56% and s= 88 MPa)

A saturated oedometer test was carried out on the powder at a dry density $\rho_{d\,pow}$ =1.10 Mg/m^3 (e = 1.52), with initial conditions of water content w = 9.51% and total suction of 86 MPa, and with a sample size of 50 mm in diameter and 14 mm high. The vertical stress steps applied were from 50 kPa to 2 MPa. At 200 kPa of total vertical stress, the water pressure was applied at the bottom boundary with PVC using distilled water to create a gradient and saturate the sample for 11 days.

Figure 3-9 presents the compression curve on loading/unloading of the saturated powder (C to D). The compressibility parameter on virgin loading (post-yield) is $\lambda(0)$ = 0.291. The saturated powder shows pre-consolidation stress around 0.5 – 0.6 MPa. From C to D, the water pressures at the boundaries were kept constant.

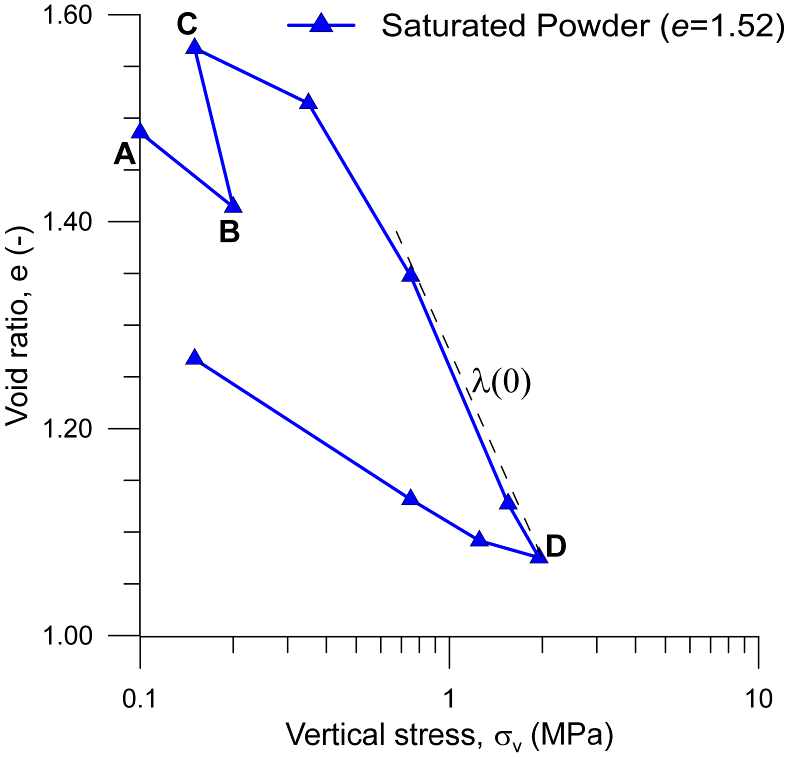

Figure 3-9. Compression behaviour on loading/unloading of saturated powder with an initial state of e = 1.52, s=86 MPa and w = 9.51%.

3.4.2. Packing of pellets compressibility

Different compressibility tests were performed on five packings of pellets prepared at different initial dry densities (1.11, 1.17, 1.19 and 1.20 Mg/m^3) (e = 1.49, 1.37, 1.33 and 1.31). The size of the sample is 50 mm in diameter with a height of 21 mm. The cell avoids water loss while keeping air pressure under atmospheric conditions. The tests have been carried out at a constant water content of around 7.57% and with an initial total suction around 114 MPa measured with a dew-point mirror psychrometer. Two packings of pellets were rotated at an angle of 90° (called organised), and three were performed under non-rotated conditions (called disorganised) (**Error! Reference source not found.**). The objective here is to investigate the effect of pellets' orientation on the compressibility behaviour of the material. Figure 3-11 shows the compressibility curves on loading/unloading for different packing of pellets at several initial dry densities. A stiffer behaviour is observed for packing with non-rotated pellets, while higher compressibility was observed for the rotated packing, probably due to the existence of fissures orthogonal to the loading direction. As expected, the packing of pellet with a dry density of 1.11 Mg/m^3 displayed the highest post-yield compressibility $\lambda(s) = 0.37$. The packing of pellet with a dry density of 1.19 Mg/m^3 with non-rotated pellets present the lowest post-yield compressibility $\lambda(s) = 0.14$. Two Packing of pellets tests rotated by an angle of 90° (called organised) displayed the same post-yield compressibility $\lambda(s) = 0.26$ indicating higher compressibility in comparison with the disorganised packing of pellets ($\lambda(s) = 0.14$).

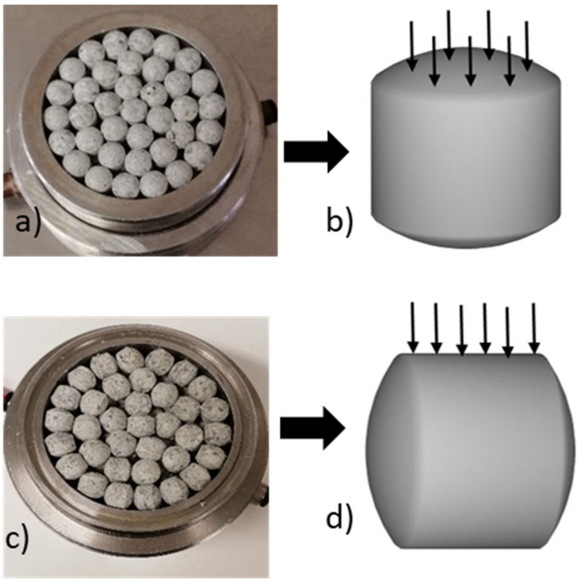

Figure 3-10. a) Sample of packing of pellets rotated at an angle of 90°(organised), b) pellet rotated at an angle of 90°, c) sample of packing of pellets under non-rotated conditions (disorganised), d) non-rotated pellet.

A saturated oedometer test was carried out on the packing of pellets at an initial dry density $\rho_{d\ pack}$ = 1.19 Mg/m^3 (e = 1.33) with initial conditions of w = 7.56% at a total suction of 112 MPa with a sample size of 50 mm in diameter and 22 mm high. The water pressure was applied at the bottom boundary with PVC using distilled water to create a gradient. The vertical stresses steps applied were from 100 kPa to 4 MPa. At 1 MPa of total vertical stress, the water pressure of 500 kPa was applied at the bottom boundary (point ‘a’). After that, at point ‘b’ the vertical stress was increased until 1.6 MPa. Finally, an increment of 1.4 MPa was applied to reach a total vertical of 4 MPa. Figure 3-12 presents the compression curves on loading/unloading of the saturated packing of pellets. The compressibility parameters on virgin (post-yield) loading was *λ(0)* = 0.24. The saturated packing of pellet pre-consolidation stress was around 0.9 MPa-1.3 MPa.

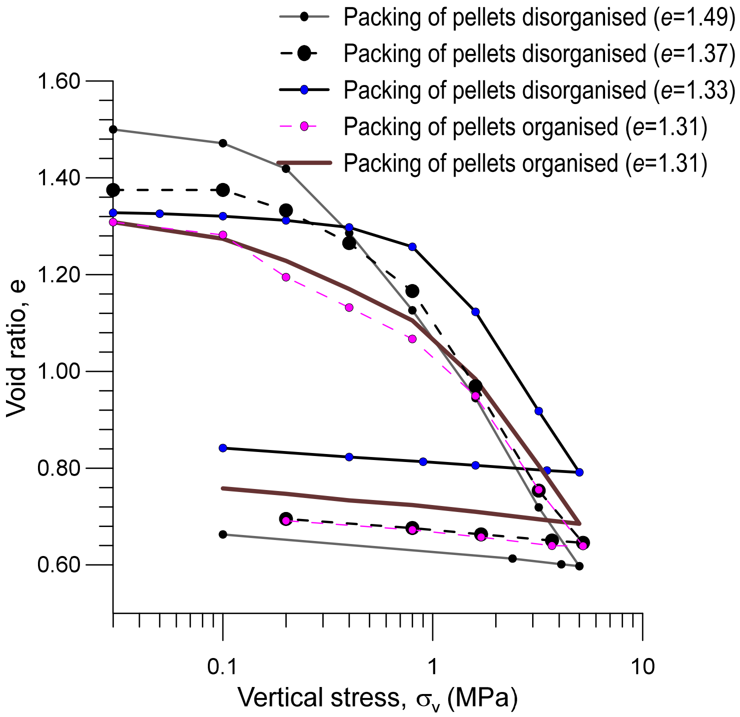

Figure 3-11. Compression behaviour on loading/unloading of packing of pellets with different orientation of pellets.

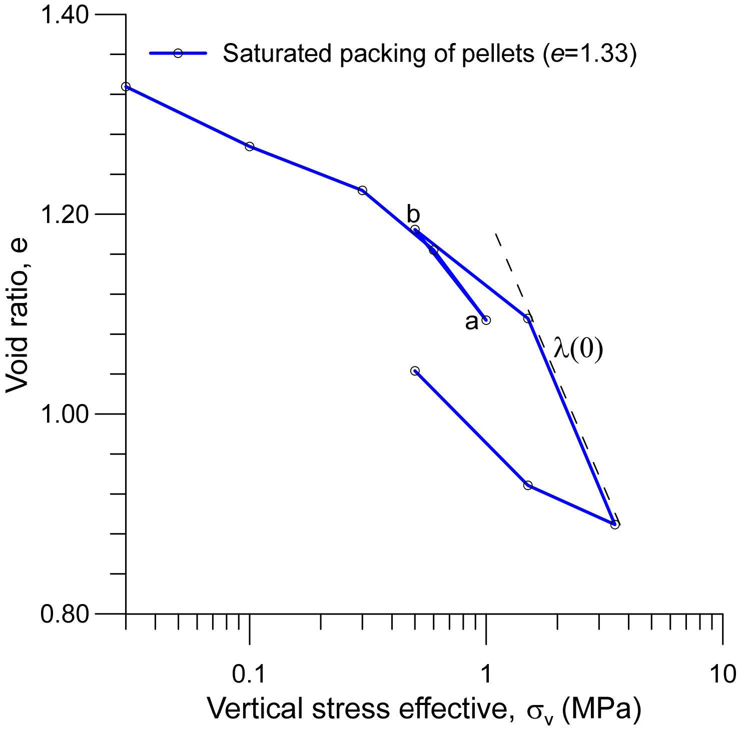

Figure 3-12. Compression behaviour on loading/unloading of saturated packing of pellets with an initial state of e = 1.33, s = 112 MPa and w = 7.56%.

3.4.3. Mixture compressibility

Two oedometer tests were carried out with an initial dry density of 1.49 Mg/m^3 (e = 0.86). The initial water contents were w = 8.51% (s = 115 MPa) with organised and disorganised packing of pellets. Moreover,

A saturated oedometer test of the mixture (blue line) was carried out on the organised packing of pellets with a void ratio of 0.86 and starting at an initial water content of w = 8.76% and total suction of 118 MPa. The vertical stresses steps applied were from 100 kPa to 5 MPa. At 1.6 MPa (point a) of total vertical stress, the water pressure of 1 MPa was applied at the bottom cap with PVC and using distilled water and then, when the deformation achieved less than 0.01%/day has increased the vertical stress at 3.6 MPa. Finally, was applied 1.4 MPa to increase the total vertical stress to 5 MPa. Figure 3-13 displays the compressibility of the mixture at two different installations of the pellets (organised and disorganised).

As observed, the packing of pellets consistently displayed larger compressibility on loading with lower pre-consolidation stress (around 0.4 – 0.5 MPa) and higher post-yield compressibility compared to the compressibility of the mixture. When the powder is filling the inter-pellet space, the pre-consolidation stress increases at around 0.8 MPa. As expected, the mixture composed of an organised packing of pellet displays the highest compressibility.

The compression curve on loading/unloading of the saturated mixture presented a compressibility parameter on virgin loading (post-yield) of $\lambda(0)$ = 0.146. The saturated mixture showed pre-consolidation stress around 1-1.5 MPa.

Table 3-4 summarises compressibility parameters for the mixture obtained in this study together with the results by Romero & Gonzalez-Blanco (2017) of compacted granular bentonite at an initial void ratio of 0.806, as well as the saturated pre and post-yield compressibility values of MX80 bentonite reported by Navarro *et al.,* (2016). The table highlights the important compressibility on loading that undergoes the dry pellet/powder mixture compared to a compacted powder of bentonite.

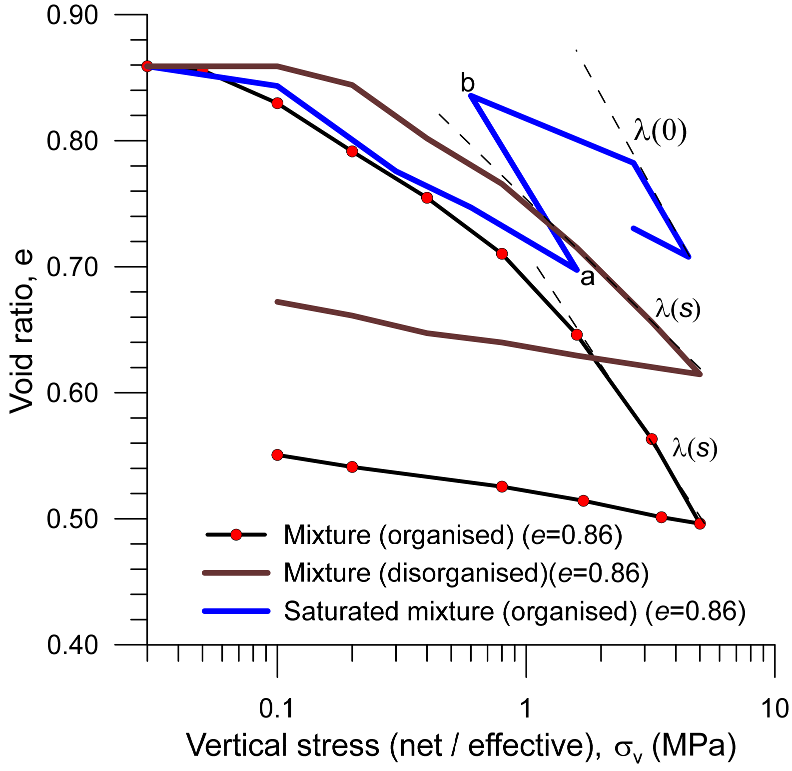

Figure 3-13. Compression behaviour on loading/unloading of the mixture at initial and saturated states. Point a started the hydration of water at 1 Mpa and point b applied vertical stress of 3.6 MPa.

Table 3-4. Compressibility parameters on loading/unloading.

Test	**Water content (%)**	**Total suction (MPa)**	**Compressibility (pre and post-yield)** **κ (-), λ (-)**
Present study *e* = 0.86 (organised mixture)	8.51	115	κ = 0.013 λ = 0.132
Present study *e* = 0.86 (Disorganised mixture)	8.51	115	κ = 0.014 λ = 0.09
Present study *e* = 0.86 (organised mixture at saturated state)	30.9(saturated)	0.78	κ = 0.044 λ = 0.146
Romero & Gonzalez-Blanco (2017)(bentonite at initial *e* = 0.806)	20.0	21.1	κ = 0.02 λ = 0.11
Navarro *et al.* (2016) saturated bentonite (*e* = 0.63)	Saturated	0 (matric suction)	κ = 0.05 λ = 0.15

3.5. Modelling of oedometer tests on pellet-powder bentonite

A loading/unloading oedometer test at constant water content has been performed on the mixture with organised packing of pellets (experimental test is explained in **section 3.4, Figure 3-13**, organised mixture), which has been modelled using the finite element Code_Bright (Olivella *et al.*, 1996). The constitutive model used to represent the mechanical response is the Barcelona Expansive Model (BExM) (Alonso *et al.*, 1999), since a multi-modal pore size distribution characterises the pore network of the mixture. The Barcelona Expansive Model (BExM) (Alonso *et al.*, 1999; Sanchez *et al.*, 2005) is a mechanical constitutive model particularly suitable for geomaterials with bimodal pore-size distribution (i.e., macro and micro-porosity). The main equations and assumptions of this model are explained in **chapter 6, section 6.2.2.**

During the oedometer test at constant water content, an increase in the degree of saturation and a consequent reduction of suction is induced. Consequently, two competing effects occur at different pore-size scales: (i) compression due to mean net stress increase; and (ii) expansion on induced suction reduction that mainly affects the micro-porosity level inside aggregates. A sensitivity analysis has been performed to explore these effects, in which the elastic compressibility parameter at the micro-porosity scale for changes in mean effective stress plays an important role (Mesa-Alcantara *et al.*,2020b).

Figure 3-14a shows the model geometry with a plane of symmetry. Figure 3-14b displays the boundary conditions, in which horizontal displacements are restricted. The model is applied under plane strain conditions with normal (out-of-plane direction) displacements not allowed. Four 2D simulations are performed considering different values of compressibility parameter at the micro level for changes in mean effective stress $\kappa^{micro} = 0.04, 0.06, 0.08 \text{ and } 0.10$ and elastic compressibility parameter at the macro level for changes in mean net stress $\kappa^{Macro} = 0.035$.

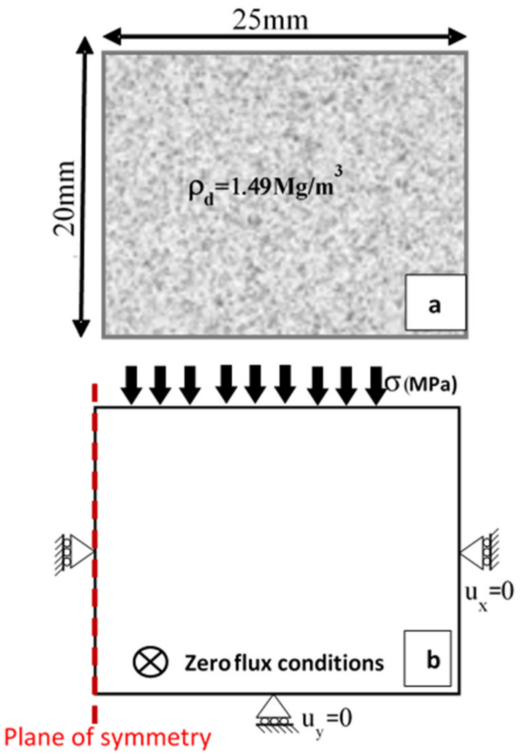

Figure 3-14. (a) Model geometry under plane strain conditions. (b) Mechanical and hydraulic boundary conditions.

The parameters of the mechanical model and their values are summarised in Table 3-5. As observed, BExM involves several parameters associated with both elastic and plastic behaviour. Some parameters have been obtained from experimental results on the mixture, such as the saturated elastoplastic compressibility parameter $\lambda(0)$ (in terms of void ratio), and the saturated pre-consolidation (yield) stress p_0^*. Parameters not directly obtained from experimental results were taken from (Toprak *et al.*, 2018).

Table 3-5. Mechanical parameters of BExM taken from Toprak et al (2018) and experimental data.

Parameters	Values			
	1	**2**	**3**	**4**
κ^{Macro} BExM elastic compressibility parameter at macro level for changes in mean net stress	0.035	0.035	0.035	0.035
κ^{micro} BExM elastic compressibility parameter at micro level for changes in mean effective stress	0.04	0.06	0.08	0.10
κ_s^{Macro} BExM elastic macro compressibility parameter for changes in (total) suction	0.01			
v^m BExM Poisson's ratio	0.3			
f_{S0} *BExM parameter for micro–macro coupling functions when SD is activated*	-0.1			
f_{S1} *BExM parameter for micro–macro coupling functions when SD is activated*	1.1			
n_S *BExM parameter for micro–macro coupling functions when SD is activated*	2			
f_{C0} *BExM parameter for micro–macro coupling functions when SI is activated*	-0.1			
f_{C1} *BExM parameter for micro–macro coupling functions when SI is activated*	1.1			
n_C *BExM parameter for micro–macro coupling functions when SI is activated*	0.5			
M BBM and BExM slope of the critical state line	1			
r BBM and BExM parameter for the slope void ratio – mean net stress at variable suction	0.8			
β BBM and BExM parameter for the slope void ratio – mean net stress at variable suction [MPa-1]	0.0001			
p_c BBM and BExM reference pressure for the p_0 function [MPa]	0.1			
P_{to} BExM cohesion for suction equal to zero [MPa]	0.01			
$\lambda(0)$ BBM and BExM slope of void ratio mean net stress curve at null suction	0.146			
p_0^* BBM and BExM pre-consolidation mean stress for saturated soil [MPa]	1			

Regarding the hydraulic behaviour, the van Genuchten equation (van Genuchten., 1980) has been used to describe the water retention curve of the mixture (Table 3-6). The hydraulic behaviour in BExM is complemented with an equation for the intrinsic permeability evolution, which is an exponential function of the macro-porosity proposed by Sánchez (2004). The intrinsic permeability equation is defined in **chapter 6 section 6.2.1 equation 6-1.** The dependency of liquid relative permeability on the degree of saturation is explained in **chapter 6 section 6.2.1 equation 6-2.**

Table 3-6. Summary of hydraulic properties from the mixture taken from experimental results.

Parameters	**Values**
van Genuchten water retention parameters	
P_0(MPa)	10
λ	0.35
S_{rl}	0
S_{ls}	1
Intrinsic permeability	
K (m^2)	1.17x10^{-20}
ϕ_0^{Macro}	0.29
b	1
Relative permeability	
n	3
S_{rl}	0
S_{ls}	1

Figure 3-15 shows the measured vertical (net) stress-void ratio relationship together with the modelling results for different values of κ^{micro}(Table 3-4). As observed, small changes in this parameter affect the simulated deformation response of the mixture. The model prediction for $\kappa^{micro} = 0.08$ appears to follow the experimental results satisfactorily.

Figure 3-16 displays the time evolution of the simulated degrees of saturation for the different loading/unloading steps and the different κ^{micro}values. Loading to vertical stress of 5 MPa induces an increase in the degree of saturation to 0.53 – 0.59 while unloading to 0.1 MPa generates a decrease up to 0.48 - 0.52. As observed, even for the vertical stress increase the degree of saturation decreases as a consequence of the reduction in the void ratio.

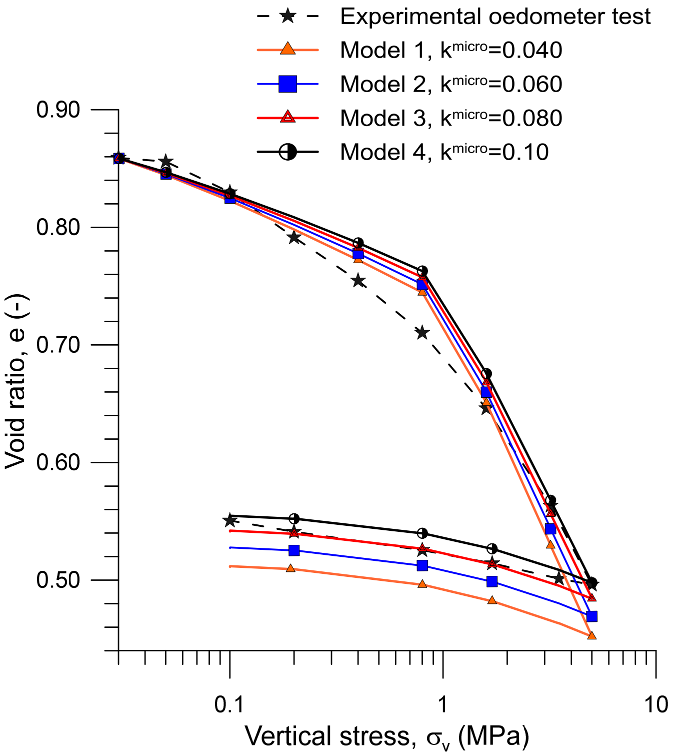

Figure 3-15. Evolution of void ratio against axial stress. Experimental and modelling results.

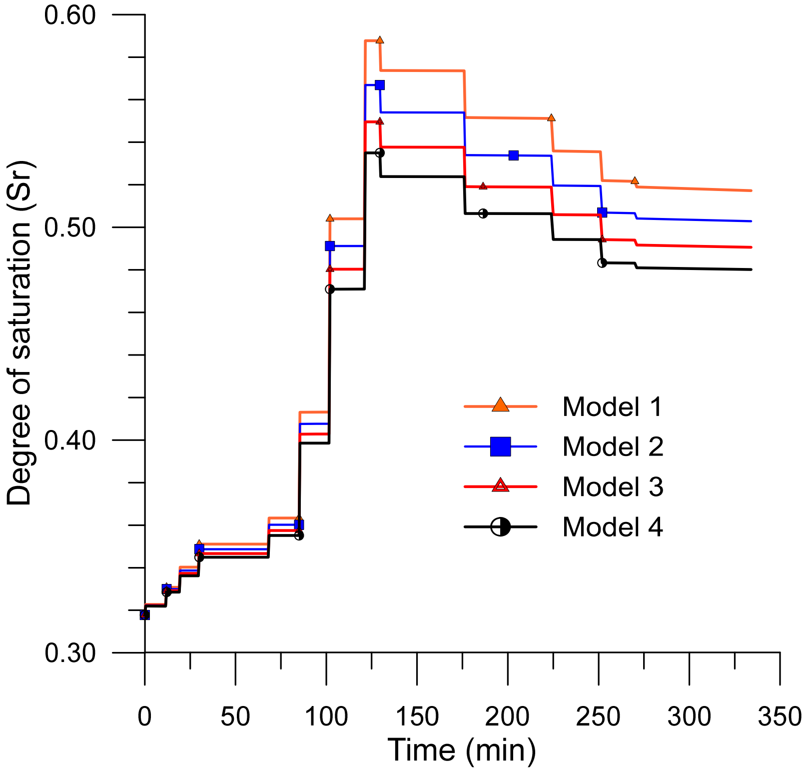

Figure 3-16. Evolution of the degree of saturation as a function of time.

Figure 3-17 plots the time evolution of the computed changes in (total) suction associated with the changes in the degrees of saturation. On loading to vertical stress of 5 MPa, the suction reduces to around 22 – 28 MPa (s = 85 MPa is the value at the initial state). On unloading to vertical stress 0.1 MPa, the suction reaches values around 30 - 46 MPa.

Figure 3-18 plots the modelled time evolutions of both total and micro-porosities. The total porosity decreases inducing the increase of the degree of saturation and the decrease of suction. For $\kappa^{micro} = 0.08$, the total porosity decreases to 0.33 at 5 MPa starting from ϕ = 0.46 at the initial state. Interestingly, this decrease in total porosity on loading is accompanied by an increase in micro-porosity. In fact, two competing effects are occurring at the microstructural level. The increase in vertical stress tends to induce compression in the macro-pore volume, while (total) suction decrease leads to aggregate swelling and the corresponding increase in micro-porosity. It seems that κ^{micro}plays a fundamental role since lower values reduce aggregate swelling and allow more compression of the macro-pores and the associated decrease in total porosity.

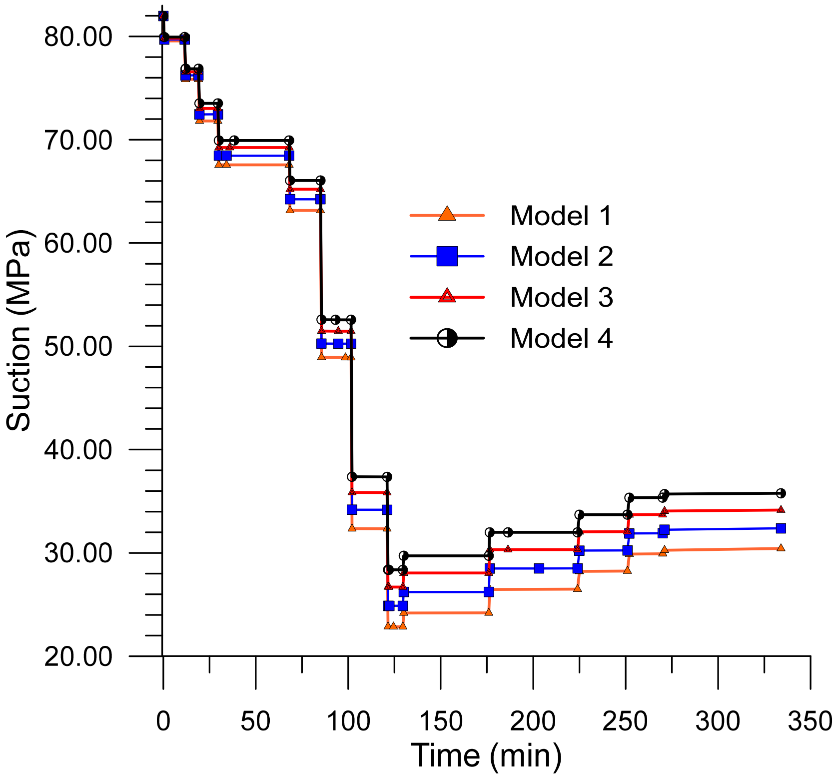

Figure 3-17. Evolution of (total) suction as a function of time.

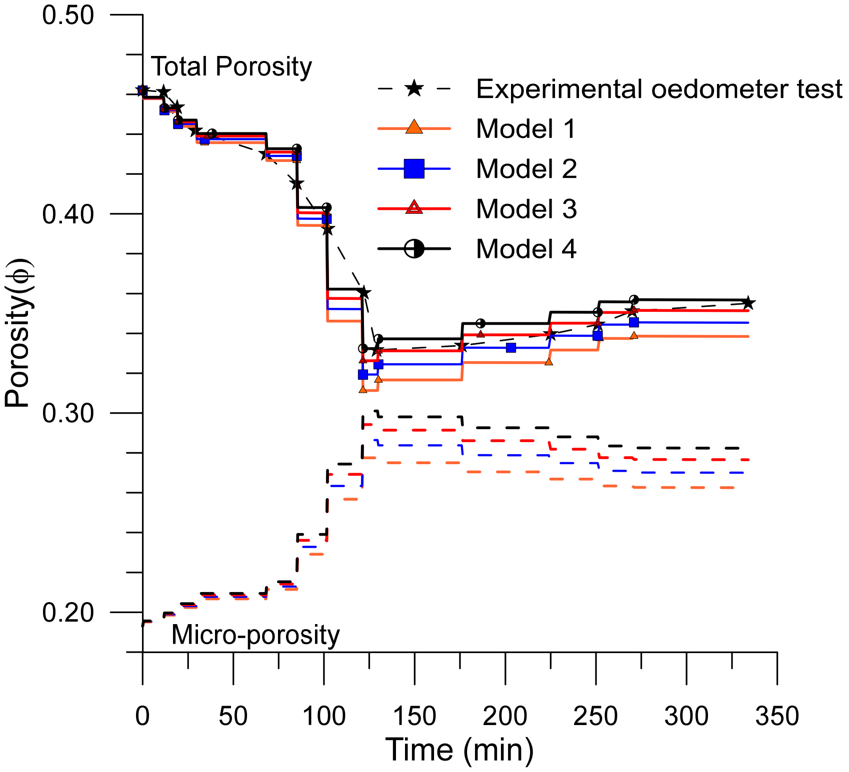

Figure 3-18. Evolution of total and micro-porosities as a function of time. Experimental and modelling results.

3.6. Swelling pressure tests

Swelling tests were carried out to know the behaviour of the swelling pressure in the mixture and the powder during soaking at constant volume. All the tests were performed under low initial stress (30-70 kPa) on the specimen before water flooding. Different water pressures were considered to verify the stability of the swelling pressure (defined in terms of effective stress). The small displacements induced by the compressibility of the constant volume system was measured with an LVDT. The final swelling stress was measured by restoring the initial volume of the sample.

Figure 3-19 presents the swelling test equipment with several sensors used and each part of the equipment. The experiment consists of several parts i) the mechanical part that hosts the soil sample; ii) the hydraulic part that enables water iii) the measurements part with all the sensors (load cell, LVDT, pressure-volume controllers) and the acquisition system (data logger and computer).

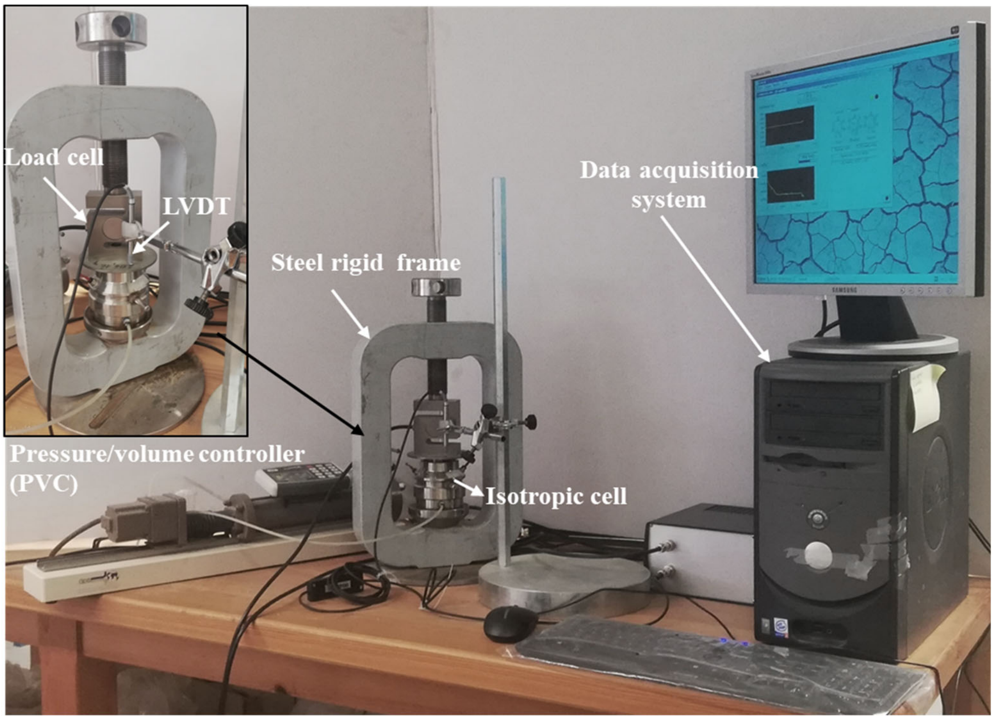

Figure 3-19. Setup for swelling pressure test. Isochoric cell from Hoffmann (2005)*.*

3.6.1. Mechanical and hydraulic elements of the cell

The cell includes several elements, such as the bottom part containing a porous stone and a drainage system; the middle cell (50 mm inner diameter and a height of 20mm) used to prevent radial swelling with two air outlets and the top part incorporating a piston in contact with the sample and load cell to monitor the swelling pressure. The assembled cell is inserted into a rigid steel frame. The rigid steel frame had been used in the different study such as to study the extreme expansive behaviour of the anhydritic-gypsiferous claystone damaging Lilla tunnel (Ramon *et al.*, 2017), Pont de Candí viaduct (Alonso & Ramon, 2013; Alonso *et al.*, 2015) and a building located in Barcelona (Ramon & Alonso, 2018).

The LVDT is located above the piston to monitor the small top displacement of the sample. The cell allows axial hydration, from the bottom and top caps. Mechanical valves are mounted at these caps allowing the inlet and outlet of water. The other two entrances were closed to avoid the outflow of water and ensuring no air entrapment. Figure 3-20 shows in detail the isochoric cell used for the swelling test (Hoffmann 2005).

Figure 3-20. Parts of the isochoric cell. Isochoric cell. From Hoffmann (2005).

3.6.2. Measurement systems

Load cell

The equipment has several sensors to monitor the HM response of the mixture. A load cell of 10kN (Utilcell, model 620) to measure the load developed by the soil in the axial direction. Before use, the load cell was calibrated to verify the performance. To calibrate the load cell, the oedometer in Figure 3-6 was used to apply several loads until reaching 10 kN. The output voltage of the sensors was recorded by the data logger. The calibration presents a linear relationship between the applied load and output voltage. The calibration curves together with the calibration equations are described in Figure 3-21a.

Linear variable differential transformer (LVDT)

Linear variable differential transformer (LVDT) from Solartron Metrology with a range of measurement of ±2.5 mm and a resolution of 0.001 mm was calibrated to measure the vertical displacement. The calibration curves together with the calibration equations are described in Figure 3-21b.

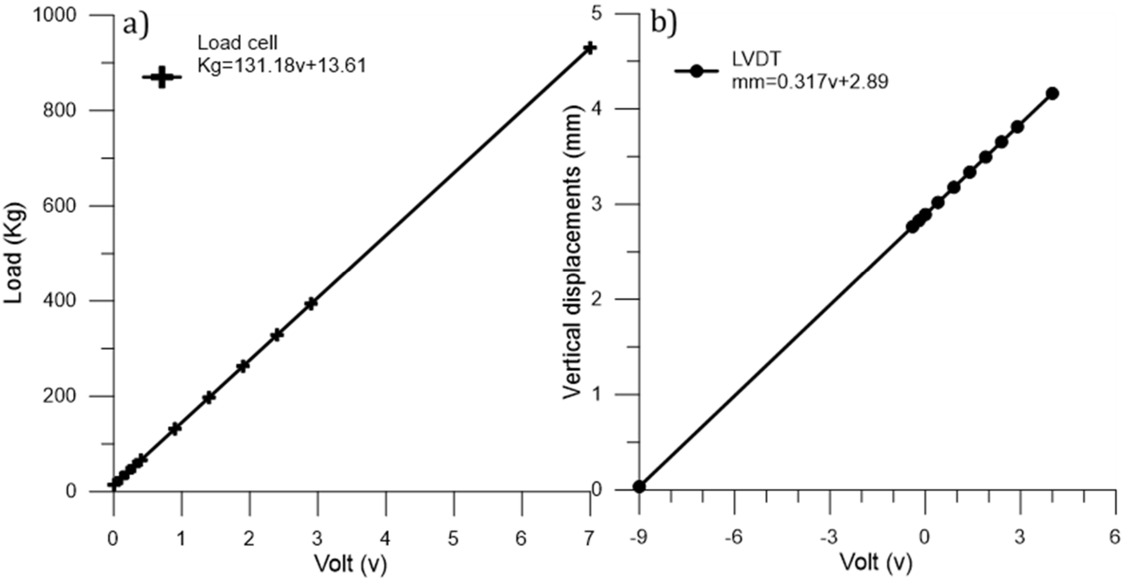

Figure 3-21. Calibration of the Load cell (a) and LVDT. (b)

Pressure-volume controllers (PVC)

Standard pressure-volume controllers (PVC) from GDS Instruments are connected to the bottom cap to apply the water pressure. The PVC has a volume capacity of 200mL and volume accuracy of 0.25% (volume resolution 1mm3). The maximum pressure range is 3 MPa (pressure resolution 1 kPa).

Data acquisition for updated equipment

The data acquisition software was developed in Visual Basic (Microsoft) under the name of Geolab-UPC to monitor the load development and the vertical displacements. A rigid steel frame was used to confine the cell and place the load cell.

3.6.3. Methodology of powder test

The swelling test for the powder was carried out for 60 days with an initial dry density of 1.10 Mg/m^3 (e = 1.52) with an initial total suction of 85 MPa and w = 9.45% with initial stress of 70 kPa before water flooding. During the test, several long-term back-pressures were applied (50 kPa, 100 kPa and 200 kPa) from the bottom cap of the cell. These different water pressures were applied to verify the effective stress (swelling pressure) at different hydraulic pressures. Nevertheless, these different water pressures affected the compressibility of the constant volume system (mainly the load cell) that also influenced the swelling pressure. This is the reason why the backpressure was set at 50 kPa at the final stage before restoring the initial volume. The initial volume was progressively restored (in several steps) with the upper screw system along a drained path that lasted 4 days.

3.6.4. Results of powder test

In the beginning, the water pressure was 50kPa. At 6 days the water pressure was increased to 100 kPa and maintained for 12 days (total 18 days), after that the water pressure was reduced to 200 kPa. At 35 days the water pressure was reduced to 50 kPa. At 56 days of hydration, there were no changes in the vertical displacement, and the initial volume was restored to the initial conditions to measure the swelling pressure. As observed, during water pressure increase to 200 kPa, the system underwent axial displacement that induced a slight expansion of the sample that reduced the vertical effective stress (swelling pressure). The vertical effective stress was partially restored by decreasing the water pressure to 50 kPa.

Figure 3-22b shows the results of the powder swelling pressure test as a function of time, as observed the powder reached a swelling pressure of 0.65 MPa at e = 1.52. The fast increase in the swelling pressure at the final stage corresponds with the restoration of the initial volume. The axial strain (negative strain is expansion) reached at the end of the swelling pressure test of the powder was -0.073% after different applied changes in the water pressure (Figure 3-22a). The volume was corrected to the initial value along a drained path at a constant water pressure of 50 kPa during 4 days.

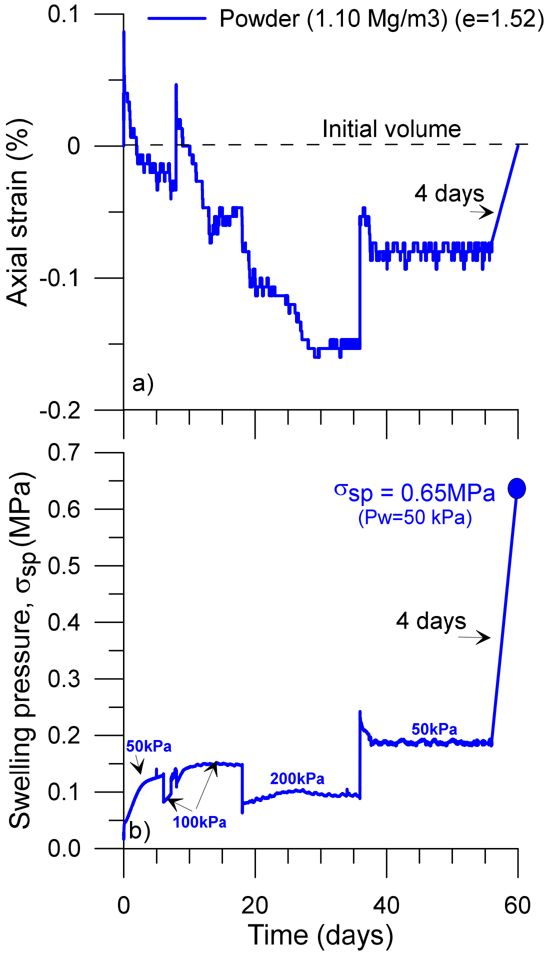

Figure 3-22.a) Evolution powder swelling pressure as a function of time (initial state $\rho_{d\ pow}$ = 1.10 Mg/m^3 (e = 1.52), s = 85 MPa, w = 9.45%.) with the different water pressure applied. b) Axial strain as a function of time (negative strain is expansion).

3.6.5. Methodology of the mixture tests

Three swelling tests for the mixture were performed using layer by layer of pellets following protocol 2 (most homogeneous protocol, explain in **section 2.5**).

The first test was carried out with a dry density of 1.40 Mg/m^3 (*e* = 0.98), initial suction of 112 MPa and water content of 8.55%. Initial stress of 70 kPa was applied before water flooding. In this test (Figure 3-23a), several long-term back-pressures between 50 kPa and 500 kPa was applied from the bottom cap.

The second and third swelling tests were carried out with a dry density of 1.49 Mg/m^3 (*e* = 0.86), (Figure 3-23). The initial water contents were *w* = 8.68% (total suction *s*= 107 MPa) and w = 8.51% (*s* = 110 MPa) for test 2 and test 3, respectively. The water pressure applied in these swelling tests was constant at 500 kPa for test 2 and 200 kPa for test 3.

3.6.6. Results of the mixture tests

The swelling test of the mixture at a dry density of 1.40 Mg/m^3 started at a water pressure of 50 kPa for almost 4 days, then it was increased to 200 kPa and maintained constant for 22 days. At 26 days the water pressure was increased to 500 kPa and maintained constant for 62 days. As observed, the increase in water pressure induced some small vertical displacement of the top cap that induced some swelling of the sample and the consequent reduction in swelling pressure (effective stress). After that, it was reduced to 200 kPa and 50 kPa respectively to decrease the water pressure and afterwards restoring the initial volume. At 102 days, the vertical displacement and axial load did not present any change and the volume of the sample was restored at the initial volume by applying axial stress at a constant backpressure of 50 kPa for 4 days. As observed the mixture with a dry density of 1.40 Mg/m^3 (e = 0.98) reached a swelling pressure of 3.40 MPa. The evolution of the small axial straining at different backpressures and the consequent changes in effective stress (swelling pressure) is depicted in Figure 3-23a.

The second test at a dry density of 1.49 Mg/m^3 reached a value of 4.2 MPa of swelling pressure at a constant backpressure of 500 kPa, and this value was obtained at 77 days when negligible changes were observed in the vertical displacement and load. Afterwards, the initial volume was restored applying vertical stress at constant backpressure of 500 kPa following a drained path for 7 days. The third swelling test at a dry density of 1.49 Mg/m^3 at a backpressure of 200 kPa was performed for 236 days reaching a value of swelling pressure of 4.35 MPa. Like other tests, the initial volume was restored (at constant backpressure of 200 kPa for 7 days) when a negligible change was observed in the load and displacement. Test 2 and test 3 present an axial strain of -0.66% and -1%, as shown the Figure 3-23b due to the different axial displacements underwent by the system at the different water pressures applied (smaller displacement at lower backpressure that induced slightly higher swelling pressure).

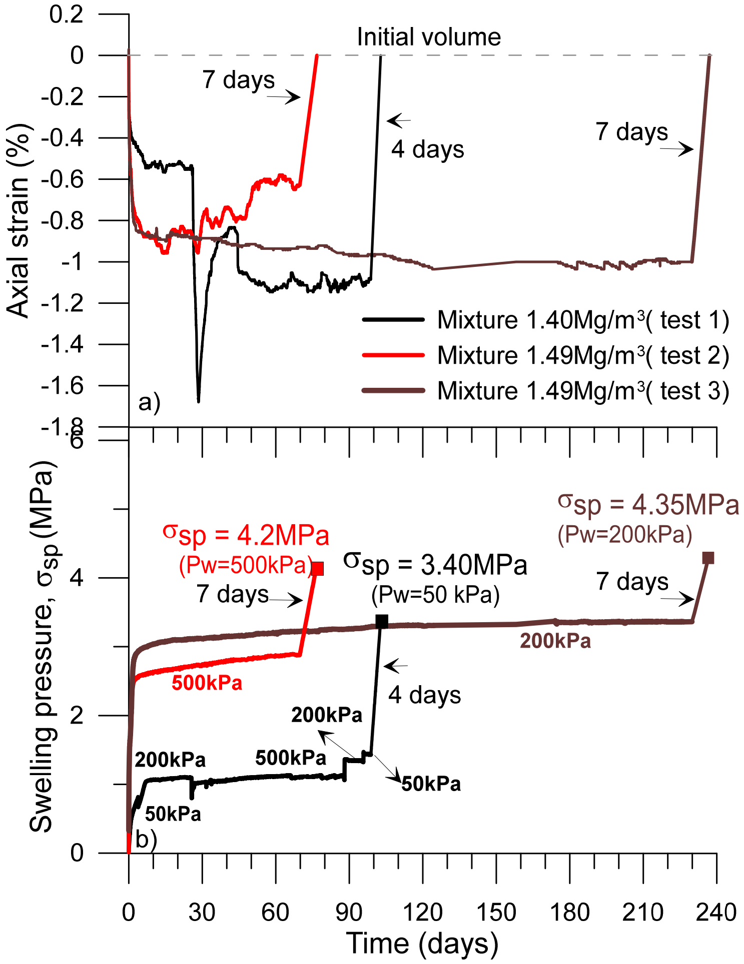

Figure 3-23. Evolution of the mixture pressure tests at different dry density and different water pressure.

These values are comparable with the results report by several authors (Lajudie *et al.*, 1994; Tripathy *et al.*, 2004; Villar, 2005; Karnland *et al.*, 2008; Gens *et al.*, 2011; Molinero-Guerra, 2018). This comparison has been presented in Figure 3-24. According to the results obtained in the different tests, the swelling pressure for the mixture (4.35 MPa) and powder (0.65 MPa) presented consistent values. An estimated (vertical) swelling pressure under saturation around 2.90 MPa can be calculated using equation 3-3 that corresponds to the mixture (e = 0.86). This equation is only taken into account results presented by Molinero-Guerra (2018) and from this study. Table 3-5 summarises the swelling pressure values for the different components of the mixture (powder and packing of pellets) and the mixture.

$$\sigma_{sp} = 35.41\, exp(-2.57e) \tag{3-3}$$

Table 3-7 Results of the swelling pressure.

Material	***Dry density (Mg/m^3)***	***Swelling pressure (MPa)***
Mixture (80%pellets/20%powder)	1.49	2.90
Packing of pellets	1.2	1.25
Powder	1.1	0.71

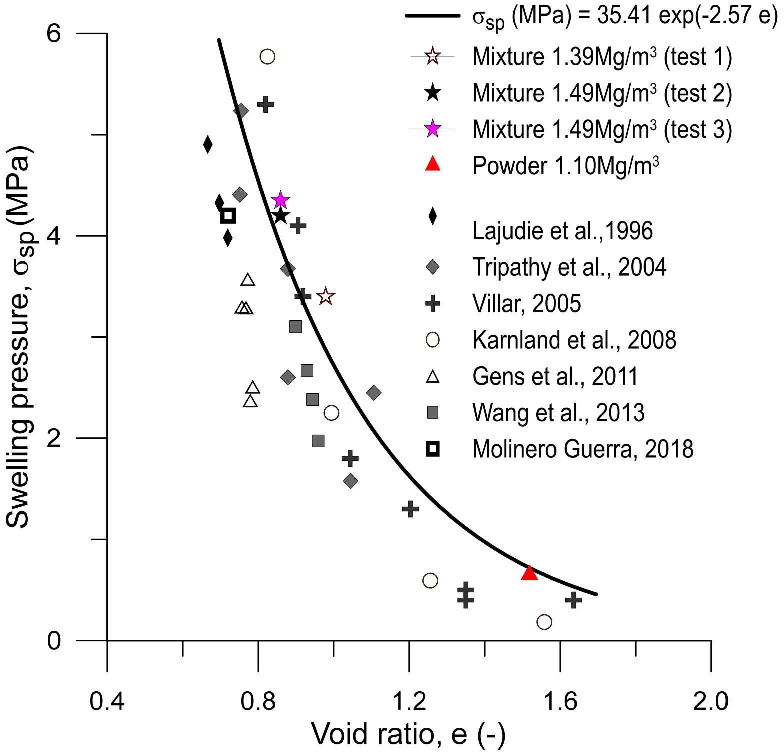

Figure 3-24. Estimated swelling pressure of the mixture. Data from different authors.

Figure 3-25 presents the swelling pressure at the end of the tests plotted versus the final total suction after the test measured in Decagon WP4 dew point chilled-mirror psychrometer. This suction is induced on total stress decrease. It is not the suction of the saturated sample in the cell. The suction within the cell has to be zero (close to zero).

The change in total stress on sample retrieval is equal to the change in pore pressure by assuming null volume change of the saturated sample and, therefore, null change in effective stress. The initial vertical stress before retrieval is equal to the swelling pressure (vertical effective stress) plus the water backpressure applied. So, the change in water pressure is also the addition of vertical effective stress (swelling pressure) and the water backpressure applied at the end of the test. Therefore, the final water pressure (negative) or measured suction should be equal to the swelling pressure registered before dismantling (Figure 3-26). Any change concerning this value may be associated with some drying of the sample or some air entry on unloading

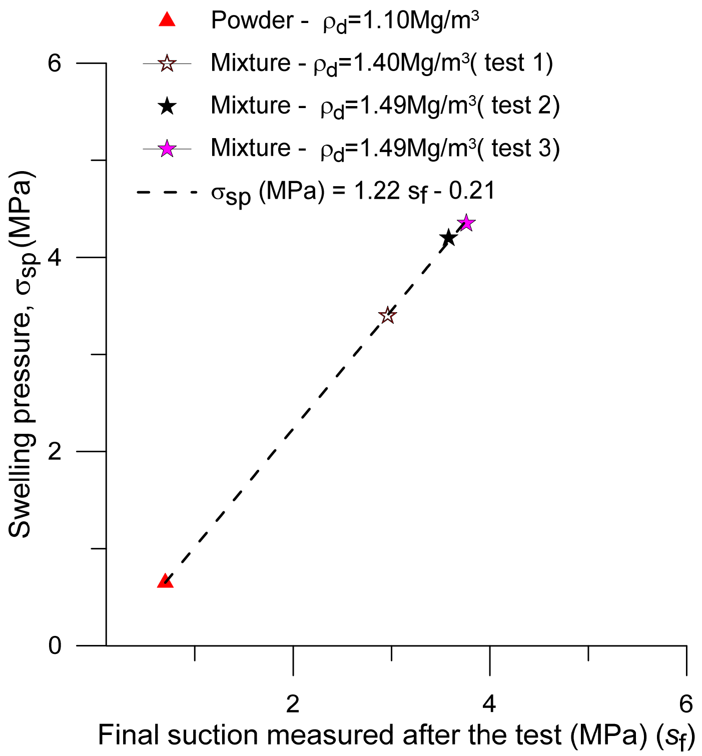

Figure 3-25. Evolution of swelling pressure as a function of the total suction after the tests.

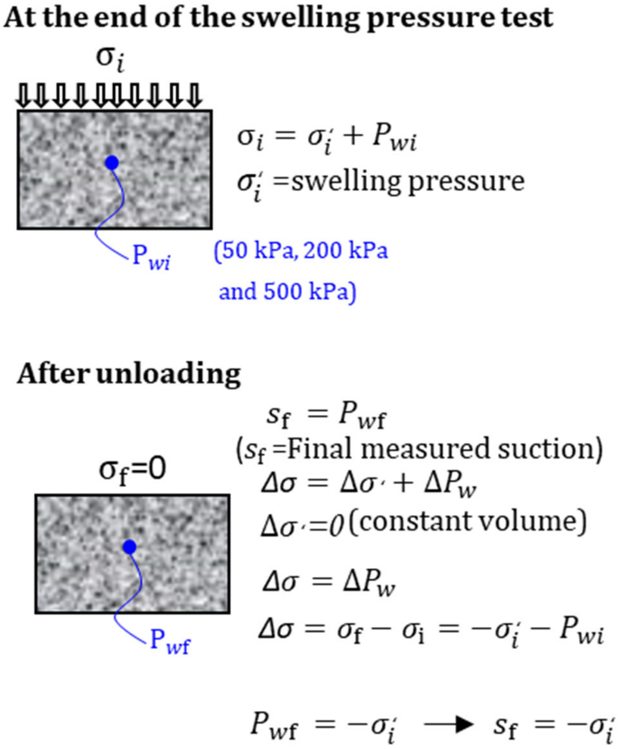

Figure 3-26. Scheme at the end of the swelling pressure test (initial state) and after unloading (final state)

3.7. Concluding remarks

This chapter presented different hydro-mechanical experiments that were carried out (intrinsic permeability, water retention, swelling under load, swelling pressure and compressibility properties of the mixture and components (powder and pellets), together with the modelling of the loading/unloading tests with a double-porosity framework.

The water permeability of the powder and mixture were measured in long-term hydration obtaining values of 5.64 x10^{-20} m^2 (e = 1.52) and 1.17 x10^{-20} m^2 (e = 0.86), respectively. In contrast, the intrinsic permeability of the pellet was estimated by MIP data interpreted with Hagen-Poiseuille equation (1.60 x10^{-21} m^2 at e = 0.39). As expected, the pellet presents the lowest intrinsic permeability and the powder the highest.

The water retention results in terms of water content present no important total suction changes at water contents w<10% for the mixtures and components. This fact indicates that at these water contents the water retention curve of MX80 is not sensitive to void ratio and pore size distribution changes. There are important differences in the water retention curve of pellets when they hydrate under free swelling because they reach a total porosity higher than the total porosity of powder.

Several swelling pressure tests were carried for the MX80 bentonite mixture at different dry densities (1.40-1.49 Mg/m^3) and the powder (1.10 Mg/m^3), applying different water pressure from the bottom cap. As expected, the powder displayed lower swelling pressure (0.65 MPa) than the mixture (4.35 MPa).

The compressibility on loading of the components and the mixture presents consistent results. As expected, the powder consistently displayed larger compressibility on loading compared to the pellet packing and the mixture. The saturated powder test displayed compressibility ($\lambda(0)$ = 0.29) higher than the organised saturated packing of pellets ($\lambda(0)$ = 0.24). A stiffer behaviour is observed for packing with non-rotated pellets while higher compressibility was observed for the rotated packing, probably due to the existence of fissures orthogonal to the loading direction. The same behaviour is presented in the oedometer mixture, obtaining a value of $\lambda(s) = 0.09$ for a mixture with non-rotated (disorganised), corresponding to a value lower than the mixture with organised packing of pellets ($\lambda(s) = 0.132$).

Modelling results of an oedometer test performed under constant water content conditions on a binary mixture of MX80 show that total porosity decreases inducing the increase of the degree of saturation and the decrease of suction. The sensitivity analysis demonstrates that changing values of κ^{micro} affects the mechanical behaviour of the binary mixture significantly. For lower values of κ^{micro} the material shows larger compressibility resulting in a higher decrease in total porosity. These results show how crucial it is to choose a reliable value when modelling experimental mock-up tests. The model prediction for $\kappa^{Macro} = 0.035$ and $\kappa^{micro} = 0.08$ (model 3) appears to follow the experimental results satisfactorily. These parameters were used for the model of the mock-up test presented in **chapter 6.**

4. MOCK-UP OF VSEAL IN SITU TEST

4.1. Introduction

The first publications on gas migration experiments in bentonites were focused on breakthrough pressure (Pusch & Forsberg, 1985; Horseman et al., 1999) to know which gas pressure overpassed the minor principal stress. The most common cells for the gas experiments are the triaxial and isotropic cells because of their better control of isotropic or anisotropic stresses. However, studies under oedometer conditions (Gonzalez-Blanco et al., 2020) have been performed to understand better deformations during the gas injection. Furthermore, under constant volume conditions (Harrington & Horseman, 1999; Horseman et al., 2004; Harrington et al., 2012; Liu et al., 2014; Harrington et al., 2017) have also been carried out because of better control of injected fluids and the total stress generated in gas tests.

In this work, a mock-up test was designed and carried out in the laboratory at a scale of 1/10 of the large scale in situ experiments (VSEAL) performed by IRSN **(**explain in detail in **chapter 1, section 1.3**) to investigate the impact of gas migration on the performance of vertical bentonite-based sealings. The designed experiment, being also at a scale of 1/100 of Vertical Sealing Systems (VSS) of the future French reversible geological disposal facility project for radioactive waste (Cigeo), reproduces the same boundary conditions. The cell allows applying hydraulic and gas loadings, both asymmetric: rapid increase of water pressure on the top with independent control of lateral hydraulic boundary conditions and bottom gas pressure increase. Fluid injection (water or gas) are allowed independently from the top, bottom and lateral sides.

In this chapter, the mock-up test consisting of a mechanical part that ensures constant volume conditions, a hydraulic part that enables water and gas injections and a measurement part including twelve sensors (total stresses, water pressure and relative humidity sensors) is described in details. Radial swelling pressure, pore pressure and relative humidity at different positions, as well as axial swelling pressure monitored during hydration from both sides (axial and radial), are presented. Further testing results, especially during the gas injection, are presented in **chapter 5.**

4.2. New infiltration/Gas injection column (Mock-up test)

The layout of the small-scale infiltration/gas injection cell (mock-up test cell) is presented in Figure 4-1. The dimensions correspond to 1/100 of VSS at real repository conditions (100 mm in diameter and 350 mm in height). The mock-up test is carried out under constant volume conditions. Liquid pressure will be applied radially to simulate water coming from the clay formation, and axially to simulate water coming from the calcareous formation.

Several phases are envisaged for this test: (i) saturation phase at time t_0 (Figure 4-1a): low radial saturation and rapid axial saturation, (ii) gas injection (Figure 4-1b) at time $t_0+\Delta t$ (initial time plus the change of time) to investigate the impact of gas injection during saturation process of the bentonite seal, and (iii) gas injection once the sample is fully saturated (Figure 4-1c).

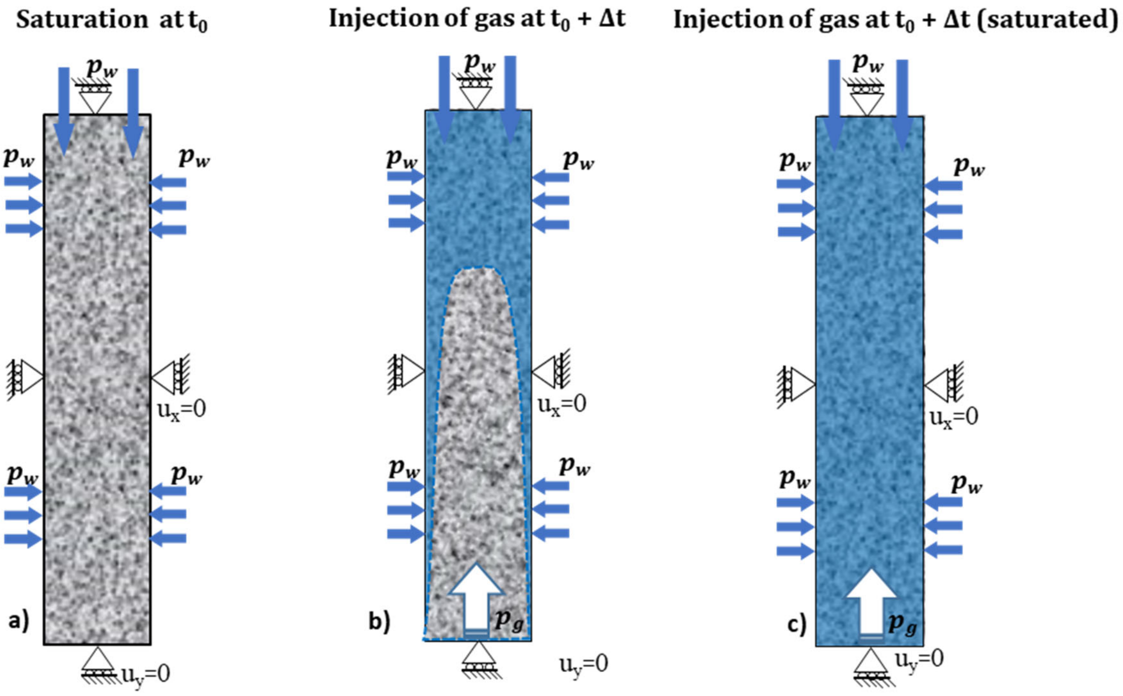

Figure 4-1. Mock-up testing phases.

The designed experiment consists of several parts (Figure 4-2): i) the mechanical part that hosts the soil sample; ii) the hydraulic part that enables water and gas injections iii) the measurements part with all the sensors (total pressure, force transducer, relative humidity sensor) and the acquisition system (data logger and computer).

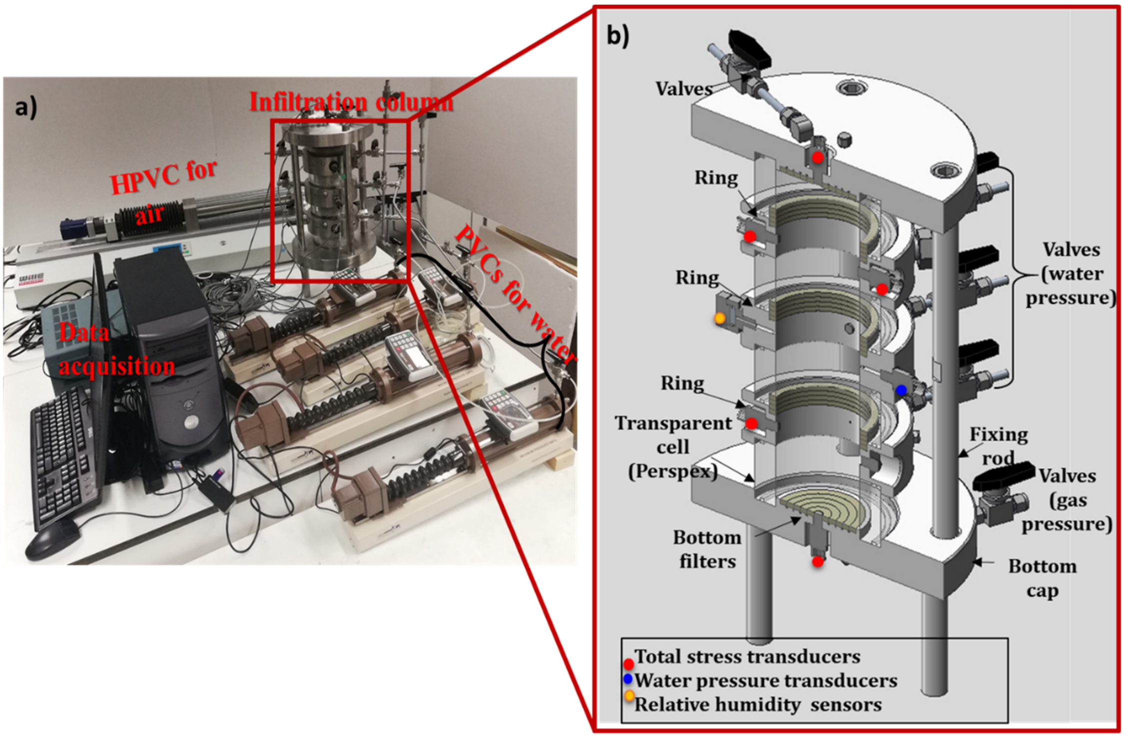

Figure 4-2. General set up of Vseal mock-up test. a) Infiltration column and auxiliary devices. b) Schematic of the column with the different elements and transducers

4.2.1. Mechanical Part

The mock-up cell is designed to ensure confined conditions mechanically. The testing cell (100 mm in diameter and 350 mm high) is composed of four transparent cylinders, made of Perspex to visualize processes occurring at the interface during the hydration and gas injection phases, assembled to three stainless steel cylinder that ensures radial water injection (Figure 4-3). The assembled cell is inserted into a rigid frame composed of two stainless steel disks on the two sides of the cylinder connected by four metallic rods. It is worth noting that using a 25mm thick cylinder allows resisting the mechanical stresses originating from the specimen swelling.

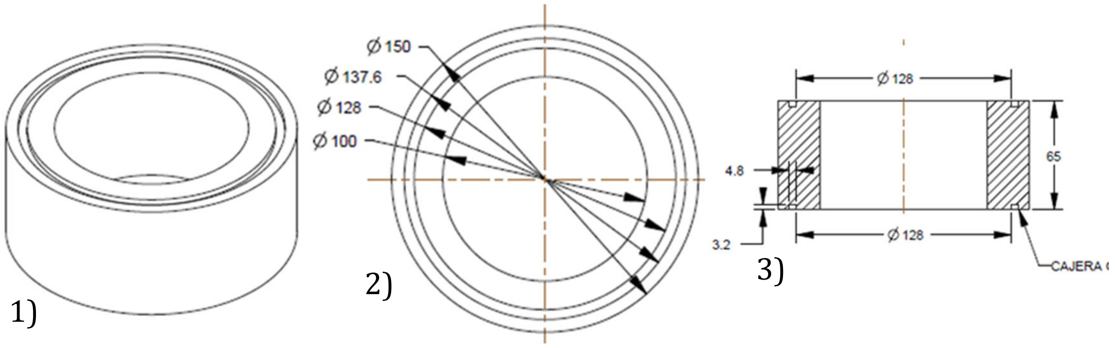

Figure 4-3. Scheme of transparent Perspex cylinders.

The volumetric deformation (equation 4-1) of the column was evaluated to know the change of deformation when the equipment is pressurised.

$$\varepsilon_v = \varepsilon_a + 2\overline{\varepsilon_r} \tag{4-1}$$

The axial deformation (ε_a) of the column is assumed equal to the deformation of the steel bars and bolts. The axial displacement of the column with applied stress σ_{ap} = 8 MPa (applied during the calibration of the sensors) was measured. An axial deformation of $\varepsilon_a = 0.034\%$ was obtained (in this case expansion is considered positive).

The radial deformation of Perspex was calculated assuming a thin-wall pressure analysis, in which a weighted radial strain was considered with two different types of rings (steel and Perspex rings). The radial deformation of the steel ($\varepsilon_{r\ steel}$) rings was considered to be zero. The radial deformation of the Perspex (ε_r) was calculated considering an elastic modulus (E_{pex}) of 3000 MPa. The weighted radial strain was dtermined considering the total length of the specimen (350 mm), where the length of the Perspex (L_{pex}) is 260 mm (4 rings of 65 mm in height), and the length of the steel (L_{steel}) is 90 mm (3 rings of 30 mm in height). Further details are indicated in Equation 4-2.

In addition, the tensile stress (σ_t) on maximum pressure application was also calculated. It was determined taking into account the maximum applied stress σ_{ap} = 8 MPa, where the Perspex thickness (e_{pex}) is 25 mm, and the internal radius (r_i) of the specimen is 50 mm. Equation 4-2 compares the tensile stress (16 MPa) in the Perspex ring with the maximum tensile strength σ_{tmax} =70 MPa.

$$\sigma_t = \frac{\sigma_{ap}\, r_i}{\mathrm{e}_{pex}} = 16\ \mathrm{MPa}\ \leq\ \sigma_{tmax}$$

$$\varepsilon_r = \varepsilon_t = \frac{\sigma_t}{E_{pex}} \tag{4-2}$$

$$\overline{\varepsilon_r} = \frac{\varepsilon_r L_{pex} + \varepsilon_{r\,steel} L_{steel}}{L_{pex} + L_{steel}}$$

$$\overline{\varepsilon_r} = 0.74\varepsilon_r = 3.94 \times 10^{-3}$$

The volumetric deformation obtained at σ_{ap} = 8 MPa was $8.22\text{x}10^{-3}$ (ε_v = 0.82%). This value corresponds to compressibility of the system of $1.03\text{x}10^{-3}$ MPa^{-1}, which is adequate for a constant volume system. The volumetric deformation is small enough to be neglected in the analyses of the results.

4.2.2. Hydraulic part

The mock-up cell is designed in such a way that fluid injection (water or gas) are allowed independently from top, bottom and lateral sides (Figure 4-2) to mimic real saturation conditions (a rapid increase of water pressure on top under controlled lateral hydraulic boundary conditions and gas injection on bottom). To allow axial hydration, the base and top stainless steel disks are equipped with a fluid inlet and outlet. The latter is needed to evacuate the air present in all the system near the inlets during the saturation phase and to evacuate water and/or gas during gas injection phase. The three stainless steel individual rings allow lateral fluid injection and evacuation through fluid inlets and outlets. Mechanical valves are mounted at the faces of each inlet and outlet, allowing the entrance and/or the evacuation of water and/or gas to be controlled. Passing tubes for water and gas are connected to the valves to pressure/volume controllers (PVC) to apply and monitor fluid pressures and volumes (Figure 4-2).

The top and bottom plates and lateral steel rings are equipped with filters made of peek (Figure 4-4) to ensure homogenous hydration. The top and bottom filters include five grooves with a separation distance of 30 μm. The lateral filters placed between stainless-steel ring and transparent Perspex cylinder includes four grooves with a separation distance of 37.5 μm.

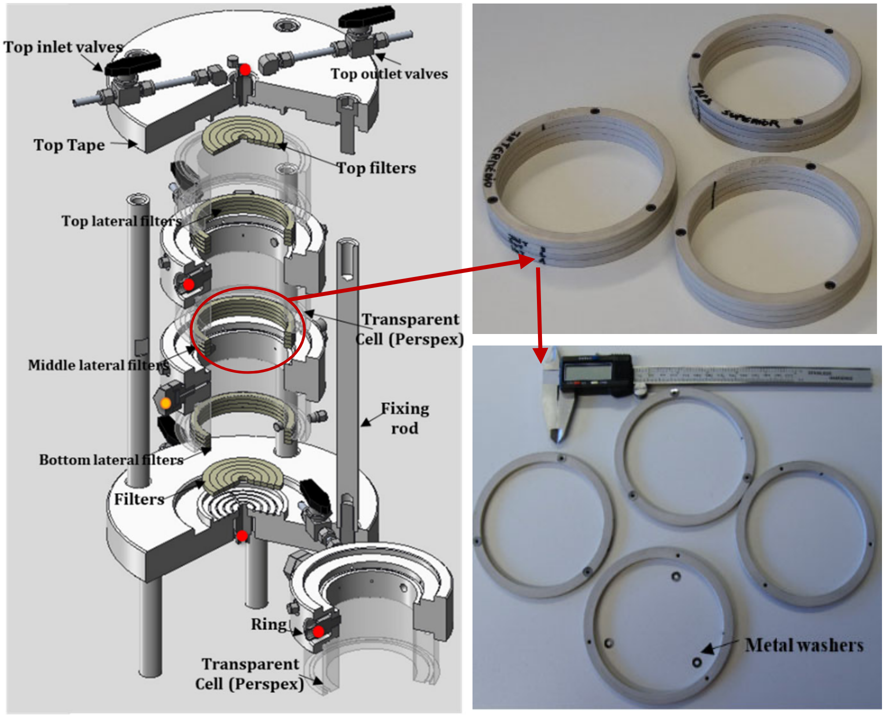

Figure 4-4. View of Peek filters.

4.3. Measurement parts

The mock-up cell is equipped with several sensors to monitor the HM response of the mixture at top, bottom and lateral boundaries at different heights.

4.3.1. Total stresses transducer

Six total pressure sensors (Honeywell model A-105 manufactured with a unitized stainless steel diaphragm and no dead volume with a range of 14 MPa and pressure resolution 70 kPa) are used to measure the total stress at different positions where the transducers are in contact with the sample to measure the real total stress. Figure 4-5a shows the location of the total stresses transducers. Prior to their use, the sensors are calibrated to verify their performance. To this end, the cell is filled with water and a series of water pressures is applied to the measuring face of each sensor. Water pressure was increased between 0.5 to 7 MPa by means of a pressure-volume controller. The output voltage of the sensors was recorded by the data logger. All the used total pressure sensors were calibrated and they all gave a linear relation between imposed pressure and output voltage. The calibration curves together with the calibration equations are described in Appendix-A.

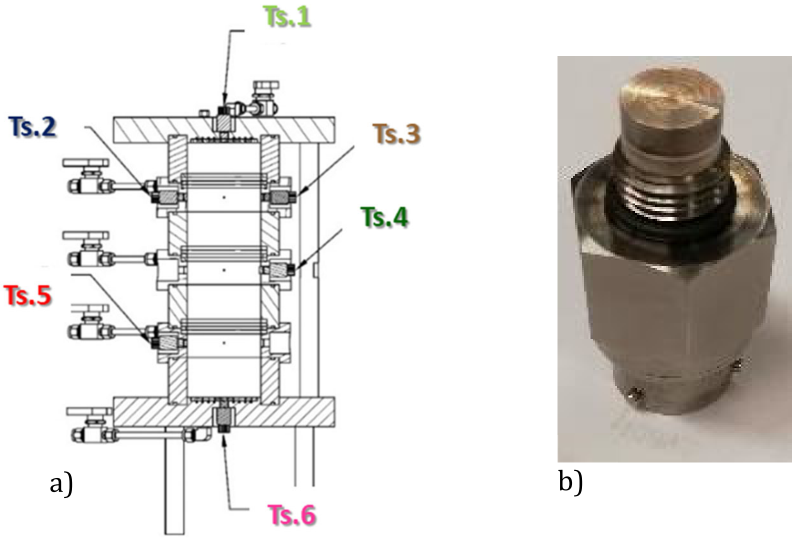

Figure 4-5. a) View of the infiltration column with the ubication of the total stresses transducer and b) images of the total stress transducer Honeywell model A-105.

4.3.2. Water pressure transducer

Three water pressure sensors (Honeywell model A-105) are used to measure water pressure at different positions with some modifications, as shown in (Figure 4-6). Figure 4-7 shows the location of the water pressure transducers. To avoid clay particle migration a filter paper and a geotextile were used to cover the sensors. To reduce the dead water volume a small diameter stainless steel tube was placed between the head sensor and filter paper (Figure 4-6). The same calibration protocol as for the total pressure sensors was applied. The calibration curves, together with the calibration equations, are presented in Appendix A.

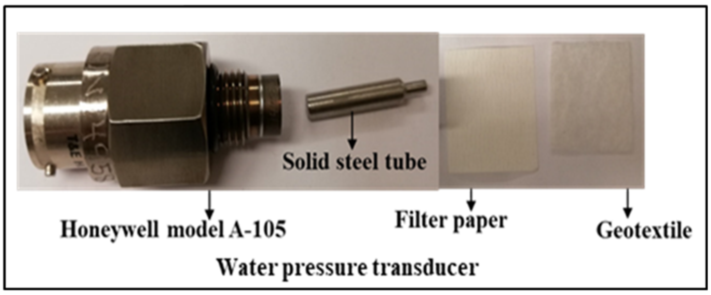

Figure 4-6. Images of the water pressure transducer with the solid steel tube, filter paper and geotextile.

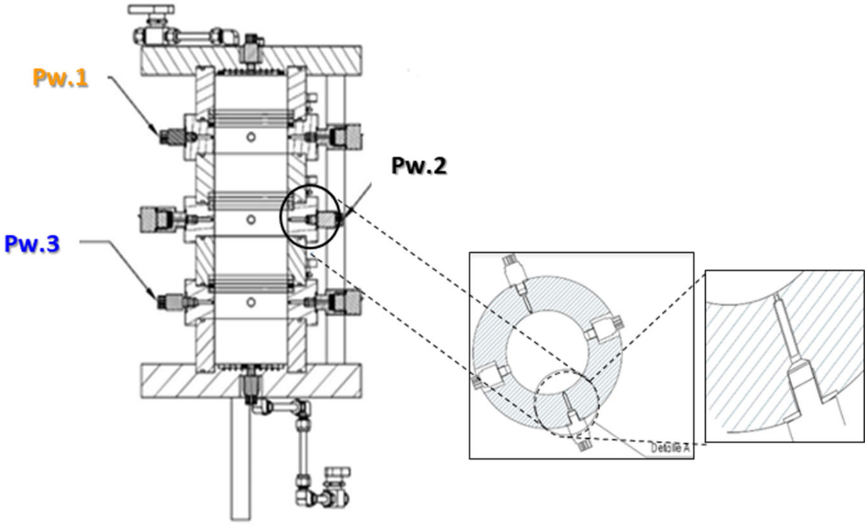

Figure 4-7. Schematic cross-section of infiltration column with location ubication of water pressure transducer.

4.3.3. Relative humidity sensor

Relative humidity is recorded by three sensors (Hygrochron iButton DS1923 rugged and self-sufficient system that measures temperature and/or RH < 95%) placed at different heights in the cell (Figure 4-8c). The Hygrochron iButton (Figure 4-8b) is configured to communicate with a computer through the serial 1-Wire® protocol, which requires only a single data lead and a program called Express Thermo to set and collect the data. The sensors have a diameter of 17.35 mm and a height of 5.89 mm. For the proper installation of these sensors in the stainless steel cylinders wall, an extra piece is needed (Figure 4-8d). This fitting piece enables an easier installation of the sensors in the cell wall by simply screwing them into their dedicated holes.

Prior to their use, the sensors are calibrated to verify their performance. To this end, they are placed in different saline solution for a week till reaching equilibrium. The used solutions are NaCl (36g/100H_20), LiCl(86g/100H_2O) and distilled water (relative humidity of 95-100%). The iButtom calibrations are shown in Appendix B.

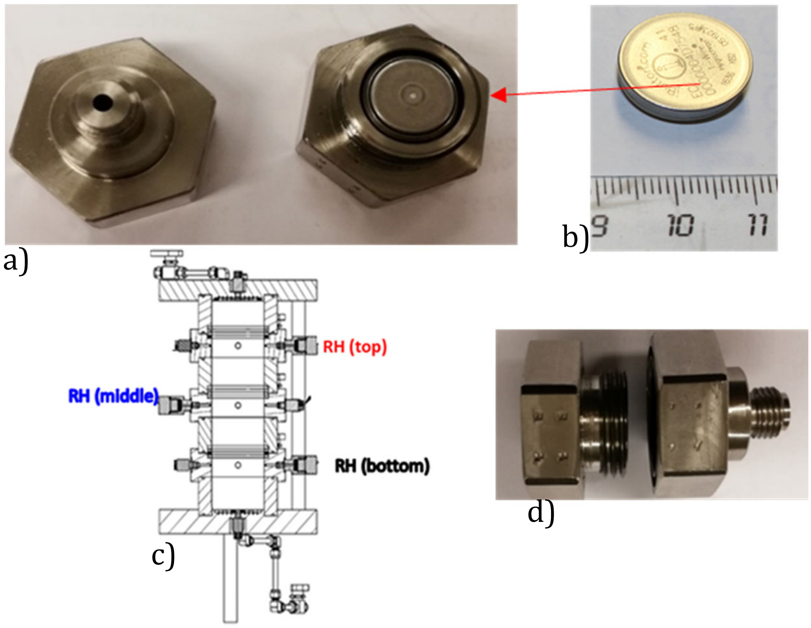

Figure 4-8. View of iButton sensors and fitting piece.

4.3.4. Pressure-volume controllers

Four standard pressure-volume controllers (PVC) from GDS Instruments are connected to the top and lateral inlets located on the top stainless steel disk and ring to control independently axial and radial water injection pressures (Figure 4-9b). The PVC have pressure application from 0 up to 4MPa of water, with accurate measurement of volume change. The PVC has a volume capacity of 200mL and volume accuracy of 0.25% (volume resolution 1mm3). The maximum pressure range is 4 MPa (pressure resolution 0.1kPa).

In addition, the high-pressure volume controller (HPVC) from WILLE Geotechinik is connected to the bottom/top disk inlet to control gas injection pressure and flow rate (Figure 4-9a). The HPVC is a pressure controller according to the electro-mechanic principle. The pressure piston inside the cylinder is moved by a precision stepping drive. The pressure and volume control of the device can be done in two main operations modes such as volume flow and pressured-controlled. The HPVC control volume rates between 10^{-4} mL/min and 100 mL/min (volume resolution <0.005mL) with a capacity of 500 mL and a maximum pressure range of 20 MPa (pressure resolution 0.01 MPa).

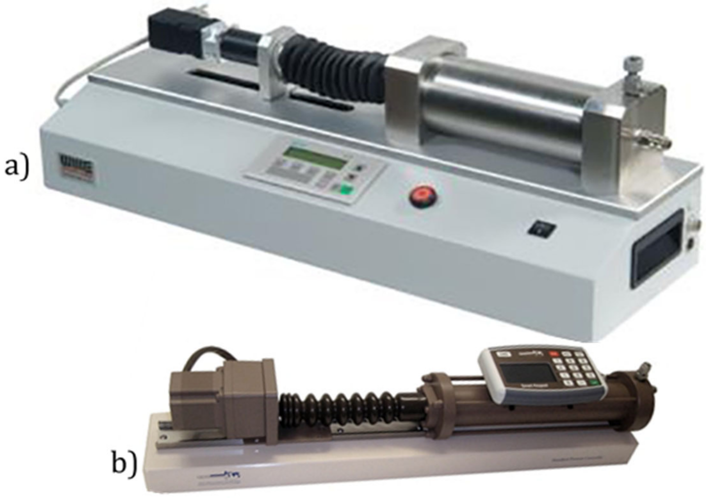

Figure 4-9. a) High-pressure volume controllers for air b)Pressure volume controller for water.

4.3.5. Software for mock-up test

The data acquisition software was developed in Visual Basic (Microsoft) under the name of ***GeoLab*** in order to monitor the pressures and volumes of controllers and the total and water pressures sensors.

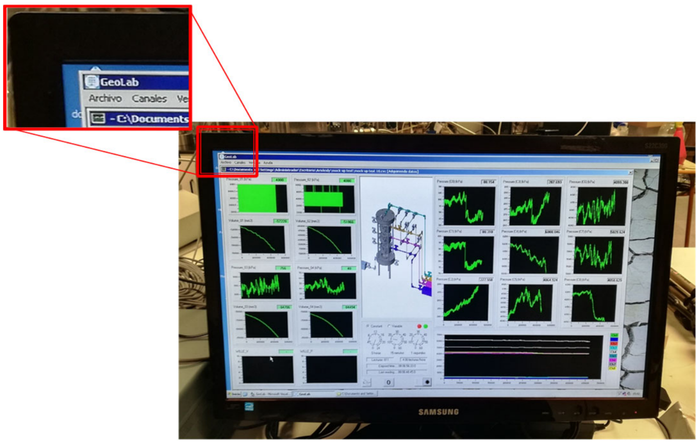

Figure 4-10. Software designed for column infiltration test GeoLab.

4.4. Testing procedure

4.4.1. Sample preparation

The sample was prepared directly into the cell following the second protocol (see chapter 2), which ensures a dry density of 1.47 Mg/m^3 and allows a homogenous sample to be obtained. Figure 4-11a shows the first layer of the packing of pellets, and Figure 4-11b shows the first layer of the mixture. Each layer is composed of 148 pellets. The sample was made by calculating the amount of layer and amount of dry mass of MX80 bentonite by layer. Finally, 148 pellets can be placed by layer with a mass of 0.46 g to get the dry density near the target dry density.

The Perspex cylinder and rings were assembled progressively as sample preparation was advancing (Figure 4-12). Sample preparation lasted 28 days, during which 50 layers of pellets (7400 pellets) were placed. It has to be noted that sample preparation induced humidification of the mixture (initial suction decrease). The water contents of the pellets and powder before sample preparation are 6.72% and 10.47% consequently.

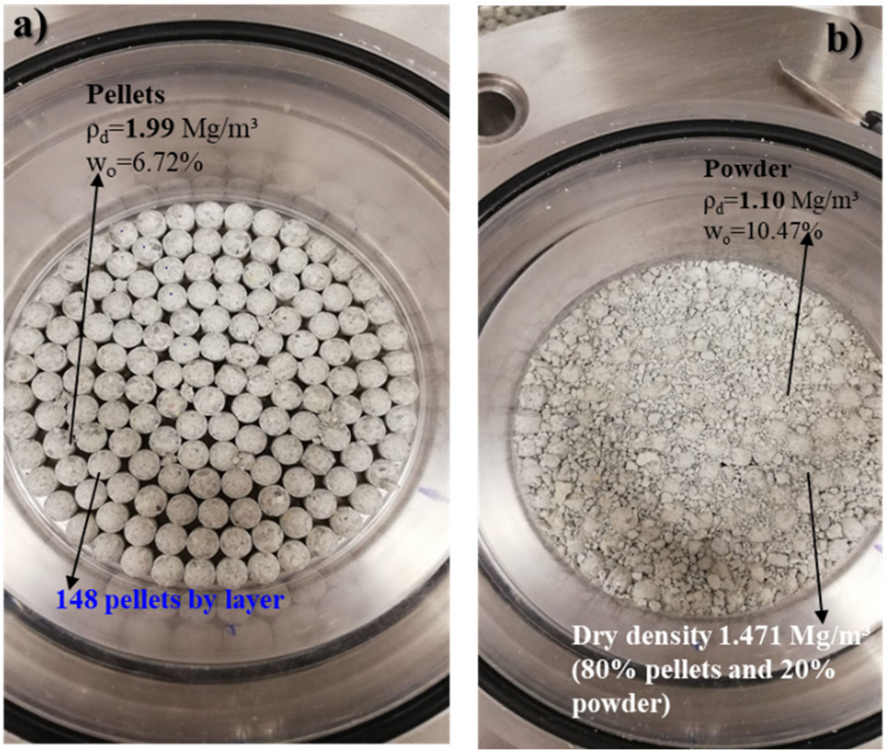

Figure 4-11. a) Packing of pellets (148 pellets by layer); b) mixture with dry density 1.47 Mg/m^3 (80% pellets an 20% powder).

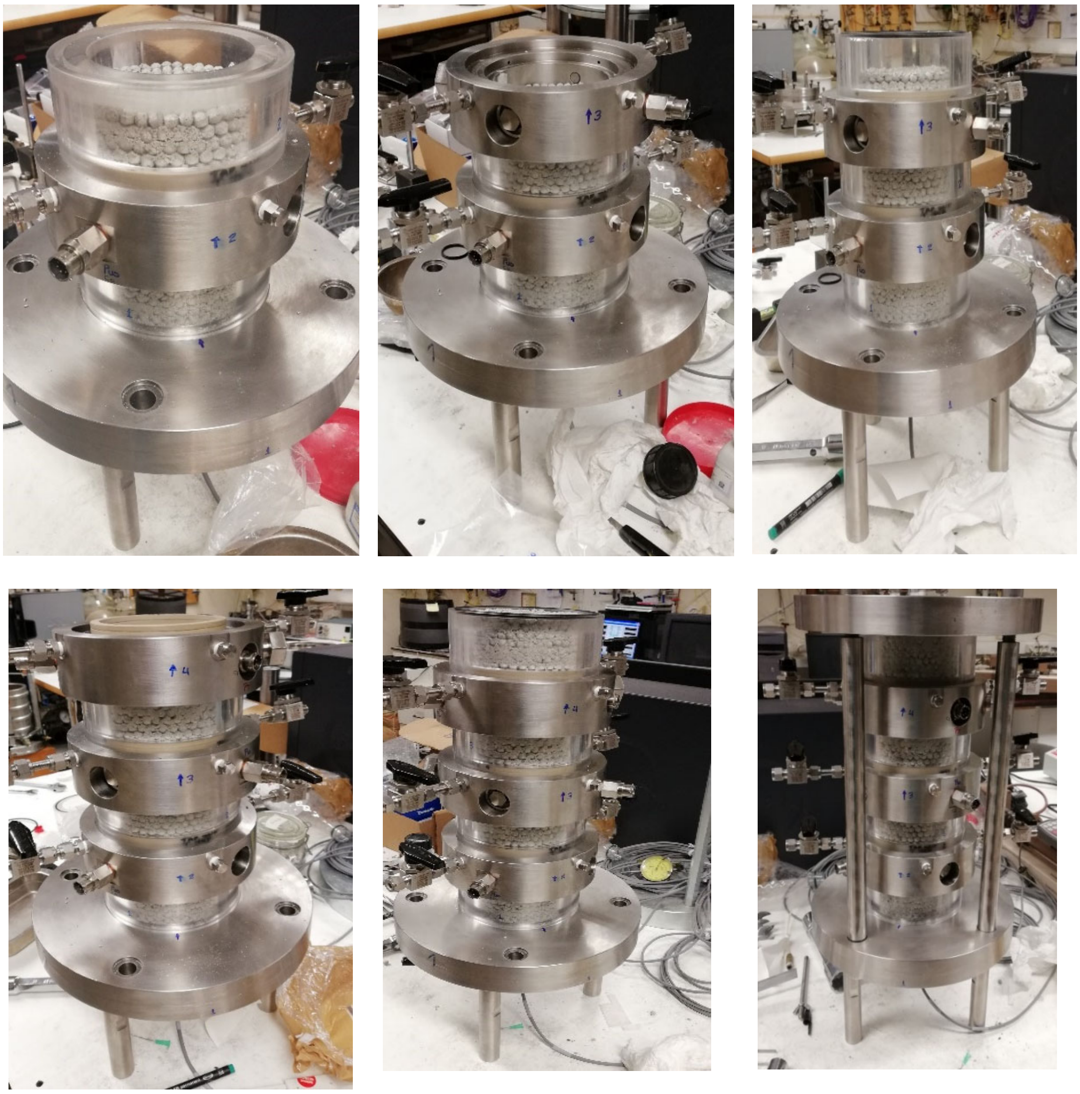

Figure 4-12. Progressive preparation and assembling of the testing sample and the mock-up cell.

4.4.2. Testing protocol

Once the sample is prepared, the upper stainless steel disk was placed on the top of the Perspex cylinder and fixed with the four rods. The total pressure sensors were then screwed to the cell wall and adjusted so that an initial pressure of 100 kPa was applied to ensure good contact between the sensor and the sample. The test started by setting on the data acquisition program to record all the initial values before the hydration started.

4.4.3. Saturation phase

Prior to water injection, sample hydration was performed using the vapour equilibrium technique. Two saline solutions were used a lithium chloride and saturated sodium chloride solutions. Calibration data for both solutions are presented in Figure 4-13 and Figure 4-14.

A relative humidity RH = 31% (s = 160 MPa) was imposed on the top and lateral inlets using a lithium chloride solution (0.52 g LiCl /100 g H_2O) for 25 days. The objective here is to recover the initial suction of the material, s = 160 MPa, measured before the mixture preparation**.** To accelerate the process, an air pump with a small air pressure, varying between 30 to 50 kPa, was used to force vapour convection through the sample (Figure 4-15).

After 25 days, a relative humidity RH = 75% (s = 39 MPa) was imposed on the top and lateral inlets using a saturated sodium chloride NaCl solution (36 g NaCl/100 g H2O). During this phase, the air pump was turned off for several days to allow equilibrating the initial total suction (the gradient of pressure induced by the convection of air throughout the sample's height affected the distribution of relative humidity within the specimen as observed by the RH sensors).

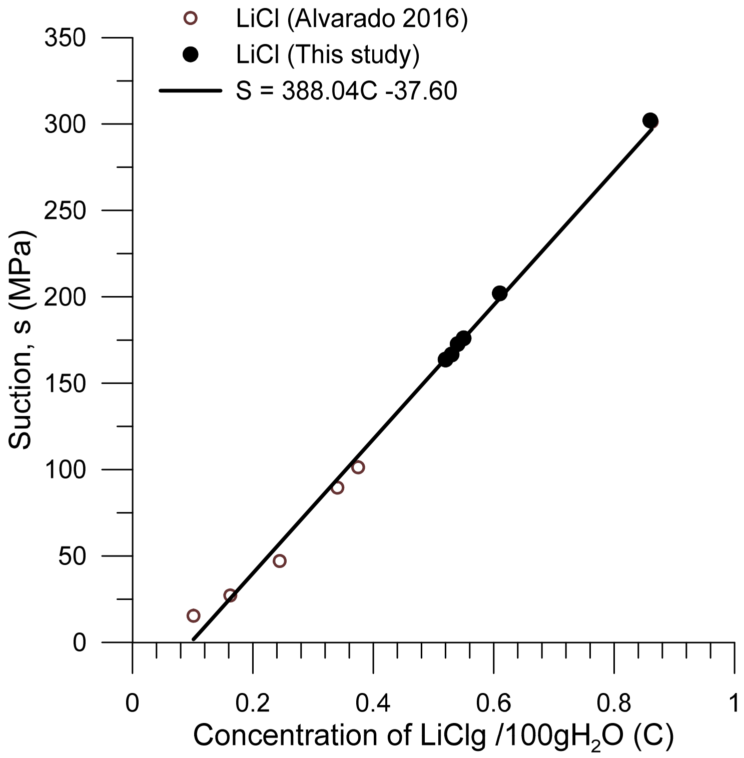

Figure 4-13. a) Calibration of the LiCl solution, along with data from Alvarado (2017).

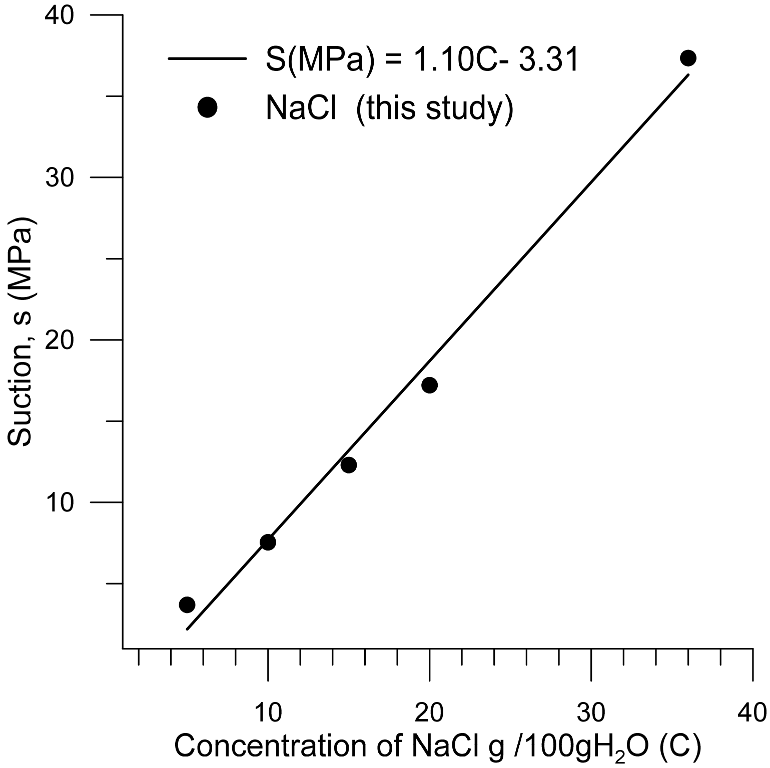

Figure 4-14. a) Calibration of saturated NaCl solution.

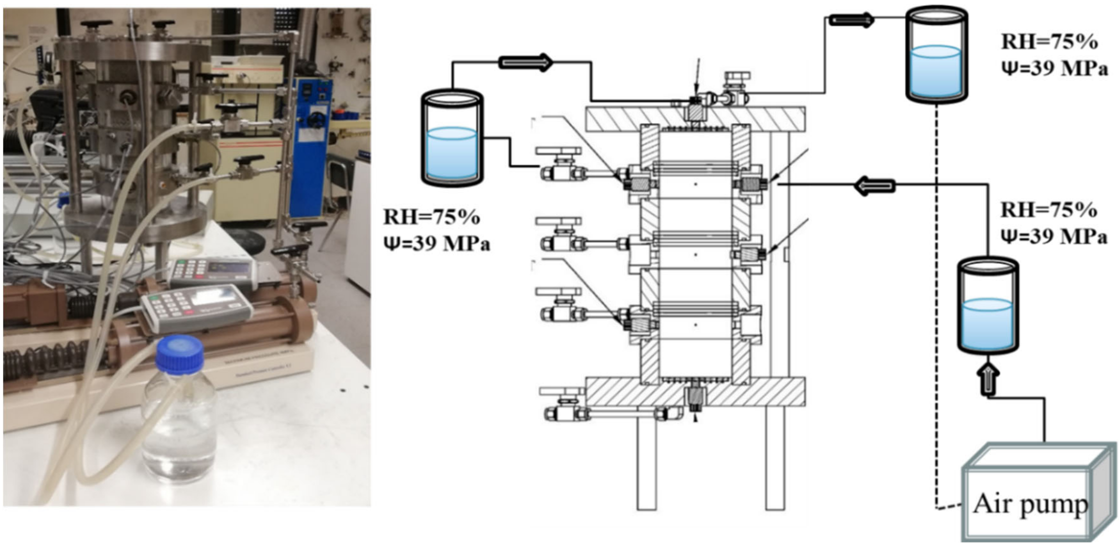

Figure 4-15. Layout of the mock-up test with a view of the forced convection system for RH control using a NaCl solution (RH = 75%).

Table 4-1and Figure 4-16 shows the evolution of air pressure and total stresses with RH = 75% (considering 25 days is the beginning of the hydration phase since started to measure the relative humidity with the sensor iButtom). An increase of stresses and pressures was observed when air pressure was imposed (air pump on).

Table 4-1. Range of each stage of the forced convection system

stage	Time (Days)	Imposed suction (MPa)	Air pump on/off
A-B (20/07/18-15/08/18)	26	39	Air pump off (Relative humidity started to be measured)
B-C (15/08/18-14/09/18)	30	39	Air pump on
C-D (14/09/18-20/09/18)	6	39	Air pump off
D-E (20/09/18-21/09/18)	1	39	Air pump on
E-F (21/09/18-19/10/18)	28	39	Air pump on during six hours then the air pump off
F- End (19/10/18-30/10/18)	11	39	Balanced without air pump

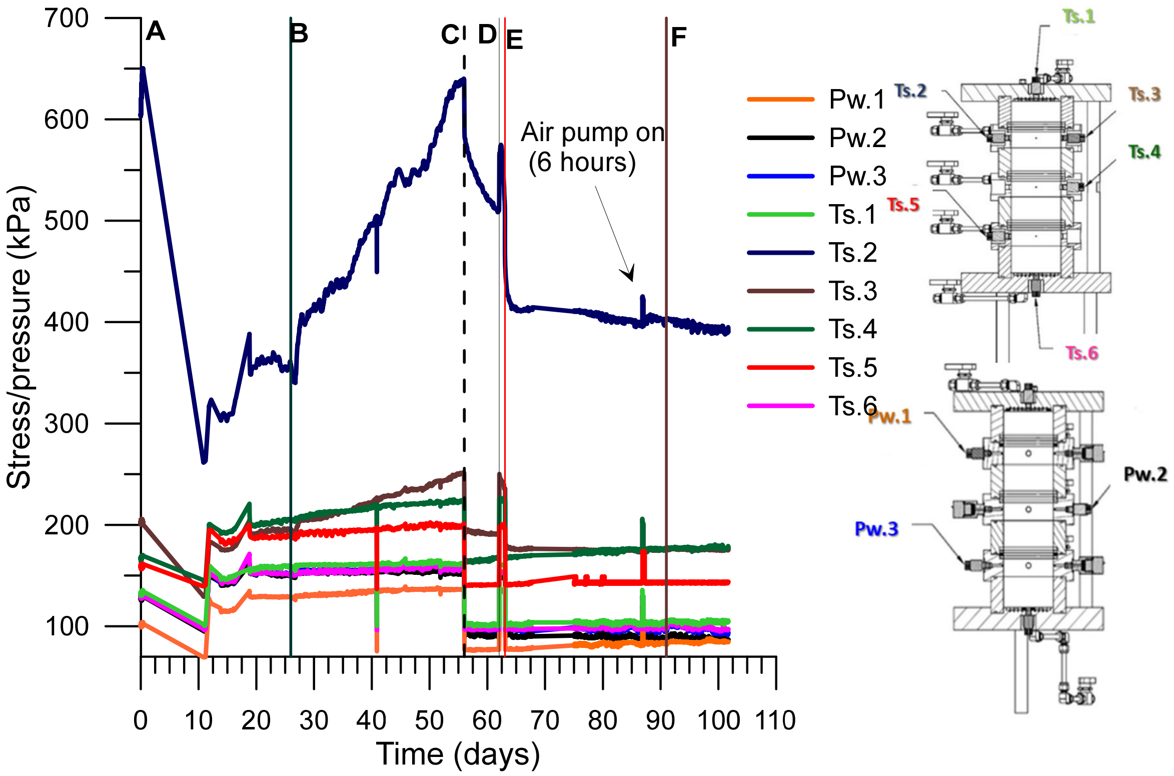

Figure 4-16. Evolution of air pressure and total stresses during the forced convection system for a relative humidity of 75% (suction of 39 MPa).

The vertical top flow rate was based on simulations calculated using Code_Bright (Olivella *et al.*, 1996) to ensure reaching a water pressure at the top boundary of 4 MPa at around 15 days. The average flow on the top boundary was also based on the estimation of the degree of saturation changes during top infiltration. The vertical flow was $q_v = 2.11\text{x}10^{-5}$ mm/s ($Q_v = 0.166$ mm^3/s) and the horizontal flow rate was 50 lewer than the vertical flow $q_h = q_v /50 = 4.22\text{x}10^{-7}$ mm/s ($Q_h = 0.046$ mm^3/s). Table 4-2 summarises the water injection rates during the initial stage.

Table 4-2. Data for the injection of water in the column infiltration.

Day	Injection	Flow rate injection
30/10/2018 (0 days)	Top injection	0.166mm^3/s up to 4 MPa (then constant pressure)
15/11/2018 (15 days later of top injection)	Lateral injection	0.0153mm^3/s on each ring up to 4 MPa (then constant pressure)

After 101 days the injection tubes were connected to the pressure-volume controllers (PVCs) while keeping the valves closed. The flow rate was applied until reaching a water pressure of 4 MPa, after that, a constant pressure of 4 MPa imposed with the PCVs was used. The 4 MPa is used trying to mimic the complex hydration of the VSS.

Initially, a flow rate of 0.166 mm^3/s was imposed on the top side to ensure the axial fast hydration of the mixture, after several scoping calculations with Code_Bright. After almost 116 days, water pressure in the top reached up to 4 MPa (the PVC1 fixed a 4MPa) (Figure 4-17). A lower flow rate (0.0153 mm^3/s) was imposed at the lateral boundaries (the three lateral PVC placed in the steel rings of the mock-up test) to simulate the delayed radial hydration of the vertical seal at the real repository conditions (Figure 4-18). Water pressure reached 4 MPa at PVC2 and PVC3 located at the top and middle rings after 147 and 254 days respectively (the water pressure was fixed at 4 MPa in the PVCs), while it increased only to 1.8 MPa at PVC4 located on the bottom ring after 298 days (Figure 4-17). The pressure was then kept constant (4 MPa) during the rest of the saturation phase at PVC1 to 3 except at PVC4 where a constant flow rate was maintained but stopped to start the first gas injection. The imposed hydraulic boundary conditions are displayed in Figure 4-17.

During hydration, the evolution of total stress and relative humidity were monitored. The injected water at both boundaries was continuously recorded and used to calculate the sample degree of saturation.

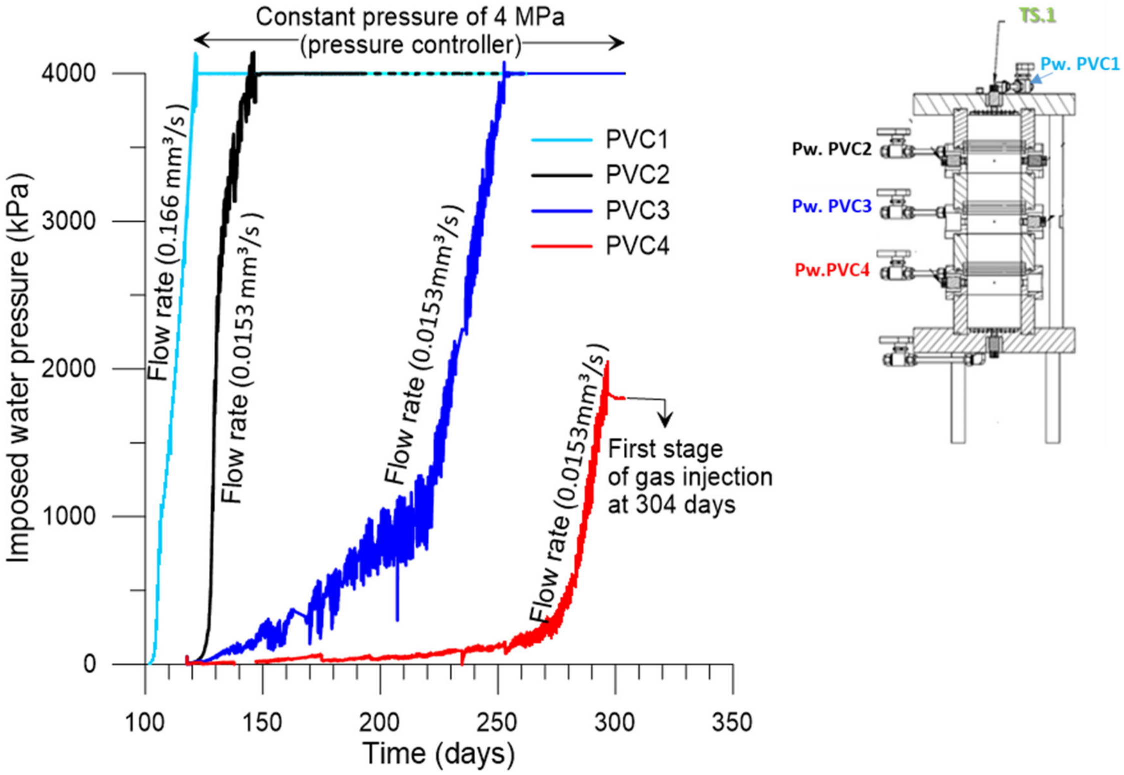

Figure 4-17. Imposed water pressure at axial and lateral boundaries applied with the PVCs.

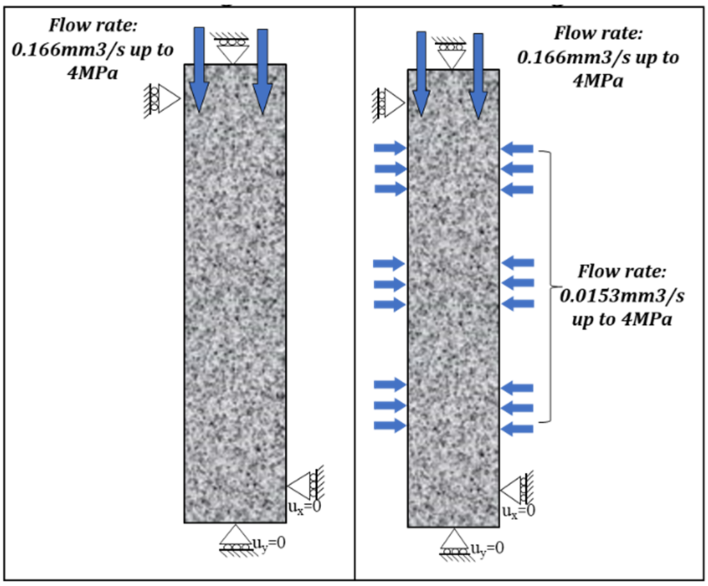

Figure 4-18. Schematic view of imposed hydraulic axial and lateral boundary conditions.

4.5. Results and discussion

4.5.1. Total suction

Variations with time of total suction measured at different distances from the axial hydration front are displayed in Figure 4-19. Total suction is related to relative humidity (*RH)* via the psychrometric (Kelvin's) equation,

$$s = -\frac{RT\rho_w}{M_w} lnRH \tag{4-3}$$

Where R is the gas constant, T the absolute temperature, M_w the molecular mass of water and ρ_w the density of pure water.

During hydration by forced vapour convection (path AH from 0 to 100 days), total suction increased from 80 to approximately 90 MPa with some fluctuation when air pressure was imposed (air pump on) Figure 4-19. At 101 days, once axial hydration started, total suction decreased rapidly at the top sensor and reached zero after 160 days. Total suction at the middle and bottom sensors started to increase once lateral injection started at 116 days. It reached 0 MPa after almost 250 days.

The first download of information from the relative humidity sensors (iButtom) after the hydration started at 25 days. At this moment, some gas was released and fine particles of dry bentonite were observed to migrate because as the hydration front progresses due to the top and lateral wetting, gas is displaced and trapped at the lower part of the sample. The iButtom information was downloaded 18 times during the hydration of the sample. The iButton placed on the top ring reached 100% of RH earlier than the bottom, therefore, it had less download of information. Nevertheless, not all of the entrapped gas can quickly be released, so that the accumulated gas at the bottom prevents the sample from being completely saturated (for more details, see chapter 5, section 5.5).

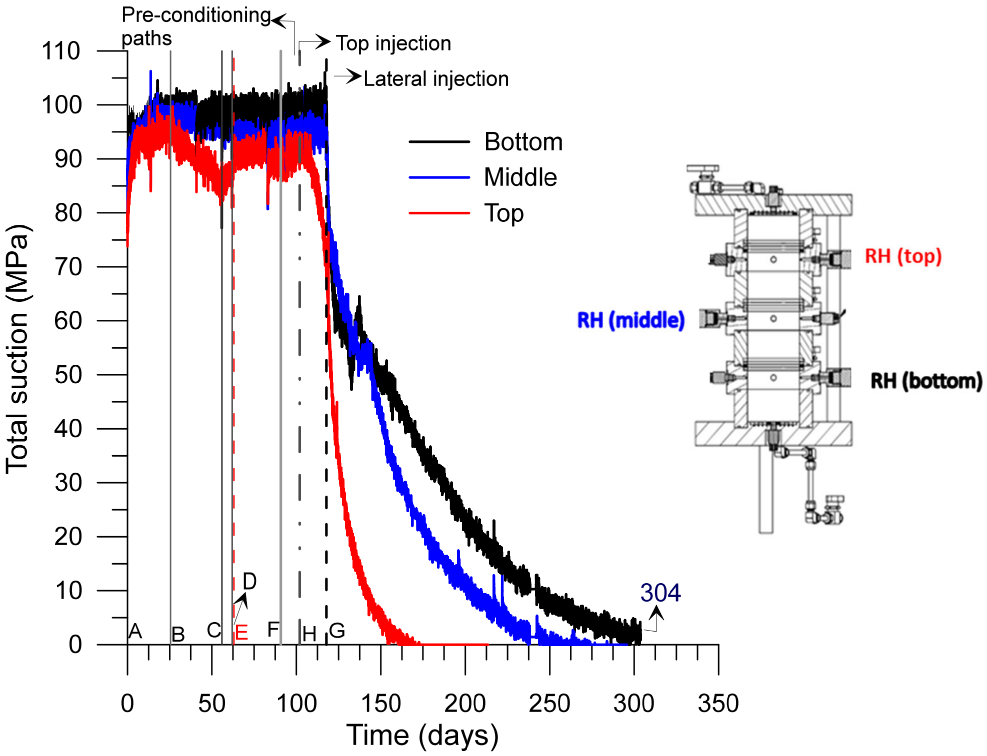

Figure 4-19. Evolution of total suction at different points within the mixture as a function of time.

The volume of injected water that was monitored with different PVCs (4 PVCs) is presented versus time in Figure 4-20. Water volumes were corrected by calculating the grams of water escaping per unit time through the Perspex rings (Keller & Kouzes, 2017) and using a permeability coefficient from Bhadha (1999) for the Perspex material at 25°C. At the beginning of the test, the water injection started from the top (PVC1) with a fast controlled volume rate of injection (0.166 mm^3/s) until it reached 4 MPa (120 days), mimicking the VSSs. The highest volume injected was in the top of mock-up equal to 3.46x10^5 mm^{3,} corresponding to 41.2% of the water of volume injected until 303 days. The lateral injection started 16 days after the injection in the top in different PVCs (three PVCs). The PVC2 injected the lowest water volume because the axial hydration front reached this zone and increased the water pressure to 4 MPa, and then the water flow slowed down (Figure 4-20) reaching 9.19x10^4 mm^3, corresponding to 10.92% of the water volume injected. PVC 3 and PVC4 reached 22.1% and 24.96%, respectively. Before 303 days the PVC3 was kept closed to avoid any fluid shortcut. The total volume injected during the stage is 3.46x10^5 mm^3. As it can be observed, the rate of increase is still positive after 300 days of hydration, suggesting that the sample is not entirely saturated, as also observed in Figure 4-22.

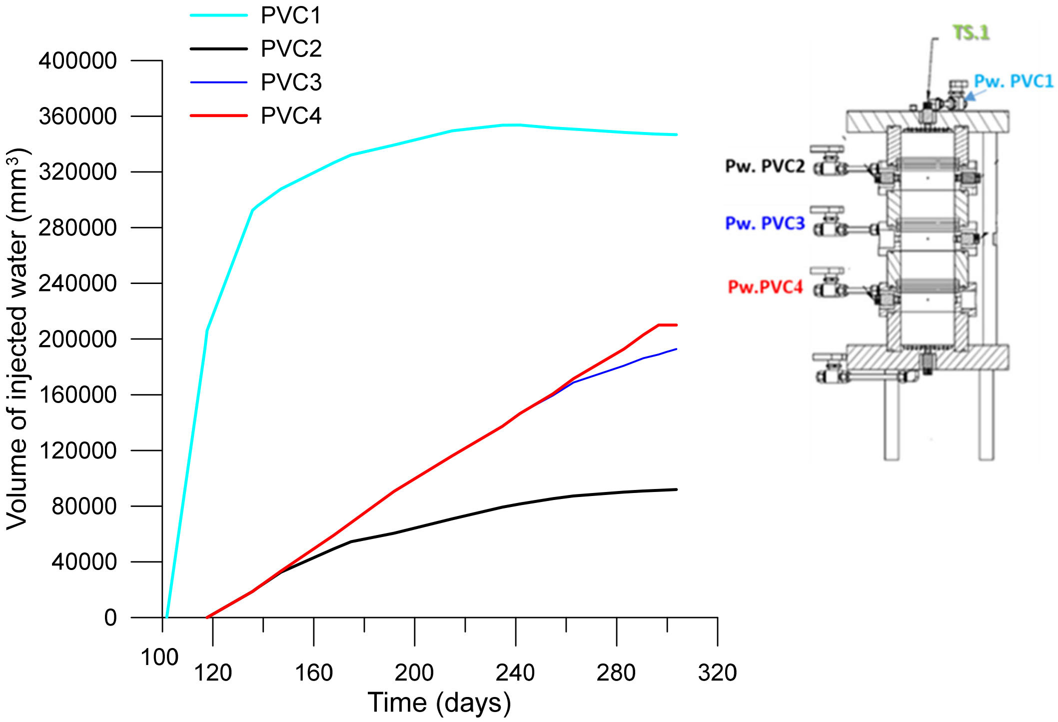

Figure 4-20. Evolution of the injected water volume over time.

The evolution of the global degree of saturation as a function of time is displayed in Figure 4-21. It was calculated with the injected water at both boundaries. The theoretical total volume corresponding to the fully saturated state of the sample is calculated as the volume of the total voids in the sample: initial total volume multiply by total porosity plus the change of volume calculated with the volumetric deformation of the cell. It is assumed that this theoretical total volume is equal to 1.3×10^6 mm^3. The water density considered was 1 Mg/m^3.

Figure 4-22 shows the progressive saturation of the mixture during the hydration phase. Eleven days after axial hydration started, the upper layers of the mixture appear to be fully hydrated (Figure 4-22), while the global degree of saturation was 39% (initial degree of saturation is equal to 26.54%). At 241days, water reaches two-thirds of the mixture’s pore volume and the global degree of saturation increases to 81.3%. The hydration front continues to progress and reaches the bottom part of the sample; however, full saturation is not achieved after 304 days.

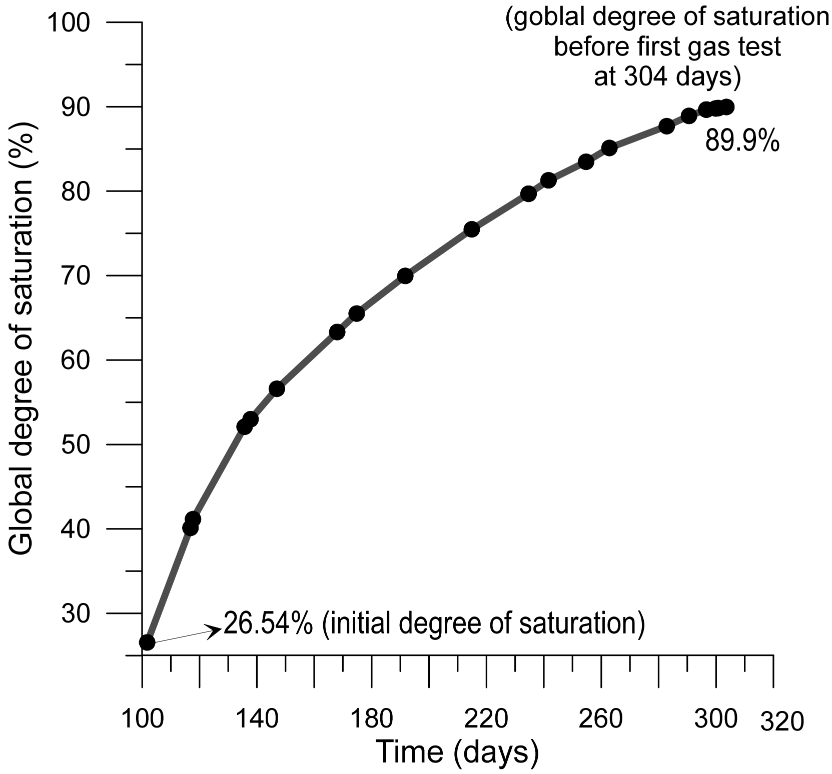

Figure 4-21. Evolution of degree of saturation against time.

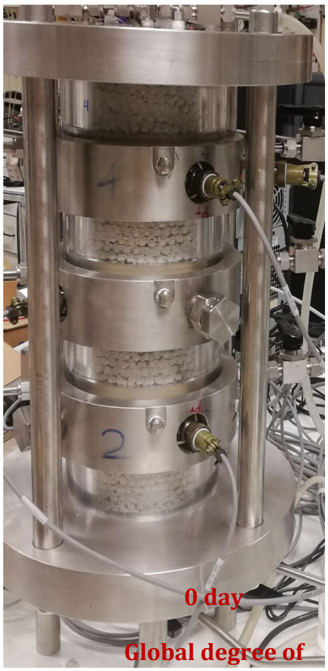
0 day

Global degree of
saturation = 26.54%


112 days

Global degree of
saturation =


161 days

Global degree of
saturation = 62.82%

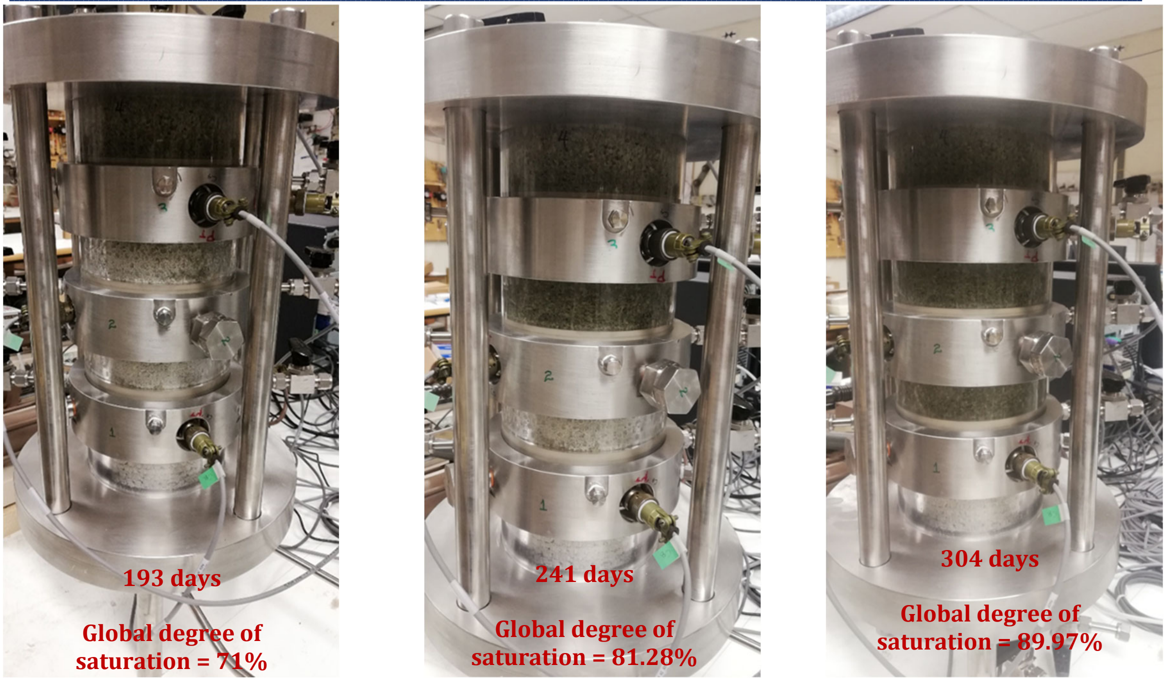

Figure 4-22. Progressive saturation of the sample inside of the mock-up cell.

4.5.2. Pore pressure

The evolution of the water pressure measured at three positions within the mixture is shown in Figure 4-23. Sensor Pw.1 located on the top ring started increasing after 160 days when the bentonite mixture reached saturation at this zone. It reached 3.5 MPa at 304 days. A slightly lower value is registered for sensor Pw.2 located at the middle ring, where the water pressure reached 1.5 MPa after 300 days. Pw.3 located at the bottom ring registered no significant variation suggesting the hydration front had not arrived, as shown in Figure 4-23. The dependence (decrease) of the saturation and pore pressure rates on the sample height suggests that at the bottom layers, the mixture is denser with lower permeability.

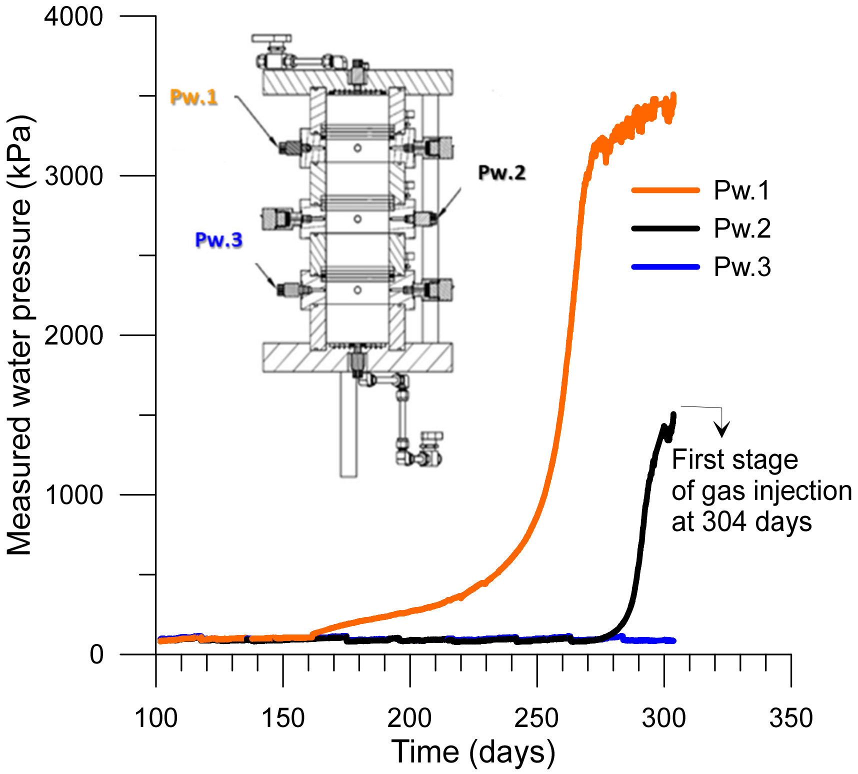

Figure 4-23. Measured water pressure in the mock-up test in the different sensors when the sample reaches the saturation

4.5.3. Total stresses

The evolution of total stresses at different sensors locations are shown in Figure 4-24. A different rate of increase is identified for each sensor. For sensor TS1, located on the top of the cell, an initial fast increase of total stress is observed. It reached a value of 4 MPa then remained constant till 254 days. Afterwards, a slight increase is observed and the total stress reached a value of 4.5 MPa after 304 days. The lowest total stress value and increase rate are observed for sensor TS6 located on the bottom of the cell at the furthest position from the hydration front. Similarly to TS1, an initial fast increase of total stress is observed at TS3 located at the upper stainless steel ring on the right-hand side, reaching a peak value of 4.75 MPa, then a slight decrease until 4.5 followed by an increase to reach stabilization at about 5.25 MPa. After almost 149 days, the total stress increased again and reached a peak value at 6.7 MPa followed by a slow decrease until 6 MPa after 205 days. Unexpectedly, the total stress does not stabilize but increases again to reach a peak at 6.7 MPa followed by a slow decrease till a value around 6.25 MPa after 300 days. A different evolution trend is observed at TS2 located on the left-hand side of the upper ring. The total stress increased with a slower rate compared to TS3 and reached a peak at 5.25 MPa followed by a slow decrease until a value of 5 MPa after 200 days then it increased with a slower rate and stabilized at 5.25 MPa after 240 days.

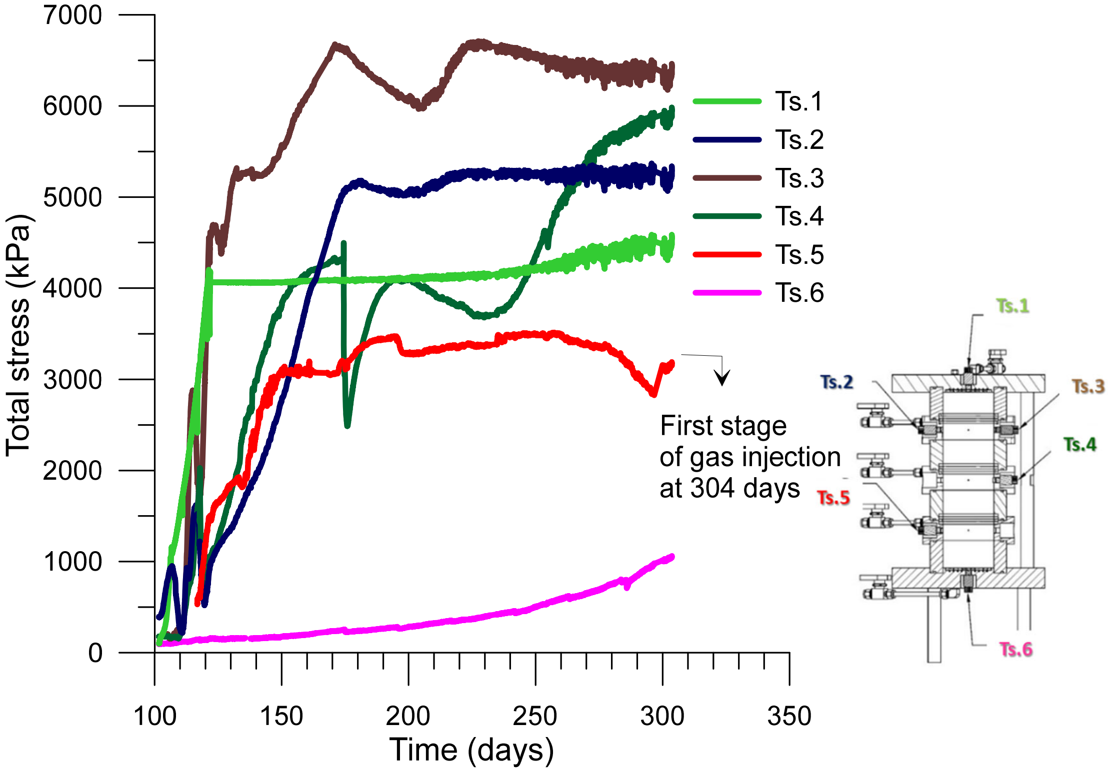

Figure 4-24. Total stress evolution in the mock-up test.

The observed difference demonstrates that the increase rate depends not only on the hydration front but also on the local porosity of the material characterized by an initial heterogeneous distribution of macro-porosity. For sensors TS4 and TS5 located at the middle and bottom rings respectively the total stress increased initially with a similar rate as TS2. It reached a peak value around 4.5 MPa at TS4 followed by a fast and large decrease to 2.5 MPa. The total stress increased again rapidly to reach a peak at 4 MPa, followed by a slow decrease to reach 3.5 MPa after 230 days. The total stress increased again with a similar rate as initially and stabilized at 6 MPa after 300 days. At TS5 the total stress stabilized rapidly around 3.5 MPa after 200 days.

At steady-state and after 250 days, the total stress registered at different locations within the mixture varied between 3 MPa and 6.25 MPa for TS1 to 5 with a lower value around 1 MPa at the bottom of the cell at TS6. This anisotropy of swelling pressure can be interpreted based on two key features: (i) the dependence of the swelling pressure on the dry density of bentonite and (ii) the initial heterogeneous distribution of the material. The observed peaks correspond to the reorganization of the macrostructure of the soil induced by the collapse of the larger voids. During hydration, pellets start swelling and filling the larger voids between them. The increasing rate depends on the local density of the material which depends on the pellet/powder structural distribution at the corresponding position.

4.6. Concluding remarks

This study describes an experimental mock-up designed to provide experimental support at VSEAL in situ tests performed in the Tournemire underground research laboratory of the French Institute for Radiation Protection and Nuclear Safety (IRSN). This new axisymmetric cell (100 mm in diameter and 350 mm high) has been developed at a reduced scale of 1/10 of the VSEAL in situ tests to reproduce this asymmetric hydration using independent top (fast injection) and radial (slow injection) water pressure systems. It also allows performing gas injections at different locations of the core of the bentonite mixture (top and bottom boundaries) and under various hydraulic states.

The testing cell was composed of four transparent (Perspex) cylinders in order to visualize processes occurring at the interface (progress of hydration front and what happen during gas tests) and three stainless steel rings (these metallic rings also hold the different lateral transducers) into a rigid frame composed of two stainless steel disks connected by four metallic rods. The cell is equipped with three types of sensors: total stress sensors placed on the top and bottom (stainless steel disks) and the lateral (stainless steel ring), allowing the top and lateral total stresses at various heights to be monitored; three water pressure transducers placed on each stainless steel ring of the cell, allowing to monitor the water pressure; three relative humidity sensors located on each stainless steel ring installed in small chambers that measure the evolution the relative humidity over time.

The sample was prepared directly into the cell following the second protocol (layer by layer), which ensures a dry density of 1.47 Mg/m^{3}and allows a homogenous sample to be obtained. Sample preparation lasted 28 days, emplacing 50 layers of pellets (7400 pellets). The volume of injected water was monitored, allowing to calculate the global degree of saturation of the sample. The sample preparation induced material humidification (initial suction decrease), inducing a lower suction value of the mixture (~100 MPa) in comparison to the pellet and powder initial suctions (around 160 MPa for the pellet and 85 MPa powder). These observations show that the designed cell is suitable for testing a binary bentonite mixture with the monitoring of total stresses, water pressure and total suction at different location of the cell.

The evolution of total stresses at different locations within the mock-up test show a diverse rate of increase. The observed difference demonstrates that the increase rate depends not only on the hydration front but also on the local porosity of the material, which depends a lot on the fact that the material close to the hydration front swells earlier, inducing a decrease in dry density of the bottom material on compression. The anisotropy of swelling pressure can be interpreted based on two key features: (i) the dependence of the swelling pressure on the dry density of bentonite and (ii) the initial heterogeneous distribution of the material. The observed peaks correspond to the reorganization of the macrostructure of the soil induced by the collapse of the larger voids. During hydration, pellets start swelling and filling the larger voids between them. The heterogeneous distribution of pellets and powder within the sample plays an important role in the creation of these larger voids. The fast vertical hydration (axial hydration) is the one that governs the hydration of the column as observed in the trend of all the sensors and also observing the water volume injected from the top. The slow radial hydration has a more negligible effect on the hydration of the column, inducing some air entrapment at the bottom of the cell.

5. GAS INJECTION EXPERIMENTS

5.1. Introduction

The production and migration of gas generated in deep geological disposal of radioactive are one of the long-term critical issues. The gas will be generated by several mechanisms, such as the anaerobic corrosion of the metallic canisters, the microbial degradation of organic substances and the radiolysis of water, which generate hydrogen, oxygen, sulphide, methane and carbon dioxide. The gas production rate will depend on the waste composition, availability of water and disposal concept. Nevertheless, in scenarios where the gas production rate exceeds the rate of gas diffusion in the pore water, gas will build up and can induce local overpressure on the engineering barrier systems generating other transport mechanisms, such as two-phase flow and dilatancy-controlled gas flow through pathways and interfaces (Horseman *et al.*, 1996; Harrington *et al.*, 2017).

Traditionally gas tests have been carried out under saturated conditions. The most common cells for the gas experiments are the triaxial and isotropic cells (Hildenbrand *et al.*, 2004; Arnedo *et al.*, 2008; Angeli *et al.*, 2009; Romero *et al.*, 2013; Villar *et al.*, 2013; Gutiérrez-Rodrigo, 2018; Carbonell *et al.*, 2019; Liu *et al.*, 2020; Villar *et al.*, 2020; Villar *et al.*, 2021) that allow better managing the isotropic or anisotropic stresses. Nevertheless, in these cells, it is not always straightforward to measure the small changes in soil volume during gas injection and subsequent gas dissipation.

Accordingly, studies under constant volume conditions with measurements of total stresses have also been performed because they present a better control of injected fluids in the soil volume (Horseman *et al.*, 2004; Graham *et al.*, 2012; Harrington *et al.*, 2017; Gutiérrez-Rodrigo, 2018; Cui *et al.*, 2021; Gutiérrez-Rodrigo *et al.*, 2021). Furthermore, oedometer cells with precise soil volume change measurement have also been carried out (Gonzalez-Blanco *et al.*, 2017; Gonzalez-Blanco *et al*., 2020).

The gas injection can display more homogeneous propagation of the fluid pressure throughout the sample when the inlet filter covers the whole area of the sample and the gas flow is applied in the axial direction. Nevertheless, when injection of gas is through point like inlet filters, it might be challenging to predict the pore pressure distribution (Shaw, 2013; Harrington & Horseman, 2003; Harrington *et al.*, 2017). The gas pressure can be applied through constant pressure ramps (Cuss *et al.*, 2014; Villar *et al.*, 2020; Liu *et al.*, 2021), instantaneous pressure gradient (Hildenbrand *et al.*, 2004; Gutiérrez-Rodrigo, 2018), gas pressure increased stepwise (Shaw, 2013; Cui *et al.*, 2021), and constant volumetric rate (Gonzalez-Blanco *et al.*, 2020; Horseman *et al.*, 1999; Harrington & Horseman, 2003; Arnedo *et al.*, 2008).

Several investigations have been carried out to better understand the pathway generation and propagation, and the breakthrough pressure of the gas (Horseman *et al.*, 2004; Gonzalez-Blanco, 2017; Harrington *et al.*, 2017). The pathways are usually unstable, with sudden changes and producing a non-uniform gas flow distribution throughout the sample (Horseman *et al.*, 1999). Moreover, some experiments have been carried out to perform a 'soft' breakthrough (Gonzalez-Blanco *et al.*, 2020) at given inlet gas pressure, constant inlet gas volume, and allowing sample deformation (expansion) to occur before recording gas outflow. Other authors induce a clear breakthrough when the gas inlet pressure decreases suddenly with an important outflow of gas (Horseman *et al.*, 1999; Harrington & Horseman, 2003; Hildenbrand *et al.*, 2004; Harrington *et al.*, 2017). Damians *et al.* (2020) carried out modelling of the results present by Harrington *et al.* (2017) reproducing satisfactory results observed in the test even the existences of preference pathways.

In this study, different gas injection tests have been performed to evaluate the impact of gas injection on the mixture at different locations in the mock-up (top and bottom boundaries). The mixture will be under partially saturated conditions. It will be an excellent opportunity to study whether the gas pathways develop internally throughout the sample or, on the contrary, follow the interface (cell wall/mixture) since the swelling pressure has not reached its maximum capacity.

A preliminary gas test was performed with an MX80 mixture under oedometer conditions with a high-pressure cell used before for Gonzalez-Blanco *et al.*(2017 and Gonzalez-Blanco *et al*. (2020). The test was intended to assess the gas overpressure (over the water pressure) required to start desaturating an initially saturated sample since to the author's knowledge there were no previous gas injection studies on this type of mixtures composed of pellet and powder of bentonite. A high total vertical stress was applied to ensure adequate horizontal stress to avoid gas passage through the ring/sample interface.

A first gas test was performed in the mock-up at a global degree of saturation around 89.9% and injecting gas from the bottom boundary of the cell with a controlled volume rate of 0.1mL/min and starting from atmospheric pressure. The water pressure at the top and lateral boundaries were kept at 4 MPa. The test aimed at studying the possible gas breakthrough, and verifying if interface problems occurred even when not all swelling pressures had developed.

The second gas test was performed in the mock-up under slightly higher saturated condition (global S_r>97%). In this case, a water pressure boundary conditions of 1 MPa was kept to mimic the in-situ VSEAL test. This second gas test had two stages where the gas injection was applied from the cell's top boundary. The first stage was carried out using a flow rate of 0.1 mL/min starting from gas pressure of 1.67 MPa to 5.3 MPa, and then the gas pressure was kept constant for several days to observe the possible gas breakthrough. Once the breakthrough was detected, the upper lateral valve PCV2 was closed, and a second stage was started by increasing gas pressure from 5.3 MPa to 6 MPa. During the second stage, no breakthrough was detected.

This chapter describes and interprets the experimental results of the different gas injection tests. It presents the preliminary gas injection test under oedometer conditions, followed by the two gas tests performed on the infiltration column and hydration results after the first gas injection test.

5.2. Preliminary gas test under oedometer conditions

A preliminary gas test was done in a high-stress oedometer cell to approximately estimate the gas breakthrough pressure. The cell is described in Gonzalez-Blanco *et al.* (2016) and Gonzalez-Blanco *et al*. (2020). Figure 5-1 shows a schematic of the oedometer and the different auxiliary devices used.

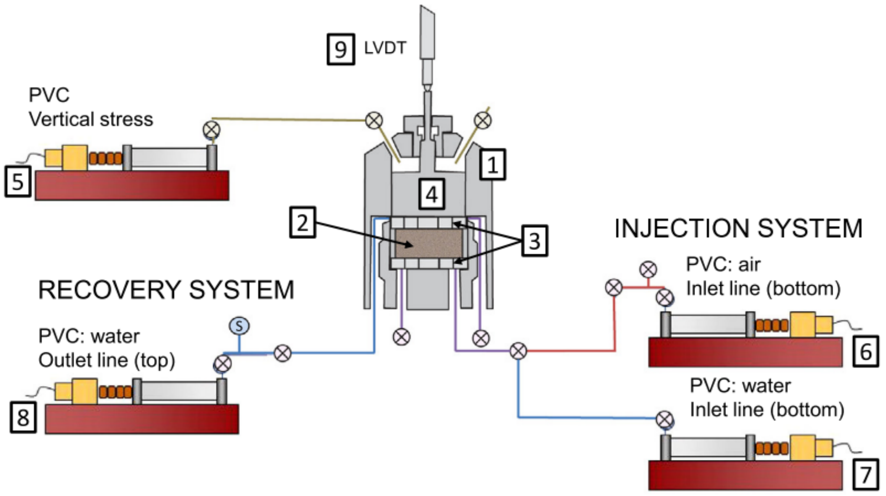

Figure 5-1. Schematic of the experimental set-up. (1) Oedometer cell; (2) sample; (3) coarse porous concentric rings; (4) axial loading piston; (5) pressure/volume controller for vertical stress; (6) gas pressure/volume controller; (7) and (8) water pressure/volume controllers; and (9) LVDT

The sample of the mixture with a diameter of 50mm, height of 20mm and dry density of 1.49 Mg/m^3 was previously saturated under isochoric condition for more than 300 days.

It is important to follow a strict protocol to ensure any significant volume change of the sample between the constant volume condition and the set-up in the oedometer. The protocol involves first unloading from the isochoric test that involves generating high matric suction even when the material is saturated. During the long-term hydration under constant volume, the mixture reached an average swelling pressure of around 3.3 MPa (see chapter 3).

5.2.1. Test protocol followed

The protocol described below and depicted in Figure 5-2 is an update of the protocol followed by Gonzalez-Blanco *et al*. (2016). The gas injection was applied from the bottom boundary trying to mimic the first test on the mock-up test.

Stage 1. Pre-conditioning path. The total vertical stress was increased at a rate of 15 kPa/min until reaching 4 MPa (top and bottom boundaries were under atmospheric conditions). Afterwards, the total vertical stress of 4 MPa was kept constant for pore pressure equalisation. This loading path induced the high initial matric suction to reduce to zero and continue with a consolidation phase.

Stage 2. Water permeability determination. The water permeability of the sample was determined under steady-state at a pressure gradient of 0.5 MPa (bottom and top water pressures were kept at 0.5 and 1 MPa, respectively, to mimic the downward flow of the mock-up). During this stage, the sample underwent some expansion due to effective stress decrease (the effective vertical stress changed from 4 MPa at the end of the consolidation to an average value of 3.25 MPa under steady-state flow conditions).

Stage 3. Drainage of bottom cap. Water pressure in the bottom vessel was quickly reduced to atmospheric conditions to allow for its fast replacement by gas.

Stage 4. Gas injection below the air entry value. Maximum gas pressure was limited to 1.5 MPa to avoid exceeding the total minor principal stress. After consolidation, the effective lateral stress would be around 3.4 MPa, based on $K_0 = 1 - \sin\varnothing' = 0.861$(for an estimated drained friction angle for MX80 of $\varnothing' = 8°$). A minimum of 1 MPa can be accepted as the difference between total vertical stress and maximum gas pressure to avoid preferential gas flows between the sample and the oedometer ring (Gonzalez-Blanco *et al.*, 2017).

Gas injection of the bottom of the cell was applied through four fast injection pressure ramps. The injection piston was shut-off at each step of the gas pressure, and it was let to decay at a constant gas volume of the inlet line. During the first three steps, the gas pressure was maintained constant, indicating no breakthrough. Nevertheless, a pressure drop was observed in the last injection pressure step.

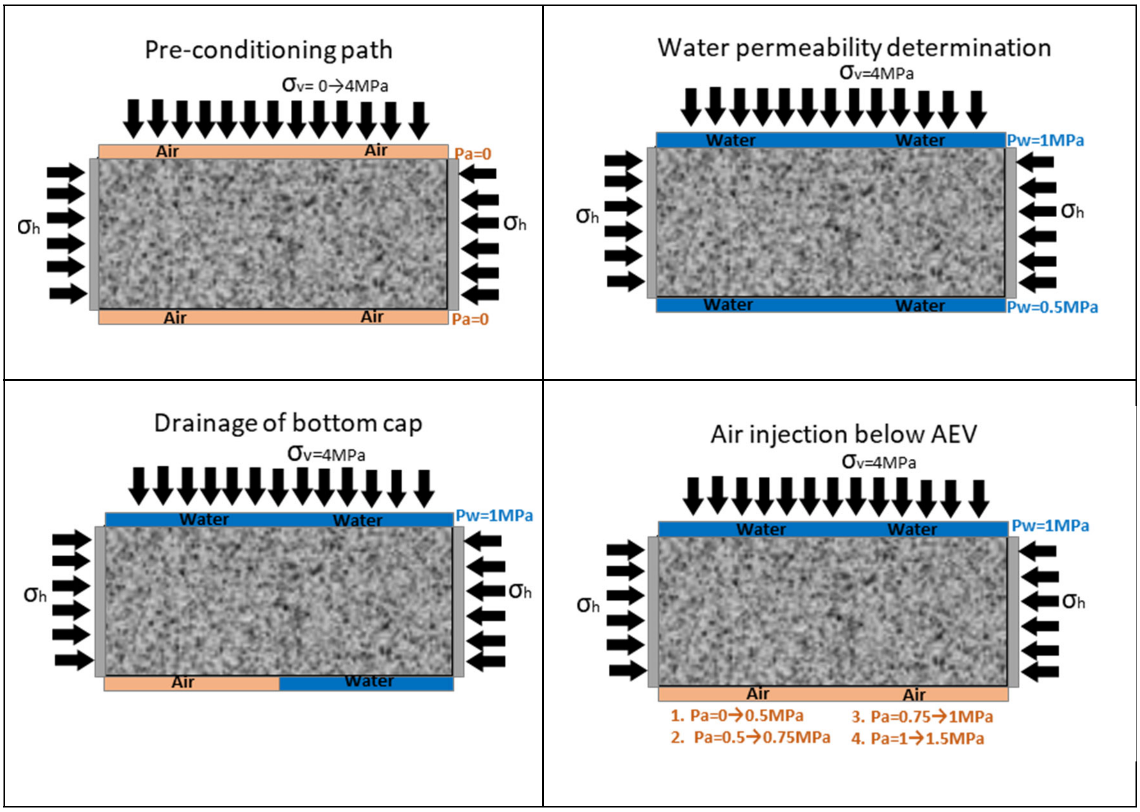

Figure 5-2. Schematic representation of protocols followed.

5.2.2. Test results

As observed in Figure 5-3, at the end of the consolidation, the sample reached an axial deformation of 1.49%. Besides, the sample underwent some swelling (0.59%) when reducing the vertical effective stress from 4 MPa to the average value of 3.25 MPa reached under steady-state flow conditions.

Figure 5-4 shows the time evolution of outflow volume, axial displacement, outflow pressure and injection pressure at a constant total vertical stress of 4 MPa. The injection pressure at the bottom boundary (injection point) increased in time following four injection pressure steps (from A to D in Figure 5-4). The first injection pressure step from 0 to 0.5 MPa for one day (A to B). The second one, from 0.5 to 0.75 MPa during 1.98 days (B to C). Afterwards, the injection pressure step was from 0.75 MPa to 1MPa for 2.44 days (C to D). Finally, the last step was from 1 MPa to 1.5 MPa (D-F). After each injection pressure ramps, the injection piston was closed (shut-off at constant injection volume). The increases in injection pressure were accompanied by expansion (positive axial displacement in the figure). The injection pressure steps generated a decrease in the effective vertical stress because of the increase in the pore pressure. During this expansive behaviour (cumulative axial strain close to 1%), the pathways tend to develop inducing some outflow to occur. At 5.5 days, the injection pressure began to decrease, and the outflow volume increased, indicating a ‘soft’ breakthrough pressure at 1.5 MPa (0.5 MPa over the top backpressure). This maximum injection pressure was 2.5 MPa below the total vertical stress. So, it was expected that the minor principal stress was not exceeded and no gas flows between the sample and the oedometer ring. Moreover, after dismantling, a fissure was observed in the central part of the sample, indicating that the gas pathway developed inside the sample.

This preliminary test reported a relatively low gas pressure over the water pressure (0.5 MPa above the water pressure). Therefore, it was not useful to upscale it to the conditions of the infiltration column. Nevertheless, this test allowed evaluating the gas permeability during the dissipation stage at constant inlet volume, as discussed in the next section.

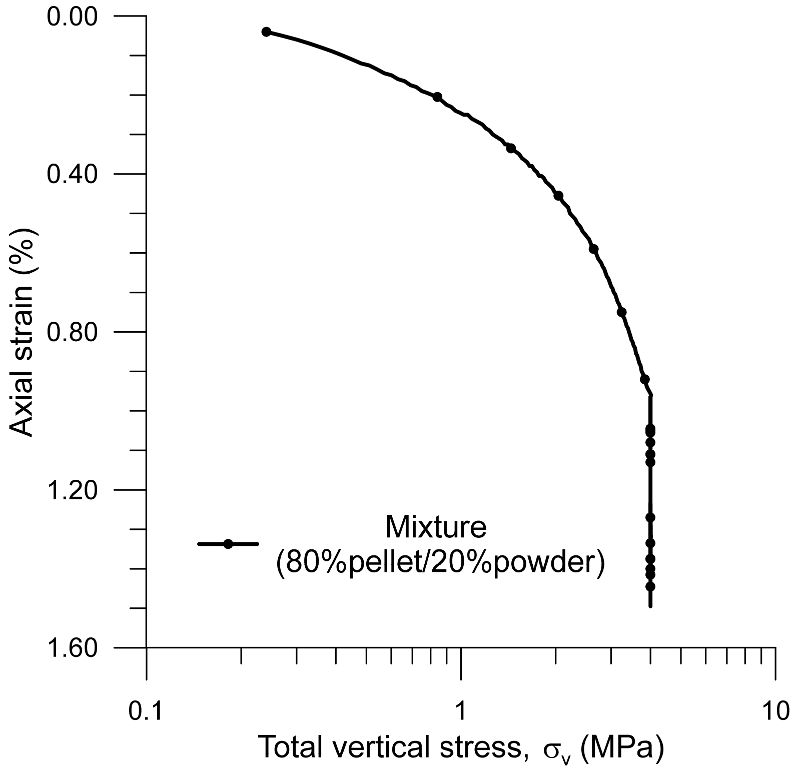

Figure 5-3. Axial deformation on loading under saturated state.

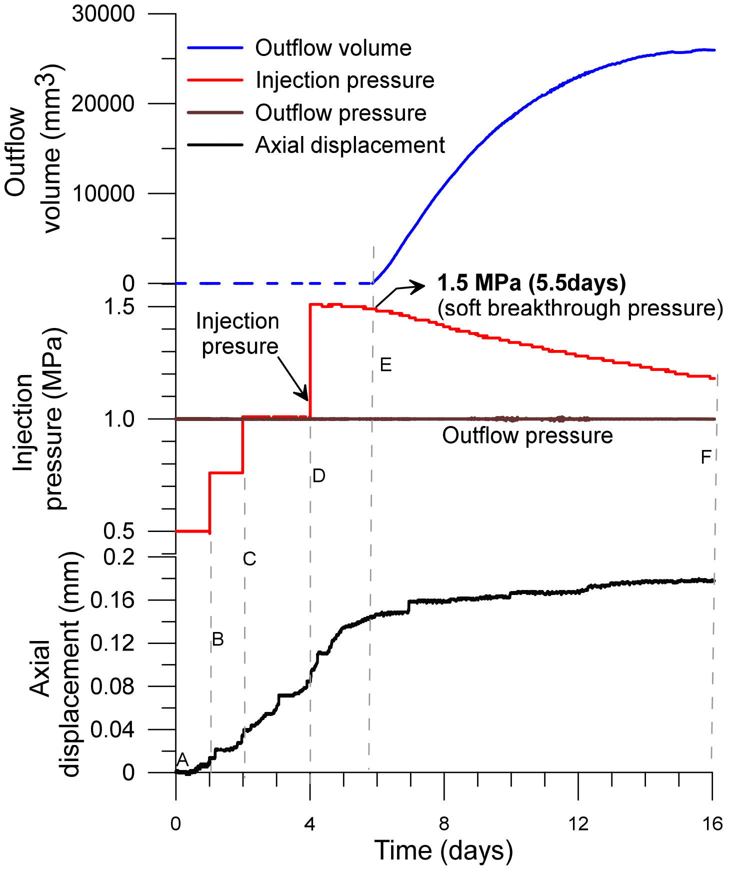

Figure 5-4. Time evolution of injection pressures, outflow volume, outflow pressure and axial displacements at a constant vertical stress of 4 MPa.

5.2.3. Permeability results

The evolution of the global gas permeability was evaluated during the final part of the dissipation stage at constant gas inlet volume involving the entire sample area. Nearly steady-state conditions were measured during this dissipation stage. Desaturated pathways were assumed with a relative permeability to air equal to 1. The advective (volumetric) flux of gas across the sample, q, was computed from the measured outflow volume in the recovery piston at 1 MPa. This determination assumed negligible diffusion through saturated bentonite. The intrinsic permeability to gas (K_g) was then calculated using Darcy's law for compressible fluids:

$$q = -\frac{K_g}{\mu_a}\frac{du}{dx} \tag{5-1}$$

The pressure differences, du, were measured from gas pressures at the injection and recovery points (and the pressure gradient is calculated with the sample height dx)

and μa (1.83×10^{-5} Pa.s at 20°C) is the air dynamic viscosity at standard room temperature and atmospheric pressure.

Figure 5-5 shows the evolution of the gas intrinsic permeability calculated at the final part of the dissipation stage. The figure also includes values of the intrinsic permeability to water (indicated with a horizontal line), which was determined from outflow data reported in chapter 3 section 3.2. As observed, the intrinsic permeability when transferring gas is slightly higher than when water is flowing. The observed differences in intrinsic permeabilities can be associated with the fact that gas flows through different localised pathways compared to the ones followed by water. Nevertheless, some differences could also be explained because of the pore pressure dependence on gas permeability of the Klinkenberg slippage effect (Klinkenberg, 1941). This effect is relevant when the intrinsic permeability is low ($< 10^{-18}$ m^2) or when the average pore pressure is low (Zimmerman, 2018).

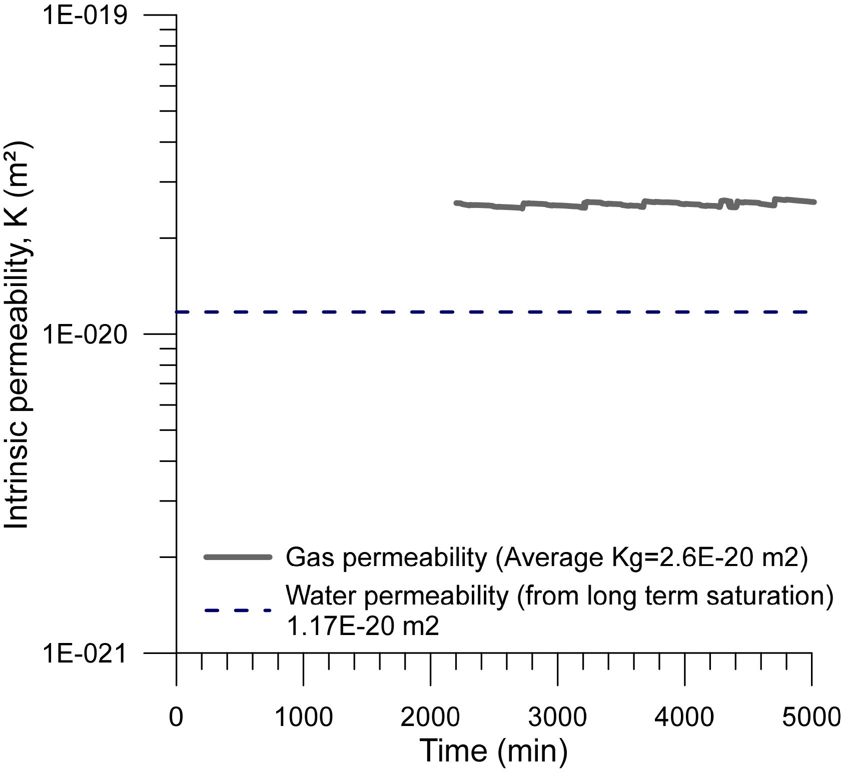

Figure 5-5. Evolution of intrinsic permeability during gas dissipation compared to the intrinsic water permeability.

5.3. First gas injection on the mock-up test

The first gas test in the mock-up test was carried out at a global degree of saturation around 89.9% and injecting gas from the downstream boundary (bottom) with a flow rate of 0.1 mL/min. The gas injection started from atmospheric conditions to almost 8 MPa with water pressure at the top and lateral boundaries of 4 MPa, except for PVC4 (valve was kept closed to avoid any fluid shortcut). The purpose of this test is to verify the impact of gas injection when the core is still under partially saturated conditions (particularly at the bottom of the column), and the lateral swelling pressure has not reached its full capacity. Figure 5-6 shows the initial state of the gas test with the values of water pressures and total stresses at the boundaries. The expected fully saturated zone in blue and the partially saturated zone of the mixtures in grey have been highlighted in the figure just for comprehension of the phenomena that will be further described (the global degree of saturation was around 89.9%). To better highlight the different zones, Figure 5-7on the left presents a picture of the column, in which the bright bottom ring of the cell indicates a partially saturated zone. In contrast, the remaining darker rings show a saturated or nearly saturated zone, which is better identified in the picture on the right.

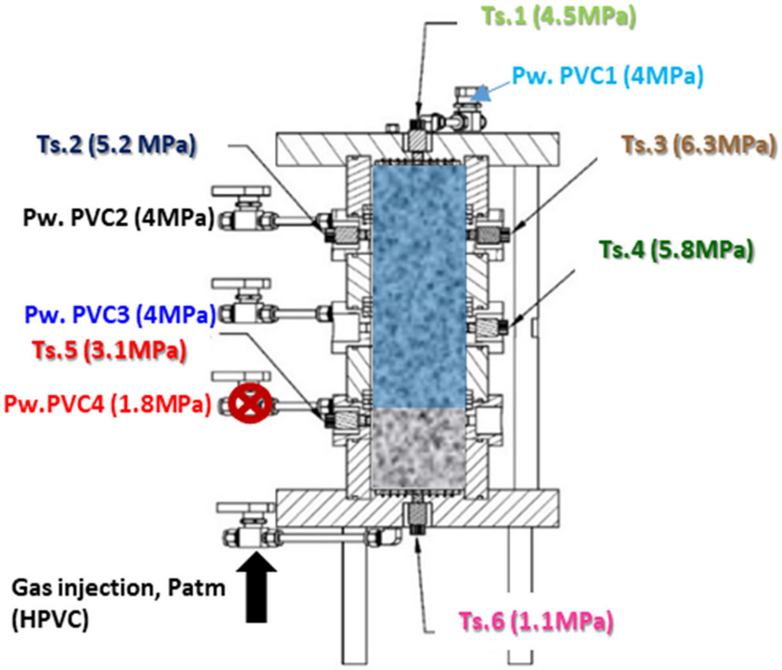

Figure 5-6. Initial state of the first gas injection test.

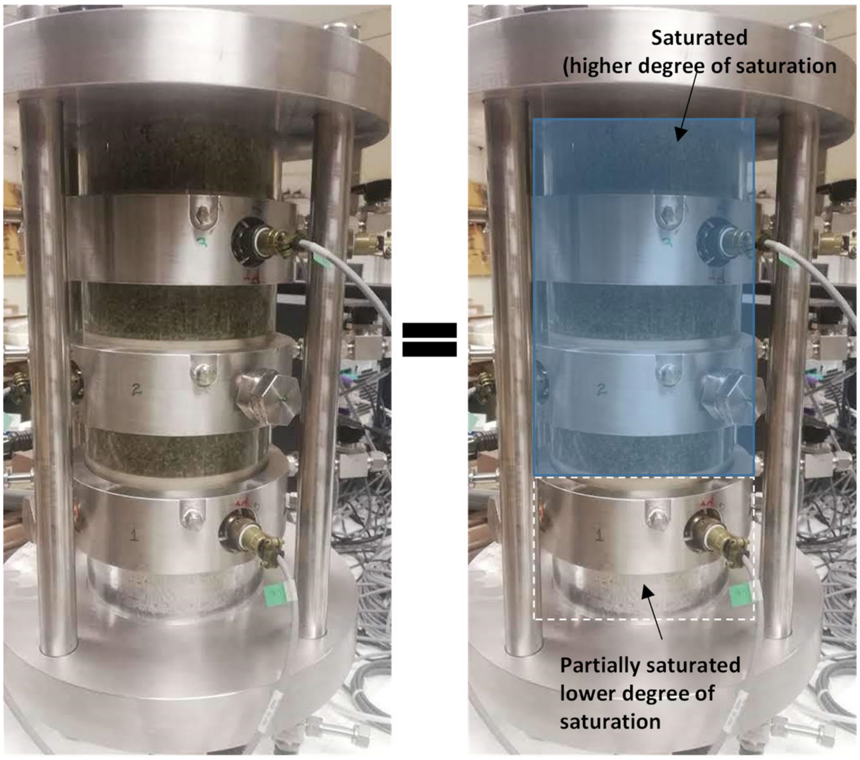

Figure 5-7. State of the sample before the first gas injection test highlighting the saturated and partially saturated zones.

5.3.1. Experimental protocol of the gas test

The protocol described below and summarised in Figure 5-8 was followed in the first gas test. Gas injection was applied from the bottom boundary to mimic the *in situ* VSS test.

Stage 1. Initial state. At 304 days the bottom gas injection valve was opened to atmospheric conditions ($P_a = 0$). The total stresses at the boundaries were different depending on the location and considering the hydration front (see Figure 5-6).

Stage 2. Gas injection. The gas injection started from atmospheric conditions reaching a gas pressure of almost 8 MPa (Figure 5-8) at a controlled volume rate of 0.1 mL/min with a high-pressure volume controller (HPVC). To achieve this gas injection pressure (8 MPa), it was necessary to re-fill the volume of HPVC four times. This re-filling had some impact on the gas pressure evolution, as it will be shown later.

It is important to remark that in the last high-pressure re-filling stage, the pressure duplicated from 4 MPa to 8 MPa in only two days. It was initially expected that the bentonite mixture could not sustain these high gas pressures, so no decision was taken on the maximum pressure. The gas pressure was expected to drop over 6 MPa, i.e. 2 MPa above the water pressure and representing four times the excess detected in the preliminary oedometer test (0.5 MPa above the water pressure). However, at 8 MPa, the cell started to show tightness problems, so the gas pressure was drastically reduced to repair this lack of tightness.

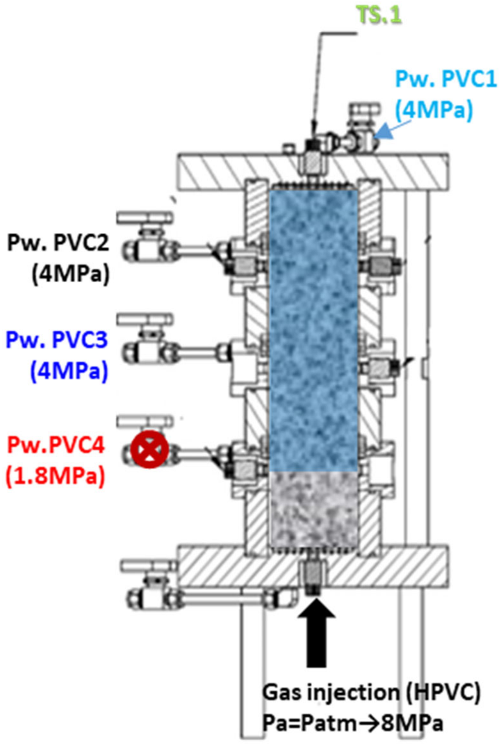

Figure 5-8. Schematic representation of gas injection in the mock-up test.

5.3.2. First gas injection results

Figure 5-9 summarises the time evolution of the gas injection pressure together with the evolutions of total stresses at different points. The wavy shape of the time evolution of the gas injection pressure results from the different gas volumes used in the four re-filling stages.

After almost 13 days (at 316 days) of gas injection, the gas injection pressure reached almost 8 MPa, the test was stopped, and the pressure was drastically reduced as previously indicated to repair the lack of tightness. The TS5 sensor (located at the bottom ring) increased with a fast rate similar to the gas injection pressure because this zone is partially saturated with good connectivity of the gas pressure. This sensor started at 3.1 MPa and reached total stress of 8.7 MPa, i.e. 1

MPa higher than the gas injection pressure (7.7 MPa). As observed, the initial net swelling stress of 3.1 MPa reduced during the gas pressurisation process to 1.0 MPa. This relatively low swelling stress will affect the potential development of pathways close to the wall/soil interface, as will be discussed below. Like TS5 and due to the high gas connectivity, an initial fast increase of the total stress is also observed at TS6 (located at the bottom of the cell), reaching a value of 7.8 MPa close to the gas injection pressure. The net swelling stress at the bottom boundary (TS6) reduced from 1.0 MPa to 0.1 MPa after the gas pressurisation.

TS3 (located at the upper stainless steel ring) and TS4 (at the middle ring) displayed approximately constant values with different magnitudes until 310 days (A to A1 in Figure 5-9b). TS3 started at 6.3 MPa and TS4 at 6.0 MPa. After 310 days, TS4 displayed a slightly higher increase rate that resulted in approximately the same value of 6.7 MPa as TS3 at 314 days (B in Figure 5-9b), when the gas pressure reached a value of 4.9 MPa (0.9 MPa over the water pressure at the boundaries). After this point B, TS4 and TS3 increase in pressure at the same rate and magnitude towards point B1, and from there on, the rate increases sharply to coincide with TS5. The total stresses of TS4 and TS3 increase up to 8.2 MPa at point C that is slightly higher than the maximum gas injection pressure (net swelling stress of 0.5 MPa). The consistency in the rate and magnitude of TS4 and TS6, particularly after point B1 coinciding with TS5, indicates that a gas pathway developed along (or very close to) the sample/wall interface. However, it is important to remark that this pathway was not clearly observed in the upper transparent ring. This pathway has been driven by the significant reduction of the net swelling stress (around 0.5 MPa).

The total stress sensors TS1 (located at the upper part of the cell) and TS2 (located at the top ring) presented a relatively constant value up to 310 days (A1) with different magnitudes, followed by a small increase up to point B1. Subsequently, an increasing rate response was observed on both sensors on passing point B1 (at this point the gas injection pressure reached a value of 4.9 MPa). In fact, the slope in the span B1 and C is very similar for sensors TS1 and TS2, as well as for sensors TS3 and TS4. TS1 started from 4.8 MPa (close to the injection gas pressure) at B1 and reached 6.3 MPa (lower than the injection gas pressure) at C. It appears that the upper saturated zone of the column develops as a plug, in which the gas injection pressure acts as a piston effect pushing the plug upwards and increasing the total stress TS1.

On the other hand, the upward piston effect induces the reduction of the net swelling stress recorded on TS6 (close to 0.1 at the maximum injection pressure). In a similar way, the upper plug is pushed by piston effect against sensor TS2, which increases the total stress just as the pathway near the interface of sensors TS3 and TS4 develops at point B1. TS2 started at 5.5 MPa at B1 (gas injection pressure 4.9 MPa) and reached 6.9 MPa at C (below the final gas injection pressure).

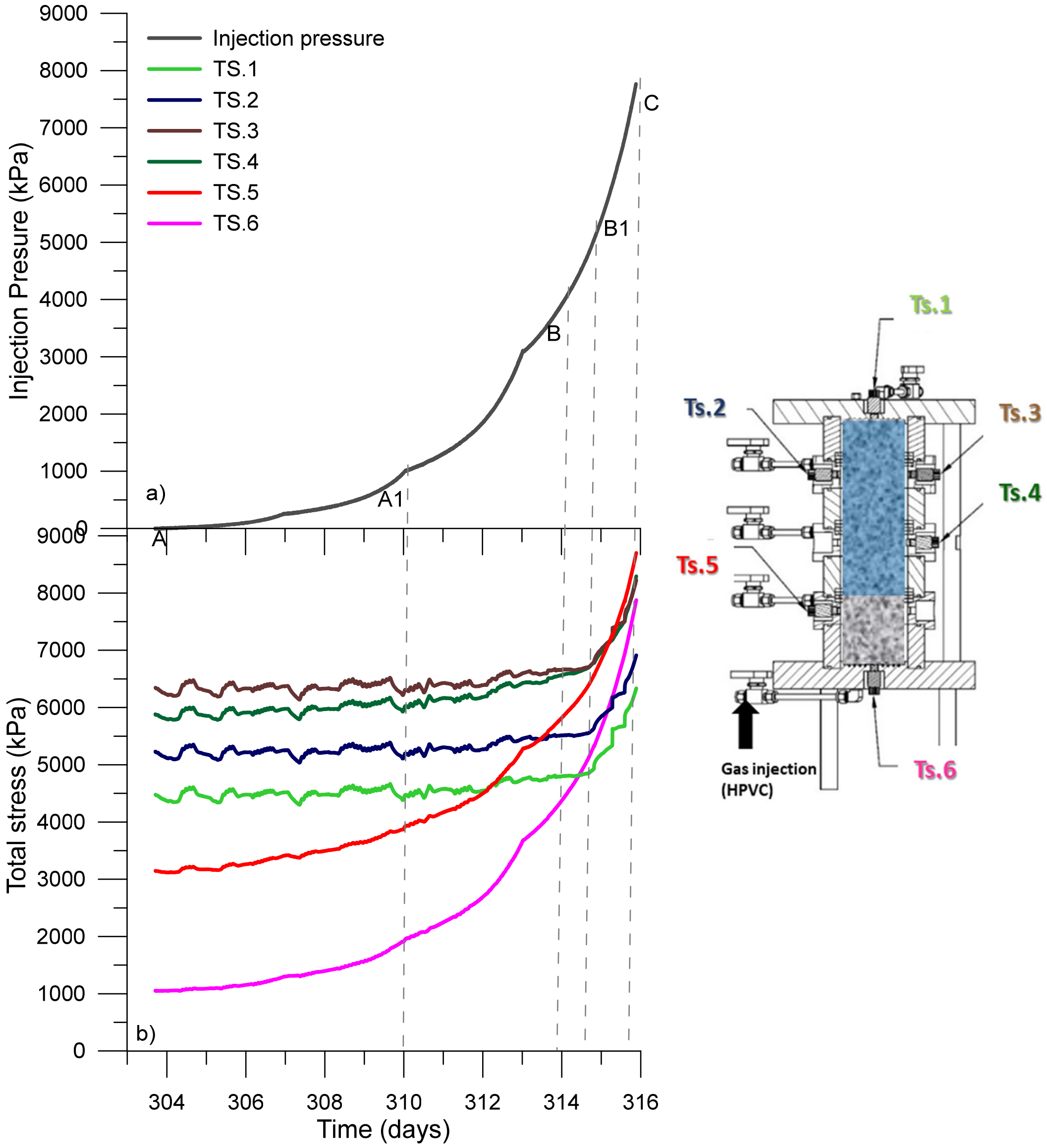

Figure 5-9. Injection pressure as a function of time compared with total stresses developed in the mock-up during the first gas test

Figure 5-10b summarises the time evolution of pore pressures recorded by sensors Pw1, Pw2 and Pw3 during the gas injection stage; also Figure 5-10a presents the gas injection pressure applied from the bottom part using HPVC. The sensor Pw3 (located at the bottom ring) increased the pressure (gas pressure) with a fast rate similar to the gas injection pressure because this zone is partially saturated with good internal connectivity of the gas pressure. It increases from a low water pressure of 0.08 MPa to 7.7 MPa, this last value equal to the gas injection pressure (7.7 MPa).

The water pressure sensors Pw1 (located at the upper ring) and Pw2 (located at the middle ring) display a similar increase rate until 314 days (A to B). Nevertheless, Pw2 presents an important change in the slope in comparison with Pw1 from points B1 to C. This pore pressure changed from 2.2 MPa at B1 to 3.5 MPa at C, while the gas injection pressure increased from 4.9 MPa at B1 to 7.7 MPa at C. These changes in the water pressure of Pw2 are associated with the pathway generated close to the sample/wall interface and detected by sensors TS3 and TS4. It is important to highlight that the pore pressure at Pw2 was always lower than the gas injection pressure and the values recorded by TS3 and TS4 since Pw2 sensor protruded a few millimetres into the sample and the pressure increase was delayed.

Sensor Pw1 kept a constant value around 3.5 MPa from A to B (Figure 5-10b), and slowly increased from 3.6 MPa at B (gas injection pressure at 4.5 MPa) to 4.1 MPa at C (gas injection pressure 7.7 MPa). It is evident that no gas pathway is generated along or close to the wall/sample interface in this zone of the cell. The small pressure increase can be associated with the rapid (undrained) total stress increase of TS2 originated when pushing the upper plug by piston effect (when a pathway near the interface of sensors TS3 and TS4 develops at point B1).

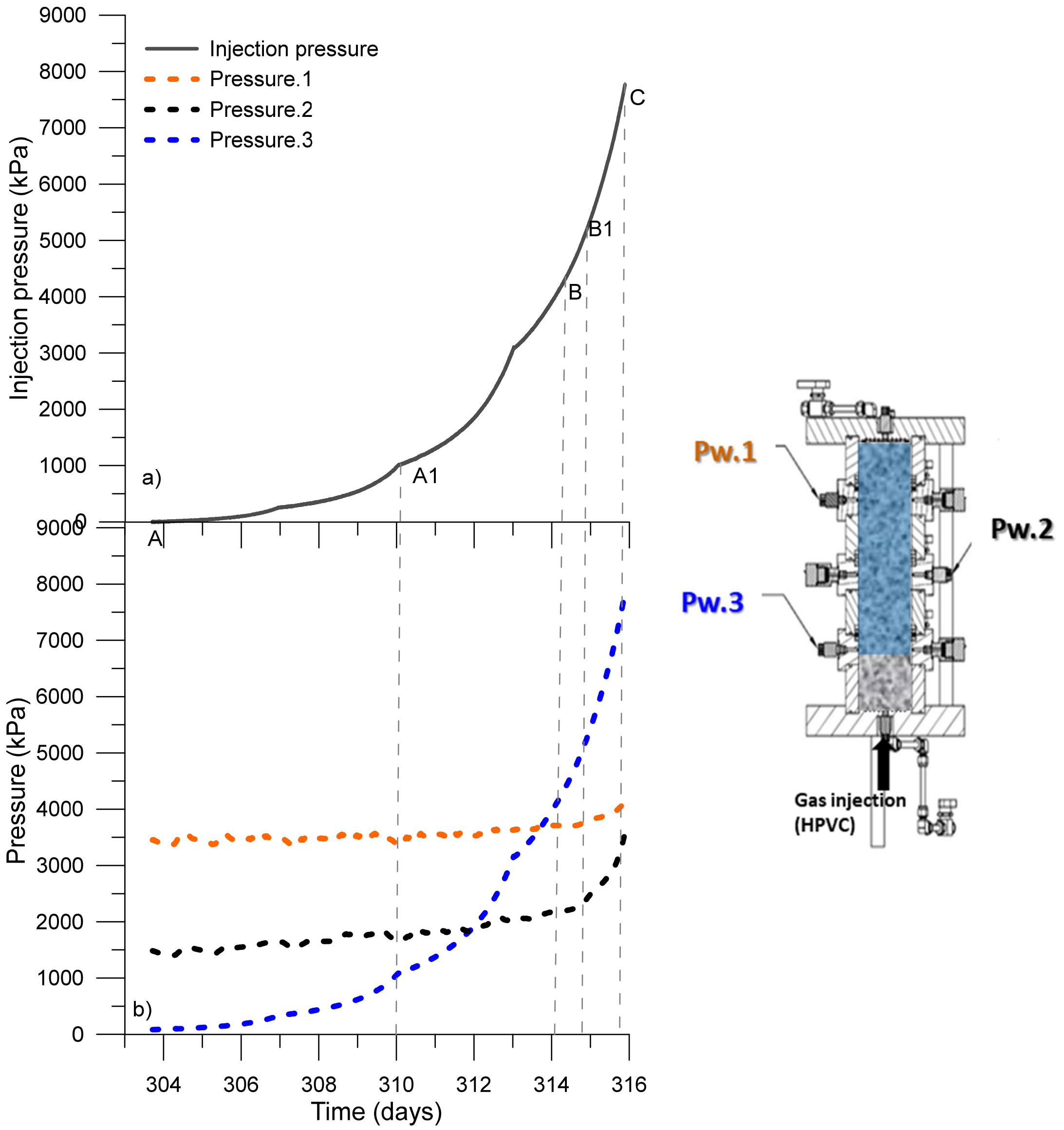

Figure 5-10. Injection pressure as a function of time compared with pressure (gas and water) in the first gas test

Figure 5-11 shows the time evolutions of outflow volumes (outflow from the sample is positive) during the first gas test. The PVC4 was closed before the gas test to avoid a gas shortcut since the sample was partially saturated in this zone.

In the first part, from point A to A2 (Figure 5-11b), the sensors PVC2 (connected to the upper ring) and PVC1 (connected to the top boundary) showed opposite volume change trends. This fact suggests that there has been some transfer of water between these controllers (water entering the sample at PVC2 and outgoing at PVC1). Nevertheless, from point A2 on (at a gas injection pressure of 3.1 MPa), PVC1 at the top displayed a change in the outflow rate that coincided with the change in the trend detected in PVC2, although in the latter pressure/volume controller, the increase of outflow volume with time is slower. This outflow volume from the sample is expected to be driven mainly by the water pressure increase originated due to total stress increase originated when pushing the upper plug by piston effect, rather than due to any gas outlet.

Gas diffusion through water is a slow phenomenon and difficult to be detected within the elapsed time, and if a preferential advective gas pathway had occurred, the volume increase would have been larger. Regarding PVC3, the controller detects some inflow on the early stage (before A2) that follows the same inflow rate as in the previous stage before the gas injection stage as observed in Figure 4-20. Only after A2 (Figure 5-11b), some tendency to slow down and slightly revert the flow (towards outflow) is detected. Again, as stated before, this slight outflow trend is expected to be originated mainly by the water pressure increase on gas pressurisation (to maintain the imposed pressure, the PVCs have to draw water out of the sample), rather than due to any gas pathway outflow.

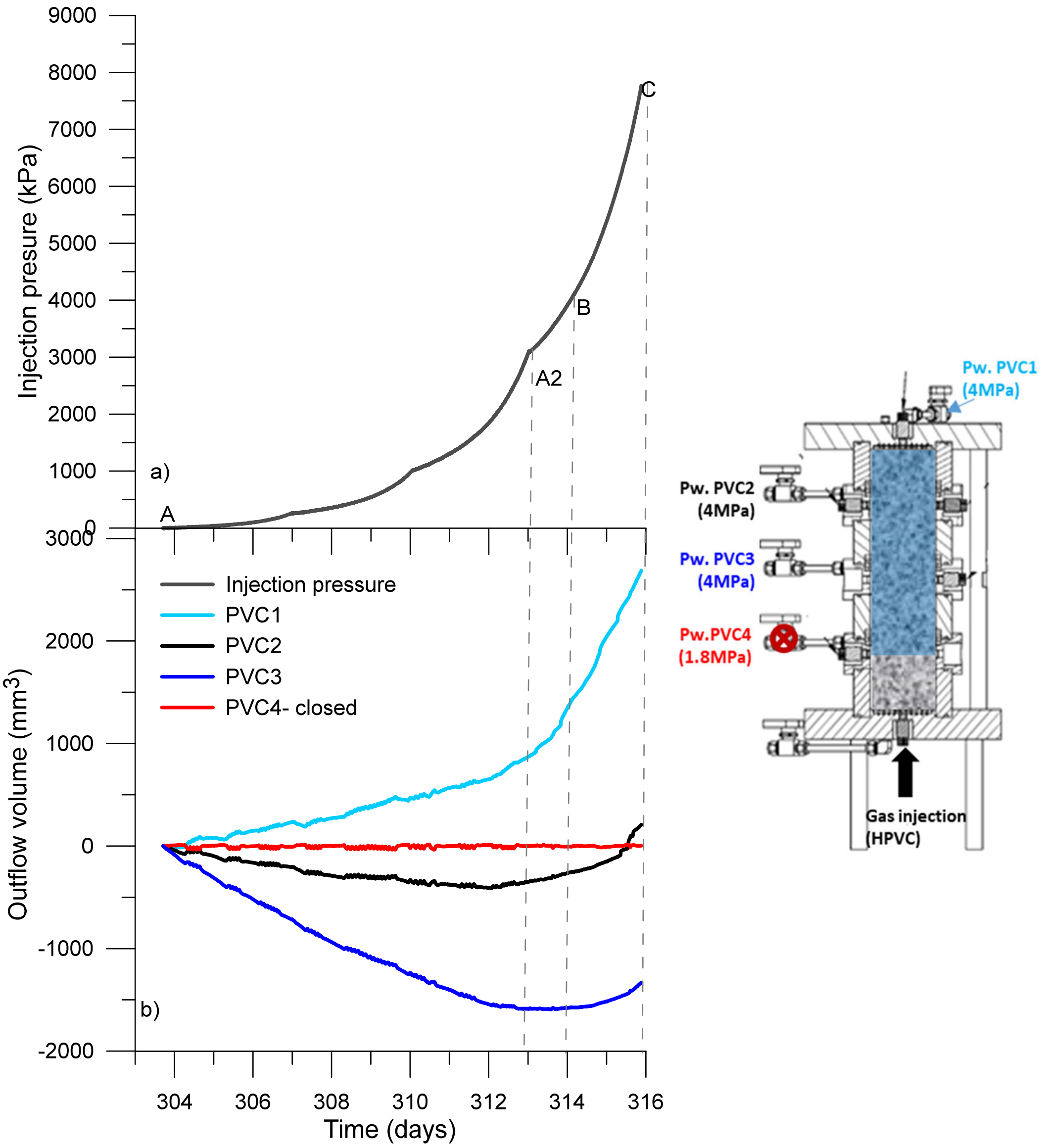

Figure 5-11. Outflow volume during the first gas injection compared with the injection pressure (outflow from the sample is positive).

Although the total pressure transducers TS3 and TS4 revealed the formation of gas pathways (close to the wall/sample interface), these pathways were not clearly observed through the Perspex wall. However, in the central Perspex ring of the column (second from bottom), the interface between a partially saturated / highly gas-connected zone and a saturated zone acting as a plug is clearly observed in Figure 5-12. This transition is not observed at the initial state before the gas test (Figure 5-12a), which indicates that the saturated plug has been compressed (consolidated) during the gas injection (piston effect). Incipient pathways are also detected at the bottom of the plug (Figure 5-12b), which could explain the development of the preferential pathways at the wall/sample interface.

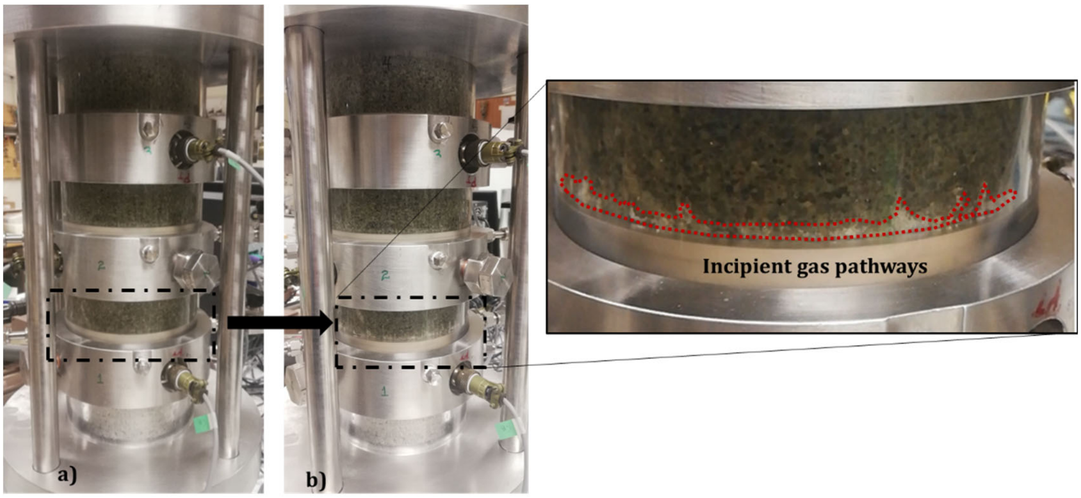

Figure.5-12a Pictures before the first gas injection test. b) Interface between partially saturated zone and saturated plug and incipient gas pathways during the first gas test.

Figure 5-13 displays the time evolution of the total suction at different elevations of the column (bottom, mid-height and top) and along the hydration stage and first gas injection test. As observed, during the gas injection process the bottom RH undergoes an increase in total suction (decrease in RH), which was not detected in the sensors close to the saturated zone. This decrease in RH has been observed and interpreted by Delage *et al*. (2008) when using a forced convection system (gas pressure gradients) to transport vapour (the higher the gas pressure the drier the sample).

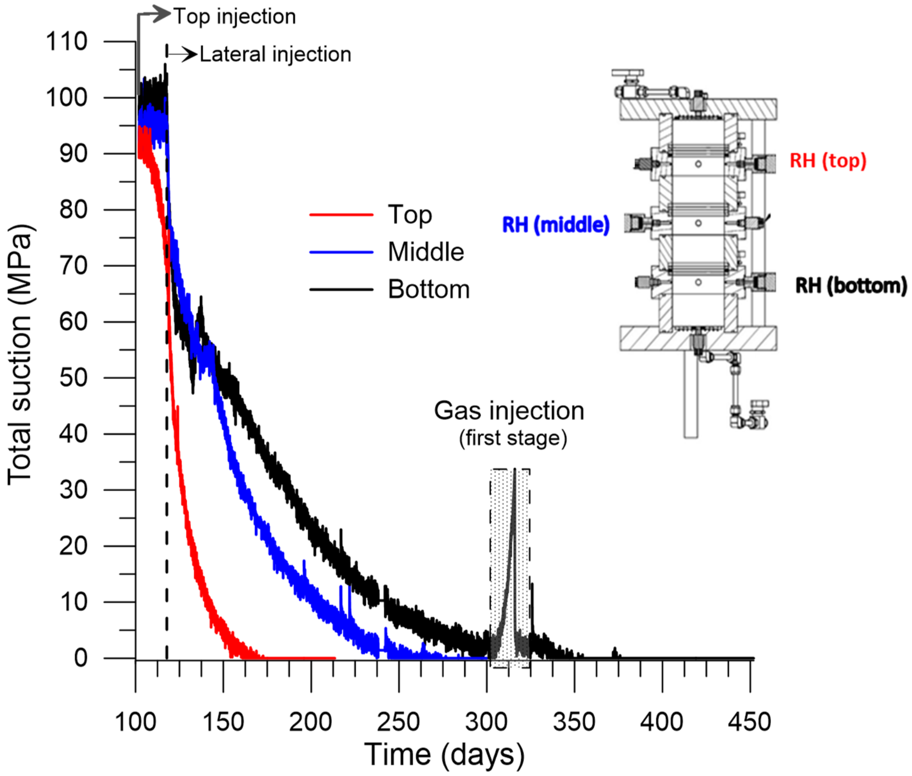

Figure 5-13. Evolution of total suction measured at different heights of the column.

5.5. Results of hydration after the first gas injection

Before the second gas injection test, a reduction in the imposed water pressure at the boundaries by the 4 PVCs has been applied in a stepwise way. The idea is to mimic the water pressures at in situ conditions of the VSEAL test (maximum pressures around 1 MPa). After the first gas injection, the imposed water pressure was kept at 4 MPa for 97 days before the first reduction. In the first step, the imposed water pressure was reduced to 2 MPa and maintained constant for 80 days. It was then decreased to 1 MPa and remained constant for 43 days (a total of 536 days) until the second gas test (Figure 5-14). After the first gas injection, hydration of the sample has been ongoing for 220 days.

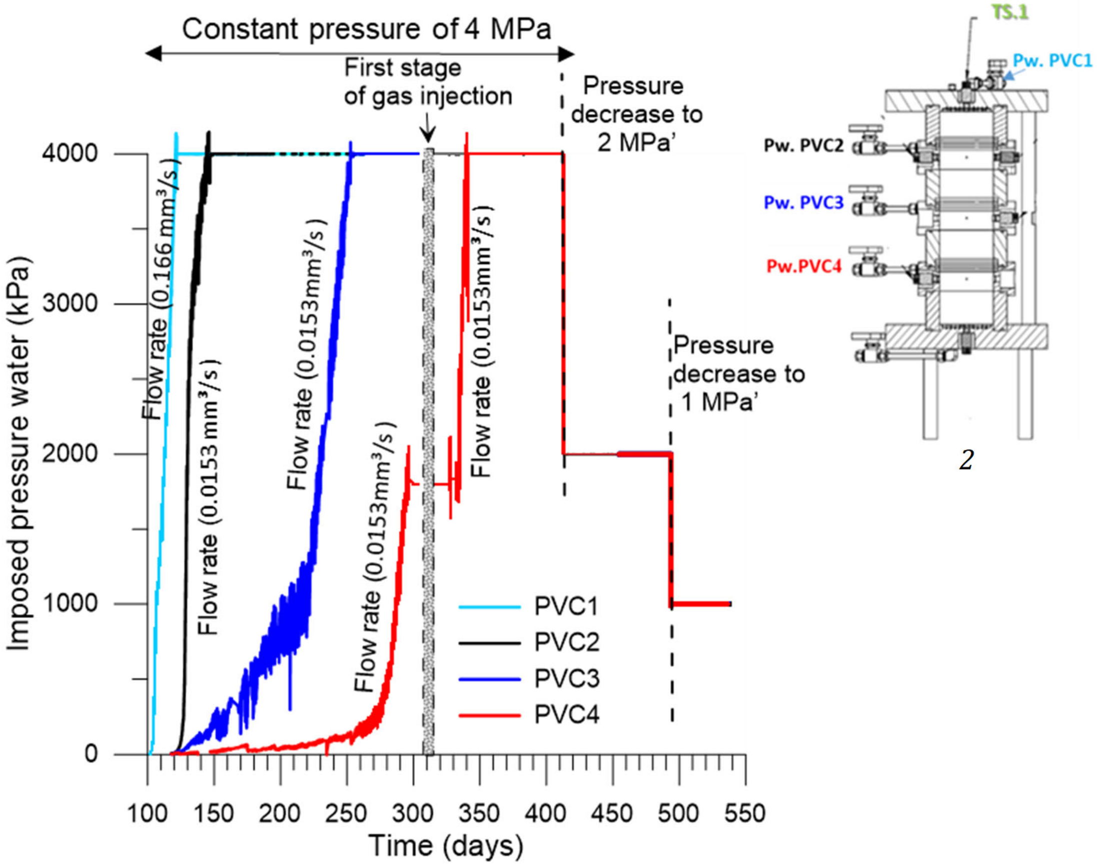

Figure 5-14. Imposed water pressure at axial and lateral boundaries applied with the PVCs.

The evolutions of the pore pressures measured at three positions at the boundaries of the sample are shown in Figure 5-15. Sensor Pw1 at the top ring reached 3.8 MPa after 350 days. A slightly lower value is registered for sensor Pw2 located at the middle ring, where the water pressure reached 3.4 MPa after 400 days.

Nevertheless, Pw3 located at the bottom ring registered any significant changes suggesting a malfunction of this sensor.

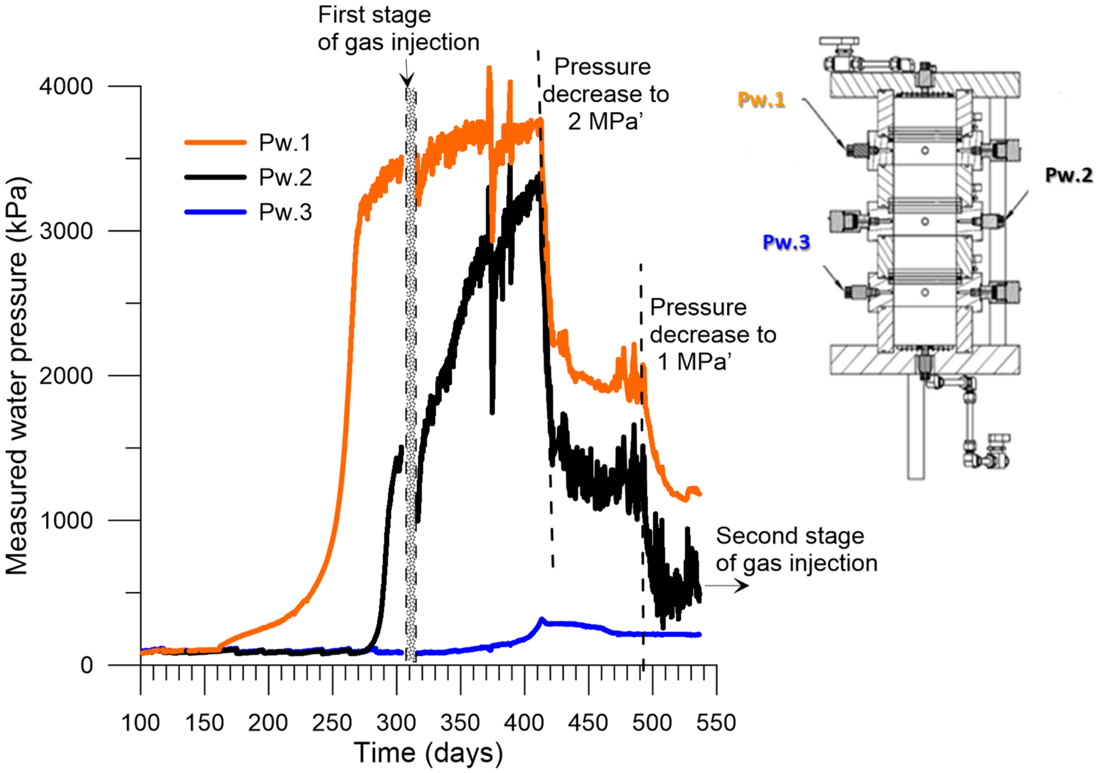

Figure 5-15. Water pressure (measured) evolution in the mock-up test.

However, a higher dry density and consequently a lower intrinsic permeability is expected at the bottom of the sample, due to swelling on hydration of the upper part. Likewise, the low degree of saturation with low relative permeability to water also contributes to the low permeability conditions in this bottom zone, which explains the delay in the saturation. The entrapment of gas in this zone is also affecting the saturation.

Figure 5-16 presents the time evolution of total stresses at different sensor locations after the first gas injection stage. Sensor TS1 after the first gas injection displayed total stress of 4.6 MPa and remained constant till 412 days, and reduced to 2.5 MPa and 1.6 MPa during the subsequent water pressure steps. An axial swelling (effective) stress of 0.6 MPa is detected at the top cap, which is relatively low due to the reduced dry density of the saturated (and expanded) material. This axial swelling (effective) stress displays the same magnitude as the value before the water pressure reduction at the boundaries. Nevertheless, this low swelling (effective) stress will affect the response of the material during the second gas injection test, as will be discussed later.

TS2 and TS3 at the top ring displayed a similar response to TS1, but with different values. After the first gas test, TS2 and TS3 presented values of 5.3 MPa and 6.3 MPa, respectively, and then remained constant till 412 days. Afterwards, a fast decrease was observed during water pressure reduction to 2 MPa, reaching values of 3.2 MPa and 3.8 MPa for TS2 and TS3, respectively. At 493 days, the applied water pressure was again decreased to 1 MPa, implying a reduction of total stresses to values of 2.4 MPa and 2.8 MPa for these sensors. Considering a boundary water pressure of 1 MPa, the radial swelling stresses were 1.4 MPa to 1.8 MPa on the top part (these values were also close to the radial swelling stresses in the range between 1.3 MPa and 2.3 MPa before the pore water reduction at the boundaries).

The TS4 sensor located at the middle ring reached a high value of 6.7MPa before the first water pressure decrease. TS4 decreased to 4.7 MPa at 492 days (after the first water pressure reduction). The total stress decreased again due to the change in water pressure to 1 MPa and stabilised to 3.9 MPa after 536 days. The radial swelling (effective) stress before the reduction of water pressure at the boundaries was 2.7 MPa, and after the two water pressure reduction steps, it stabilised to a slightly larger value of 2.9 MPa. TS5 reached a maximum value of around 5.9 MPa followed by a fast decrease to 4.7 MPa due to the reduction of the imposed water pressure to 2 MPa. At 493 days, the second change in the applied water pressure of 1 MPa induced the total stress to stabilise at 4.4 MPa. The radial swelling (effective) stress after water pressure reduction is relatively high, reaching a value of 3.4 MPa (this value is much higher than the radial swelling stress of 1.9 MPa measured before the reduction of the water pressures). TS6 at the bottom cap of the cell presented the same behaviour with a maximum value around 4.7 MPa. Nevertheless, at 412 days and despite the first water pressure reduction step, TS6 presented an opposite response and it slightly increased to 4.8 MPa. At 493 days the applied water pressure was decreased to 1 MPa, and TS6 presented a slight reduction, reaching a value of 4.6 MPa. The axial bottom swelling stress reached a high value of 3.6 MPa after water pressure decrease.

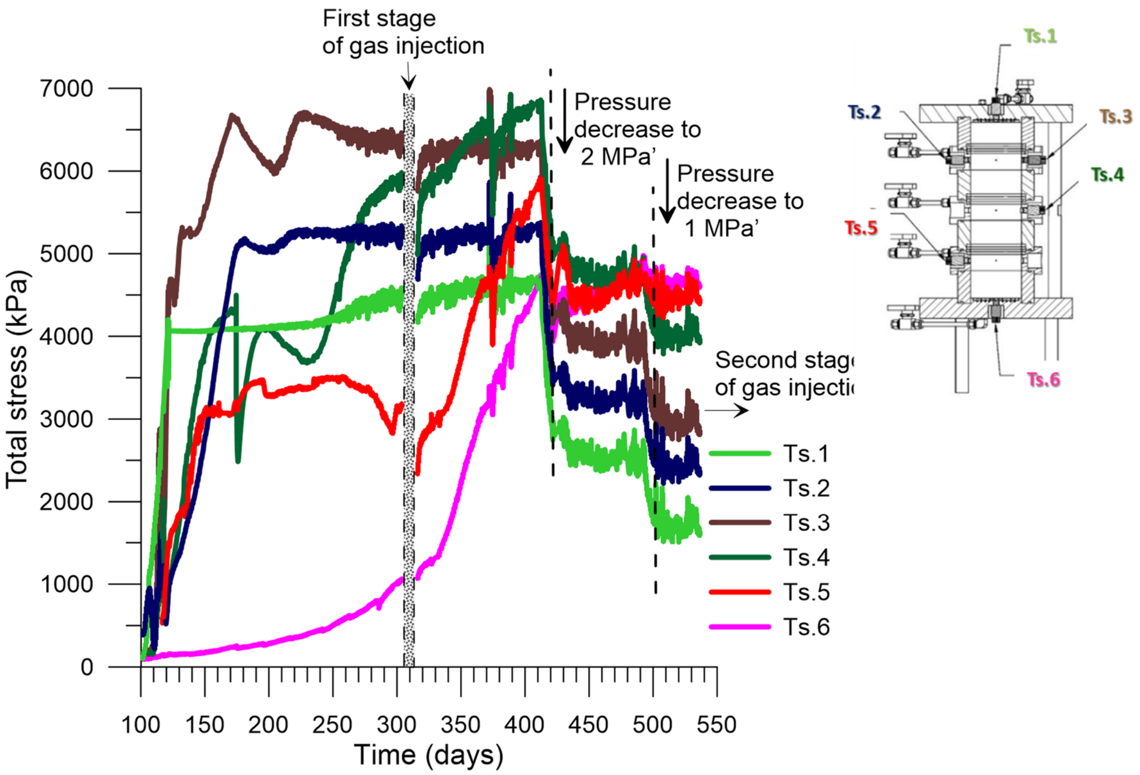

Figure 5-16. Evolution of total stresses in the mock-up test.

The bottom part of the sample presented the highest values of the effective stress (swelling stress). These high values are a consequence of the densification undergone by the material at the bottom of the cell during the early stage of top and lateral hydrations. The observed differences in the effective stresses registered at different locations of the cell after the first gas test showed the important role played by the hydration front and the local dry density of the material. In addition, anisotropy features can be discussed in terms of this dependence of the swelling pressure on the dry density, as well as on the initial heterogeneous distribution of the material.

The volume of injected water that was monitored with different PVCs (4 PVCs) is presented versus time in Figure 5-17 until 536 days. The highest volume injected in the sample was from PVC1 with 3.36x10^5 mm^{3,} corresponding to 36.1% of the water of volume injected. The PVC2 injected the lowest water volume because the axial hydration front reached this zone and increased the water pressure to 4 MPa, and then the water flow slowed down, reaching 9.7x10^4 mm^3 that correspond to 10.3%. PVC 3 and PVC4 reach 24.5% and 29.1%, respectively. The total volume injected during the stage is 9.36x10^5 mm^3. As it can be observed, the rate of increase is still positive after 536 days of hydration (taking into account the volume of the 4 PVCs), suggesting that the sample is not entirely saturated.

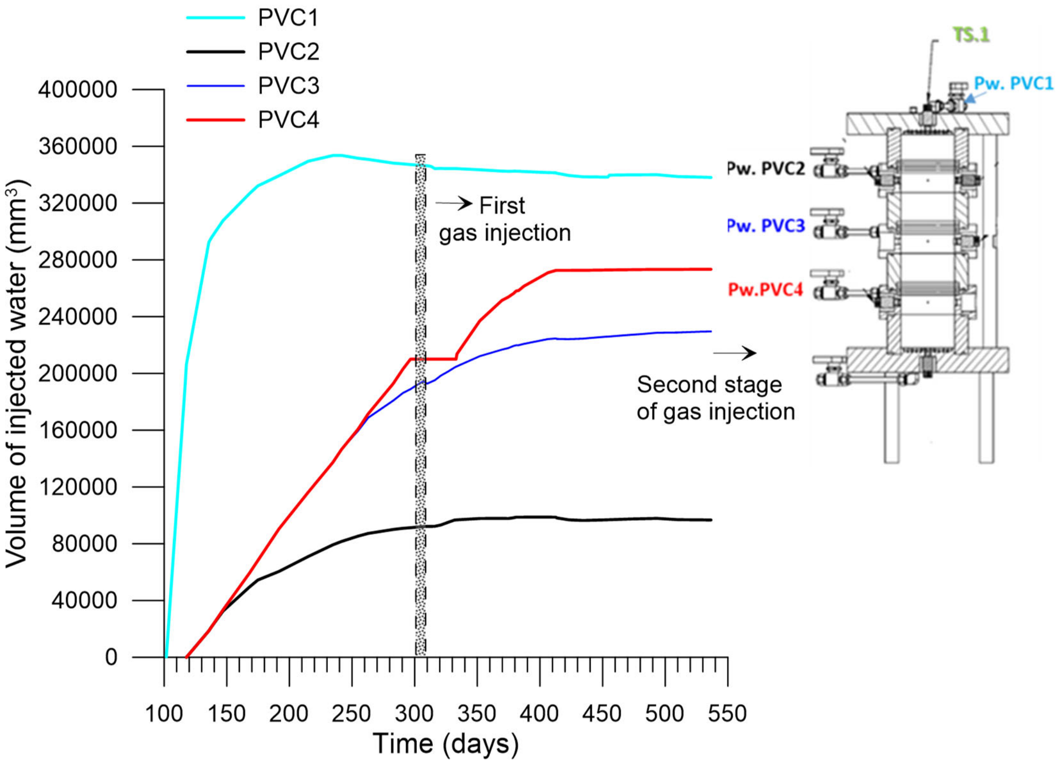

Figure 5-17. Evolution of the injected water volume over time.

As the hydration front progresses due to the top and lateral wetting, gas is displaced and trapped at the lower part of the sample. This gas is released on the removal of the relative humidity sensors (iButtom) to download the logged information. Even after 25 days of hydration, the first download of the information of the iButtom was carried out where some gas was released, and fine particles of dry bentonite were observed to migrate. The iButtom information has been downloaded 18 times during the hydration of the sample. Nevertheless, not all of the entrapped gas can easily be released, so that the accumulated gas at the bottom prevents the sample from being completely saturated. This phenomenon was observed in the mock-up, since the bottom part of the sample took a long time to complete saturation, indicating that there is entrapped gas that the pore pressure has not been able to dissolve. This behaviour is verified with the global degree of saturation around 97.4% (Figure 5-18) calculated with the injected water applied with the PVCs at the boundaries.

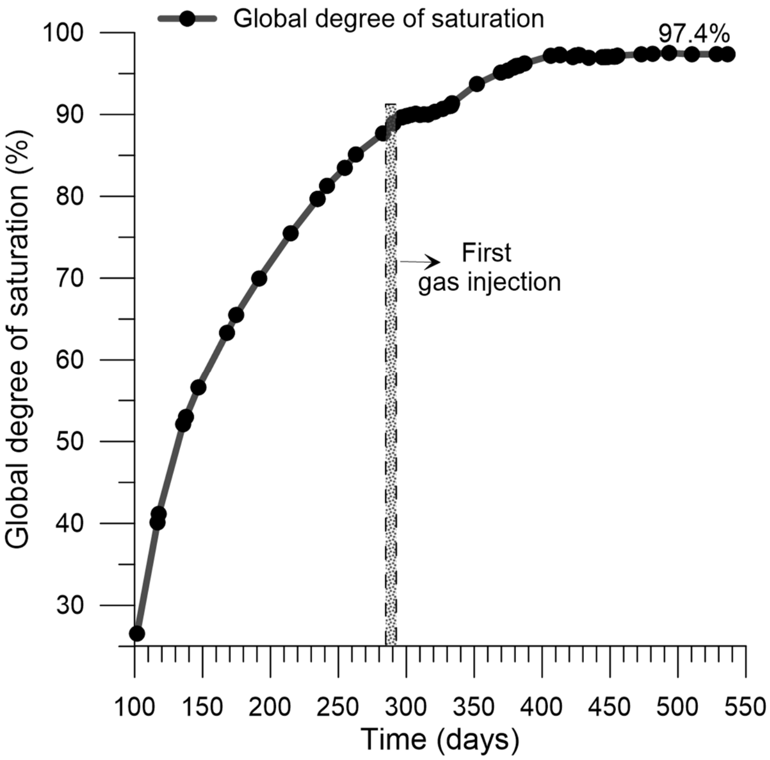

Figure 5-18. Evolution of global degree of saturation against time, Calculates in the water volume applied with the PVCs.

5.6. Second gas injection test in the mock-up

To mimic the hydraulic conditions of the in-situ VSEAL test (at an in-situ water pressure around 0.8 MPa), water pressures at the boundaries decreased from 4 MPa to 1 MPa. The second gas test in the mock-up was performed at a global degree of saturation of 97.4% after hydration for more than 500 days (536 days). In this case, the gas injection was carried out from the top boundary with a flow rate of 0.1 mL/min starting from 1.67 MPa to 5.3 MPa in the first stage using the HPVC. The bottom boundary (used during the first gas test) presented a Perspex ring with tightness problems. This problem was fixed, and the ring was reinforced. Nevertheless, it was preferred to inject the gas from the top boundary to avoid any problem due to the high gas pressures reached.

This second test aimed at verifying the occurrence of gas pathways at the interface between the wall and the sample at a smaller water pressure. In fact, these pathways generate at the interfaces where lower swelling (effective) stresses were developed. The second gas test started at 537 days at an initial gas pressure of 1.67 MPa, which is higher than the top vertical swelling (effective) stress Figure 5-19 on the left shows the initial state of the second gas test with the values of water pressures applied and the total stresses measured at the boundaries. The figure on the right summarises the different axial and radial swelling (effective) stresses (identified as Tfs.1 to Tfs.6). As observed, the lowest value develops in the upper part (Tfs.1 of 0.6 MPa), while in the bottom boundary, the swelling stress is higher due to the densification of the material (Tfs.6 at 3.6 MPa). Regarding the lateral swelling (effective) stresses, they increase with depth (upper part of the cell between 1.4 MPa and 1.9 MPa, and lower part at 3.4 MPa). As a consequence, when applying the initial pressure of 1.67 MPa, a pathway at the upper interface is expected to develop between the top of the sample and the cap. Nevertheless, at the beginning of this second gas test, the radial swelling (effective) stress withstands this high initial pressure (except for the upper lateral swelling stress 1.4 MPa at Tfs.2). In this test, PVC5 was added to the bottom valve and kept open to allow any potential outlet flow.

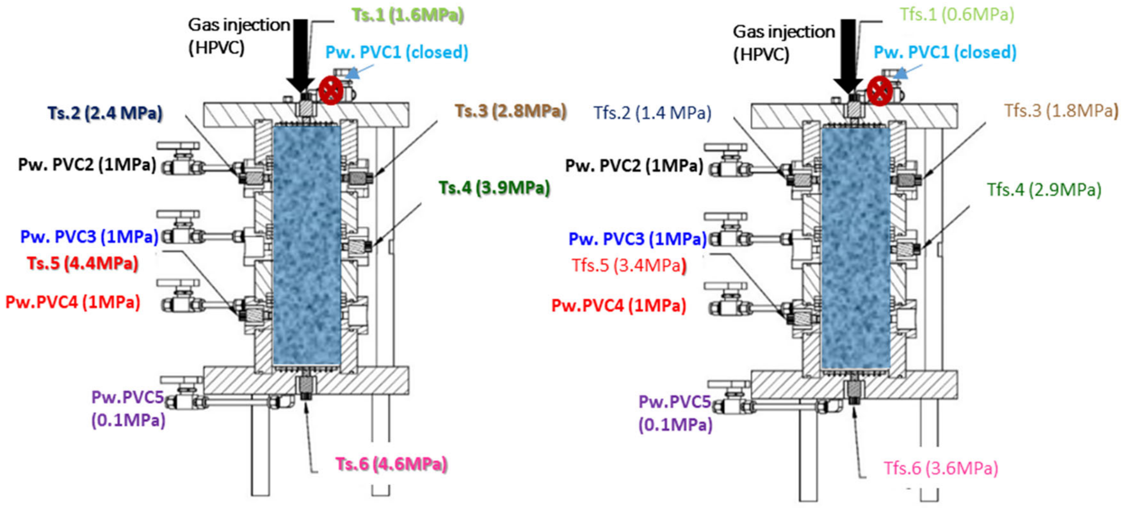

Figure 5-19. Initial state of the second gas injection test (on the left). Different axial and radial swelling (effective) stresses (Tfs.1 to Tfs.6 on the right).

5.6.1. Test protocols followed

The protocol followed in the second gas test is briefly described below and in Figure 5-20.

Stage 1. Pre-conditioning path: At almost 537 days, the sample was nearly saturated, with a global degree saturation of around 97.4% due to gas entrapment. The water pressure applied by PVCs was maintained constant at 1 MPa during the test except for PVC1 located at the top boundary that was kept closed to avoid by-pass (Figure 5-20a). The bottom valve was kept open and connected to PVC5 at a low gas pressure (0.1 MPa) to allow any potential outlet flow. The gas injection point at the top started at 1.67 MPa, slightly higher than the vertical total stress (1.6 MPa) using the HPVC.

Stage 2. First gas injection: The injection was carried out at a controlled volume rate of 0.1mL/min up to a gas pressure of 5.3 MPa with the HPVC. Afterwards, the injection pressure was kept constant (Figure 5-20b).

Stage 3. Closure of the upper ring outflow valve (PVC2): The gas injection pressure was kept constant at 5.3 MPa. The valve connected to PVC2 was kept closed to avoid fluid by-pass during the subsequent gas pressure increase ramp (Figure 5-20 c).

Stage 4. Second ramp of gas injection: A pressure ramp was used in this stage at a rate of 0.9 kPa/min, from 5.3 MPa to 6 MPa (Figure 5-20d). Afterwards, the injection pressure was kept constant at 6 MPa until an abrupt passage of gas (breakthrough) was detected.

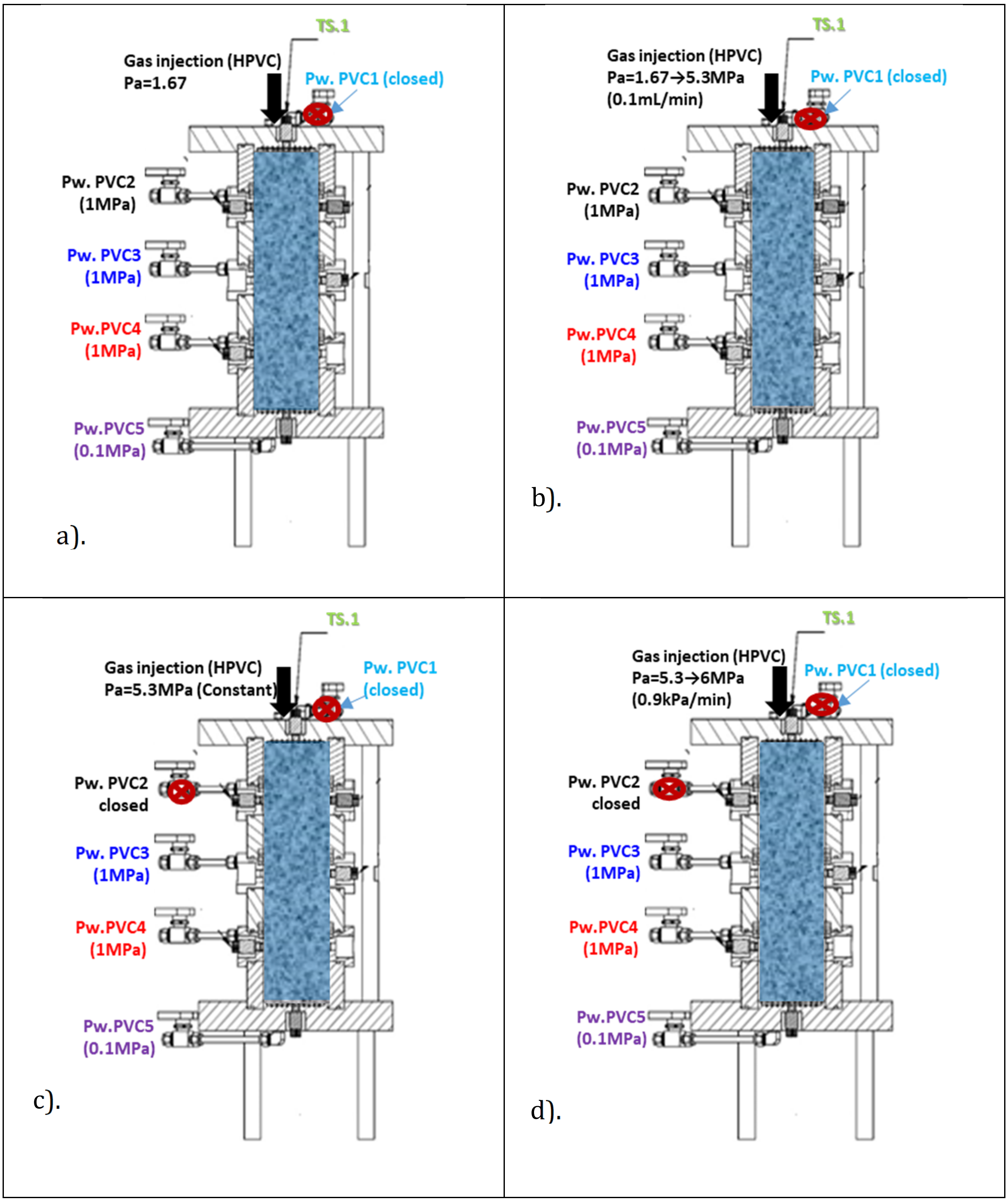

Figure 5-20. Schematic representation of protocols for gas injection in the mock-up test. 1: Pre-conditioning path. 2: First gas injection. 3: Closure of the upper ring outflow valve. 4: Second gas injection stage.

5.6.2. Results of the second gas injection test

The results are better discussed by grouping them into two phases. The initial one included the pre-conditioning and first gas injection stages (Stages 1 and 2). The final phase included the closure of the upper ring outflow valve before the second gas injection stage (Stages 3 and 4).

Initial phase (stages 1 and 2)

During the gas pressurisation and constant pressure phase, some incipient gas pathways (Figure 5-21b) and gas entrapment (not connected bubbles in the figure) were observed between the upper Perspex ring and the sample. These incipient pathways were the origin of the breakthroughs observed in the constant pressure stage described below. The top of the sample has turned into a gel-like material with a swelling pressure of 0.60 MPa (before the second gas test) and close to the swelling pressure of the powder (0.65 MPa, **chapter 3, section 3.6.3).** According to modelling results (**chapter 6**), this gel-like material's total porosity in this zone is around 0.62, corresponding to a very soft material with a dry density of 1.04 Mg/m^3.

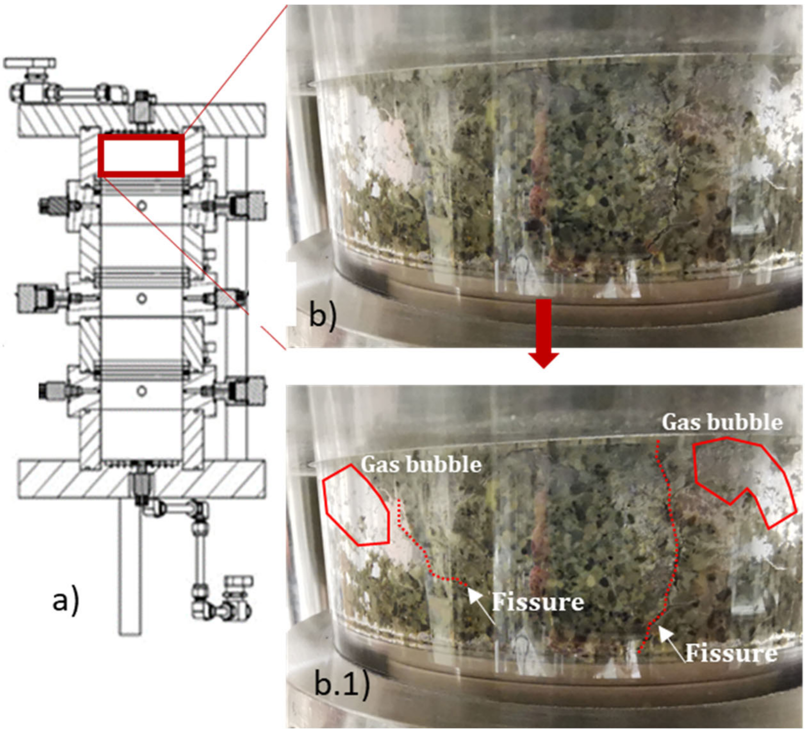

Figure 5-21a). Schematic view of the mock-up test and b) interface problem during the second gas test in an initial phase (stages 1 and 2).

The second gas test started at an initial gas pressure of 1.67 MPa and was increased until 5.3 MPa with a controlled volume rate of 0.1mL/min. It reached 5.3 MPa at 539 days and then kept constant (Figure 5-22a). The first breakthrough was detected at 548 days, and outflow was observed on the PVC2 of the upper ring. When the volume of the PVC2 was filled (capacity of 200 mL), the gas injection pressure increased again to 5.3 MPa. The second breakthrough (outflow at PVC2) took place at 551 days, and injection pressure decreased to 4.9 MPa. The system recovered the gas injection pressure of 5.3 MPa once the recovery volume of the PVC2 was filled by mainly gas Figure 5-22.

The total stresses increased towards different magnitudes during the gas injection test (Figure 5-22b). For the top sensor TS1, the total stress increased from 1.5 MPa to 5.3 MPa following the gas injection pressure since a gap generated between the gel-type material and the top cap. The gas pressure acted as total stress (piston effect) that pushed the sample against the bottom total stress transducer TS6, which increased from 4.6 MPa to 5.1 MPa. TS2 and TS3 at the upper metallic ring also increased towards 5.2 MPa and 6.3 MPa, respectively. As TS2 sensor reached a value close to the maximum gas pressure, it was considered that a pathway was generated through the interface between the sample and the sensor, which is consistent with the breakthrough and the outflow detected by PVC2. In fact, the zone close to PVC2 displayed the lowest initial total lateral stress of 2.4 MPa (i.e. 1.4 MPa of lateral effective stress), which renders this zone prone to pathway development throughout the interface. Total stress at TS3 increased on gas pressurisation due to piston effect of the upper zone that is pushed against the sensor due to pathway opening at the opposite side (pathway close to TS2).

TS4 and TS5 presented similar increasing rates but different magnitudes. TS4 reached a value of around 5.7 MPa higher than TS5, which increased to 5.1 MPa. TS4 was also higher than the maximum gas pressure, which indicated that no gas pathway developed through this interface (also consistent with TS3). The gas pressure drop during the two breakthrough processes affected the response of the different total stress sensors, which displayed an equivalent decrease/increase response (Figure 5-22b).

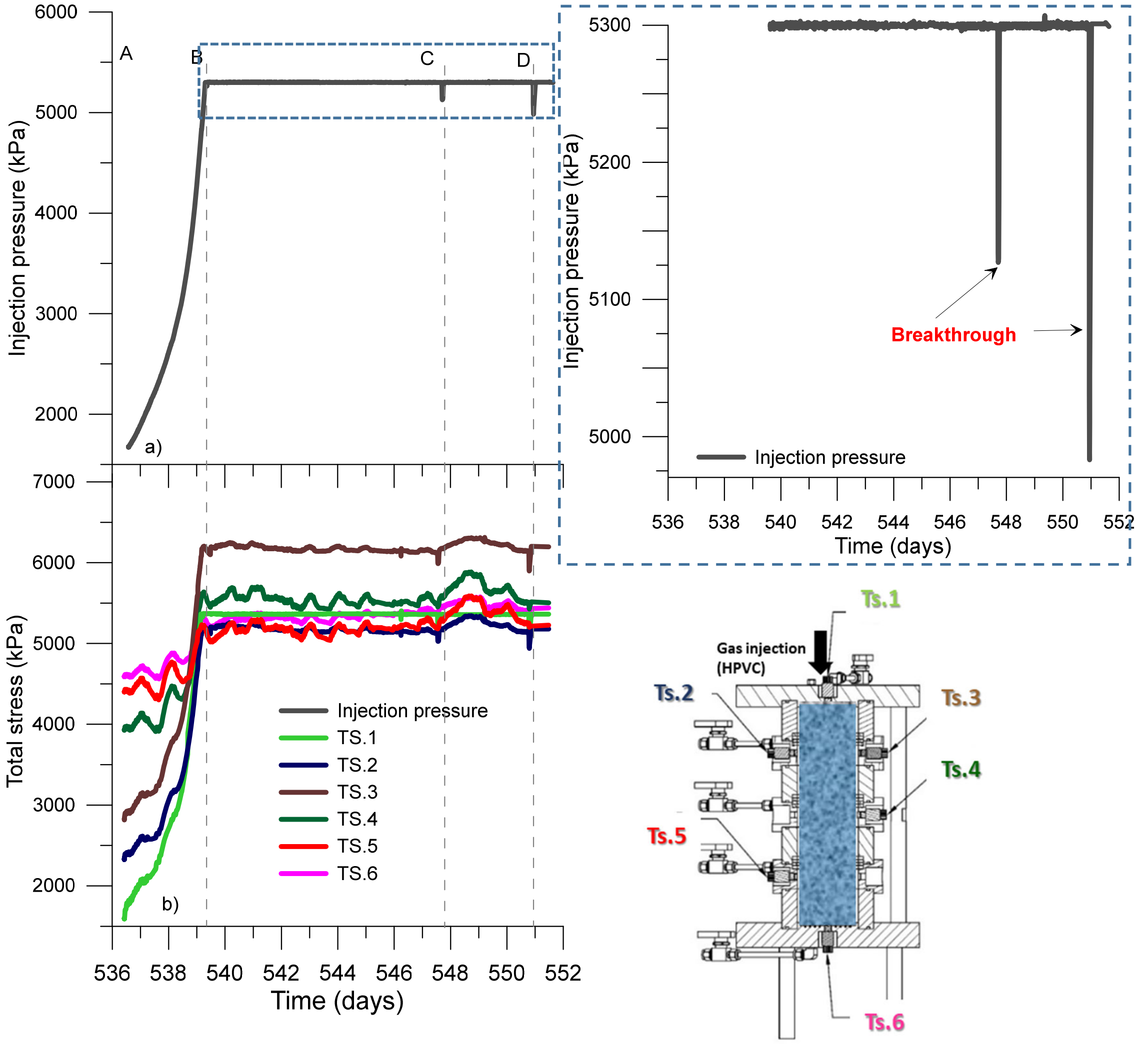

Figure 5-22a). Evolution of gas injection pressure for the second gas test using the HPVC (initial phase) and b) evolution of total stress measured by sensors during the injection pressure.

Evolution of the injection pressure (initial stage) and behaviour of pore pressure transducers Figure 5-23. Pore pressure sensors Pw1 and Pw2 displayed a quite similar increasing rate during the gas test, as observed in Figure 5-23b. Pw1 at the upper ring reached a value of 3.5 MPa, whereas Pw2 located at the middle ring stabilised at 2.1 MPa. There was no direct interaction of these sensors with the injected gas pressure through a pathway, which is consistent with the total stress results (TS4 and TS5). Pw3 displayed a constant response during the gas injection (probably the porous filter may be clogged, affecting pore pressure measurement). The Pw1 and Pw2 sensor responses were not significantly affected by the fast drop and recovery of the gas injection pressure, which confirms that there was no direct contact of the gas pressure with these sensors. Nevertheless, after the first breakthrough and gas pressure recovery (C to D), there was a slight increase in the pore water pressures of Pw1 and Pw2 (associated with the delayed response on gas pressurisation), followed by a reduced decay towards the values before the breakthrough.

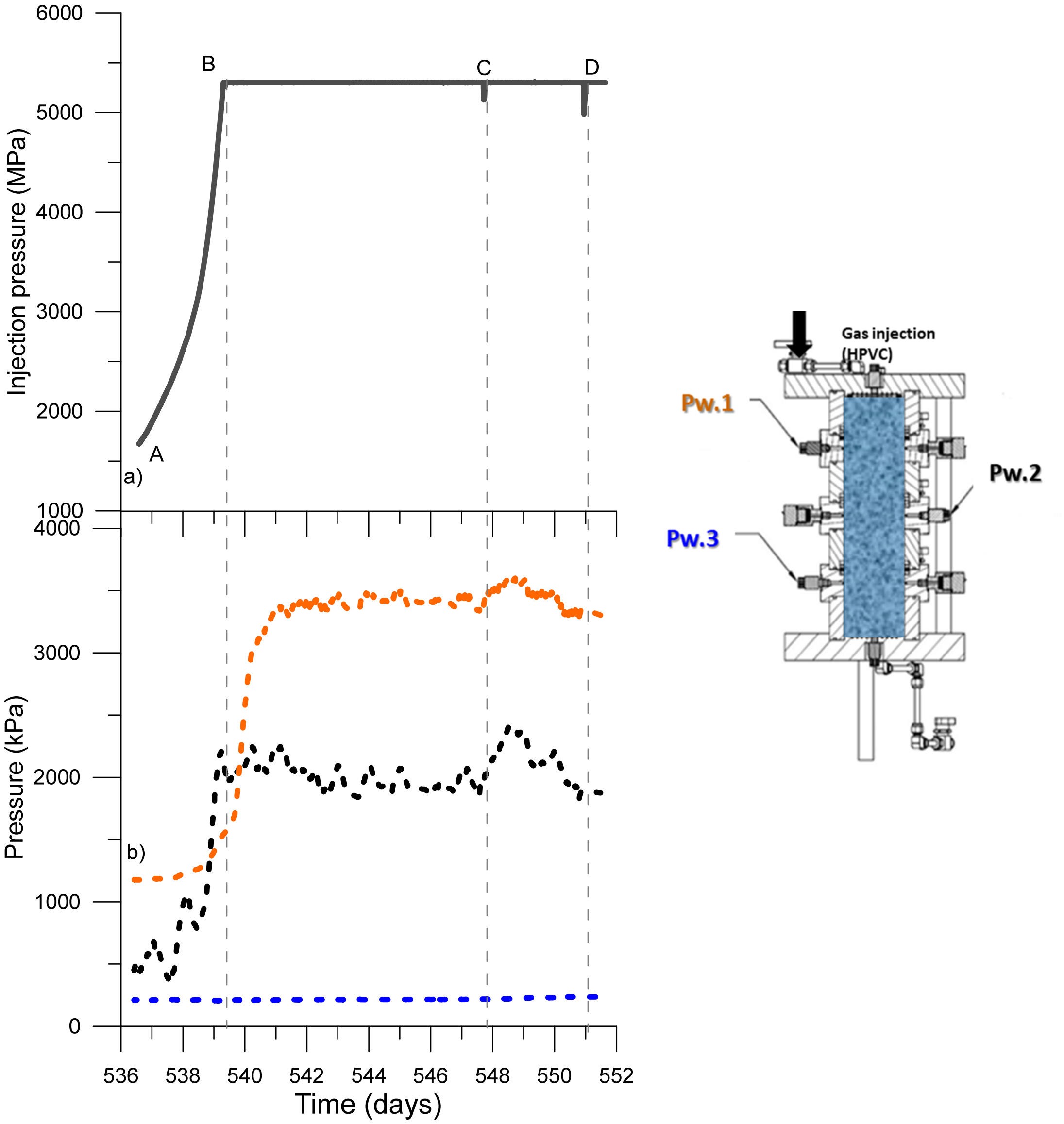

Figure 5-23a). Evolution of the injection pressure (initial stage) and b) behaviour of pore (gas/water) pressure transducers.

Figure 5-24 shows evolutions of injection pressure, the inflow volume for the second gas injection (first stage) and evolutions of outflow volumes. Once the constant gas pressure of 5.3 MPa was reached (measured with the HPVC) (Figure 5-24a), there was some inflow (Figure 5-24b) (inflow from the sample is positive) and outflow volumes of gas recorded (B to C). Figure 5-24c summarises the evolutions of inflow volume measured by the HPVC and outflow volumes measured by the PVCs (outflow from the sample is positive). PVC3 at the mid-height ring also recorded some incipient outflow starting from B. At approximately 546 days, the outflow rate increased at PVC2. Another significant increase in the outflow rate of PVC2 occurred at 548 days. A higher rate was also detected in the inflow rate from 546 days onwards, which indicated a clear breakthrough through the interface (as previously discussed)(Figure 5-24c). At point C (548 days), both inflow and outflow rates increased, inducing a gas pressure drop (the system was not able to keep the constant gas injection pressure). This increased rate in the outflow volume induced the filling of PVC2 (the pressure/volume controller was not able to keep the constant pressure at 1 MPa). This situation caused the inflow gas pressure to recover (after the loss of pressure controllability). During some time (up to 550 days) there was no outflow volume recorded in PVC2 since it was filled entirely (inducing the boundary pressure at PVC2 to increase). Nevertheless, PVC3 continued detecting outflow, as shown in Figure 5-24c, in agreement with the increase in inflow gas volume measured between C and D. Immediately after repositioning the PVC2 cylinder to allow collecting additional gas volume, a new gas outflow in PVC2 was recorded. This outflow developed initially at a slow rate, but then abruptly increased after 551 days (refer to the encircled zone in Figure 5-24c). The gas injection pressure lost its controllability again due to the breakthrough and dropped to 4.9 MPa (Figure 5-24a). Moreover, PVC4 continued injecting water in the sample at a very slow rate and no outflow volume was recorded in PVC5 (Figure 5-24c).

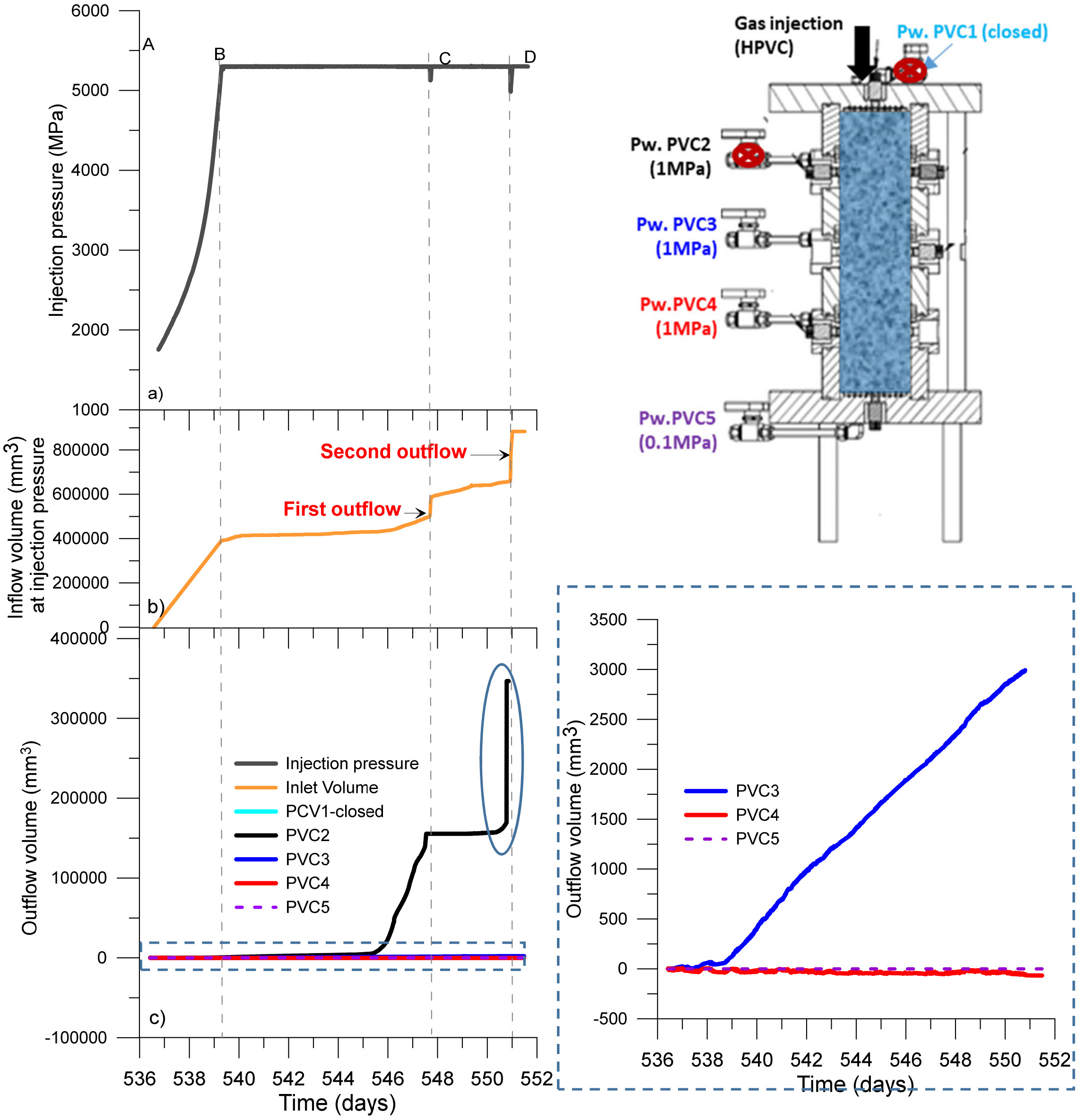

Figure 5-24.a) Evolutions of injection pressure from HPVC, b) inflow volume of gas for the second gas injection (first stage) (inflow from the sample is positive)and evolutions of outflow volumes (water/gas) (outflow from the sample is positive).

Final phase (stages 3 and 4)

Despite having already detected gas breakthrough processes during the initial phase (significant outflow at PVC2 and some outflow volume at PVC3), it was decided to continue with a second gas pressure ramp. The test focused on closing the PVC2 valve and checking if the gas pathway was directed to the PVC3 outlet, which was partially activated with an incipient outflow during the initial phase. So, PVC3 and PVC4 were kept open at a water pressure of 1 MPa and the gas injection pressure was maintained constant at 5.3 MPa for 26 days (578 days). After this initial equalisation phase, in which outflow (water/gas) took place at PVC3, the gas injection pressure was increased to 6 MPa at a fast rate of 0.9 kPa/min.

Figure 5-25a shows the evolution of injection pressure using the HPVC. The total stress results from the sensors of the final phase are presents in Figure 5-25b. For sensor TS1 at the top boundary, the total stress increased from 5.3 MPa to 6 MPa, which exactly corresponds to the applied gas pressure (gap generated between the gel-type material and the top cap). The piston effect induced the increase of TS6 (at the bottom) to 6.7 MPa. TS2 and TS3 at the upper metallic ring increased to 5.8 MPa and 7.1 MPa, respectively. As observed through the Perspex wall (Figure 5-28), the gas pressure detached the material from the top and lateral part of the first Perspex ring (pathway near TS2). This observation is consistent with the value reached by TS2, which is close to the maximum gas pressure. Furthermore, the TS2 sensor underwent a sharp increase in total stress, which strictly follows the gas pressure. This fact confirmed the development of a gas pathway at the sensor interface (Figure 5-25b). Total stress at TS3 is affected by the piston effect of the upper saturated zone that is pushed against this sensor. This sensor also follows an increase in total stresses in correspondence with the rise in gas pressure by detecting a rapid jump in total stresses that is just the same magnitude as the increase in gas pressure. Sensors TS4 and TS5 reached values of 6.4 MPa and 6.2 MPa, respectively, which are higher than the maximum gas pressure. This fact indicated that no interfacial pathways affected these sensors. These sensors registered a more gradual increase in total stresses (although at the end of the phase, there is a slight decrease). The sharp increase in gas pressure was also detected in these sensors, although the jump was less pronounced than the gas pressure jump. This progressive increase and the jump in total stresses are associated with the pore pressure increase as the gas pressure propagated.

A better insight into this pore pressure increase on fast gas pressurisation is shown in Figure 5-26b and the behaviour of the time evolutions of the gas injection pressure is presented in Figure 5-26a. The pore pressure transducers' response. Pw1 and Pw2 showed constant response from A to B with values of 3.5 MPa and 2.0 MPa, respectively. These values are consistent with the increased distance of Pw2 from the injection point. Nevertheless, Pw1 and Pw2 displayed an equivalent jump on the pore pressure (around 0.6 MPa) consistent with the rapid increase in gas pressure (change of 0.7 MPa). This gas pressure change acted as a total stress change on the upper saturated plug, inducing this immediate increase in the pore pressure. During B to C, the pore pressure Pw1 tended to dissipate progressively. On the contrary and during B to C, Pw2 still increased until day 620, displaying some small dissipation afterwards. Sensor Pw3, which was previously relatively constant (probably due to a clogging problem of the porous stone in contact with the measuring system), started to increase, reaching a value close to 1.3 MPa. Since it was placed in a zone with higher compressibility of the interstitial fluid, this sensor did not detect the jump during the rapid gas injection.

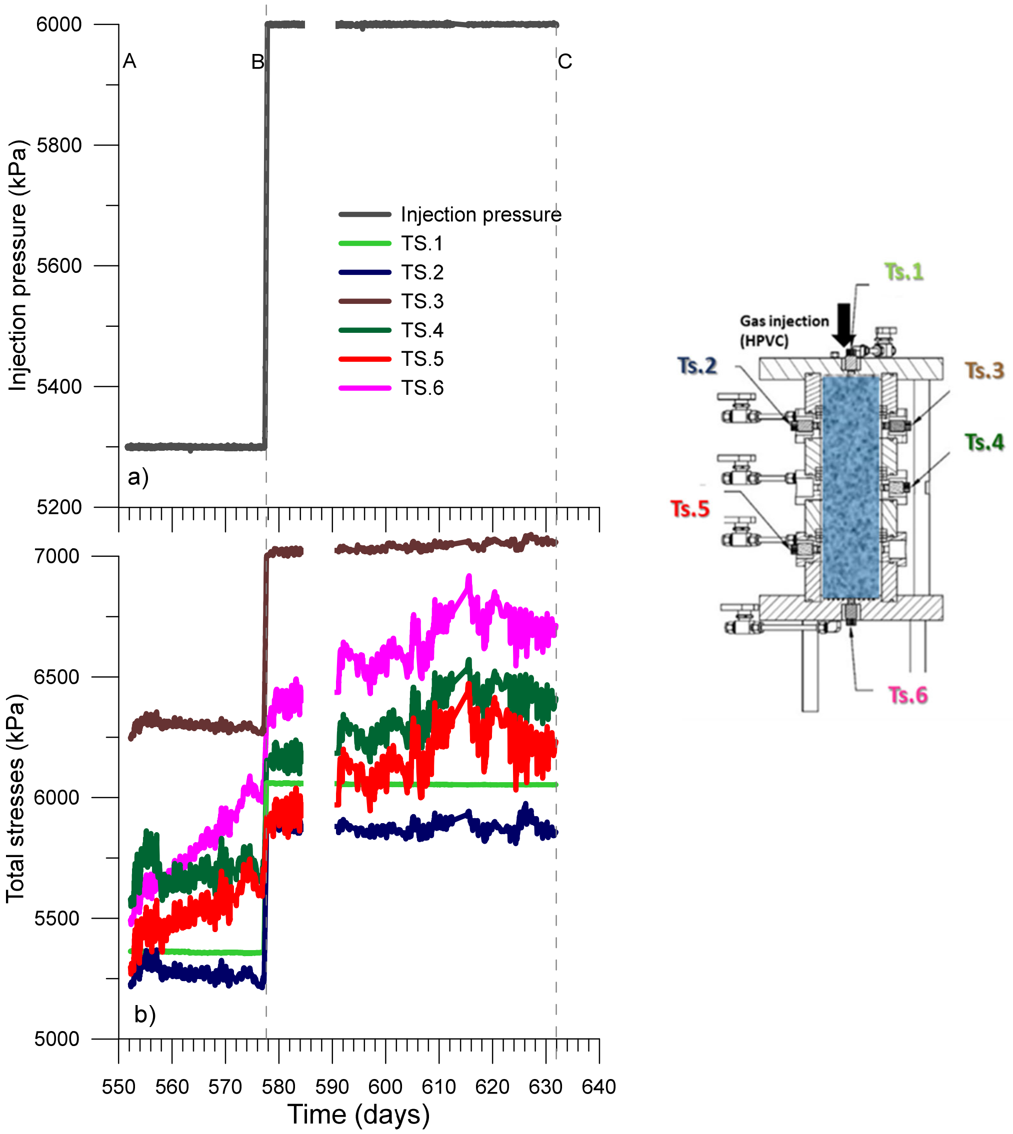

Figure 5-25a). Evolution of gas injection pressure for the second gas test using the HPVC (final phase) and b) evolution of total stress measured by sensors during the injection pressure.

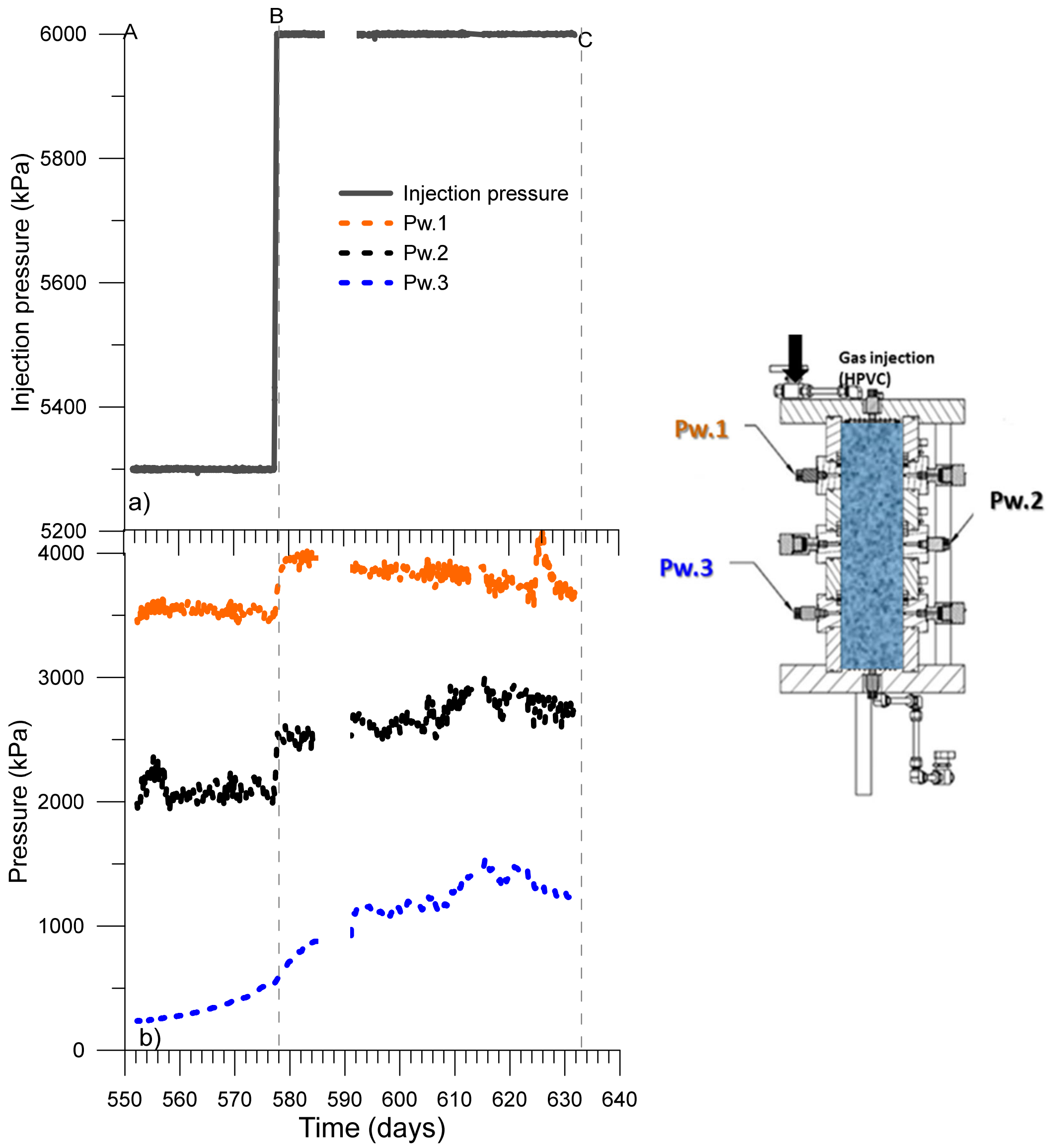

Figure 5-26. Evolution of injection pressure for the second gas injection (final phase) and evolutions of pore pressures sensors.

After closing valve PVC2, no significant increase in the outflow volume rate was detected on PVC3, as evidenced in Figure 5-27b with an outflow volume rate of 101 mm^3/day. However, during quickly increasing the gas pressure (0.7 MPa change), a slight increase in the outflow volume rate was observed, reaching a value of 109 mm^3/day. As can be seen, there is a clear gas pathway that progressively filled this recovery system. On the contrary, PCV4 did not record any outflow volume, since it always registered a small inflow volume into the sample. Also, no outflow volume was recorded in PVC5.

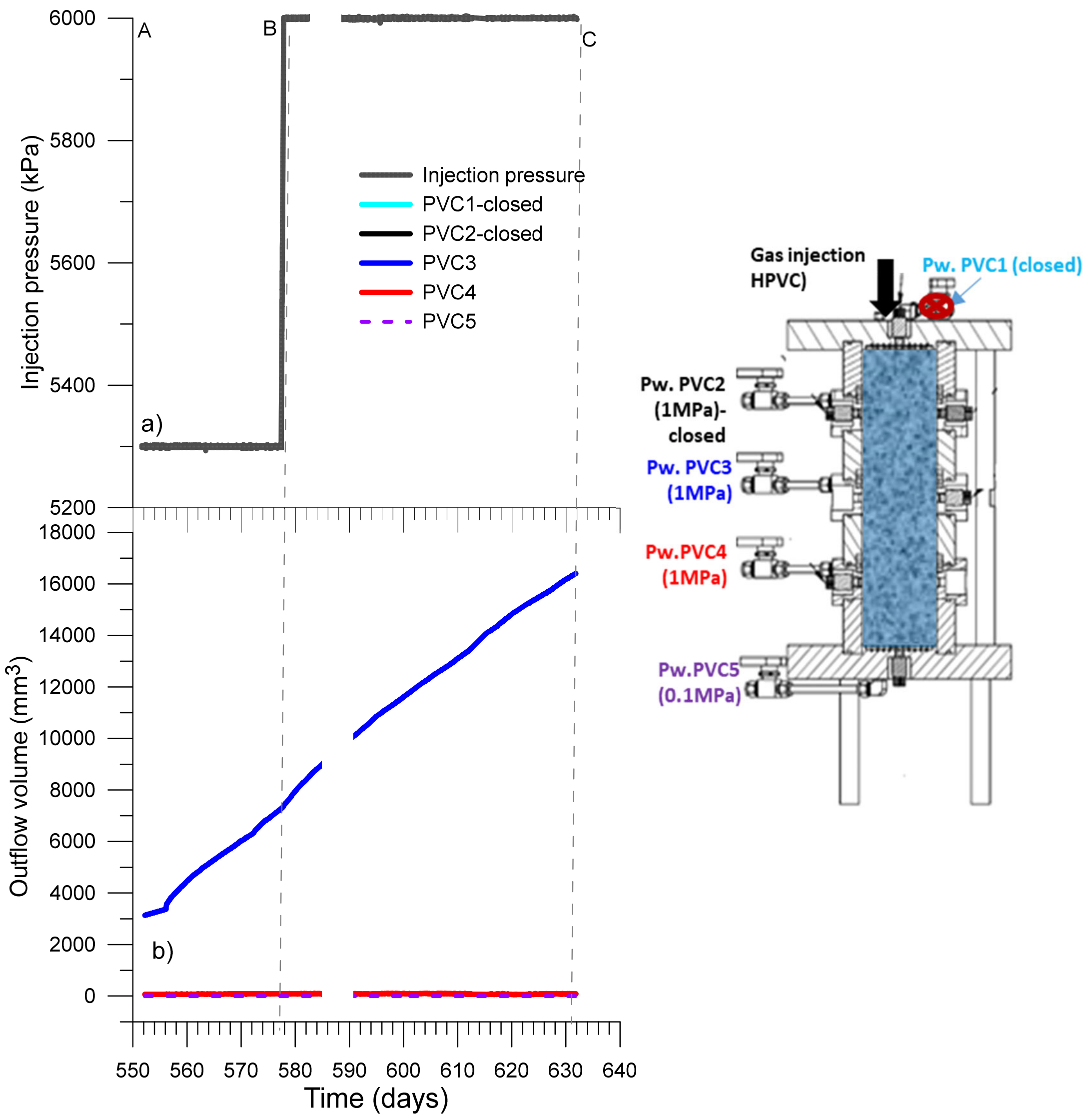

Figure 5-27. Evolution of injection pressure for the second gas injection (final phase) and evolutions of outflow volumes (outflow from the sample is positive).

Despite the clear breakthrough and the gas pathway detected between the injection point and PVC3, no discernable detachment or gas pathway was seen in the second Perspex ring (refer to Figure 5-28). This fact was different from what was found in the upper ring, in which detachment of the sample and fissures were observed. Probably, the gas pathway developed inside the material and close to the interface before reaching the outlet point PVC3.

Figure 5-28. Second gas test with Perspex/bentonite interface problems in the top ring. Second ring with no discernable detachment or fissures.

5.7. Concluding remarks

In this chapter, different gas injection tests, both at oedometer and mock-up scale, were described and interpreted to investigate the impact of gas migration on the nearly saturated mixture. The primary concern was to find at what gas pressure these breakthrough phenomena occur and determine whether they develop through the interface or throughout the material. The tests were carried out at different water pressures at the boundaries, injecting gas at both the bottom and top boundaries of the mock-up.

The preliminary gas oedometer test at total vertical stress of 4 MPa reported slow gas passage at a relatively low gas overpressure of 0.5 MPa above the water pressure applied at the top, and it was not helpful to upscale it to the conditions of the infiltration column. The test allowed evaluating the gas permeability during the dissipation stage at constant inlet volume. The intrinsic permeability was slightly higher than when water was flowing, and differences were associated with the fact that gas flows through different localised pathways compared to those followed by water.

The first gas test in the mock-up was performed by injecting gas at the bottom boundary at a volume rate of 0.1 mL/min up to nearly 8 MPa. The water pressure at the boundaries was held at 4 MPa. The bottom part of the sample was under partially saturated conditions (global degree of the specimen of 89.9%). This unsaturated zone did not develop high swelling stresses. The consistency in the increasing rate and magnitude of the lateral and top total stress sensors TS3 and TS4 –close to the gas injection pressure– indicated a gas pathway remarkably near the sample/wall interface. However, this pathway was not clearly observed in the upper transparent ring. The pathway close to the Perspex/bentonite interface was driven by the significant reduction of the lateral swelling stress (around 0.5 MPa). In the second Perspex ring (from the bottom), the interface between a partially saturated / highly gas-connected zone and a saturated zone acting as a plug was clearly observed. During the fast gas pressure increase, this saturated plug was pushed –due to piston effect– against the top (TS1) and lateral (TS2) boundaries. Outflow volumes were detected in the upper PVC1 and PVC2 driven by the water pressure increase on gas pressurisation.

Hydration in the mock-up continued for 200 days after the first gas test. The pore pressure was reduced to 1 MPa to mimic the water pressure under in situ conditions of the VSEAL test (around 0.8 MPa). Some gas entrapment at the bottom zone affected reaching full saturation at a global degree of saturation of 97.4% of the sample. An axial swelling (effective) stress of 0.6 MPa at the top was reached due to the reduced dry density (gel-like structure) that resulted in important consequences on the second gas test.

This second gas test was performed by injecting from the top boundary with reduced swelling stress. The initial gas pressure (1.67MPa) was higher than the top axial swelling stress and a gap generated between the gel-type material and the top cap. The gas pressure acted as total stress (piston effect) that pushed the sample against the bottom total stress transducer. In parallel, preferential paths developed at the lateral interface near TS2 sensor with low initial effective stress of 1.4 MPa. TS2 sensor reached a value close to the maximum gas pressure (5.3 MPa), which is consistent with the two breakthroughs and the outflows detected by PVC2. A subsequent gas injection stage was carried out by increasing pressure to 6 MPa and keeping PVC2 valve closed. TS2 sensor underwent a sharp increase in total stress, which strictly followed the gas pressure and confirmed the gas pathway's preservation at the sensor interface. A slight increase in the outflow volume rate was also observed in PVC3. During this stage, the gas pressure detached the material from the top Perspex's ring. Nevertheless, no discernable detachment or gas pathway was observed in the second Perspex ring (from top).

6. MODELLING OF THE HYDRO-MECHANICAL BEHAVIOR OF THE MIXTURE

6.1. Introduction

Expansive materials characterised by multimodal porous distributions such as bentonite are best described by conceptual and mathematical models accounting for various structural levels (e.g. micro and macrostructural levels) and their interactions.

An essential characteristic of the bentonite pellet/powder mixture is the multimodal nature of its porous network, which governs all of its Hydro-Mechanical (HM) properties **(Chapter 2, Section 2.7., Figure 2-14)**. The mixture is also obviously highly heterogeneous. The degree and distribution of heterogeneities will vary during hydration, and the average dry density might not be sufficient to characterize its final state. In order to quantify the effect of both double structure distribution and initial heterogeneity on the mixture HM behaviour during hydration, two modelling approaches were adopted.

In the first approach, a fully coupled elastoplastic model which takes into account the multimodal nature of the bentonite pellet/powder mixture is used (e.g. Alonso *et al.*, 1999; Gens *et al.*, 2011). The model is based on the distinction within the mixture of two dominant pore levels (macro and micro-pores) but neglects the initial heterogeneities.

In the second approach, a numerical dual-porosity model is adopted. The basic idea of the model is the appropriate representation of the pellets and of the powder to account for the initial structural heterogeneities of the mixture since pellets and powder are represented as two distinct materials. The model focus on the local response of both the mixture components (pellet and powder). However, given the model geometrical complexity, the component's mechanical behaviour is assumed as simple as possible using a non-linear elastic model (volumetric deformations are induced by net mean stress and suction changes).

In this chapter, the proposed modelling approaches are first outlined and then used to model the 1/10 mock-up of VSEAL *in situ* tests during the hydration phase. The model's parameters were determined essentially based on the back-analysis of laboratory test results on the pellets, the powder and the mixture.

6.2. A double structure elastoplastic model

The mixture displays a multi-modal PSD **(Chapter 2, Section 2.7, Figure 2-14)** with micro-porosity (intra-aggregate pores in powder and pellets), macro-porosity (inter-aggregate pores in powder and pellets), and larger macro-pores between the shielding skeleton of the pellets and the powder (inter-grain porosity considered hereafter as part of the macro-porosity). Initial micro and macro-porosities were deduced from the PSD curves displayed in Figure 2-12 and Figure 2-13. A pore size of 1μm has been selected as a delimiting value between micro and macro-pores. Initial micro and macro-porosities are estimated to ϕ^{micro} = 0.18, $\phi^{Macro} = \phi - \phi^{micro}$= 0.29.

6.2.1. Hydraulic constitutive laws

The dependency of intrinsic permeability on macro-porosity is expressed as exponential law in equation 6-1 proposed by Sánchez (2004). This expression was introduced in the numerical code to fit better many experimental data of water permeability performed on bentonite-based materials (Sánchez, 2004; Sánchez & Gens, 2006). The exponential law assumed that the main transport of fluid species is through macro-pores and that the contribution of the mass flow of fluid species through micro-pores can be neglected.

$$K_{exp} = k_0 \; exp\left\{b(\phi^{Macro} - \phi_0^{Macro}\right\} \qquad (6\text{-}1)$$

Where $\phi^{Macro}$is the macro-porosity and k_0 is the intrinsic permeability at a reference macro-porosity ϕ_0^{Macro}. For the mixture, k_0 = 1.17×10-20 m^2 was measured in the laboratory using long-term hydration permeability tests **(Chapter 3, section 3.2, Figure 3-2).**

The dependency of liquid relative permeability on the degree of saturation is expressed as shown in Equation 6-2.

$$k_{rl} = S_e^n = \left(\frac{S_r - S_{rl}}{S_{ls} - S_{rl}}\right)^n \qquad (6\text{-}2)$$

Where *n* is a material parameter, and *Se* is the effective degree of saturation, S_r is the degree of saturation, S_{rl} is a residual degree of saturation, and S_{ls} is the degree of saturation at saturated conditions.

The water retention model adopted in the analysis is a modification of the expression proposed by van Genuchten (1980), where *s* is suction and P_0 a material parameter **(Section 3.3, equation 3-2).** The hydraulic parameters used in the model for the mixture are presented in **chapter 3, section 3.5, table 3-6.**

6.2.2. Mechanical constitutive laws

The Barcelona Expansive Model (BExM) (Alonso *et al.*, 1999) is based on the Barcelona Basic Model (BBM) presented by Alonso *et al.* (1990). The BExM is a mechanical constitutive model for geomaterials with two levels of porosity (i.e., macro and micro-porosity). This distinction allows taking into account the phenomena that affect each porosity levels and the interaction between them (Alonso *et al.*, 2011; Gens *et al.*, 2011). The macro-porosity is considered to be partially saturated. Moreover, the model assumes that the microstructural behaviour is purely elastic and independent of the macrostructural state. It means that microstructural response only depends on the changes in suction and stresses at this structural level. However, the microstructural deformations can irreversibly affect the macrostructural deformations according to Gens & Alonso (1992).

The increment of the total elastic volumetric strain of the medium is computed as the sum of the increments of macro and micro-elastic deformations (Alonso *et al.*, 1999):

$$d\varepsilon_v^e = d\varepsilon_v^{eMacro} + d\varepsilon_v^{emicro} \tag{6-3}$$

where $d\varepsilon_v^e$ is the increment of the volumetric elastic strain; $d\varepsilon_v^{eMacro}$ the increment of the volumetric elastic strain related to changes in the macro-porosity; and $d\varepsilon_v^{emicro}$ the increment of the volumetric elastic strain related to changes in the micro-porosity.

The increment of the macrostructural volumetric elastic strain $d\varepsilon_v^{\mathrm{eMacro}}$ is expressed as a function of the increments of mean net stress and suction as

$$d\varepsilon_v^{eMacro} = \frac{\kappa^{Macro} dp}{(1+e^{Macro})p} + \frac{\kappa_s^{Macro} d(s+p_{atm})}{(1+e^{Macro})(s+p_{atm})} \tag{6-4}$$

where p refers to the mean net stress, s is the (total) suction, p_{atm} the atmospheric pressure; κ^{Macro} the elastic compressibility at the macro-porosity level for changes in mean stress, κ_s^{Macro} the elastic macro-compressibility for changes in suction and e_{Macro} the macrostructural void ratio. $e^{Macro} = \frac{\phi^{Macro}}{1-\phi^{Macro}}$, not taking into account the volume of the pores within the particles.

The following equation defines the variation of pre-consolidation pressure (p_o) associated with increasing suction and the collapse phenomena observed in wetting paths

$$p_o = p_c \left(\frac{P_0^*}{p_c}\right)^{[\lambda(0)-\kappa^{Macro}]/[\lambda(s)-\kappa^{Macro}]} \tag{6-5}$$

$$\lambda(s) = \lambda(0)\left[r + (1-r)e^{-\beta s}\right] \tag{6-6}$$

Where p_c is reference stress; $\lambda(s)$ is the slope of the virgin consolidation line at suction S; $\lambda(0)$ is the slope of the virgin saturated consolidation line; P_0^* is the saturated pre-consolidation pressure; r and β model parameters.

The mean effective stress (p') controls mechanical behaviour at the microstructural level (Gens & Alonso, 1992; Alonso *et al.*, 2011; Gens *et al.*, 2011).

$$p' = p + s \tag{6-7}$$

Where p is the net stress and S is suction

In the *p-s* plane, the neutral loading line (NL), correspond to constant microstructural mean stresses; therefore, no microstructural deformations could happen while the stress path moves on it. (Figure 6-1). The NL line divides the *p-s* plane into two main microstructural stress paths identified as microstructural swelling (MS) when there is a decrease in p' and microstructural compression (MC) when there is an increase in p' (Alonso *et al.*, 1999; Gens *et al.*, 2011).

The increment of the microstructural strain $d\varepsilon_v^{\mathrm{e}micro}$ is assumed to be volumetric, nonlinear elastic and proportional to the increment of the mean effective stress as equation 6-8.

$$d\varepsilon_v^{emicro} = \frac{\kappa^{micro} d(p')}{(1 + e^{micro})\, p'} \tag{6-8}$$

Where e_{micro} is the microstructural void ratio, and κ^{micro} the elastic compressibility at the micro level for changes in mean effective stress.

The BExM considers that the plastic deformations of the macrostructure induced by microstructural effects are proportional to the microstructural strain according to the following two interaction functions. The interaction functions depend on the ratio *p/p₀*, with p₀ as the yield mean net stress at the current macrostructural suction value.

The interaction of micro-swelling (equation 6-9 and 6-10) is defined in the case of suction decrease and interaction of macro-swelling when the suction increases

$$f_c = f_{c0} + f_{c1} \left(\frac{p}{p_0}\right)^{n_c} \tag{6-9}$$

$$f_s = f_{s0} + f_{s1} \left(1 - \frac{p}{p_0}\right)^{n_s} \tag{6-10}$$

The total plastic macrostructural strain ($d\varepsilon_v^{p\,Macro}$) is obtained as the sum of the inelastic deformations of microstructure through the interaction mechanism and the plastic deformations ($d\varepsilon_{vLC}^{p}$) induced when yielding of macrostructure takes place (when the stress path reaches the loading collapse). LC curve is explained in detail in the BBM model by Alonso *et al.*(1990).

$$d\varepsilon_v^{p\,Macro} = d\varepsilon_{vLC}^{p} + f_\alpha d\varepsilon_v^{e\,micro} \tag{6-11}$$

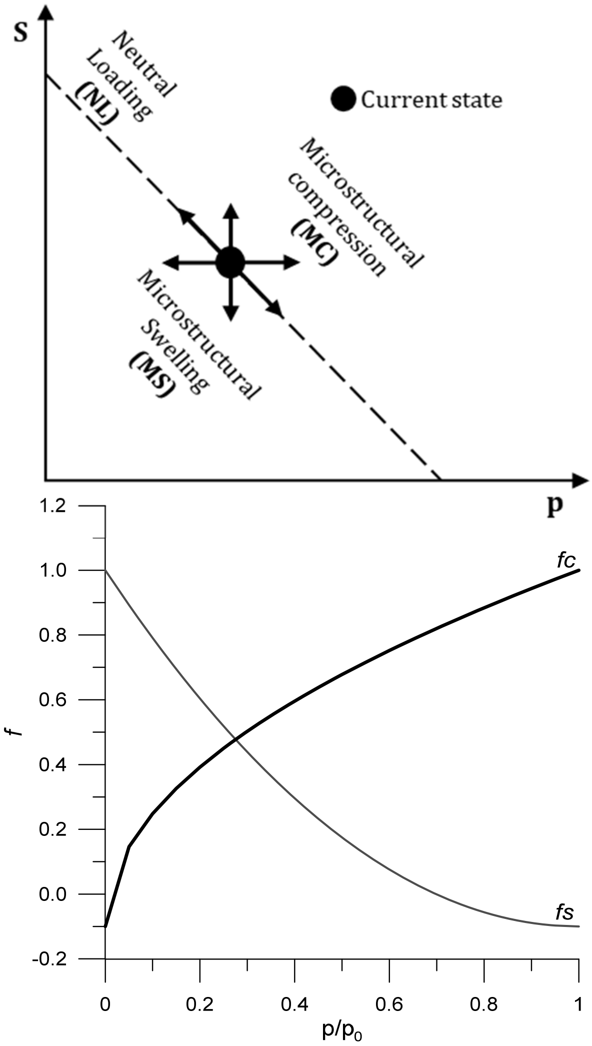

Figure 6-1 Double structure deformation model for expansive clays: (a) microstructural model; (b) interaction functions.

6.2.3. Determination of mechanical parameters

The compressibility parameters were determined using the results from the modelling of oedometer tests on pellet-powder bentonite under constant water content at s = 86 MPa (see **chapter 3, Section 3.5** and Mesa-Alcantara *et al.* (2020b) for more details). The parameters of the mechanical constitutive model are presented in Table 3-5. Figure 6-2 presents the experimental data from the oedometer, and the model with better fitting to the loading/unloading curves were with $\kappa^{\mathrm{Macro}} = 0.035$ and $\kappa^{\mathrm{micro}} = 0.08$. This compressibility parameter was used in the simulations of 1/10 Mock-up of the VSEAL *in situ* test. Parameters not directly obtained from experimental results as interaction function parameters were taken from Toprak *et al*. (2018).

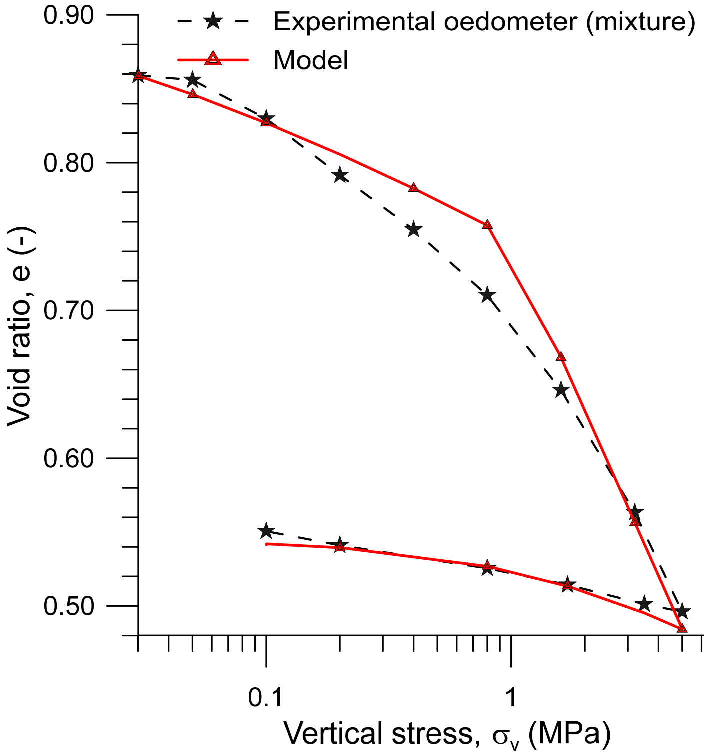

Figure 6-2 Oedometer test under constant water content at s = 86 MPa, together with experimental and modelling results

6.2.4. Modelling of 1/10 Mock-up of VSEAL in situ test

Geometry and boundary conditions

The numerical modelling was carried out using the finite element program Code_Bright (Olivella *et al.*, 1996).

The 1/10 mock-up test is simulated using the proposed model outlined above. The hydro-mechanical parameters are summarised in Table 3-5 and Table 3-6. The HM coupled analysis has been performed on a 2D axisymmetric finite element geometry with linear quadrilateral elements with four integration points (Figure 6-3). Initial conditions are summarised in Table 6-1. A mechanical boundary condition restraining displacement is assigned at the outer boundaries of the model domain.

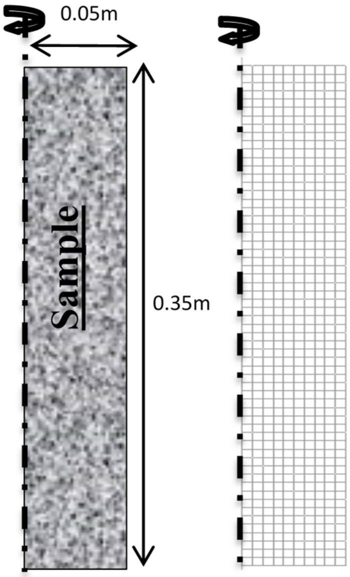

Figure 6-3. Materials, geometry and mesh for the numerical simulation.

Table 6-1 Initial conditions.

Initial state/stress	**Mixture (80% pellets and 20% powder)**
Initial suction (MPa)**	100
Initial porosity (-)	0.47
*Dry Density (Mg/m^3)	1.47
Initial stress (MPa)	0.01

**Measured in the laboratory ** Measured (average) in the experimental mock-up test*

Different water pressures were imposed on the top and lateral boundaries to ensure a fast axial and slow lateral hydration**.** The lateral boundary conditions were applied at three different points (Table 6-2, Figure 6-4 and Figure 6-5) to mimic the water pressure of the experimental mock-up test applied through the stainless steel rings.

Table 6-2. Hydraulic boundary conditions for the simulation.

Boundary condition #1 (Top)		Boundary condition #2 (Lateral above)		Boundary condition #3 (Lateral middle)		Boundary condition #4 (Lateral below)	
Time (days)	Suction/Water pressure (MPa)	Time (days)	Suction/Water pressure (MPa)	Time (days)	Suction/Water pressure (MPa)	Time (days)	Suction/Water pressure (MPa))
0	-100	0	-	0	-	0	-
0.5	-40	0.5	-	0.5	-	0.5	-
1	0.02	1	-	1	-	1	-
2	0.07	2	-	2	-	2	-
3	0.27	3	-	3	-	3	-
4	0.7	15	-	15	-	15	-
5	1	15.1	0	15.1	0	15.1	0
5.1	1	16	0.007	16	0.007	16	0.001
11	2	16.1	0.007	16.1	0.007	16.1	0.001
11.1	2	25	0.225	25	0.025	25	0.003
15	3	25.1	0.225	25.1	0.025	25.1	0.003
15.1	3	26	0.5	26	0.03	26	0.007
19	4	26.1	0.5	26.1	0.03	26.1	0.007
19.1	4	26.6	1	26.6	0.046	26.6	0.008
130	4	26.7	1	26.7	0.046	26.7	0.008
150	4	28.3	2	28.3	0.056	28.3	0.009
200	4	28.4	2	28.4	0.056	28.4	0.009
200	4	31.5	3	31.5	0.086	31.5	0.012
200	4	31.6	3	31.6	0.086	31.6	0.012
200	4	47	4	47	0.24	47	0.021
200	4	47.1	4	47.1	0.24	47.1	0.021
200	4	100	4	76	0.5	76	0.023
200	4	150	4	76.1	0.5	76.1	0.023
200	4	200	4	113	1	113	0.057
200	4	200	4	113.1	1	113.1	0.057
200	4	200	4	130	2	130	0.071
200	4	200	4	130.1	2	130.1	0.071
200	4	200	4	140	3	135.6	0.087
200	4	200	4	140.1	3	135.7	0.087
200	4	200	4	152	4	163.1	0.15
200	4	200	4	152.8	4	176.9	0.34
200	4	200	4	152.9	4	180.8	0.53
200	4	200	4	200	4	180.9	0.53
200	4	200	4	200	4	186.1	1
200	4	200	4	200	4	186.2	1
200	4	200	4	200	4	200	1.8

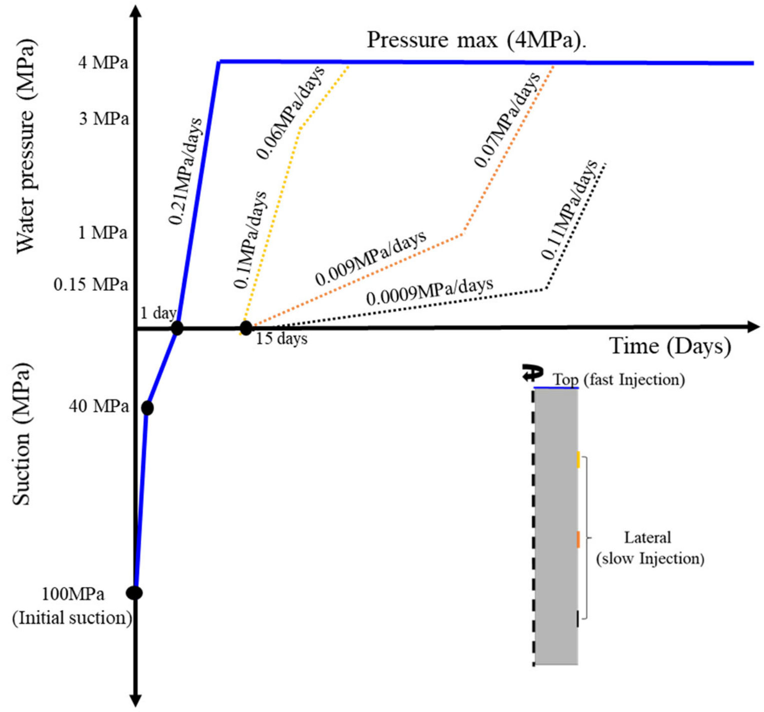

Figure 6-4. Imposed hydraulic boundary conditions..

Mechanical boundary conditions	**Hydraulic boundary conditions**	
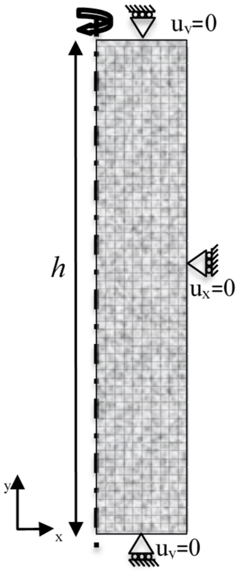	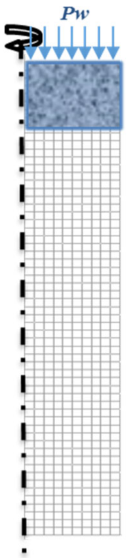	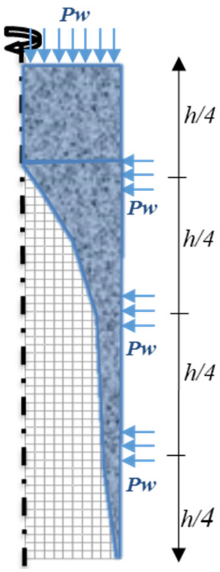
Initial state	Boundary condition (top)	Boundary condition (lateral)

Figure 6-5. Mechanical and hydraulic boundary conditions used in the simulation.

6.2.5. Modelling results

Total stress evolution

The measured and predicted axial and radial total stresses evolutions are displayed in Figure 6-6. The total stresses increase at different rates depending on the distance to the hydration front. In general, the swelling rate is underestimated for TS3, TS4 and TS5 and overestimated for TS6. The magnitude of the total stress is overestimated by the model, except for the TS1 where the pattern of the behaviour is very similar to the measurements. At his location, the total stress increases rapidly and stabilizes at 4 MPa after 15 days. This rapid increase corresponds to the increase of water pressure (Figure 6-7) reducing effective stress to zero at this location. As a consequence of the fast axial hydration, the mixture on the top of the sample becomes a very soft material.

Different evolutions trends are recorded at TS2 and TS3 located at left and right hand sides of the top stainless steel ring demonstrating the strong influence of the local structural heterogeneities at the vicinity of the sensors. Obviously, the model fails to capture this difference given the assumed axisymmetric conditions and the homogenous initial porosity field.

At TS4 large difference are observed between the modelling and the experimental results. The model fails in predicting the peak occurrence at 73 days. This suggests that at this zone, a difference possibly exist between the real local porosity and the modelled one, and also that permeability in this zone is different from the permeability used in the model. A sudden increase of total stress is predicted at 115 days induced by the increase in the imposed water pressure (1 MPa to 4 MPa) (Figure 6-7). After that, the total stress was maintained almost constant with a value of 7.5 MPa with an imposed water pressure of 4 MPa (swelling pressure of 3.2 MPa). Similar behaviour is predicted at TS5 but with a slower swelling rate. At TS6 both evolution rate and magnitudes are overestimated by the model suggesting the existence of local variation (hydraulic, mechanical) not well captured by the homogenous model.

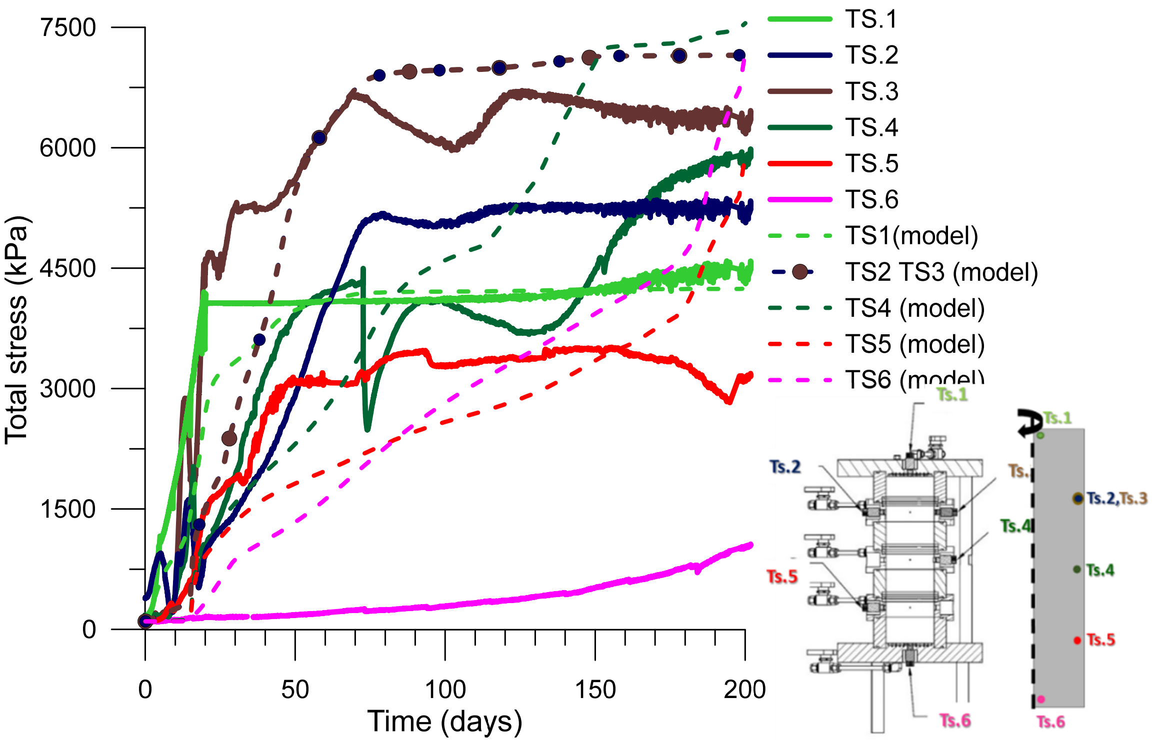

Figure 6-6. Evolution of total stresses at different positions for the mock-up test. Experimental and model results.

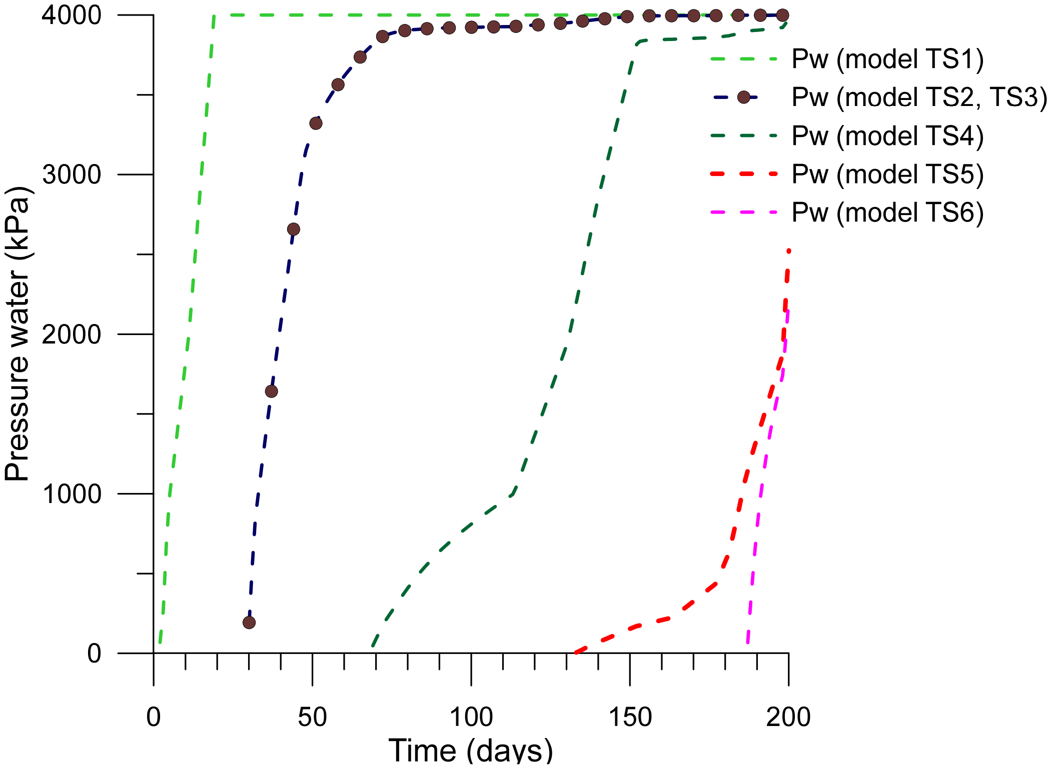

Figure 6-7. Evolution of water pressure of the model at the same location of total stresses.

Relative humidity and saturation evolutions

Figure 6-8 displays the evolution of total suction measured at different distances from the axial hydration front (top, middle and bottom) together with the modelling results. Similarly to the experiment, the initial suction of the model was set to 100 MPa. A monotonic decrease of the measured suction corresponding to the progress of hydration caused by water drawn from both axial and lateral boundaries is observed. Once axial hydration started, total suction decreased rapidly at the top sensor and reached 0 MPa after 60 days. It started to decrease at the middle and bottom sensors once lateral injection started at 15 days. A slower rate is observed at the bottom sensor located at further distance from the axial upper hydration boundary. Some differences are observed between the model predictions and the hydraulic evolution of the test. Globally, a faster saturation rate is predicted by the model. The predictions could probably be improved using a constitutive HM model that considers a heterogeneous dry density distribution (heterogeneous macro-porosity field). The conventional HM model used in this analysis considers the progressive change of intrinsic permeability as a function of macro-porosity (Equation 6-1). Figure 6-9 and Figure 6-10 shows the evolution of porosities (macro and micro) and the induced evolution of permeability at different positions (top, middle and bottom). Upon hydration, there is a reduction of the macro-pores while the micro-pores are expanding (Figure 6-9) resulting in a decrease in permeability. However, the slowest rate observed in the experiment suggests that the locally intrinsic permeability of the mixture is lower than predicted by the model. A similar decreasing rate is predicted at the three positions (top, middle and bottom) because of their location at the same distance from the lateral hydration boundary in addition to the uniform (homogenous) evolution of permeability.

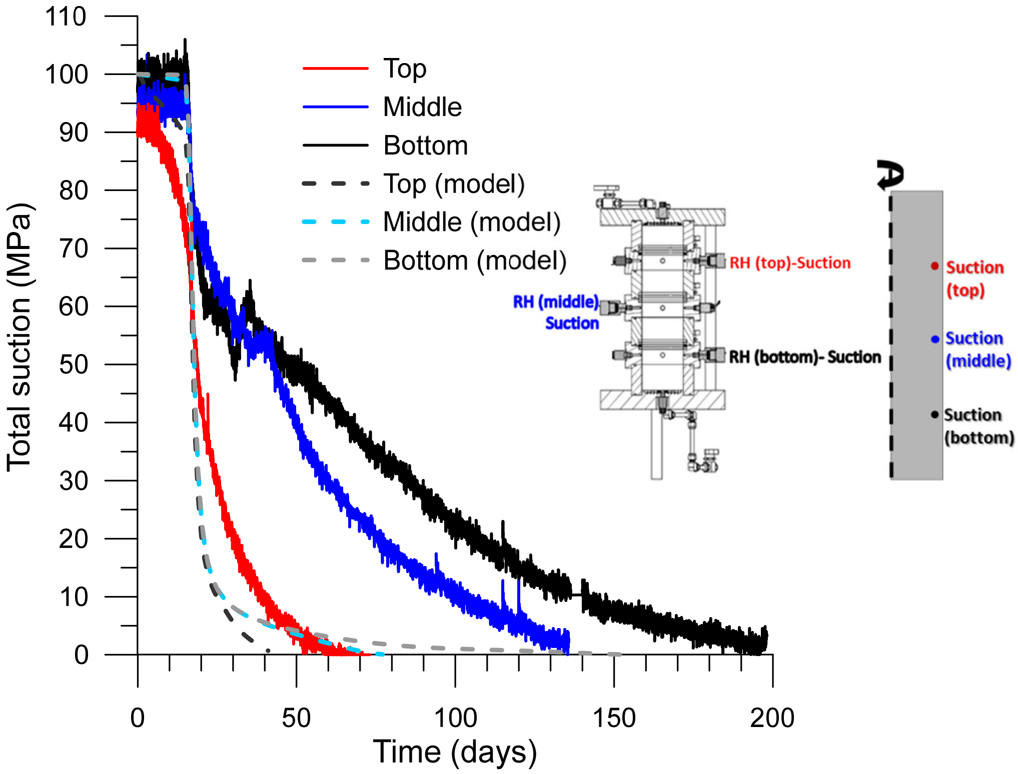

Figure 6-8. Evolution of suction at a different positions. Experimental and modelling.

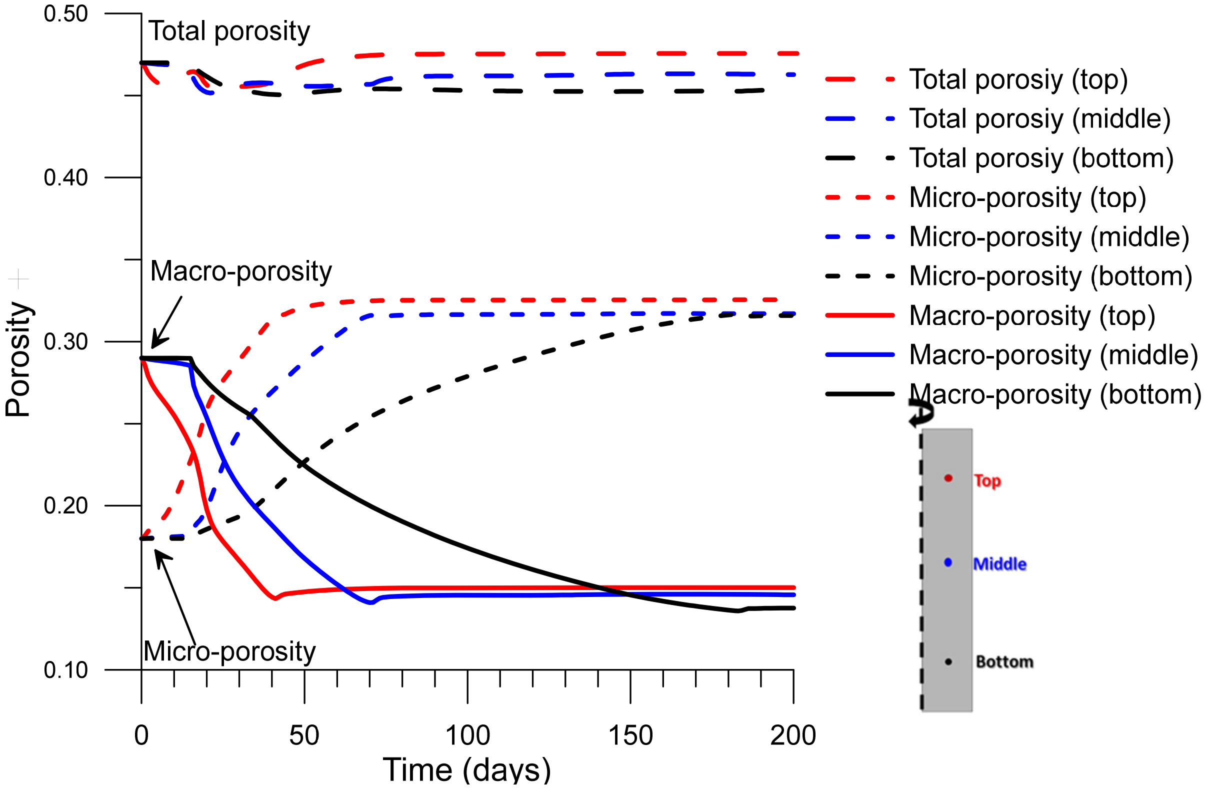

Figure 6-9. Evolution with time of total porosity, macro and micro-porosity. Modelling results.

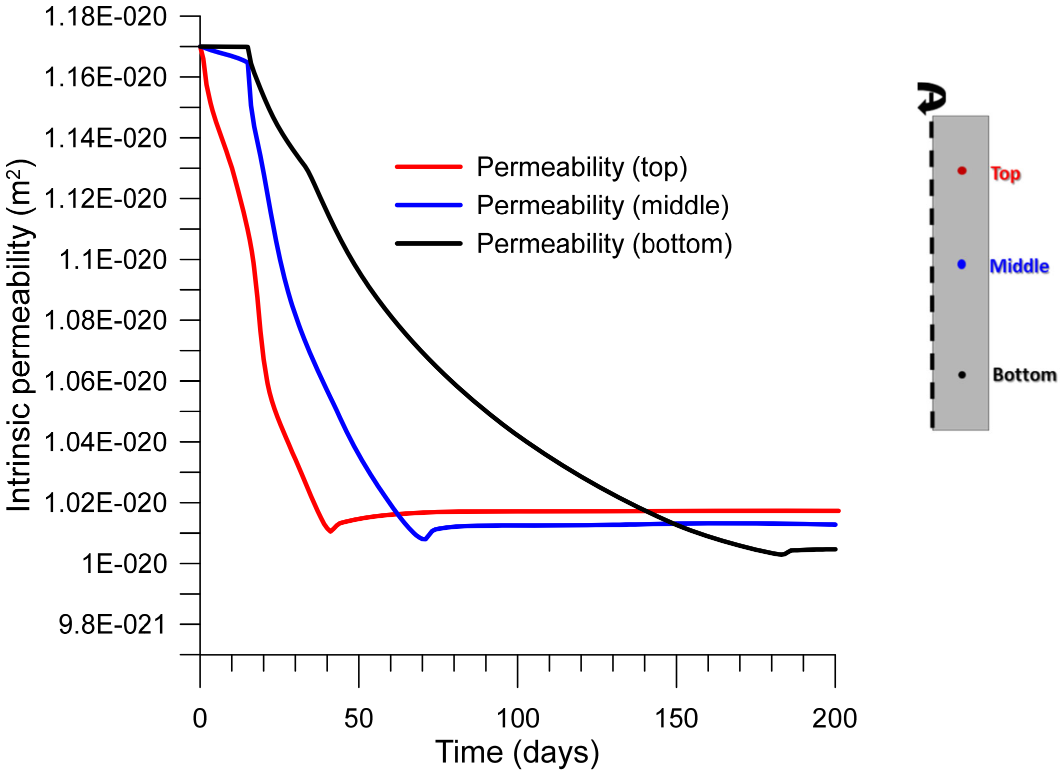

Figure 6-10. Evolution of intrinsic permeability at different positions. Modelling results.

Figure 6-11 shows the distribution of degree of saturation at 15, 16, 40 and 200 days after hydration. As expected, an increasing saturation in the zones close to the hydration boundaries is observed. An increase of S_r is observed during the first 15 days due to the fast top hydration. At 16 days S_r starts to increase at the zones close to the lateral injection boundaries. Equal values of S_r are obtained at equal distances from lateral hydration boundary. Full saturation is reached after 200 days.

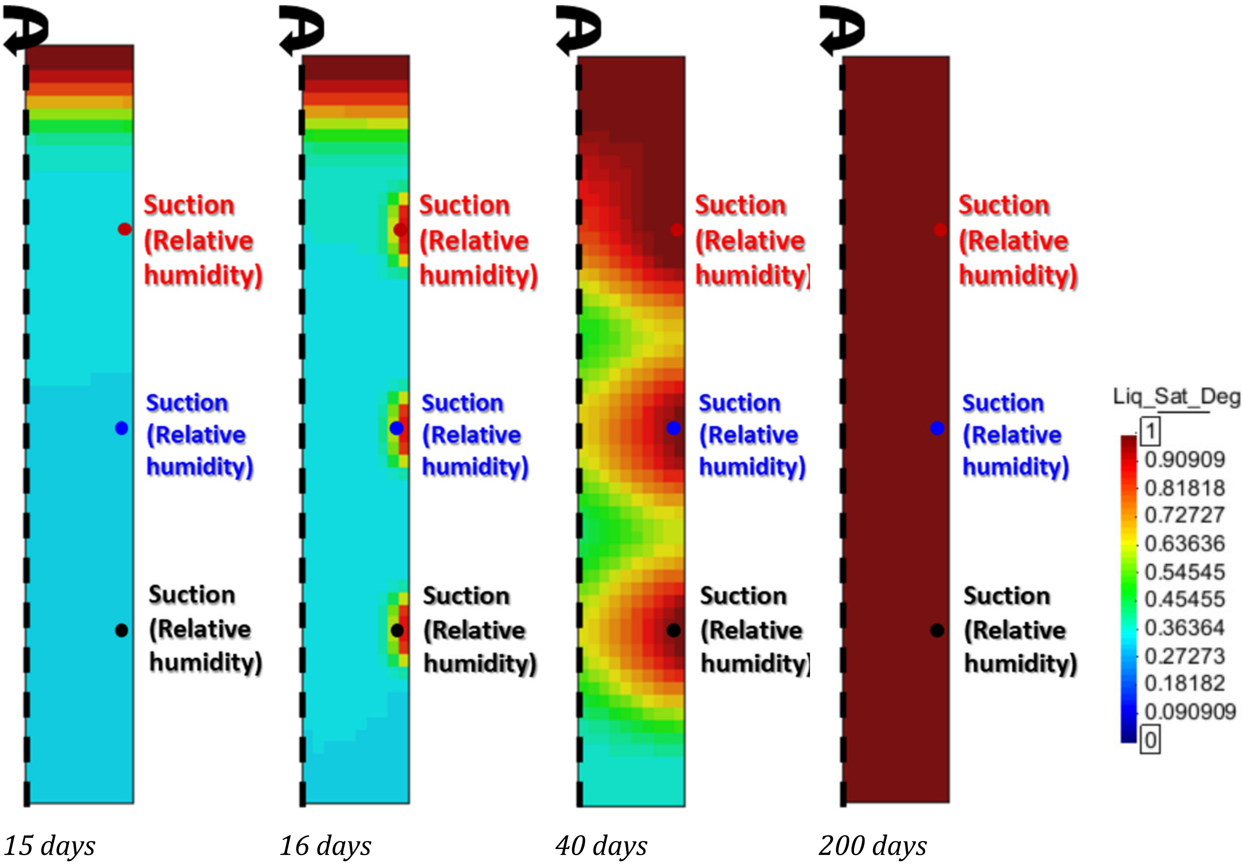

Figure 6-11. Distribution of degree of saturation at different elapsed times.

6.2.6. Permeability effect

To investigate the effect of initial permeability on the modelling results, the reference permeability parameter was set to a lower value of 4.94 x10^{-21} m^2 (Mokni *et al.*, 2019). Figure 6-12 depicts the evolution of total stress and suction at different positions within the mixture. A slower swelling rate is predicted by the model but no significant difference in the saturation kinetics is observed. This confirms that the behaviour of the mixture of bentonite powder and highly compacted pellets is more complex, so there is the necessity to account for an initial heterogeneous dry density distribution (heterogeneous porosity field) to improve the predictive capability of the model.

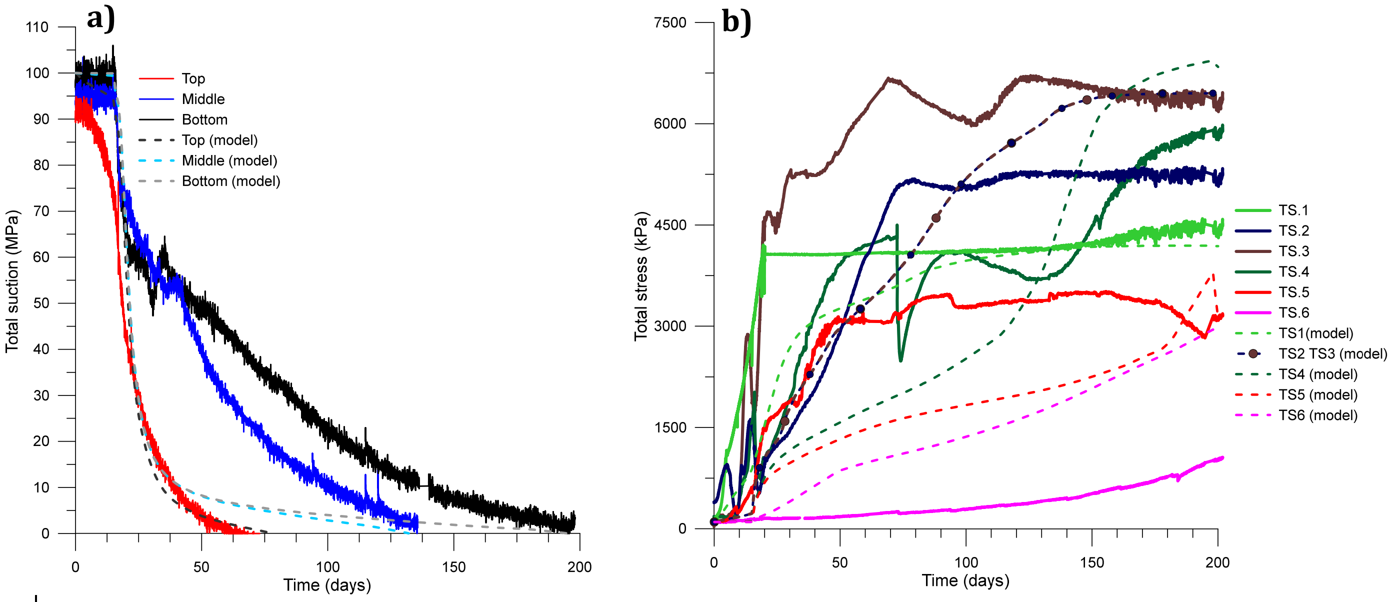

Figure 6-12. Effect of initial permeability on total stresses (a) and suction evolutions (b). Experimental and modelling results.

6.3. A Numerical dual-porosity model

In an attempt to account for the heterogeneous dry density distribution of the mixture, a numerical dual-porosity model is adopted. The basic idea of the model is the appropriate representation of the pellets and the powder. Since pellets and powder are represented as two distinct materials, the double structure nature of the mixture is also accounted for.

6.3.1. Model geometry and boundary conditions

The geometry used corresponds to a mock-up scale infiltration column at constant volume (100 mm in diameter and 350 mm high). Model geometry and boundary conditions are depicted in Figure 6-13. A 2D analysis is assumed, with plane strain conditions (normal displacement not allowed). 252 pellets surrounded with powder are represented with a circular shape (diameter of 8mm to better assess the mass ratio of the mixture). The adopted geometry allows introducing a uniform heterogeneous distribution of initial porosity.

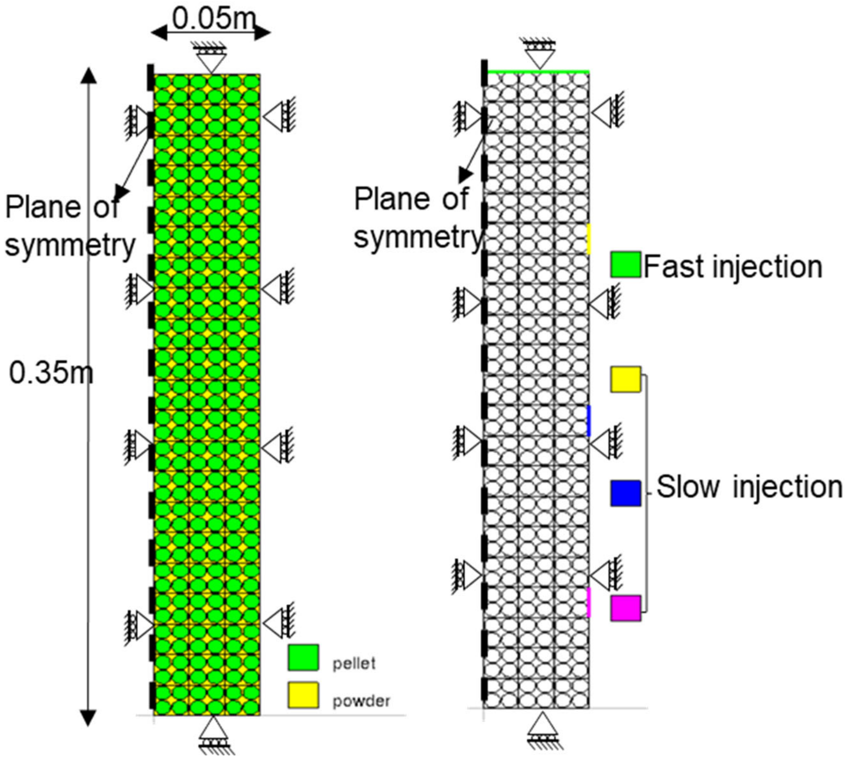

Figure 6-13. Geometry and hydraulic boundary conditions.

The generated numerical mixture has a proportion of 77.55% pellets and 22.45% powder (by mass). These proportions were calculated, taking into account the volume of each material (pellet and powder) in the model and the corresponding mass. The dry mass of each component of the sample was calculated considering the unit mass of bentonite particles of 2.77 Mg/m^3 (Saba, 2014; Saba *et al.*, 2014) and the total porosities of each material (0.60 for the powder and 0.281 for de pellets). This corresponds to a dry density of 1.65 Mg/m^3 due to the fact that powder filled the inter-pellet porosity. It has to be noted that the dry density of the tested mixture is 1.47 Mg/m^3. Although the represented mixture has an ideal well-ordered packing of pellets and powder (no large macro voids between the pellets as observed by Molinero-Guerra (2018), it introduces a uniform heterogeneous distribution of initial porosity.

Mechanical boundary conditions restraining displacement are assigned at the outer boundaries of the model domain. The water pressure was imposed at the top boundary considering a fast increasing rate (0.04 MPa/day) and at the lateral boundary at three different points considering a slowly increasing rate (0.02 MPa/day) to mimic the VSS at real disposal conditions with higher hydration rates reaching from the top calcareous Oxfordian formation (Table 6-3 and Figure 6-14).

Table 6-3. Hydraulic boundary conditions used in modelling mimicking the real VSS.

Axial injection		**Lateral Injection**	
Time(days)	**Water pressure/suction (MPa)**	**Time(days)**	**Water pressure/suction (MPa)**
0	-100	0	-
3.5	-85	3.5	-
5	-40	5	-40
30	0	50	0
30.1	0	50.1	0
32.5	0.1	55	0.1
32.6	0.1	55.1	0.1
42.5	0.5	75	0.5
42.6	0.5	75.1	0.5
55	1	100	1
55.1	1	100.1	1
80	2	150	2
80.1	2	150.1	2
105	3	200	3
105.1	3	200.1	3
130	4	250	4
130.1	4	250.1	4
350	4	350	4

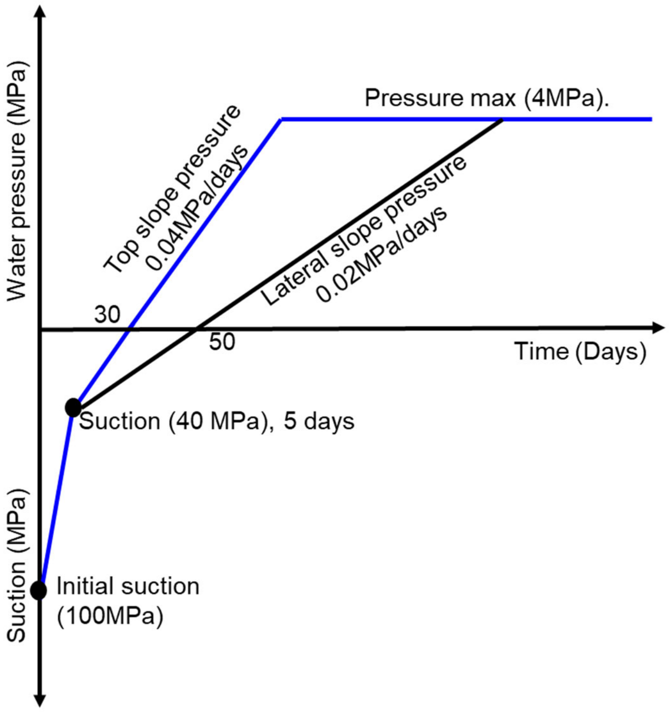

Figure 6-14. Imposed hydraulic boundary conditions.

6.3.2. Hydraulic constitutive laws

The dependency of intrinsic permeability on porosity based on the Kozeny-Carman is presented in equation 6-12.

$$K_{Ko} = k_o \frac{\phi^3}{(1-\phi)^2} \frac{(1-\phi_0)^2}{\phi_0^3} \tag{6-12}$$

Where ϕ *is total* porosity and k_o is reference intrinsic permeability at a reference porosityϕ_0.

Variations of intrinsic permeability with porosity have been derived from permeability tests performed on the mixture components (pellet and powder) and the mixture **(Chapter 3, section 3.2).** Figure 6-15 shows the experimental measurements together with the Kozeny-Carman model fitting. The reference intrinsic permeability adopted is k_o= 2x10^{-21}m^2 for reference porosity ϕ_0 = 0.30 for the pellet and powder. Although the same permeability function and the same reference permeability are considered for the binary mixture component, initial values of permeability for the pellet and the powder are different (5.64x10^{-20}m^2 for the powder and 1.60x10-^{21}m^2 for the pellet).

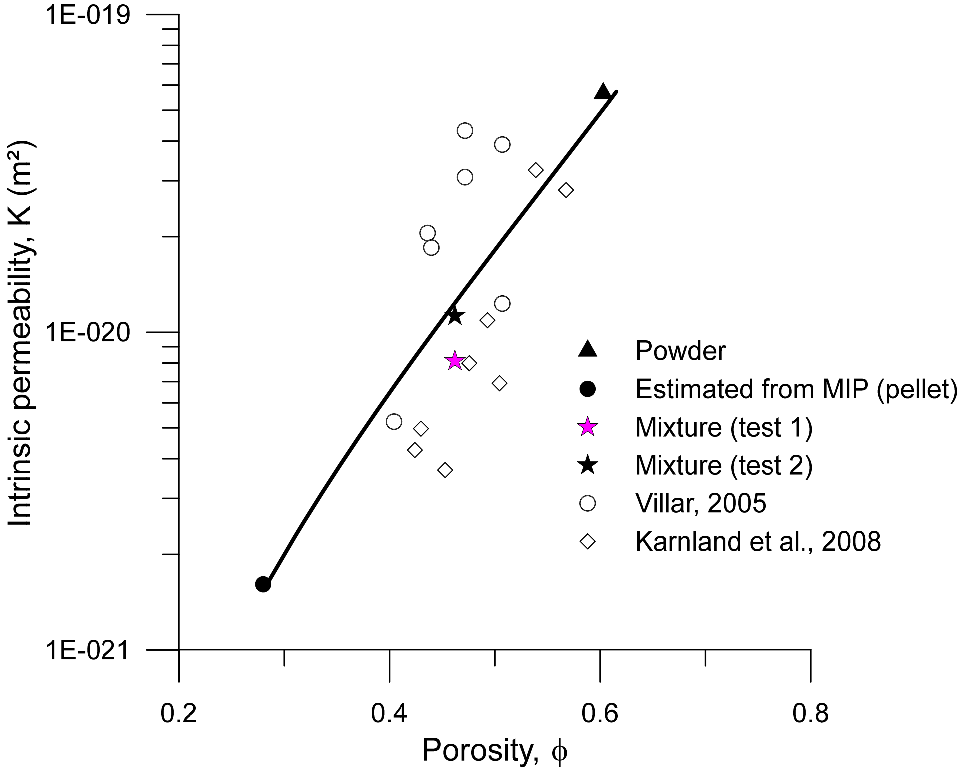

Figure 6-15. Intrinsic permeability as a function of porosity, together with the Kozeny-Carman model.

The dependency of liquid relative permeability on the degree of saturation is expressed as shown in Equation (6-2). The same water retention model as adopted in section 6.2 is used (Equation 6-3). The parameters of the water retention curve for the powder and pellet were fitting using experimental results presented in **section 3.3 in Figure 3-4and Figure 3-5**. The hydraulic parameters are summarised in Table 6-4.

Table 6-4. Summary of hydraulic properties for the powder and pellet.

Hydraulic parameters		
Properties	Powder	Pellet
Intrinsic permeability-Koseny's model ($\boldsymbol{K_{Ko}}$)		
Reference intrinsic permeability (m^2) ($\boldsymbol{k_o}$)	2 x10^{-21}	2 x10^{-21}
Reference porosity (ϕ_0)	0.3	0.3
Total Porosity (ϕ)	0.60	0.28
Retention curve		
Fitting parameter P_0 (MPa)	2	35
Fitting parameter (λ)	0.32	0.32
S_{ls} degree of saturation in saturated conditions	1	1
S_{rl} residual degree	0	0

6.3.3. Mechanical constitutive laws

Given the model geometrical complexity, the component's (pellet and powder) mechanical behaviour is assumed as simple as possible using a non-linear elastic model. Elastic volumetric deformation is defined for changes in mean effective stress and suction as,

$$d\varepsilon_v^e = a_1 \frac{dp'}{p'} + a_2 \frac{ds}{s+0.1} \tag{6-13}$$

$$a_1 = \frac{\kappa_i}{1+e} \ and \ a_2 = \frac{\kappa_s}{1+e} \tag{6-14}$$

Where the subscript i refer to pellets or powder, e is the void ratio of pellets or powder, κ_i is the slope of the unloading/reloading curve in the (e - lnp') plot, and κ_s is the slope of the unloading/reloading curve in the (e - ln((s+0.1)/0.1)) plot. p' is the net mean effective stress, and s is total suction.

Shear strain (ε_q^e)is expressed as,

$$\varepsilon_q^e = \frac{\mathrm{q}_s}{3G} \tag{6-15}$$

Where q_s is deviatoric stress and G the Shear modulus.

The compressibility parameters were determined using the results from oedometer tests performed on pellets and powder **(Chapter 3 section 3.5).** The parameters of the mechanical constitutive model ($\kappa_i$and κ_s) were fitted to experimental data for both pellets and powder. Measured and calculated void ratio values are presented in Figure 6-16. Table 6-5 summarises the fitted parameters.

Table 6-5. Initial mechanical properties for pellets and powder.

Materials	***Void ratio***	***Fitting parameters***		
		a_1	a_2	***G(MPa)***
Pellet	*0.39*	*0.011*	*0.03*	*18*
Powder	*1.52*	*0.085*	*0.008*	*4.5*

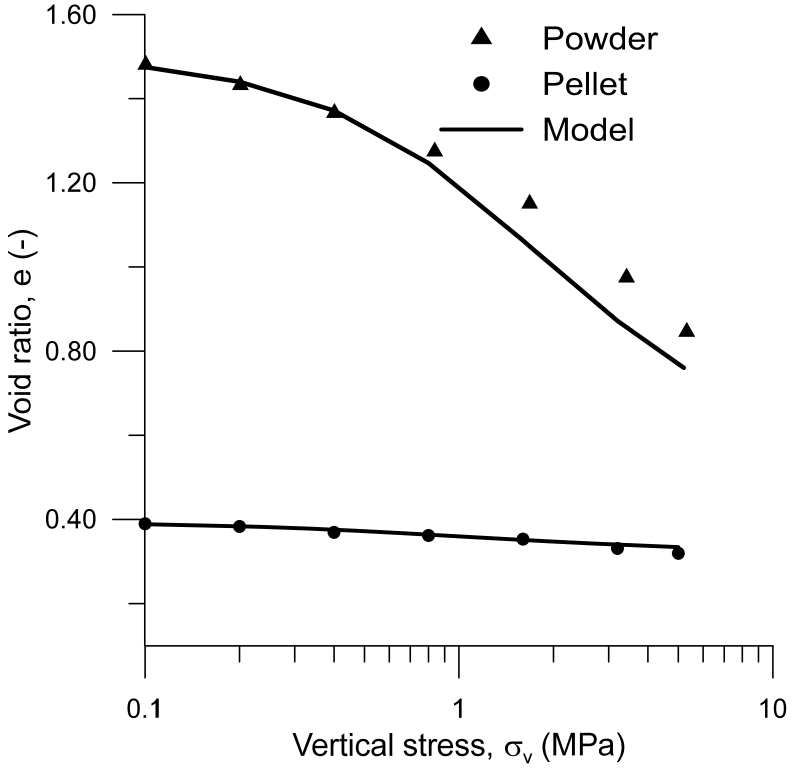

Figure 6-16. Oedometer test on pellets and powder. Experimental and modelling results.

6.3.4. Modelling results

The numerical modelling was carried out using the finite element code Code_Bright (Olivella *et al.*, 1996). Given the simplicity of the mechanical constitutive law adopted in this section, no tentative comparison with the experimental results (1/10 mock-up test) is made. However, interesting information not readily available from direct laboratory measurements might be obtained by analysing in more detail some of the results of the calculations.

The variations in time of porosity of both pellets and powder at three different points located at the top, middle and bottom of the sample are shown. Although constant volume conditions are imposed, local variations of the components porosity are observed. During hydration, there is swelling of the pellets inducing porosity within the highly compacted bentonite spheres to increase. As a result, the powder is compressed inducing a decrease in powder porosity. The pattern of behaviour is similar at all position except for the powder located at the top close to the axial hydration boundary. At this point, a transient increase in porosity is observed (Figure 6-17). At 114 days, the powder at this location reached saturation, and the mean effective stress decreased due to the increase of water pressure (Figure 6-18 and Table 6-5). This causes a local expansion of the sample, which decreases when the saturation front advances and the bottom material shows a volumetric deformation increase and compresses the top material. Similar but less significant behaviour is observed for the powder located at the middle and bottom, probably because the material (powder) at this location is more compressed. This could be checked in Figure 6-18 in which the mean effective stress at middle and bottom is higher when full saturation is reached.

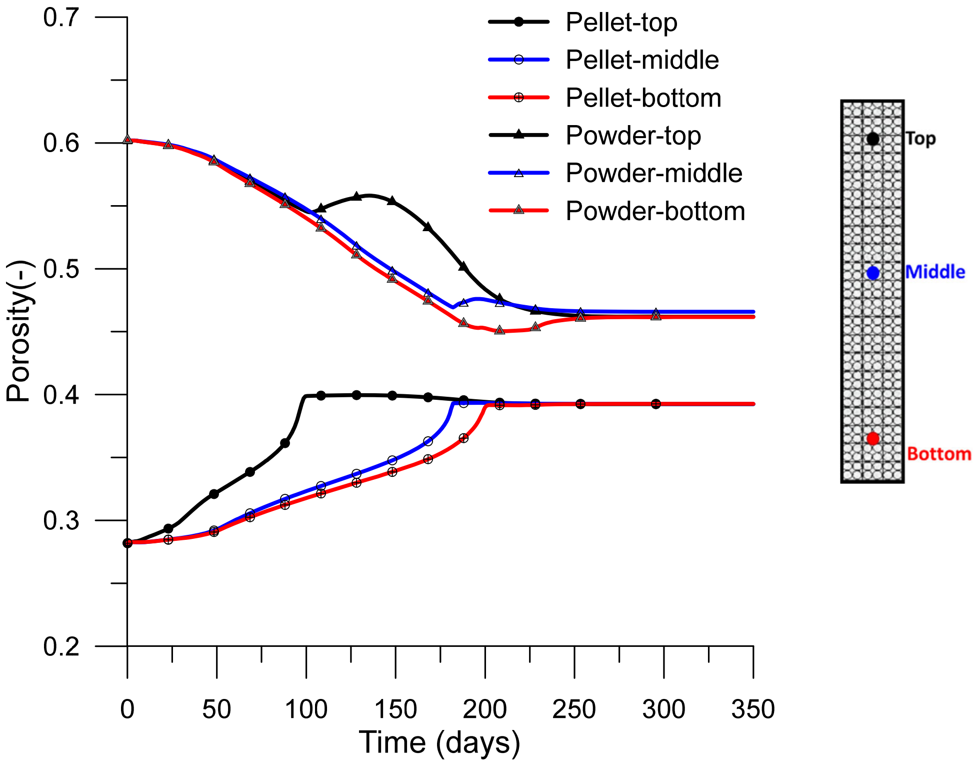

Figure 6-17. Porosity evolution at different elapsed times.

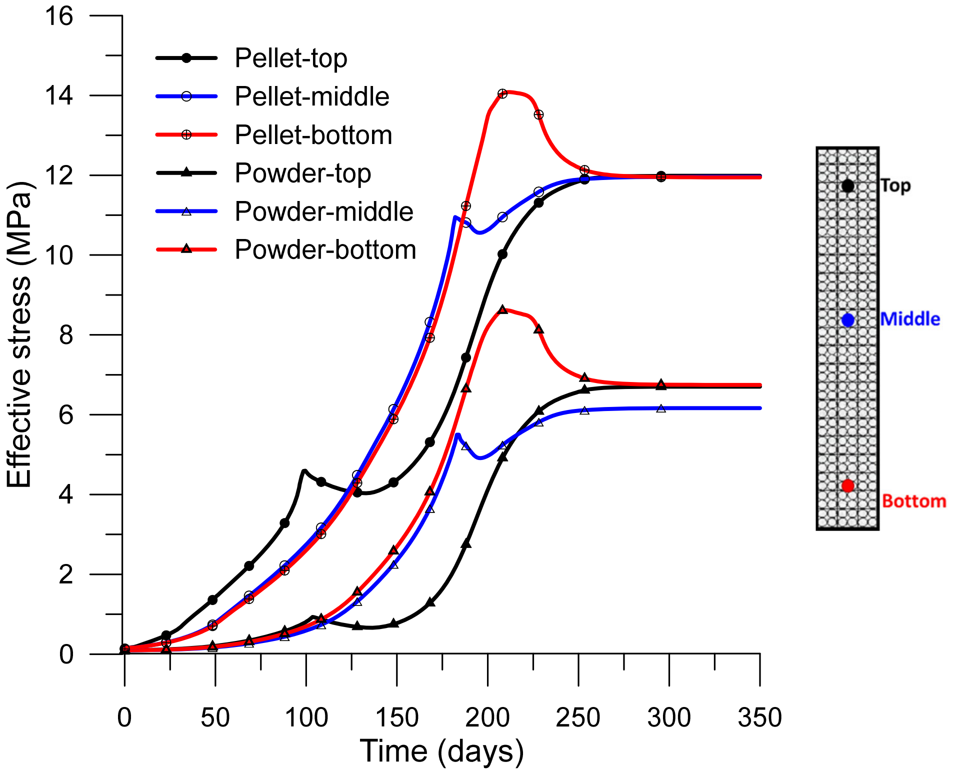

Figure 6-18. Effective stress evolution at different elapsed times for the powder and pellets.

Figure 6-19 shows the variations in time of suction within the pellets and powder at three different positions (top, middle and bottom). At the top boundary, the model shows a relatively fast decrease of suction within the pellets and powder as top hydration started. A reduction in suction at the middle and bottom zones is also observed but with a delay associated with the slow hydration rate imposed at the lateral boundary. At the three locations, suctions within the pellets and powder remain in equilibrium and decrease at a similar rate. Although a higher suction value was imposed within the pellets (s_{pe} = 160 MPa; s_{pow} = 85 MPa), this initial gradient dissipates rapidly due to the local transfer of water from the powder to the pellets in addition to the slight difference in permeability's initial values of both mixture components.

Figure 6-20 shows distributions of the degree of saturation at different times. Initially, the pellets show a higher degree of saturation because different retention properties were considered for the mixture components. As expected, an increasing saturation is observed at the zones close to the hydration boundaries. At the top of the mixture, a rapid increase of S_r is observed within the pellets and the powder due to the fast axial hydration. Equal values of S_r are obtained at equal distances from the lateral hydration boundary (Figure 6-20 and Figure 6-21). The pellets at different locations reach faster full saturation because different hydraulic properties were considered for each component (Figure 6-15 and Table 6-6).

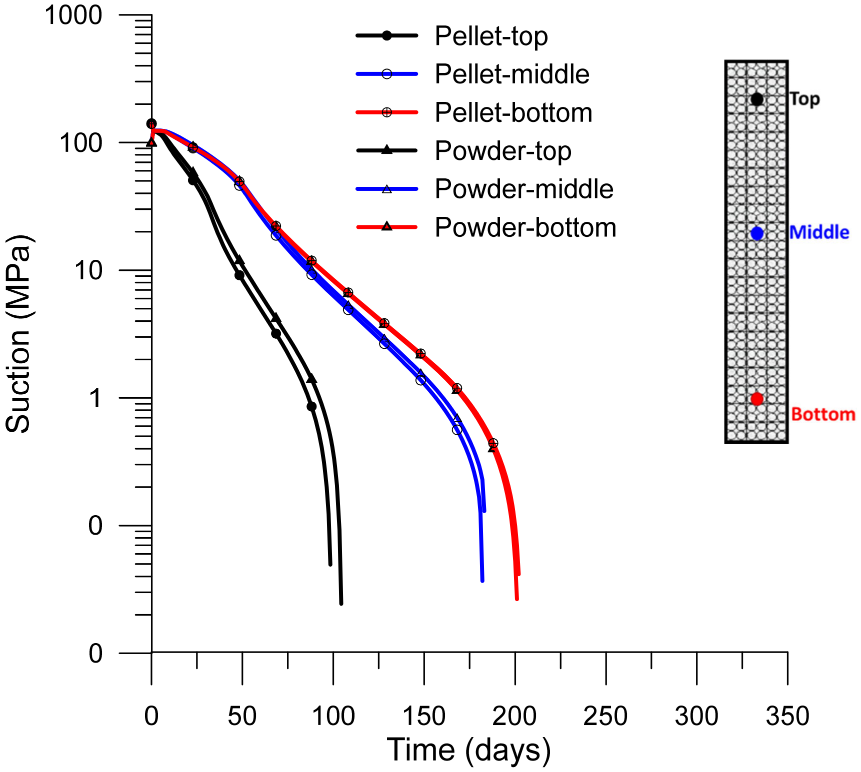

Figure 6-19. Suction evolution within the pellet and the powder at different elapsed times and positions.

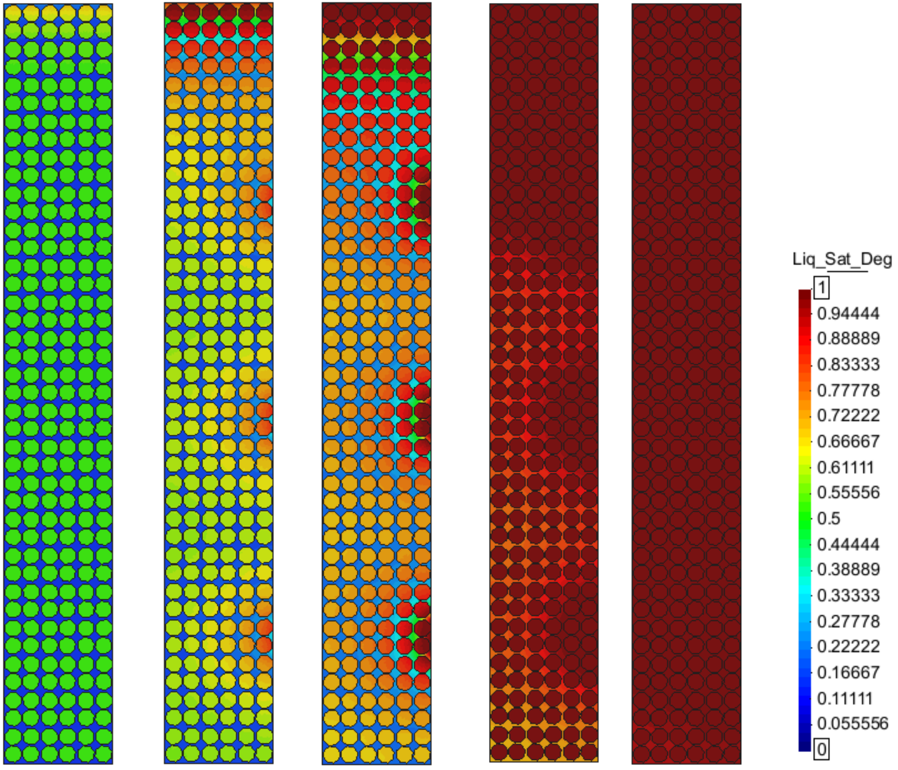

5 days 30 days 50 days 150 days 200days

Figure 6-20. Distribution of degree of saturation at different elapsed times.

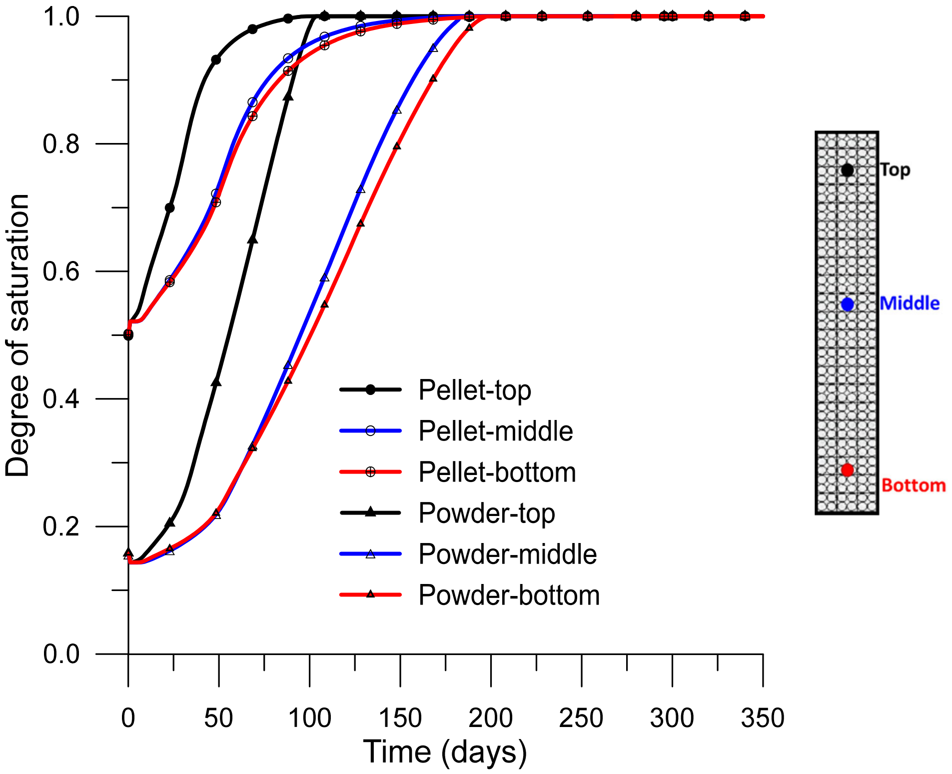

Figure 6-21.Degree of saturation evolution at different elapsed times.

The numerical dual-porosity model allows exploring the distinct evolution of pellets and powder hydraulic properties. Figure 6-22 shows the water retention curves of the pellets and powder at the initial state and after hydration as predicted by the model. The results are compared to experimental data obtained by Molinero-Guerra (2018) on the mixture tested under constant volume condition and on pellets equilibrated at different suction values under free swelling condition (different final porosities). Obviously, each point of Molinero-Guerra's data on the pellets lies on a distinct water retention curve. The predicted water retention curves of the pellets and the powder adequately follow the trend of the data reported by Molinero–Guerra (2018). At a given degree of saturation, a reduction of matric suction is obtained for the pellets, while the reverse pattern of behaviour was observed for the powder. The observed behaviour is in agreement with the expected change in retention properties due to porosity change (Figure 6-22). Interestingly, the predicted pellet and powder water retention curve seem to meet the mixture model data suggesting a homogenization of the retention properties of the material after hydration.

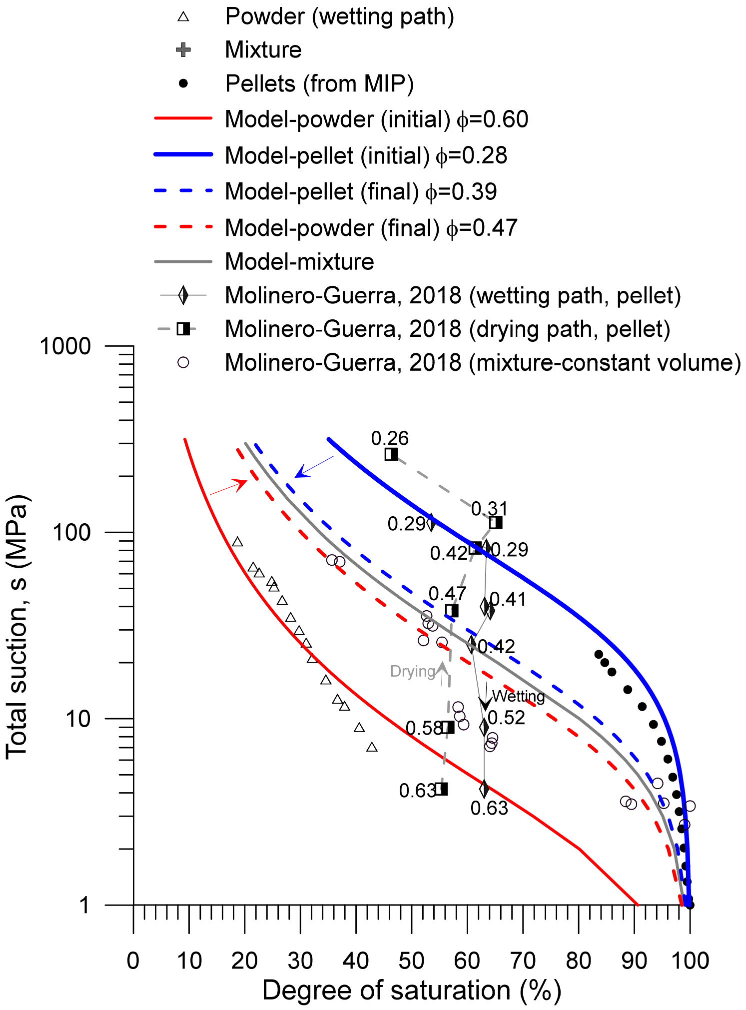

Figure 6-22. Suction evolution as a function of the degree of saturation.

Figure 6-23 shows the evolution of pellets and powder permeability's at different positions (top, middle and bottom). Upon hydration, there is a decrease in the powder permeability as a consequence of the powder compression while the pellets are expanding (Figure 6-17). The reverse trend is observed for the pellet permeability. Taking into account the assumed elastic behaviour of the components, a reduction of the initial permeability gradient is predicted suggesting the possible long term homogenisation of the mixture again.

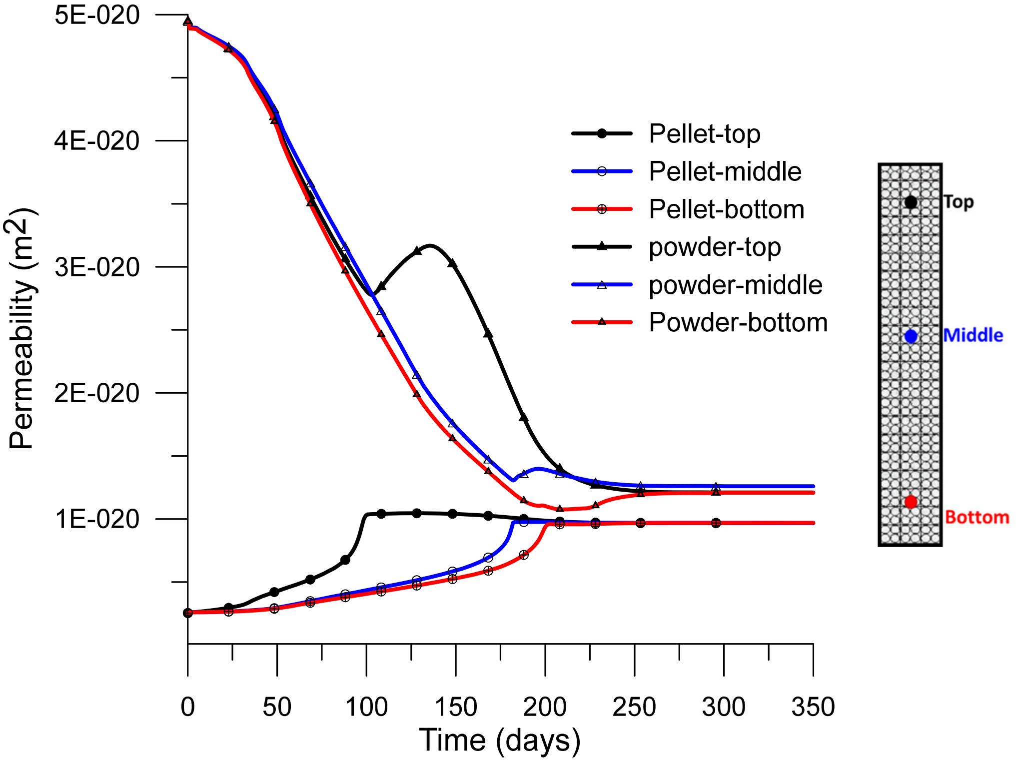

Figure 6-23.Permeability evolution at different elapsed times.

6.3.5. Concluding remarks

The HM behaviour of the MX80 bentonite pellet/powder mixture (80/20 in dry mass) intended as a sealing material in underground repositories for radioactive waste was analysed using two complementary modelling approaches. In the first approach, a fully coupled elastoplastic model which takes into account the multimodal nature of the bentonite pellet/powder mixture is used while in the second approach a numerical dual porosity model allowing to introduce a uniform heterogeneous distribution of initial porosity is adopted. In both cases, model parameters were determined based on laboratory experimental results. The analysis carried out has demonstrated a number of interesting features. Both modelling approaches show an increasing saturation in the zones close to the hydration boundaries. In addition, when different hydration properties are assumed for the mixture components, the pellets at different locations reach faster full saturation (numerical dual porosity model).

The total stress evolution rates and magnitudes are not well reproduced by the elastic-plastic model suggesting the existence of local variations (hydraulic and mechanical) not well captured by the homogenous model. Some differences are observed between the model predictions and the hydraulic evolution of the test. Globally, a faster saturation rate is predicted by the model. This can be because the behaviour of the mixture of bentonite powder and highly compacted pellets is more complex so the necessity to account for an initial heterogeneous dry density distribution (heterogeneous porosity field) to improve the predictive capability. The numerical dual porosity model allowed to introduce a uniform heterogeneous porosity field so to explore the distinct evolution of pellets and powder hydraulic properties. Interestingly, the predicted pellet and powder water retention curve seem to meets at the mixture experimental data. A reduction of the initial permeability gradient is also predicted. These results suggest a possible long term homogenization of the mixture.

7. CONCLUSIONS AND PERSPECTIVES

7.1. Summary and main contributions of the thesis

The thesis has explored the behaviour of MX80 bentonite pellet-based mixture within the context of the French shaft 'Vertical Sealing Systems' (VSS, Cigeo) to appropriately seal these critical vertical pathways between the long-lived radioactive waste and the biosphere. The bentonite-based barrier, placed at an adequate dry density to close gaps and fissures of the excavation damaged zone correctly, will be subjected to complex hydration scenarios since the long VSSs cross different formations. Specifically, it will experience fast hydration from the upper Calcareous Oxfordian formation and slower lateral hydration from the more impermeable Callovo-Oxfordian sedimentary rock. This particular hydration also induces gas entrapment with time at the bottom of the seal, which will also be affected by gas generated by other long-term processes, such as anaerobic corrosion of metallic canisters and the degradation of organic substances. Therefore, a complete understanding of the VSSs under hydraulic and gas solicitations is required for assessing their correct long-term performance.

The French Institute for Radiological Protection and Nuclear Safety (IRSN), which supported the current research, decided to undertake experiments at contrasting scales to understand and upscale the behaviour of VSSs during hydraulic and gas entrapment/generation processes. On the one hand, the 'VSEAL Project: Long-term performance of vertical sealing systems and impact of gas migration' (IRSN, 2016) relied on the VSEAL *in situ* tests currently being performed in Tournemire URL (France) at a scale of 1/10 of the VSS. On the other hand, IRSN started a collaboration with CIMNE/UPC within the present thesis framework to set up and run mock-up tests at a scale of 1/100 of the VSS.

The thesis initially addressed thoroughly characterising the mixture's initial and saturated states (both at the microstructural and macroscopic scales) and the mixture's hydro-mechanical behaviour and its components (high-density pellets and poured crushed granular powder). The perfectly installed high-density pellets (dry density of 2.0 Mg/m^3) at a mass ratio of 80% constituted the shielding skeleton, whereas the crushed powder (at a dry density of 1.1 Mg/m^3) filled the inter-pellet space to reach an overall dry density of 1.47 Mg/m^3 that ensured a swelling pressure around 4 MPa. The hydro-mechanical characterisation involved water permeability tests under constant volume, water retention curves on wetting under different mechanical boundary conditions, wetting under constant stress, swelling pressure tests and loading/unloading oedometer tests at different hydraulic states.

A mock-up with independent control of fast hydration at the top and slow lateral hydration was developed, calibrated, and set up, in which a column of the bentonite mixture (100 mm in diameter and 350 mm high) was asymmetrically wetted under constant volume conditions. The hydration cell was fully instrumented: three pore pressure transducers besides four independent water pressure/volume controllers (one at the top boundary and three lateral ones on hydration rings), six total stress sensors and three relative humidity sensors to monitor all processes comprehensively. A long-term hydration stage (around 300 days) was initially performed. At the end of this stage (before reaching saturation and therefore without having the entire swelling pressure developed), gas was injected at a controlled volume/pressure rate at different boundaries (top and bottom) to determine the maximum gas overpressure that the bentonite-based barrier could withstand. The gas experiments were also devoted to detecting gas flows at the interface in zones with low effective stresses.

The experimental program's information (mock-up test, hydro-mechanical characterisation and multimodal pore size distributions) allowed using different double porosity models and their interactions via Code_Bright (Olivella et al., 1996). The model parameters were determined based on the back-analysis of laboratory test results on the pellets, powder, and mixture. Two modelling approaches were adopted to simulate the hydration phase at constant volume. A fully coupled elastoplastic model (Barcelona Expansive Model in 2D axisymmetric representation) that considers two dominant pore levels (micro and macro-porosity) was initially used to simulate infiltration results and better understand the different coupled and double porosity processes involved. A numerical dual-porosity model (2D plane strain) was also considered to account for the mixture's heterogeneous dry density distribution and represent the mixture's double structure with pellets and powder as two distinct materials.

7.2. Conclusions

The main conclusions drawn from this thesis during the achievements of the main contributions (objectives) mentioned above are summarised in the following.

7.2.1. Pellet-based mixture and hydro-mechanical properties

- The homogeneity of different mixture's installation protocols was verified by computed axial tomography. A strict installation protocol of the mixture was followed in the mock-up, reach the target dry density (1.49 Mg/m^3), and ensure less heterogeneity. First, the pellet shielding skeleton (80% mass ratio) was correctly arranged layer by layer (emplacing 50 layers) to achieve a minimum coordination number of 8, which allowed reaching a dry density close to 1.19 Mg/m^3 of the packing of pellets. The dry crushed powder at 1.10 Mg/m^3 was afterwards poured to fill the inter-pellet porosity partially (filling ratio around 61%).

- It was important to check the possibility of powder movement (segregation) during pouring through the shielding skeleton. In the case of the 7 mm pellet size, no significant movement of the crushed powder was expected and observed during the installation of the mixture in the mock-up. Nevertheless, segregation effects should be checked when using larger sizes of pellets (> 16 mm).

- The components and the mixture displayed multi-modal PSDs that significantly evolved during saturation. The micro and macrostructural porosities of the mixture at the two hydraulic states (as-prepared and saturated) were useful for double porosity approaches (Barcelona Expansive Model BExM) and pellet representation models as those implemented in the thesis. Particularly, it was helpful to address the effect of the compressibility parameter for changes in mean effective stress at the micro-porosity scale during loading at constant water content. Two competing effects occur at different pore-size scales: (a) compression due to mean net stress increase; and (b) expansion on induced suction reduction that mainly affects the micro-porosity level.
- In relation to hydraulic aspects, the powder and mixture's intrinsic permeability was measured under controlled-gradient conditions (5.642 $\times10^{-20}$ m^2 and 1.17 $\times10^{-20}$ m^2, respectively). In contrast, the pellet's intrinsic permeability was estimated by MIP data interpreted with the Hagen-Poiseuille equation (1.60 $\times10^{-21}$ m^2). The consistent permeability results of the mixture and components were fitted to a unique Kozeny-Carman equation depending on porosity. The water retention results on wetting of the mixture and components in terms of water content presented no significant changes at water contents $w < 10\%$ (the water retention curves at these low water contents were not sensitive to void ratio and pore size distribution changes). Nevertheless, essential differences were observed at higher water contents because of porosity variations. The water retention curves in terms of the degree of saturation are thus highly dependent on the total porosity evolution.
- Regarding the mechanical response on wetting, the mixture attained a swelling pressure close to 4.4 MPa on wetting (for comparison, the crushed powder at the poured dry density reached 0.7 MPa). Anisotropy effects were observed when loading the packing of pellets or the mixture at different orientations of the pellets (higher compressibility when loading the pellets along the axis of symmetry, which is associated with the fissuring of the spherical caps of the pellet detected by FESEM micrographs).

7.2.2. Hydration and gas injection tests performed in the mock-up

- During the long period of the mixture installation in the mock-up (28 days during which 50 layers of pellets were placed), the dry mixture underwent a total suction decrease associated with the relative humidity prevailing under laboratory conditions (RH around 50%). There was also an initial difference between the pellets' initial total suction (around 160 MPa) and the crushed powder (around 80 MPa). Therefore, the first step was to use a forced convection circuit for vapour transfer for 25 days to homogeneously set and restore an initial total suction of 160 MPa (RH = 31%), close to the one initially measured in pellets.

- The hydration phase started by imposing a relative humidity RH = 75% (s = 39 MPa) on the top and lateral inlets for 101 days, which allowed developing low swelling (total) stress at the column's upper zone before liquid injection. There was some concern raised during the initial equalisation phase to set the initial total suction (160 MPa) that the sample would shrink and not ensure some swelling pressure at the boundaries.

- Afterwards, liquid water was injected at a controlled volume rate (initially fast on the top boundary until reaching 4 MPa and later at a slower volume rate on the lateral boundaries). Water pressure reached 4 MPa at the top and middle rings after 147 and 254 days, respectively, while it increased only to 1.8 MPa at the bottom ring after 298 days. The volume of injected water was continuously recorded and used to determine the sample's global degree of saturation. The dominant hydration at the top boundary induced gas entrapment at the mixture's bottom zone, which prevented the sample from being fully saturated and developing high swelling stresses (the water pressure at the bottom was not able to dissolve this volume of entrapped gas). The overall degree of saturation reached a value around 89.9% before the first gas injection test at 304 days.

- The evolution of total stresses at different locations showed differentiated evolutions and final values. The rate of increase of total stresses was affected by the hydration front and the material's local porosity, which depended on the pellet/powder structural distribution at the corresponding position. The observed peaks corresponded to macrostructural rearrangements induced by the collapse of the larger voids associated with (net) stress increase. During hydration, pellets swelled and lost stiffness, inducing the filling of these larger pores between them, tending towards a dominant monomodal pore size distribution.

- The material at the top boundary (approx. 20 mm) developed low axial swelling stress (around 0.64 MPa), partially due to the fast water pressure increase at the top (4 MPa) when swelling stress had not reached its total capacity. The high porosity induced at the top –observed in the upper ring and confirmed by modelling– induced the creation of a gel-like structure. According to modelling results, this gel-like material's total porosity is around 0.62, corresponding to exceptionally soft material with a dry density of 1.04 Mg/m3. It is worth remarking that this behaviour was not expected, as the material was supposed to develop high axial swelling stress. This result highlighted the importance of using a slower volumetric water injection rate to allow axial stress to develop.
    - Higher radial swelling (effective) stresses (between 1.2 and 2.3 MPa) were measured at the column's upper saturated zone before the first gas injection test. The partially saturated and denser zone reached a bottom axial (net) stress of 1.1 MPa before the first gas injection test. On saturation, this bottom zone developed a high axial effective stress of 3.6 MPa due to the material's densification at the bottom of the cell during the early stage of top and lateral hydrations.
    - During the first gas injection (bottom boundary) at a global degree of saturation of 89.9% (water pressure at the boundaries was held at 4 MPa), no clear gas pathways were observed throughout the transparent rings. However, the consistency in the rate and magnitude of the top lateral total stress sensors –close to the gas injection pressure of 5 MPa– indicated a gas pathway remarkably near the sample/wall interface. The pathway close to the interface was driven by the significant reduction of the lateral swelling stress (around 0.5 MPa). Nevertheless, no significant outflow (gas breakthrough) was detected in the pressure/volume controllers. During the fast gas pressure increase, the saturated upper plug was pushed –due to piston effect– against the top and lateral boundaries, where some outflow

volumes (consolidation of the plug) were detected driven by the water pressure increase. The interface between the partially saturated / highly gas-connected zone and the saturated zone acting as a plug was clearly observed in the second Perspex ring (from the bottom).

- The second gas test (global degree of saturation of 97.4% and water pressure at the boundaries of 1 MPa) was performed at a high-pressure rate by injecting gas from the top boundary and starting from 1.67 MPa. This initial gas pressure was higher than the top axial swelling stress and a gap generated between the gel-type material and the top cap. The gas pressure acted as total stress (piston effect) that pushed the sample against the bottom boundary. Preferential paths developed at the top lateral interface with low initial effective stress, which was consistent with the outflows detected by the lateral pressure/volume controller (around a gas pressure 5.3 MPa). A by-pass to the next pressure/volume controller of the gas outflow (once the top one was closed) confirmed the gas pathway's preservation at the interface (gas pressure 5.3 MPa).

7.2.3. Modelling hydration in the mock-up

- The modelling approach based on the discretisation in Code_Bright of pellets and inter-pellet powder that approximately matched the mixture's mass ratio (mass ratio of pellets 78%) provided interesting information, although the mock-up results were not directly compared with experimental data. The simulation results with non-linear elastic behaviour of the components showed that the mixture on hydration tended to a more homogeneous distribution of porosity, despite starting from contrasting porosities of the components, as the pellets expanded and compressed the highly deformable clay powder. The results also indicated that pellets reached full saturation first than the powder due to their lower porosity and higher air-entry value. This behavioural response was similar at different column positions, except for the powder located at the top close to the fast hydration boundary. The powder underwent fast saturation at this position, and the mean effective stress decreased due to the increase in water pressure. This fact caused a brief local expansion of the powder, which decreased when the saturation front advanced and compressed the top mixture. The evolution of intrinsic permeability and water retention curves of the components on hydration, which depended on porosity, tended to match the experimental data of the mixture properties, suggesting a homogenisation of the hydraulic properties of the material during saturation.

- The 2D axisymmetric representation in Code_Bright using the elastic-plastic Barcelona Expansive Model (BExM) to describe the double porosity mixture's mechanical behaviour (micro and macro-porosity) considered the correct hydraulic boundary conditions from the laboratory mock-up test. The model's results were compared with the mock-up data. The model predicted a faster total suction decrease rate (faster saturation rate). Therefore, the total stress evolutions and magnitudes were also not well captured. For example, as the mixture started hydrating and expanding at the top (with an increase in permeability), the bottom part was highly compressed, inducing a significant decrease in permeability. The model correctly captured the evolution of macro-pore reduction and micro-pore expansion, resulting in a decrease in permeability. Nevertheless, the sensitivity analyses demonstrated the significant role of intrinsic permeability as a function of macro-porosity on the mixture's hydro-mechanical behaviour.

7.3. Perspectives

The research work carried out in this PhD has enabled a better understanding of the mixture's hydration and the consequences on subsequent gas injection under varying partially saturated conditions. However, several aspects would value additional investigations to increase our understanding. Some of these new perspectives are summarised in the following.

- To run a mock-up test with a slightly lower pellet's mass fraction (75%) to ensure higher initial inter-pellet filling by powder (around 82% compared to the current 61%). This change will also allow better homogeneity and higher mixture dry density (around 1.59 Mg/m^3).

- The heterogeneity of the mixture (porosity-based, permeability-based heterogeneity) impacts saturation and gas transport processes. Gas preferential paths can be seen as a natural outcome of heterogeneity (gas pathways through low-density paths). Therefore, it is essential to characterise the initial as-installed heterogeneity and its evolution with saturation at constant volume using X-ray microtomography to track local density variations.

- To perform gas tests at a lower volume (mass) rate to slow down gas pressure increase and avoid any by-pass between inlet and outlet (originating internal erosion of fine particles), as well as any significant 'piston effect' (total stress applied by gas pressure before gas penetration).

- To describe a dismantling 'post mortem' protocol to perform an in-depth characterisation of the saturated mixture. Large sample retrieval zones and smaller sub-sampling zones for X-ray microtomography should be defined at different sample locations. The following post mortem tests are envisaged at different locations: water content, dry density, mercury intrusion porosimetry, and X-ray microtomography.

- To perform an interface test to mimic the behaviour between the host rock (Tournemire argillite) and the mixture during fast hydration of the bentonite top surface and subsequent gas injection from the bottom. The test will better understand local processes occurring throughout the bentonite/argillite interface at different stress states (erosion of fine particles at the interface, hydraulic fracturing, gas migration at the interface and pathway dilation). A hollow cylinder of Tournemire argillite will be filled with the mixture. The mixture will be hydrated at constant volume by injecting water from the top, while gas injection will be carried out from the bottom at different saturation states. Two set-ups can be used at the lateral boundary of the hollow cylinder. It can be either placed in a large triaxial cell with control of lateral stress or inserted into a rigid lateral ring to preserve the integrity of the argillite during swelling pressure development of the inner core.

- The hydro-mechanical simulations could probably be improved using a constitutive double-structure model that considers a heterogeneous porosity distribution (heterogeneous macro-porosity field) of the as-prepared configuration and based on X-ray microtomography data. Gas injection simulations could also benefit considering the impact of heterogeneity (porosity-based or permeability-based heterogeneity) or the opening of stress-dependent pathways (embedded cubic law permeability based on aperture variations during deformations to represent discontinuities and interfaces

REFERENCES

AITEMIN, 2001. The EB experiment engineered barrier emplacement in Opalinus Clay. Test Plan, version 3.0. NAGRA, Switzerland.

Alonso, E., Gens, A., & Josa, A. (1990). A constitutive model for partially saturated soils. *Géotechnique*, *40*(3), 405–430.

Alonso, E., Vaunat, J., & Gens, A. (1999). Modelling the mechanical behaviour of expansive clays. *Engineering Geology*, *54*(1–2), 173–183. https://doi.org/10.1016/S0013-7952(99)00079-4

Alonso, E., Romero, E., & Hoffmann, C. (2011). Hydromechanical behaviour of compacted granular expansive mixtures: experimental and constitutive study. *Géotechnique*, *61*(4), 329–344. https://doi.org/10.1680/geot.2011.61.4.329

Alonso, E., & Ramon, A. (2013). Heave of a railway bridge induced by gypsum crystal growth: Field observations. *Geotechnique*, *63*(9), 707–719. https://doi.org/10.1680/geot.12.P.034

Alonso, E., Sauter, S., & Ramon, A. (2015). Pile groups under deep expansion: A case history. *Canadian Geotechnical Journal*, *52*(8), 1111–1121. https://doi.org/10.1139/cgj-2014-0407

Alvarado, C. E. (2017). *Comportamiento hidro-mecánico de agregados gruesos*. Tesis Doctoral. Universitat Politècnica de Catalunya. https://upcommons.upc.edu/handle/2117/108234. Barcelona, 342 pp.

Ando, E. C. G. (2013). *Doctoral thesis: Experimental investigation of microstructural changes in deforming granular media using x-ray tomography*. Doctoral thesis. Universite de Grenoble. https://tel.archives-ouvertes.fr/tel-01144326.

ANDRA Dossier. (2005). *Safety evaluation of a geological repository*. ANDRA 270, Paris.

Angeli, M., Soldal, M., Skurtveit, E., & Aker, E. (2009). Experimental percolation of supercritical CO2 through a caprock. *Energy Procedia*, *1*(1), 3351–3358. https://doi.org/10.1016/j.egypro.2009.02.123

Arnedo, D., Alonso, E., Olivella, S., & Romero, E. (2008). Gas injection tests on sand/bentonite mixtures in the laboratory. Experimental results and numerical modelling. Physics and Chemistry of the Earth, 33(SUPPL. 1), 237–247. https://doi.org/10.1016/j.pce.2008.10.061

Barnichon, J. D. & Deleruyelle, F. (2009). *Sealing experiments at the Tournemire URL*. Technical report, IRSN. Towards convergence of technical nuclear safety practices in Europe, EUROSAFE

Barnichon, J. D., Dick, P., & Bauer, C. (2012). The SEALEX in situ experiments: performance tests of repository seals. *In: Qian, Zhou (Eds.), Harmonising Rock Engineering and the Environment.*, Taylor and Francis Group, London, pp. 1391-1394. ISRM-12CONGRESS-2011-252

Bhadha, P. M. (1999). How weld hose materials affect shielding gas quality. *Welding Journal*, *78*(7).

Carbonell, B., Villar, M. V., Martín, P. L., & Gutiérrez-Álvarez, C. (2019). Gas transport in compacted bentonite after 18 years under barrier conditions. *Geomechanics for Energy and the Environment*, *17*, 66–74. https://doi.org/10.1016/j.gete.2018.03.001

Cardoso, R., & Alonso, E. (2009). Degradation of compacted Marls: a microstructural investigation. *Soils and Foundations*, *49*(3), 315–327. https://doi.org/10.3208/sandf.49.315

Castellanos, E., Villar, M. V., Romero, E., Lloret, A., & Gens, A. (2008). Chemical impact on the hydro-mechanical behaviour of high-density FEBEX bentonite. *Physics and Chemistry of the Earth*, *33*(SUPPL. 1), 516–526. https://doi.org/10.1016/j.pce.2008.10.056

Chen, Y. G., Jia, L. Y., Li, Q., Ye, W. M., Cui, Y. J., & Chen, B. (2017). Swelling deformation of compacted GMZ bentonite experiencing chemical cycles of sodium-calcium exchange and salinization-desalinization effect. *Applied Clay Science*, *141*, 55–63. https://doi.org/10.1016/j.clay.2017.02.016

Chen, Y. G., Zhu, C. M., Ye, W. M., Cui, Y. J., & Wang, Q. (2015). Swelling pressure and hydraulic conductivity of compacted GMZ01 bentonite under salinization-desalinization cycle conditions. *Applied Clay Science*, *114*, 454–460. https://doi.org/10.1016/j.clay.2015.06.033

Cotecchia, F., Cafaro, F., & Guglielmi, S. (2016). Microstructural changes in clays generated by compression explored by means of SEM and image processing. *Procedia Engineering*, *158*, 57–62. https://doi.org/10.1016/j.proeng.2016.08.405

Cui, L. yong, Ye, W. M., Wang, Q., Chen, Y. G., Chen, B., & Cui, Y. J. (2021). Insights into gas migration behavior in saturated GMZ bentonite under flexible constraint conditions. *Construction and Building Materials*, *287*. https://doi.org/10.1016/j.conbuildmat.2021.123070

Cuisinier, O., Deneele, D., Masrouri, F., Abdallah, A., & Conil, N. (2014). Impact of high-pH fluid circulation on long term hydromechanical behaviour and microstructure of compacted clay from the laboratory of Meuse-Haute Marne (France). *Applied Clay Science*, *88–89*, 1–9. https://doi.org/10.1016/j.clay.2013.12.008

Cuss, R., Harrington, J. F., Giot, R., & Auvray, C. (2014). Experimental observations of mechanical dilation at the onset of gas flow in Callovo-Oxfordian claystone. *Geological Society Special Publication*, *400*(1), 507–519. https://doi.org/10.1144/SP400.26

Damians, I. P., Olivella, S., & Gens, A. (2020). Modelling gas flow in clay materials incorporating material heterogeneity and embedded fractures. *International Journal of Rock Mechanics and Mining Sciences*, *136*(April), 104524. https://doi.org/10.1016/j.ijrmms.2020.104524

Darde, B., Tang, A. M., Pereira, J. M., Roux, J. N., Dangla, P., Talandier, J., & Vu, M. N. (2018). Hydro-mechanical behaviour of high-density bentonite pellet on partial hydration. *Geotechnique Letters*, *8*(4), 330–335. https://doi.org/10.1680/jgele.18.00114

Darde, B., Roux, J. N., Pereira, J., Dangla, P., Talandier, J., Vu, M. N., & Tang, A. M. (2020). Investigating the hydromechanical behaviour of bentonite pellets by swelling pressure tests and discrete element modelling. *Acta Geotechnica*, 1–18. https://doi.org/10.1007/s11440-020-01040-5

De la Morena, G., Asensio, L., & Navarro, V. (2018). Intra-aggregate water content and void ratio model for MX-80 bentonites. *Engineering Geology*, *246*(July), 131–138. https://doi.org/10.1016/j.enggeo.2018.09.028

Delage, P., Marcial, D., Cui, Y. J., & Ruiz, X. (2006). Ageing effects in a compacted bentonite: A microstructure approach. *Geotechnique*, *56*(5), 291–304. https://doi.org/10.1680/geot.2006.56.5.291

Delage, P., Romero, E., & Tarantino, A. (2008). Recent developments in the techniques of controlling and measuring suction in unsaturated soils. *Unsaturated Soils: Advances in Geo-Engineering - Proceedings of the 1st European Conference on Unsaturated Soils, E-UNSAT 2008, Hilf*, 33–52. https://doi.org/10.1201/9780203884430.ch2

Desbois, G., Urai, J. L., Hemes, S., Brassinnes, S., De Craen, M., & Sillen, X. (2014). Nanometer-scale pore fluid distribution and drying damage in preserved clay cores from Belgian clay formations inferred by BIB-cryo-SEM. *Engineering Geology*, *179*, 117–131. https://doi.org/10.1016/j.enggeo.2014.07.004

Dieudonné, A.-C., Della Vecchia, G. and Charlier, R. (2017). A water retention model for compacted bentonites. *Canadian Geotechnical Journal,* 54 (7), 915-925.

Fraccica, A. (2019). *Experimental study and numerical modelling of soil-roots hydro-mechanical interaction*. Doctoral thesis. Universitat Politècnica de Catalunya. http://hdl.handle.net/2117/341613.

Gaus, I. (2011). *Long term performance of engineered barrier systems (PEBS). Mont Terri HE-E experiment*: detailed design report. NAGRA Arbeitsbericht NAB 11-01. Nagra, Wettingen, Switzerland.

Gens, A., & Alonso, E. (1992). A framework for the behaviour of unsaturated expansive clays. *Canadian Geotechnical Journal*, *29*(6), 1013–1032.

Gens, A., Sánchez, M., Valleján, B., Imbert, C., Villar, M. V., & Van Geet, M. (2011). Hydromechanical behaviour of a heterogeneous compacted soil: experimental observations and modelling. *Géotechnique*, *61*(5), 367–386. https://doi.org/10.1680/geot.SIP11.P.015

Gonzalez-Blanco, L., Romero, E., Jommi, C., Li, X., & Sillen, X. (2016). Gas migration in a Cenozoic clay: Experimental results and numerical modelling. *Geomechanics for Energy and the Environment*, *6*, 81–100. https://doi.org/10.1016/j.gete.2016.04.002

Gonzalez-Blanco, L. (2017). *Gas migration in deep argillaceous formations : Boom Clay and indurated clays*. Doctoral thesis. Universitat Politècnica de Catalunya. http://hdl.handle.net/2117/108499. Barcelona 287 pp.

Gonzalez-Blanco, L., Romero, E., Jommi, C., Sillen, X., & Li, X. (2017). Exploring fissure opening and their connectivity in a Cenozoic clay during gas injection. *Advances in Laboratory Testing and Modelling of Soils and Shales. Springer, Cham*, 288–295.

Gonzalez-Blanco, L., Romero, E., & Marschall, P. (2020). Gas transport in granular compacted bentonite: coupled hydro-mechanical interactions and microstructural features. *4th European Conference on Unsaturated Soils (E-UNSAT 2020)*, *195*, 04008. https://doi.org/10.1051/e3sconf/202019504008

Graham, C. C., Harrington, J. F., Cuss, R. J., & Sellin, P. (2012). Gas migration experiments in bentonite: implications for numerical modelling. *Mineralogical Magazine*, *76*(8), 3279–3292. https://doi.org/10.1180/minmag.2012.076.8.41

Gutiérrez-Rodrigo, V. (2018). *Transporte de gas en materiales de barrera*. Tesis Doctoral. Universidad Complutense de Madrid. Colección Documentos CIEMAT. ISBN: 978-84-7834-802-2. Madrid, 303 pp.

Gutiérrez-Rodrigo, V., Martín, P. L., & Villar, M. V. (2021). Effect of interfaces on gas breaktrough pressure in compacted bentonite used as engineered barrier for radioactive waste disposal. In *Process Safety and Environmental Protection* (Vol. 149, pp. 244–257). https://doi.org/10.1016/j.psep.2020.10.053

Harrington, J. F., & Horseman, S. T. (2003). Gas migration in KBS-3 buffer bentonite. Sensitivity of test parameters to experimental boundary conditions. In *Technical Report No. SKB-TR--03-02. Swedish Nuclear Fuel and Waste Management Co.*

Harrington, J. F., Graham, C. C., Cuss, R. J., & Norris, S. (2017). Gas network development in a precompacted bentonite experiment: Evidence of generation and evolution. *Applied Clay Science*, *147*, 80–89. https://doi.org/10.1016/j.clay.2017.07.005

Hildenbrand, A., Schlömer, S., Krooss, B. M., & Littke, R. (2004). Gas breakthrough experiments on pelitic rocks: Comparative study with N2, CO2 and CH4. *Geofluids*, *4*(1), 61–80. https://doi.org/10.1111/j.1468-8123.2004.00073.x

Hoffmann, C. (2005). *Caracterización hidromecánica de mezclas de pellets de bentonita. Estudio experimental y constitutivo.* Tesis Doctoral. Universitat Politècnica de Catalunya. ISBN 8468925411. http://www.tdx.cat/handle/10803/6235.

Hoffmann, C., Alonso, E., & Romero, E. (2007). Hydro-mechanical behaviour of bentonite pellet mixtures. *Physics and Chemistry of the Earth, Parts A/B/C*, *32*(8–14), 832–849. https://doi.org/10.1016/j.pce.2006.04.037

Horseman, S. T., Harrington, J. F., & Sellin, P. (1996). Gas migration in Mx80 buffer bentonite. *Symposium on the Scientific Basis for Nuclear Waste Management XX (Boston). Materials Research Society*, *465*. https://doi.org/http://dx.doi.org/10.1557/PROC- 465-1003

Horseman, S. T., Harrington, J. F., & Sellin, P. (1999). Gas migration in clay barriers. *Engineering Geology*, *54*(1–2), 139–149. https://doi.org/10.1016/S0013-7952(99)00069-1

Horseman, S. T., Harrington, J. F., & Sellin, P. (2004). Water and gas movenent in MX80 Bentonite buffer clay. *Mat. Res. Soc. Symp. Proc.*, *807*, 1–5.

Imbert, C., & Villar, M. V. (2006). Hydro-mechanical response of a bentonite pellets/powder mixture upon infiltration. *Applied Clay Science*, *32*(3–4), 197–209. https://doi.org/10.1016/J.CLAY.2006.01.005

Jacinto, A. C., Villar, M. V., & Ledesma, A. (2012). Influence of water density on the water-retention curve of expansive clays. *Geotechnique*, *62*(8), 657–667. https://doi.org/http://dx.doi.org/10.1680/geot.7.00127

Janssen, G.-J. (2015). Information on the FESEM (Field-emission Scanning Electron Microscope). *Radboud University Nijmegen*, 1–5. http://www.vcbio.science.ru.nl/public/pdf/fesem_info_eng.pdf

Kamiya, K., & Uno, T. (2000). Grain size and void diameter distributions of sands. In *Unsaturated soils for Asia. Proceedings of the Asian Conference on Unsaturated Soils, UNSAT-ASIA 2000, Singapore, 18-19 May, 2000 AA* (pp. 399–404).

Karnland, O., Nilsson, U., Weber, H., & Wersin, P. (2008). Sealing ability of Wyoming bentonite pellets foreseen as buffer material – Laboratory results. *Physics and Chemistry of the Earth, Parts A/B/C*, *33*, S472–S475. https://doi.org/10.1016/J.PCE.2008.10.024

Keller, P. E., & Kouzes, R. (2017). *Water Vapor Permeation in Plastics*. Technical report. Homeland Secuiry. http://www.ntis.gov/ordering.htm.

Klinkenberg, L. J. (1941). The permeability of porous media to liquids and gases. *Drilling and Production Practice. American Petroleum Inst.,* 200–213.

Lajudie, A., Raynal, J., Petit, J.-C., & Toulhoat, P. (1994). Clay-based material for engeneereed barrier: a review. *CEA Centre D´Eudes de Cadarache*, *353*(1), 221–230.

Liu, J. F., Shi, B., Zhou, J., & Tang, C. (2011). Quantification and characterization of microporosity by image processing, geometric measurement and statistical methods: Application on SEM images of clay materials. *Applied Clay Science*, *54*(1), 97–106. https://doi.org/10.1016/j.clay.2011.07.022

Liu, J. F., Davy, C. A., Talandier, J., & Skoczylas, F. (2014). Effect of gas pressure on the sealing efficiency of compacted bentonite-sand plugs. *Journal of Contaminant Hydrology*, *170*, 10–27. https://doi.org/10.1016/j.jconhyd.2014.09.006

Liu, J. F., Guo, J. N., Ni, H. Y., Zhang, Q., & Skoczylas, F. (2021). Swelling and gas transport characteristics of saturated compacted bentonite/sand samples considering the scale effect. *Geomechanics for Energy and the Environment*, *26*. https://doi.org/10.1016/j.gete.2020.100227

Lloret, A., & Villar, M. V. (2007). Advances on the knowledge of the thermo-hydro-mechanical behaviour of heavily compacted "FEBEX" bentonite. *Physics and Chemistry of the Earth, Parts A/B/C*, *32*(8–14), 701–715. https://doi.org/10.1016/j.pce.2006.03.002

Lloret, A., Villar, M. V., Alonso, E., Sánchez, M., Gens, A., & Pintado, X. (2003). Mechanical behaviour of heavily compacted bentonite under high suction changes. *Géotechnique*, *53*(1), 27–40. https://doi.org/10.1680/geot.2003.53.1.27

Marschall, P., Horseman, S. T., & Gimmi, T. (2005). Characterisation of gas transport properties of the Opalinus Clay, a potential host rock formation for radioactive waste disposal. *Oil and Gas Science and Technology*, *60*(1), 121–139. https://doi.org/10.2516/ogst:2005008

Mayor, J., García-Siñeriz, J., Alonso, E., Alheid, H., & Blümling, P. (2005). *Engineered barrier emplacement experiment in Opalinus Clay for the disposal of radioactive waste in underground repositories*. Final Report. Publicación Técnica ENRESA 02/05. Madrid, 101 pp.

Mesa-Alcantara, A. (2014). *Mezclas de bloques y pellets de bentonita Febex. Estudio de densidades secas después de una etapa de humedecimiento Tesis Master:* Universitat Politècnica de Catalunya. http://hdl.handle.net/2099.1/24218.

Mesa-Alcantara, A., Romero, E., Mokni, N., & Olivella, S. (2020a). Microstructural and hydro-mechanical behaviour of bentonite pellets and powder mixtures. *4th European Conference on Unsaturated Soils (E-UNSAT 2020)*, *195*, 04003. https://doi.org/10.1051/e3sconf/202019504003

Mesa-Alcantara, A., Mokni, N., Romero, E., & Olivella, S. (2020b). Modelling of oedometer tests on pellet-powder bentonite mixtures to support mock-up test analysis. *4th European Conference on Unsaturated Soils (E-UNSAT 2020)*, *195*, 04004. https://doi.org/10.1051/e3sconf/202019504004

Middelhoff, M. (2020). *Hydro-mechanical behavior of claystone-based backfill materials under geo-environmental conditions*. Doctoral thesis. UNIVERSITÉ DE LORRAINE. https://hal.univ-lorraine.fr/tel-03202708. Lorraine, 211 pp.

Mokni, N. (2016). *Report Vseal project: Long-term performance of vertical sealing systems - Impact of gas migration*. IRSN (France) Internal report,22 pp.

Mokni, N., & Barnichon, J.-D. (2016a). SEALEX in-situ experiments-performance tests of repository seals: experimental observations and modelling. *E3S Web of Conferences*, *9*(04006 (2016) E-UNSAT 2016). https://doi.org/10.1051/e3sconf/20160904006

Mokni, N., & Barnichon, J.-D. (2016b). Hydro-mechanical analysis of SEALEX in-situ tests — Impact of technological gaps on long term performance of repository seals. *Engineering Geology*, *205*, 81–92. https://doi.org/10.1016/j.enggeo.2016.02.013

Mokni, N., Molinero-Guerra, A., Cui, Y.-J., Delage, P., Aimedieu, P., Bornert, M., & Tang, A. M. (2019). Modelling the long-term hydro-mechanical behaviour of a bentonite pellet/powder mixture with consideration of initial structural heterogeneities. *Géotechnique*, *70*(7), 563–580. https://doi.org/10.1680/jgeot.18.p.110

Molinero-Guerra, A., Mokni, N., Delage, P., Cui, Y.-J., Tang, A. M., Aimedieu, P., Bernier, F., & Bornert, M. (2016). In-depth characterisation of a mixture composed of powder/pellets MX80 bentonite. *Applied Clay Science*, *135*, 538–546. https://doi.org/10.1016/j.clay.2016.10.030

Molinero-Guerra, A. (2018). *Experimental and numerical characterizations of the hydro- mechanical behavior of a heterogeneous material: pellet/powder bentonite mixture*. Doctoral thesis. Université Paris-Est/Ecole des Ponts ParisTech. https://pastel.archives-ouvertes.fr/tel-01982196. Paris, 190 pp.

Molinero-Guerra, A., Delage, P., Cui, Y. J., Mokni, N., Tang, A. M., Aimedieu, P., Bernier, F., & Bornert, M. (2020). Water-retention properties and microstructure changes of a bentonite pellet upon wetting/drying; application to radioactive waste disposal. *Geotechnique*, *70*(3), 199–209. https://doi.org/10.1680/jgeot.17.P.291

Navarro, V., Asensio, L., Yustres, Á., De la Morena, G., & Pintado, X. (2016). Swelling and mechanical erosion of MX-80 bentonite: Pinhole test simulation. *Engineering Geology*, *202*, 99–113. https://doi.org/10.1016/j.enggeo.2016.01.005

Navarro, V., De la Morena, G., Yustres, Á., González-Arteaga, J., & Asensio, L. (2017a). Predicting the swelling pressure of MX-80 bentonite. *Applied Clay Science*, *149*(May), 51–58. https://doi.org/10.1016/j.clay.2017.08.014

Navarro, V., Yustres, Á., Asensio, L., la Morena, G. De, González-Arteaga, J., Laurila, T., & Pintado, X. (2017b). Modelling of compacted bentonite swelling accounting for salinity effects. *Engineering Geology*, *223*(March), 48–58. https://doi.org/10.1016/j.enggeo.2017.04.016

Olivella, S., Gens, A., Carrera Ramírez, J., & Alonso, E. (1996). Numerical formulation for a simulator (CODE_BRIGHT) for the coupled analysis of saline media. *Engineering Computations*, *13*, 87–112. https://www.researchgate.net/publication/277052655

Pintado, X. (1999). *Ensayos THM para el Proyecto FEBEX realizados por la UPC-DIT*. Report 70- UPC-M-0-03. Barcelona, Spain.

Pintado, X., Lloret, A., & Romero, E. (2009). Assessment of the use of the vapour equilibrium technique in controlled-suction tests. *Canadian Geotechnical Journal*, *46*(4), 411–423. https://doi.org/10.1139/T08-130

Pousada, E. (1984). *Deformabilidad de las arcillas expansivas bajo succión controlada* [E.T.S.I. Caminos, Canales y Puertos (UPM)]. http://oa.upm.es/508/

Pusch, R. (1979). Highly compacted sodium bentonite for isolating rock-deposited radioactive waste products. *Nuclear Technology*, *45*, 153–157. https://www.tandfonline.com/doi/abs/10.13182/NT79-A32305

Pusch, R., Kärnland, O., Lajudie, A., & Decarreau, A. (1992). *MX 80 clay exposed to high temperatures and gamma radiation (No. SKB-TR--93-03). Swedish Nuclear Fuel and Waste Management Co*.

Ramon, A., Alonso, E., & Olivella, S. (2017). Hydro-chemo-mechanical modelling of tunnels in sulfated rocks. *Geotechnique*, *67*(11), 968–982. https://doi.org/10.1680/jgeot.SiP17.P.252

Ramon, A., & Alonso, E. (2018). Heave of a building induced by swelling of an anhydritic triassic claystone. *Rock Mechanics and Rock Engineering*, *51*(9), 2881–2894. https://doi.org/10.1007/s00603-018-1503-4

Rizzi, M., Seiphoori, A., Ferrari, A., Ceresetti, D. and Laloui, L. (2012). *Analysis of the behaviour of granular MX-80 bentonite in THM processes*. Nagra-Aktennotiz AN 12-102. Wettingen, Switzerland.

Romero, E. (1999). *Characterisation and thermo-hydro-mechanical behaviour of unsaturated Boom clay: an experimental study*. Doctoral thesis. Universitat Politècnica de Catalunya. ISBN8469999966. http://hdl.handle.net/2117/93536.

Romero, E., Gens, A., & Lloret, A. (1999). Water permeability, water retention and microstructure of unsaturated compacted Boom clay. *Engineering Geology*, *54*(1–2), 117–127. https://doi.org/10.1016/S0013-7952(99)00067-8

Romero, E., Garcia, I., & Alonso, E. (2003). *Project Report 03-03 GMT/IR 02-02: Laboratory gas tests on compacted sand-bentonite buffer material used in the GMT in-situ emplacement. National Cooperative for the Disposal of Radioactive Waste (nagra).*

Romero, E., & Simms, P. H. (2008). Microstructure investigation in unsaturated Soils: A Review with special attention to contribution of mercury intrusion porosimetry and environmental scanning electron microscopy. *Geotechnical and Geological Engineering*, *26*(6), 705–727. https://doi.org/10.1007/s10706-008-9204-5

Romero, E., Della Vecchia, G., & Jommi, C. (2011). An insight into the water retention properties of compacted clayey soils. *Géotechnique*, *61*(4), 313–328. https://doi.org/10.1680/geot.2011.61.4.313

Romero, E. (2013). A microstructural insight into compacted clayey soils and their hydraulic properties. *Engineering Geology*, *165*, 3–19. https://doi.org/10.1016/j.enggeo.2013.05.024

Romero, E., Senger, R., Marschall, P., & Gomez, R. (2013). Air tests on low-permeability claystone formations. Experimental results and simulations. *International Workshop Ad- Vances in Multiphysical Testing of Soils and Shales. 2012:69–83, July 2016*. https://doi.org/10.1007/978-3-642-32492-5

Romero, E., & Gonzalez-Blanco, L. (2017). *Hydro-mechanical processes associated with gas transport in MX-80 bentonite in the context of Nagra's RD&D programme*. NAGRA Technical Report NAB 17-09. 62 PP.

Saba, S. (2014). *Hydro-mechanical behaviour of bentonite-sand mixture used as sealing materials in radioactive waste*. Doctoral thesis. Université Paris-Est/Ecole des Ponts ParisTech. https://pastel.archives-ouvertes.fr/pastel-00985466. Paris, 171 pp.

Saba, S., Barnichon, J.-D., Cui, Y.-J., Tang, A. M., & Delage, P. (2014). Microstructure and anisotropic swelling behaviour of compacted bentonite/sand mixture. *Journal of Rock Mechanics and Geotechnical Engineering*, *6*, 126–132. https://doi.org/10.1016/j.jrmge.2014.01.006

Sánchez, M. (2004). *Thermo-hydro-mechanical coupled analysis in low permeability media*. Doctoral thesis. Universitat Politècnica de Catalunya. http://hdl.handle.net/2117/107703.

Sanchez, M., Gens, A., do Nascimento Guimaraes, L., & Olivella, S. (2005). A double structure generalized plasticity model for expansive materials. *International Journal for Numerical and Analytical Methods in Geomechanics*, *29*(8), 751–787. https://doi.org/10.1002/nag.434

Sánchez, M., & Gens, A. (2006). *FEBEX Project Final Report: Final Report on Thermo-hydro-mechanical Modelling*. ENRESA Technical Report 05-2/2006. Madrid, Spain.

Sau, N. (2013). *Cat scanner as a tool for geotechnical sample inspection*. Master Thesis. Universitat Politècnica de Catalunya. http://hdl.handle.net/2099.1/20721. Barcelona, 137 pp.

Schanz, T., & Al-Badran, Y. (2014). Swelling pressure characteristics of compacted Chinese Gaomiaozi bentonite GMZ01. In *Soils and Foundations* (Vol. 54, Issue 4, pp. 748–759). https://doi.org/10.1016/j.sandf.2014.06.026

Schindelin, J., Arganda-Carreras, I., Frise, E., Kaynig, V., Longair, M., Pietzsch, T., Preibisch, S., Rueden, C., Saalfeld, S., Schmid, B., Tinevez, J. Y., White, D. J., Hartenstein, V., Eliceiri, K., Tomancak, P., & Cardona, A. (2012). Fiji: An open-source platform for biological-image analysis. In *Nature Methods* (Vol. 9, Issue 7, pp. 676–682). Nature Publishing Group. https://doi.org/10.1038/nmeth.2019

Seiphoori, A. (2014). *Thermo-hydro-mechanical characterisation and modelling of MX-80 granular bentonite*. Doctoral thesis. Swiss Federal Institute of Technology. http://dx.doi.org/10.5075/epfl-thesis-6159.

Seiphoori, A., Ferrari, A., & Laloui, L. (2014). Water retention behaviour and microstructural evolution of MX-80 bentonite during wetting and drying cycles. *Géotechnique*, *64*(9), 721–734. https://doi.org/10.1680/geot.14.P.017

Sellin, P., & Leupin, O. X. (2013). The use of clay as an engineered barrier in radioactive-waste management - A review. *Clays and Clay Minerals*, *61*(6), 477–498. https://doi.org/10.1346/CCMN.2013.0610601

Shaw, R. P. (2013). Gas generation and migration. *International Symposium and Workshop, 5th to 7th February 2013 Luxembourg, Proceedings. 2013.269*.

Smellie, J., & Contrerra, A. (2001). *Wyoming Bentonites Evidence from the geological record to evaluate the suitability of bentonite as a buffer material during the long-term underground containment of radioactive wastes*. Technical Report. Sweden. ISSN 1404-0344; TRN: SE0200081017286.

Tang, A.-M., Cui, Y.-J., & Le, T.-T. (2008). A study on the thermal conductivity of compacted bentonites. *Applied Clay Science*, *41*(3–4), 181–189. https://doi.org/10.1016/J.CLAY.2007.11.001

Toprak, E., Olivella, S., & Pintado, X. (2018). Modelling engineered barriers for spent nuclear fuel repository using a double-structure model for pellets. *Environmental Geotechnics*, *7*(1), 72–94. https://doi.org/10.1680/jenge.17.00086

Tripathy, S., Sridharan, A., & Schanz, T. (2004). Swelling pressures of compacted bentonites from diffuse double layer theory. *Can. Geotech. J.*, *41*, 437–450. https://doi.org/10.1139/T03-096

Van Geet, M., Volckaert, G., & Roels, S. (2005). The use of microfocus X-ray computed tomography in characterising the hydration of a clay pellet/powder mixture. *Applied Clay Science*, *29*(2), 73–87. https://doi.org/10.1016/J.CLAY.2004.12.007

van Genuchten., M. T. (1980). A closed-form equation for predicting the hydraulic conductivity of unsaturated Soils. *Soil Science Society of America Journal Journal*, *44*, 892–898. https://doi.org/10.2136/sssaj1980.03615995004400050002x

Villar, M.V. (2002). *Thermo-hydro-mechanical characterisation of a bentonite from Cabo de Gata. A study applied to the use of bentonite as sealing material in high level radioactive waste repositories*. ENRESA Technical Publishing 01/2002. Madrid, Spain.

Villar, M. V. (2005). *MX-80 Bentonite. Thermo-Hydro-Mechanical Characterisation Performed at CIEMAT in the Context of the Prototype Project*. Informes Técnicos CIEMAT 1053. CIEMAT, Madrid, 39 pp. Febrero 2005.

Villar, M. V. (2006). Infiltration tests on a granite/bentonite mixture: Influence of water salinity. *Applied Clay Science*, *31*(1–2), 96–109. https://doi.org/10.1016/j.clay.2005.07.007

Villar, M. V. (2007). Water retention of two natural compacted bentonites. *Clays and Clay Minerals*, *55*(3), 311–322. https://doi.org/10.1346/CCMN.2007.0550307

Villar, M. V., & Lloret, A. (2007). Dismantling of the first section of the FEBEX in situ test : THM laboratory tests on the bentonite blocks retrieved. *Physics and Chemistry of the Earth, Parts A/B/C*, *32*(8–14), 716–729. https://doi.org/10.1016/j.pce.2006.03.009

Villar, M. V., & Lloret, A. (2008). Influence of dry density and water content on the swelling of a compacted bentonite. *Applied Clay Science*, *39*(1–2), 38–49. https://doi.org/10.1016/j.clay.2007.04.007

Villar, M. V., Gómez-Espina, R., & Gutiérrez-Nebot, L. (2012). Basal spacings of smectite in compacted bentonite. *Applied Clay Science*, *65–66*, 95–105. https://doi.org/10.1016/j.clay.2012.05.010

Villar, M. V., Romero, F. J., & Barcala, J. M. (2013). *Gas transport in bentonite*. Informes Técnicos CIEMAT 1301. Madrid, 63 pp. http://documenta.ciemat.es/handle/123456789/90.

Villar, M. V., Carbonell, B., Martín, P. L., Gutiérrez-Álvarez, C., & Barcala, J. M. (2020). *Gas Permeability of Bentonite Samples of the FEBEX Dismantling Project (FEBEX-DP)*. Informes Técnicos Ciemat 1431. Madrid,88 pp. http://documenta.ciemat.es/handle/123456789/761.

Villar, M. V., Carbonell, B., Martín, P. L., & Gutiérrez-Álvarez, C. (2021). The role of interfaces in the bentonite barrier of a nuclear waste repository on gas transport. *Engineering Geology*, *286*. https://doi.org/10.1016/j.enggeo.2021.106087

Volckaert, G., Dereeper, B., Put, M., Ortiz, L., Gens, A., Vaunat, J., Villar, M.V., Martin, P.L.,Imbert, C., Lassabatère, T., Mouche, E., Cany, F. (2000). "A large-scale in situ demonstration test for repository sealing in an argillaceous host rock". Reseal project - Phase I. EUR 19612 EN, European Commission, Brussels

Wang, Q., Cui, Y. J., Tang, A. M., Barnichon, J. D., Saba, S., Ye, W.-M. M., & Minh, A. (2013). Hydraulic conductivity and microstructure changes of compacted bentonite/sand mixture during hydration. *Engineering Geology*, *164*, 67–76. https://doi.org/10.1016/j.enggeo.2013.06.013

Wang, Q., Minh, A., Cui, Y., & Delage, P. (2013). The effects of technological voids on the hydro-mechanical behaviour of compacted bentonite – sand mixture. *Soils and Foundations*, *53*(2), 232–245. https://doi.org/10.1016/j.sandf.2013.02.004

Wang, Q., Tang, A. M., Cui, Y. J., Barnichon, J. D., & Ye, W.-M. M. (2013). Investigation of the hydro-mechanical behaviour of compacted bentonite/sand mixture based on the BExM model. *Computers and Geotechnics*, *54*, 46–52. https://doi.org/10.1016/j.compgeo.2013.05.011

Wang, Q., Tang, A. M., Cui, Y. J., Delage, P., & Gatmiri, B. (2012). Experimental study on the swelling behaviour of bentonite/claystone mixture. *Engineering Geology*, *124*(1), 59–66. https://doi.org/10.1016/j.enggeo.2011.10.003

Webb, P. A. (2001). An introduction to the physical characterization of materials by mercury intrusion porosimetry with emphasis on reduction and presentation of experimental data. In *Micromeritics Instrument Corp, Norcross, Georgia*.

Webb, P. A., & Orr, C. (1997). Analytical methods in fine particle technology. Micromeritics Instrument Corporation. *Micromeritics Instrument Corporation.* https://www.worldcat.org/title/analytical-methods-in-fine-particle-technology/oclc/38873031

Weber, H., & Plötze, M. (2007). *Emplacement test with granular bentonite*. Nagra Working Report NAB 07. Wettingen, Switzerland: Nagra. https://www.andra.fr/mini-sites/lille2007/abstract_lille2007/donnees/pdf/247_248_P_GSI_20.pdf.

Wieczorek, K., Gaus, I., Mayor, J. C., Schuster, K., García-Siñeriz, J. L., & Sakaki, T. (2017). In-situ experiments on bentonite-based buffer and sealing materials at the Mont Terri rock laboratory (Switzerland). *Swiss Journal of Geosciences*, *110*(1), 253–268. https://doi.org/10.1007/s00015-016-0247-y

Ye, W. M., Borrell, N. C., Zhu, J. Y., Chen, B., & Chen, Y. G. (2014). Advances on the investigation of the hydraulic behavior of compacted GMZ bentonite. *Engineering Geology*, *169*, 41–49. https://doi.org/10.1016/j.enggeo.2013.11.003

Yong, R. N., Boonsinsuk, P., & Wong, G. (1986). Formulation of backfill material for a nuclear fuel waste disposal vault. *Canadian Geotechnical Journal*, *23*(2), 216–228.

Zeng, Z., Cui, Y. J., Zhang, F., Conil, N., & Talandier, J. (2019). Investigation of swelling pressure of bentonite/claystone mixture in the full range of bentonite fraction. *Applied Clay Science*, *178*(October 2018), 105137. https://doi.org/10.1016/j.clay.2019.105137

Zhu, C. M., Ye, W. M., Chen, Y. G., Chen, B., & Cui, Y. J. (2013). Influence of salt solutions on the swelling pressure and hydraulic conductivity of compacted GMZ01 bentonite. *Engineering Geology*, *166*, 74–80. https://doi.org/10.1016/j.enggeo.2013.09.001

Zimmerman, R. W. (2018). *Imperial College Lectures In Petroleum Engineering, The-Volume 5: Fluid Flow In Porous Media*. World Scientific.

Appendix-A Calibration of total stress and water pressure transducers

The infiltration column transducers were carefully calibrated for loading water pressure from 0.5MPa to 7MPa. The Honeywell sensors model A-105 was used to measure the total stress (TS) and the water pressure (Pw) in the mock-up test where these are a flush diaphragm pressure transducer with no dead volume, stainless steel, flush-mount design and range between 1MPa to 20MPa.

In figure A-1 presents, the sensor for total stress and water pressure where the latter mentioned were added steel tube to reduce the dead volume (solid steel tube) and filter paper and geotextile to avoid the material enter in the hole.

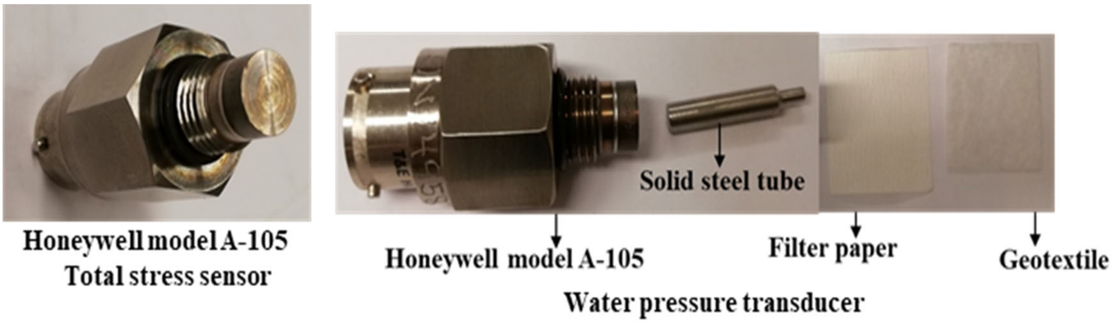

Figure A-1. Sensors Honeywell model A-105 used for measuring the total stresses and water pressure.

In figure A-2, shows the different calibrations and the equations for each sensor in the infiltration column furthermore the locations of each transducer in a different place of the mock-up test. The behaviour of each sensor is linear and presents a different equation for every transducer. During the calibration, it imposed the pressure and measured the volt to get the equation for each sensor.

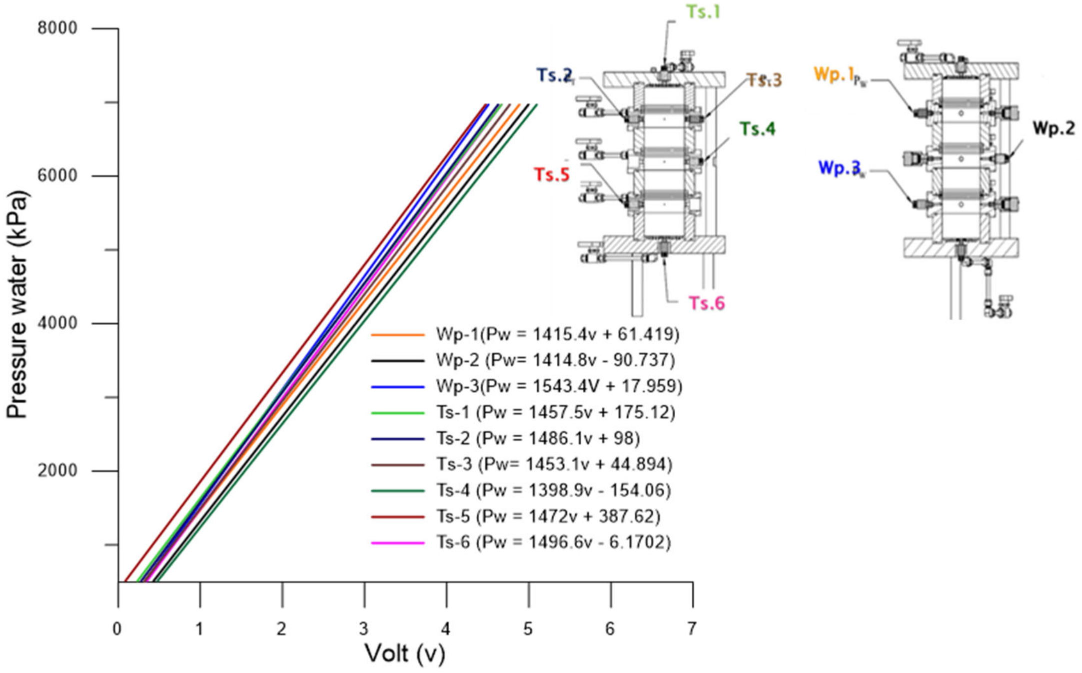

Figure A-2. Calibration of the transducer Honeywell model A-105.

Appendix-B Relative humidity probes

The sensor used to measure the relative humidity (iButton DS1923) is a rugged, self-sufficient system that measures temperature and/or relative humidity minor of 95%. The iButton is configured and communicates with a computer through the serial 1-Wire® protocol, which requires only a single data lead and a program called Express Thermo to configure and collect the data. The size is 17.35mm in diameter and 5.89mm in height. Figure B-3.1, shows the iButton and the box made to placed the sensors in the infiltration column.

The transducers are already calibrated but also was carefully confirmed the calibration with a different solution. The solutions used were NaCl ($36g/100H_20$), LiCl($86g/100H_2O$) and distilled water. Figure B-4 can see the result obtained for the various solution with the iButton. The sensor was in contact with the different vapour solution for 10 days to guarantee the equilibration.

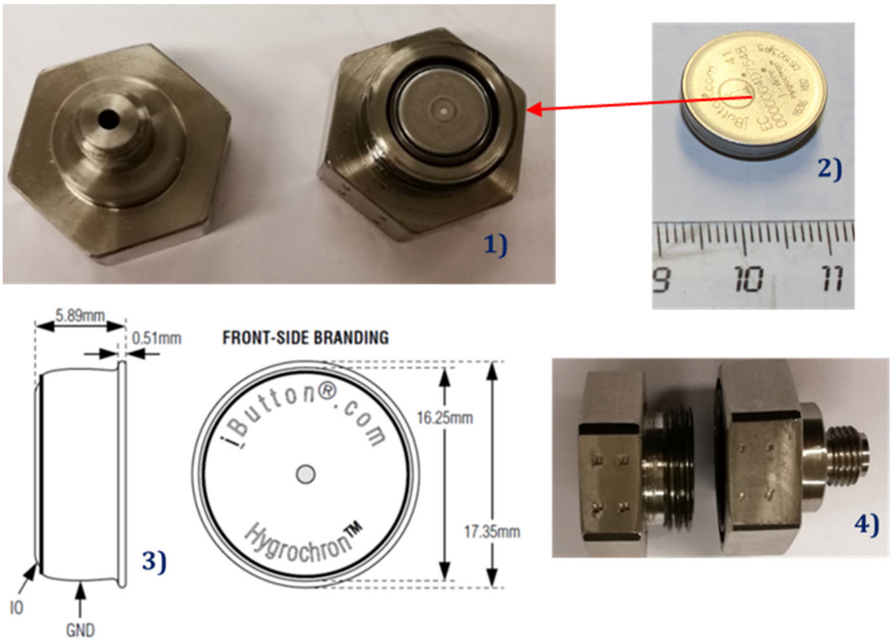

Figure B-3: 1) iButton inside the box. 2)iButton. 3) Dimensions of iButton. 4) Box built for the ibutton in the infiltration column.

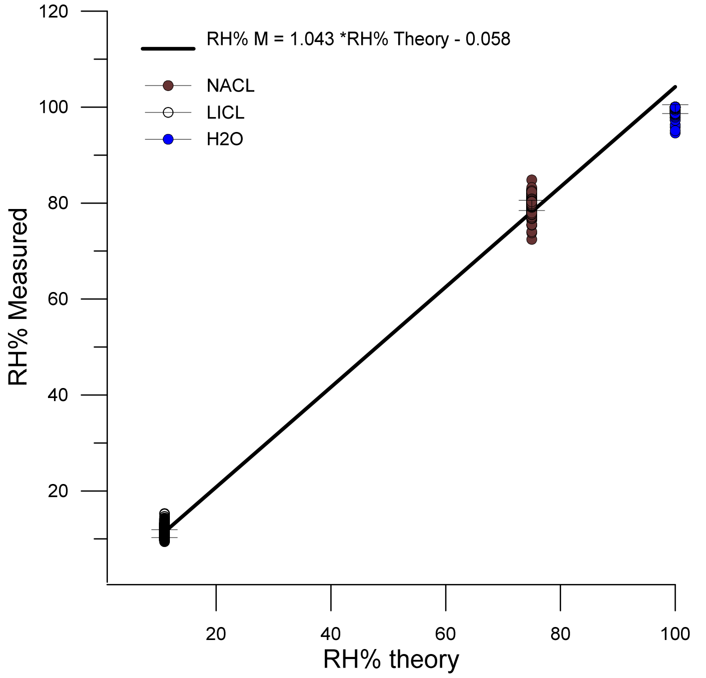

Figure B-4. The relation between RH% measured and RH% theory.

Different concentration was made to confirm the iButton calibration with Sodium chloride (NaCl). Five concentration were made (36g/100H2O, 20g/100H2O, 15g/100H2O, 10g/100H2O, 5g/100H2O) and measure with the iButton and Decagon WP4. Figure B-5 show the relationship between each one.

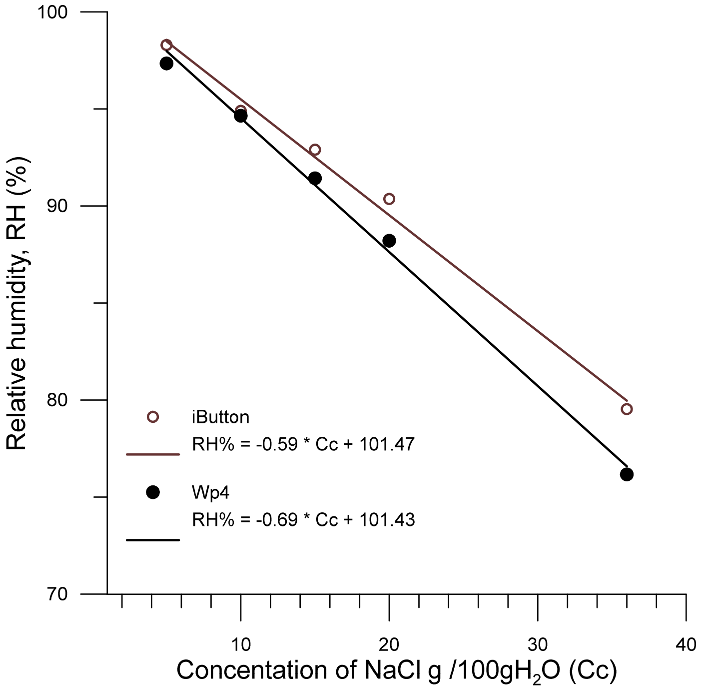

Figure B-5. Comparison between relative humidity measured with iButton and Decagon WP4 with the same concentration.